

University of Southampton Research Repository  
ePrints Soton

Copyright © and Moral Rights for this thesis are retained by the author and/or other copyright owners. A copy can be downloaded for personal non-commercial research or study, without prior permission or charge. This thesis cannot be reproduced or quoted extensively from without first obtaining permission in writing from the copyright holder/s. The content must not be changed in any way or sold commercially in any format or medium without the formal permission of the copyright holders.

When referring to this work, full bibliographic details including the author, title, awarding institution and date of the thesis must be given e.g.

AUTHOR (year of submission) "Full thesis title", University of Southampton, name of the University School or Department, PhD Thesis, pagination

UNIVERSITY OF SOUTHAMPTON

**The Development of Data Driven  
Approaches to Further Turbulence  
Closures**

by

Jack Weatheritt

A thesis submitted in fulfillment for the  
degree of Doctor of Philosophy

in the  
Faculty of Engineering and the Environment  
Institute for Complex Systems Simulation

November 2015



UNIVERSITY OF SOUTHAMPTON

ABSTRACT

FACULTY OF ENGINEERING AND THE ENVIRONMENT  
INSTITUTE FOR COMPLEX SYSTEMS SIMULATION

Doctor of Philosophy

by Jack Weatheritt

The closure of turbulence models at all levels of fidelity is addressed, using unconventional methods that rely on data. The purpose of the thesis is not to present new models of turbulence *per se*, but rather the main focus is to develop the methodologies that created them.

The main tool, Gene Expression Programming, is a versatile evolutionary algorithm. Implementations of the algorithm allow for symbolic regression of scalar and tensor fields and the clustering of data sets. The last two applications are novel algorithms.

Scalar field regression is used to construct length scale damping functions for Hybrid RANS/LES. Direct Numerical Simulation snapshots are filtered to mimic Hybrid RANS/Les flow fields and from this new damping functions are created. Two closures are constructed, one from data in a turbulent pipe and another from slices along the classic backward facing step geometry. The new closures are tested for a range of separated flow applications. Tests alongside existing closures of the same class show that both new methods adapt to the local mesh resolution and turbulence level at least as well as other hybrid closures.

Tensor field regression is used to construct non-linear stress-strain relationships in a Reynolds-Averaged Navier-Stokes framework. A common two-equation model is modified by including a further term that accounts for extra anisotropy with respect to the Boussinesq approximation. This model term, regressed from time averaged Direct Numerical Simulation data, turns the linear closure into an Explicit Algebraic Stress Model. The training data is taken from the reverse flow region behind a backward facing step. When applied to the classic periodic hills case, the subclass of models generated are found to greatly improve the prediction with respect to the linear model. A subclass of models is created in order to test the ability of the evolutionary algorithm. The deviation from the periodic hills reference data is quantified and used as a metric for model performance. The key finding is that improved performance of the Gene Expression Programming framework corresponded to improved prediction of the periodic hills.

The final application of Gene Expression Programming, the clustering of datasets, is used to group Reynolds stress structures into distinct types. Firstly, reference Direct Numerical Simulation data obtained in a turbulent channel is categorised into six distinct groups. These groups are then compared to structures from Hybrid RANS/LES. These groups help to show that Hybrid RANS/LES structures do not correctly capture the near-wall cycle of turbulence. Instead there is an artificial cycle that is characterised by an incorrect buffer layer, defined by tall, long and thin structures. Further, streaky structures lie on the interface between Reynolds-Averaged Navier-Stokes and Large Eddy Simulation. These structures are free to move in the vertical direction and seriously contribute to discrepancies in the second order statistics.

# Contents

<b>List of Figures</b>	<b>ix</b>
<b>List of Tables</b>	<b>xv</b>
<b>Nomenclature</b>	<b>xxii</b>
<b>1 Fundamentals of Turbulence</b>	<b>1</b>
1.1 Introduction . . . . .	1
1.2 Defining Scales of Turbulence . . . . .	3
1.3 Defining States of Turbulence . . . . .	4
1.4 Motivation . . . . .	6
1.5 Outline of Thesis . . . . .	7
<b>2 Methodologies for Calculating Turbulence</b>	<b>11</b>
2.1 High Fidelity Approach - Direct Numerical Simulation . . . . .	11
2.2 Reducing the Cost of Turbulence Calculations . . . . .	12
2.2.1 Large Eddy Simulation . . . . .	13
2.2.2 Turbulence Modelling - Reynolds-Averaging the Navier-Stokes . .	15
2.2.3 Closures for the Reynolds-Averaged Navier-Stokes Equations . .	17
2.2.3.1 Linear Eddy Viscosity Models . . . . .	17
2.2.3.2 Reynolds Stress Modelling . . . . .	23
2.2.3.3 Explicit Algebraic Stress Modelling . . . . .	25
2.2.4 Hybrid Modelling . . . . .	29
2.2.4.1 Global Methodologies . . . . .	30
2.2.4.2 Global URANS Closures . . . . .	32
2.2.4.3 Global LES Closures . . . . .	36
2.2.4.4 Issues with and Ongoing Development of Global Methods	40
2.3 Summary . . . . .	41
2.3.1 Choice of Prediction Strategy . . . . .	41
2.3.2 Avenues of Exploration for Current Research . . . . .	42
<b>3 Evolutionary Algorithms</b>	<b>43</b>
3.1 A Brief Note on Other Optimisation Strategies . . . . .	43
3.2 Overview of Evolutionary Algorithms . . . . .	43
3.3 Genetic Algorithms . . . . .	45
3.3.1 Overview . . . . .	45
3.3.2 Replication . . . . .	46
3.3.3 Genetic Operators . . . . .	49

3.3.4	Limitations . . . . .	50
3.4	Genetic Programs . . . . .	51
3.4.1	Overview . . . . .	51
3.4.2	Genetic Operators . . . . .	52
3.4.3	Limitations . . . . .	55
3.5	Gene Expression Programming . . . . .	56
3.5.1	Overview . . . . .	56
3.5.2	The Genome . . . . .	57
3.5.3	Multigenics . . . . .	63
3.5.4	Fitness and Selection . . . . .	65
3.5.5	Multi-Objective Fitness Criteria . . . . .	67
3.5.6	Genetic Operators . . . . .	69
3.5.6.1	Mutation . . . . .	69
3.5.6.2	Crossover . . . . .	70
3.5.6.3	Transposition . . . . .	71
3.5.6.4	Inversion . . . . .	72
3.5.7	Random Numerical Constants . . . . .	73
3.5.8	Limitations . . . . .	75
3.6	Summary . . . . .	75
<b>4</b>	<b>Implementation of Gene Expression Programming Environments</b>	<b>77</b>
4.1	Introduction . . . . .	77
4.2	Scalar Field Regression . . . . .	77
4.3	Beyond scalar fields . . . . .	82
4.3.1	Motivation . . . . .	82
4.3.2	Concept of a Plasmid . . . . .	84
4.3.2.1	Plasmids in Biology . . . . .	84
4.3.2.2	Plasmids in Evolutionary Computation . . . . .	84
4.3.3	A New Plasmid Implementation . . . . .	86
4.3.3.1	Endosymbiotic Genomes . . . . .	86
4.3.3.2	The MGEPE Algorithm . . . . .	88
4.3.3.3	Higher Dimensional Fitness . . . . .	89
4.4	Clustering Algorithm . . . . .	90
4.4.1	Individuals in GEP Clustering . . . . .	92
4.4.2	Fitness Function and Metric . . . . .	95
4.4.3	Full Algorithm . . . . .	97
4.5	Summary . . . . .	98
<b>5</b>	<b>Evolutionary Optimisation of the Anisotropy Tensor</b>	<b>99</b>
5.1	Introduction . . . . .	99
5.2	Baseline Model . . . . .	102
5.3	Methodology . . . . .	103
5.3.1	Training Data . . . . .	104
5.3.2	<i>A Posteriori</i> Test Case . . . . .	105
5.3.3	<i>A Priori</i> Optimisation . . . . .	106
5.4	<i>A Posteriori</i> Results . . . . .	111
5.5	The Link Between the Two Environments . . . . .	117

5.6	Summary	118
<b>6</b>	<b>Gene Expression Programming Applied to Flow Simulation Methodology</b>	<b>123</b>
6.1	Motivation	123
6.2	Process	125
6.3	GEP Studies	127
6.3.1	Preliminary Study - Pipe Flow	127
6.3.2	Backward Facing Step Flow	129
6.4	Creation of Full Hybrid Models	137
6.5	Summary	138
<b>7</b>	<b>Application of Hybrid RANS/LES to the Planar Channel</b>	<b>139</b>
7.1	Hybrid RANS/LES at Solid Boundaries	139
7.2	Planar Channel Flow	144
7.2.1	Problem Definition	144
7.2.2	Statistical Results and Comments	145
7.2.3	The Instantaneous Flow Field	153
7.2.3.1	Overview	153
7.2.3.2	Extracting Turbulent Shear Stress Structures	154
7.2.3.3	The Groups of Extracted Turbulent Shear Stress Structures and a Brief Defence of its Use	157
7.2.3.4	Comparisons of Extracted Turbulence Shear Stress Structures	159
7.3	Summary	173
<b>8</b>	<b>Applications of Hybrid RANS/LES to Separated Flow</b>	<b>179</b>
8.1	Introduction	179
8.2	Vertical Fence	180
8.2.1	Geometry Definition	180
8.2.2	Results and Discussion	182
8.3	Two Dimensional Periodic Hills	183
8.3.1	Flow Description	183
8.3.2	Computational Domain and Boundary Conditions	184
8.3.3	Results and Discussion	187
8.4	Inline Tandem Cylinders	193
8.4.1	Flow Description	193
8.4.2	Computational Domain and Setup Conditions	194
8.4.3	Results and Discussion	195
8.4.3.1	The Comparison of DDES with the Modified FSM	196
8.4.3.2	On the Difficulty of the Tandem Cylinder Geometry	201
8.4.3.3	Further Comments Specific to the Modified FSM	203
8.5	Summary	204
<b>9</b>	<b>Conclusions and Outlook</b>	<b>207</b>
9.1	Advances in Gene Expression Programming	207
9.2	Advances in Turbulence Modelling	208
9.3	Outlook and Recommendations	210

<b>A Equations for Each Model <math>a_{ij}^x</math></b>	<b>213</b>
<b>Bibliography</b>	<b>221</b>

# List of Figures

1.1	The Lumley triangle representing all realisable states of turbulence . . . . .	5
1.2	Dependency diagram of thesis and suggested reading orders. Lines are directed downwards. Solid lines move down one level and dashed lines move down two levels. . . . .	9
3.1	The flow of a typical Genetic Algorithm. This simplified diagram is the structure of almost all Evolutionary Algorithms. . . . .	47
3.2	Parse tree individual. Terminals exist on leaves, functions as branches. The mathematical expression of this individual is $\log(y) - (1 + x)$ . . . . .	52
3.3	Individual before mutation. The randomly generated tree to be inserted is red as is the mutation location. . . . .	53
3.4	The resulting individual of the above mutation. The mutated structure is shown in red. . . . .	53
3.5	Before (left) and after (right) the permutation operator. . . . .	54
3.6	Individuals before crossover. The material to be swapped is shown in red and black colours and the point is marked as crossover. . . . .	54
3.7	The children of the above crossover. All red genetic material constitutes the right individual whilst all the black genetic materials constitutes the left. . . . .	55
3.8	Detailed look at a GEP implementation. (—) represents overall direction, (---) the additional details behind the main process and (.....) conditional statements. . . . .	58
3.9	Example Expression Tree corresponding to Eq. 3.5. . . . .	60
3.10	Incorrectly specified genes result in incomplete ETs. Nodes are left empty due to a lack of genetic information in the genotype. . . . .	61
3.11	Example Expression Tree corresponding to Eq. 3.7. . . . .	62
3.12	Example Expression Tree corresponding to Eq. 3.8. Dashed nodes correspond to symbols from the tail. . . . .	63
3.13	The two sub-ETs formed from the above multigenic chromosome. . . . .	64
3.14	Full expression of multigenic chromosome. . . . .	65
3.15	Pareto front for 22 individuals being subjected to the fitness criteria $f(P_j^i)^k$ , $k = 1, 2$ . The Pareto front represents the individuals not strictly dominated by any other and so are feasible solutions to the optimisation problem. . . . .	68
3.16	Expression Tree before interpreting RNCs. . . . .	74
3.17	Expression Tree after interpreting RNCs. . . . .	74

4.1	The individual and plasmid ET for Eq. 4.7. The left is the higher dimensional chromosome, whilst the right is the scalar field plasmid. The link shows the point where the plasmid expression latches onto the host. . . . .	88
4.2	The general flow of the MGEP algorithm, with the plasmid step detailed. . . . .	89
4.3	Example clustering. Red and blue scatter: data points $x_i$ distinguished by the desired grouping. Black crosses: example of a good $\mathcal{C}$ . Orange crosses: example of a bad $\mathcal{C}$ . Green circle: previously unseen data point. . . . .	92
4.4	Example Cluster ET . . . . .	93
4.5	Example Cluster ET that is invalid with the original specification of Chen et al. (2007) . . . . .	94
5.1	Training data location from DNS. Filled by mean streamwise velocity $U$ , lines are the ratio of $v^{\text{rms}}/u^{\text{rms}}$ (contour levels : 0.4, 0.6, 0.8). . . . .	104
5.2	Streamlines for RANS closures, compared to Hybrid RANS/LES. . . . .	106
5.3	Computational grid. . . . .	106
5.4	First cell centre wall distance $y^+$ (left). Grid and time convergence of the skin friction along the lower surface $C_f$ . TU denotes time units $H/U_b$ . . . . .	107
5.5	Typical plot of population and best fitness $f$ . . . . .	109
5.6	Individual $P_n^j$ fitness $f$ against expression length $\ell$ , coloured by the number of distinct tensor bases $N_{Tk}$ . . . . .	109
5.7	Effect of terminal $S^k$ on individual $P_n^j$ fitness $f$ and length $\ell$ . . . . .	110
5.8	Normalised histogram of the fitness of chromosomes obtained completely at random. Green band is a normalised histogram of the best solutions from GEP (y-axis extends to 24.5). Left: full fitness domain. Right: closeup of highest values of fitness. . . . .	110
5.9	Ensemble skin friction coefficient $C_f$ . Bars are 99% confidence interval. . . . .	112
5.10	Ensemble velocity and Reynolds-stress at $x/H = 0.05$ , bars represent 99% confidence interval. Each stress component is labelled, the highest peak of each modelled line is $\overline{u'u'}$ . . . . .	112
5.11	Ensemble velocity and Reynolds-stress at $x/H = 0.5$ , bars represent 99% confidence interval. . . . .	113
5.12	Ensemble velocity and Reynolds-stress at $x/H = 2.0$ , bars represent 99% confidence interval. . . . .	113
5.13	Ensemble velocity and Reynolds-stress at $x/H = 3.0$ , bars represent 99% confidence interval. . . . .	114
5.14	Ensemble velocity and Reynolds-stress at $x/H = 4.0$ , bars represent 99% confidence interval. . . . .	114
5.15	Ensemble velocity and Reynolds-stress at $x/H = 5.0$ , bars represent 99% confidence interval. . . . .	115
5.16	Ensemble velocity and Reynolds-stress at $x/H = 6.0$ , bars represent 99% confidence interval. . . . .	115
5.17	Ensemble velocity and Reynolds-stress at $x/H = 7.0$ , bars represent 99% confidence interval. . . . .	116
5.18	Ensemble velocity and Reynolds-stress at $x/H = 8.0$ , bars represent 99% confidence interval. Notice the labelled switch between the normal stress component magnitudes. . . . .	116
5.19	Probability density function for breaking realisability, $\overline{u'v'} < \overline{u'u'} \cdot \overline{v'v'}$ (contour levels : 0.0, 0.25, 0.5, 0.75) (left) and $\overline{u'u'} < 0$ (contour levels : 0.0, 0.7) (right). . . . .	117

5.20	Linear regression of individual fitness $f(P_n^j)$ as a predictor for error in reattachment location $C_f^{err}(P_n^j)$ (left) and residual plot for regression. . . . .	119
5.21	Linear regression of the number of distinct tensors $N_{T_k}$ in individual $P_n^j$ as a predictor for error in reattachment location $C_f^{err}(P_n^j)$ (left). Influence of symbol $S^k$ on an individuals skin friction coefficient $C_f^{err}(P_n^j)$ (right). . . . .	119
5.22	Linear regression of the fitness of an individual given tensor basis $f(P_n^j S^k)$ as a predictor of the individuals error in reattachment location $C_f^{err}(P_n^j S^k)$ . Hollow circles are the individuals $P_n^j$ and coloured circles contained within show symbols $S^k$ present in given solution. . . . .	120
6.1	Instantaneous snapshot of $u'/\bar{u}$ for the pipe flow. Streamwise direction is left to right, vertical direction is the pipe diameter. . . . .	127
6.2	The idealised contribution function and the length scales calculated for the pipe flow. . . . .	128
6.3	Results from GEP process compared with FDNS data and Speziale's original function, Eq. 2.74. . . . .	129
6.4	Mean statistics from the backward facing step DNS. . . . .	130
6.5	Convergence of $\varepsilon$ . . . . .	131
6.6	Length scales for the backward facing step flow. $L_k$ has been factored by 0.04 in order to fit conveniently into the plots. . . . .	131
6.7	Idealised contribution function calculated for the backward facing step FDNS data. . . . .	132
6.8	Average frequency of length scales throughout the top 10% of the population given generation (Transient probability of occurrence). . . . .	134
6.9	Average fitness (Eq. 4.1) of the top 2% of the population given a length scale present. Average frequency of each length scale of the top 2% of the population given a length scale present. Ensemble statistics are gathered for the beginning and end of each simulation. . . . .	135
6.10	Average comprehensibility (Eq. 4.2) of top 2% of population given length scale present. Average frequency of each length scale of top 2% of population. Ensemble statistics are gathered for the beginning and end of each simulation. . . . .	136
7.1	Average streamwise velocity for all cases. . . . .	146
7.2	Shear stress for the differing wall methodologies. Dashed lines depict the modelled and resolved contributions. . . . .	147
7.3	Turbulent kinetic energy for all cases. Grey lines depicted modelled and resolved contributions. . . . .	148
7.4	Total Reynolds stress profiles for each model. . . . .	149
7.5	The length scale damping function $F$ for each case. . . . .	150
7.6	Anisotropy tensor normal components $b_{ij} = \bar{u}_i \bar{u}_j / 2k - 1/3 \delta_{ij}$ . . . . .	151
7.7	Invariant map for each case. . . . .	152
7.8	Streamwise velocity fluctuations at constant $y^+$ profiles. Left: FSM-SSG-95-5-DDES. Right: FSM-SSG-95-5-Fz. . . . .	153
7.9	Percolation diagram of the number of structures $N/N_{max}$ and volume $V/V_{max}$ ratios and against $H$ . Lines with symbols are $N/N_{max}$ and lines without symbols is $V/V_{max}$ . . . . .	155

7.10 Extracted structure from FSM-SSG-95-5-DDES. Quantities from Table 7.3 are included for visual reference. Length of the structure is approximately 650 wall units. The structure is coloured by the flow field average velocity magnitude. . . . .	156
7.11 Probability density function of $y_{\max}/h$ against $y_{\min}/h$ . Comparison of DNS with FSM-SSG-95-5-DDES and FSM-SSG-95-5-Fz. Grey contours are the full set of structures, the levels are increments of 10% the maximum value on a logarithmic scale starting from 40%. Coloured lines are contours of each cluster type, colours follow that in Table 7.4. Groups 4 and 5 have been omitted due to too few samples. The levels shown for the cluster groups are 40% and 60% of the maximum on a logarithmic scale. The constraint $y_{\max} = y_{\min}$ is included, along with $F_{\text{switch}}$ for the hybrid cases. . . . .	161
7.12 Probability density function of $y_{\max}/h$ against $y_{\min}/h$ for DNS. Grey contours are the full set of structures, levels are 10% increments of the maximum value on a logarithmic scale starting at 40%. Red scatter points are the structures that lie above the line Eq. 7.22. The included line is Eq. 7.23. . . . .	162
7.13 Probability density function of $\bar{v}^+$ against $\bar{u}^+$ . Comparison of DNS with FSM-SSG-95-5-DDES and FSM-SSG-95-5-Fz. Grey contours are the full set of structures, the levels are 10% increments of the maximum value on a logarithmic scale starting from 20%. Coloured lines are contours of each cluster type, colours follow that in Table 7.4. Groups 3, 4 and 5 (DNS only) have been scattered due to too few samples. The levels shown for the cluster groups are 10% increments of the maximum value on a logarithmic scale starting from 50%. . . . .	163
7.14 Probability density function of $\ell_z/h$ against $\ell_x/h$ . Comparison of DNS with FSM-SSG-95-5-DDES and FSM-SSG-95-5-Fz. Grey contours are the full set of structures, the levels are 10% increments of the maximum value on a logarithmic scale. Coloured lines are contours of each cluster type, colours follow that in Table 7.4. Groups 4 and 5 have been scattered due to too few samples. The levels shown for the cluster groups are 20% increments of the maximum value on a logarithmic scale. Linear regression lines are shown for the DNS (red) and hybrid (black). . . . .	166
7.15 Example large group 3 structure. Structure is 6 channel heights long. . . . .	167
7.16 Example large group 3 structure. Structure is 4 channel heights long. . . . .	167
7.17 Probability density function of $\ell_x/h$ against $\mathcal{V}/h^3$ . Comparison of DNS with FSM-SSG-95-5-DDES and FSM-SSG-95-5-Fz. Grey contours are the full set of structures, levels are 10% increments of the maximum value on a logarithmic scale. Coloured lines are contours of each cluster type, colours follow that in Table 7.4. Groups 3, 4 and 5 (DNS only) have been scattered due to too few samples. The levels shown for the cluster groups are 20% increments of the maximum value on a logarithmic scale. Regression lines are shown for the DNS (red) and hybrid (black). For the regression, $\log(\mathcal{V}/h^3)$ is used as the independent variable and the data is split into two groups, the clusterings $c_0, c_1, c_2$ and $c_3, c_4, c_5$ . . . . .	168

7.18	Probability density function of $y_{\min}/h$ against $\mathcal{V}/h^3$ . Comparison of DNS with FSM-SSG-95-5-DDES and FSM-SSG-95-5-Fz. Grey contours are the full set of structures, levels are 10% increments of the maximum value on a logarithmic scale. Coloured lines are contours of each cluster type, colours follow that in Table 7.4. Groups 4 and 5 have been omitted due to too few samples. The levels shown for the cluster groups are 20% increments of the maximum value on a logarithmic scale. . . . .	170
7.19	Violin plot of the variation in streamwise length $\ell_x/h$ given number of grid points in the spanwise direction. Scatter shows individual structures. Shape of violin is an estimate of the distribution. Dashed lines are the median and lower and upper quartiles. . . . .	171
7.20	Violin plot of the variation in streamwise length $\ell_x/h$ given number of grid points in the spanwise direction. Scatter shows individual structures. Shape of violin is an estimate of the distribution. Dashed lines are the median and lower and upper quartiles. . . . .	171
7.21	Violin plot of the variation in streamwise length $\ell_x/h$ given number of grid points in the spanwise direction. Scatter shows individual structures. Shape of violin is an estimate of the distribution. Dashed lines are the median and lower and upper quartiles. . . . .	172
7.22	Probability density function of $ \bar{u}'v'^+ $ against $\bar{v}^+$ for the FSM-SSG-95-5-DDES and FSM-SSG-95-5-Fz cases. $(\cdot)$ is the average over the structure. Only ejections and sweeps are included. Plots are for both the full flow field and the log-layer (defined by $y/h < 0.2$ ). Contours are the full set of structures, levels are 10% increments of the maximum value on a logarithmic scale. Colours follow the ordering in Table 7.4. The red dashed lines are $\bar{u}'v'^+ = \pm 2.5\bar{v}^+$ . . . . .	174
7.23	Probability density function of the modelled subgrid kinetic energy $k_{sgs}^+$ inside a structure against the average fluctuation $\bar{v}^+$ for the FSM-SSG-95-5-DDES and FSM-SSG-95-5-Fz cases. Grey contours are of structures within the buffer layer at 10% increments of the maximum value on a logarithmic scale. Coloured lines are contours for each cluster group, again only considering structures inside the buffer layer, at 20% increments of the maximum value on a logarithmic scale. Colours follow the ordering in Table 7.4. . . . .	175
7.24	Probability density function of the modelled subgrid kinetic energy $k_{sgs}^+$ inside a structure against the centre point of the structure $y_c/h$ for the FSM-SSG-95-5-DDES and FSM-SSG-95-5-Fz cases. Grey contours are the full set of structures at 10% increments of the maximum value on a logarithmic scale. Coloured lines are contours for each cluster group at 20% increments of the maximum value on a logarithmic scale. Colours follow the ordering in Table 7.4. The red dashed line is the average $k_{sgs}^+(y^+)$ for the entire flow field. . . . .	176
8.1	Vertical fence case computational domain and grid around the surface mounted obstacle. . . . .	180
8.2	Mean velocity profiles at eight streamwise locations. . . . .	181
8.3	Root mean square velocity profiles at eight streamwise locations. . . . .	182
8.4	$x - y$ plane of the two dimensional periodic hills geometry. . . . .	185
8.5	The two meshes used for the Periodic Hills test case. Left: coarse mesh. Right: fine mesh. . . . .	185

---

8.6 Skin friction along lower surface and profiles of turbulent kinetic energy, streamwise velocity and component of Reynolds stress along the plane $x/H = 2.0$ . . . . .	189
8.7 Instantaneous values of $\nu^{\text{sgs}}/\nu$ . . . . .	190
8.8 Mean values of $\nu^{\text{sgs}}/\nu$ . . . . .	191
8.9 Instantaneous values of the damping functions $F$ . . . . .	192
8.10 Mean values of the damping functions $F$ . . . . .	193
8.11 $x - y$ plane of the Tandem Cylinders geometry. . . . .	195
8.12 Mesh for the inline tandem cylinders case. . . . .	195
8.13 Isosurfaces of $Q$ criterion at $170000ms^{-2}$ , coloured by instantaneous streamwise velocity $u_x$ , for the FSM cases. . . . .	197
8.14 Isosurfaces of $Q$ criterion at $170000ms^{-2}$ , coloured by instantaneous streamwise velocity $u_x$ , for non-FSM cases. . . . .	197
8.15 Isosurfaces of $Q$ criterion at $170000ms^{-2}$ , coloured by instantaneous streamwise velocity $u_x$ , a side view comparison of FSM-SSG-95-5 and DDES-SA-95-5. . . . .	198
8.16 Mean values of $\nu^{\text{sgs}}/\nu$ . . . . .	198
8.17 Averaged streamwise velocity $U_x/U_0$ in the gap region. . . . .	199
8.18 Averaged streamwise velocity $U_x/U_0$ in the gap region. . . . .	199
8.19 Averaged two dimensional turbulent kinetic energy $k^{2D} = 0.5(\overline{u'u'}^{\text{res}} + \overline{v'v'}^{\text{res}} + \tau_{11}^{\text{rans}} + \tau_{22}^{\text{rans}})$ in the gap region. DDES is resolved $k^{2D}$ only. . . . .	200
8.20 Averaged two dimensional turbulent kinetic energy $k^{2D} = 0.5(\overline{u'u'}^{\text{res}} + \overline{v'v'}^{\text{res}} + \tau_{11}^{\text{rans}} + \tau_{22}^{\text{rans}})$ in the gap region. DDES is resolved $k^{2D}$ only. . . . .	201
8.21 Steady pressure coefficient $C_p$ on the upstream and downstream cylinders. . . . .	202
8.22 Fluctuating pressure coefficient $C_p^{\text{rms}}$ on the upstream and downstream cylinders. . . . .	202
8.23 The two different flow field states. . . . .	203
8.24 Instantaneous modified FSM damping function $F$ . . . . .	204

# List of Tables

1	List of symbols. . . . .	xxi
2	List of Acronyms. . . . .	xxi
2.1	Table of model constants for EASM models. . . . .	28
3.1	Generated Random Numerical Constants are stored with an index, so that chromosomes make use of them during the evolutionary process. . . .	73
5.1	Values of all parameters used in GEP optimisation. . . . .	107
7.1	Hybrid RANS/LES cases considered for the planar channel flow. . . . .	144
7.2	Error in skin friction, location of the peak modelled, resolved and total stresses, the RANS-LES interface and the size of the buffer layer for each case. The latter is defined by the distance between the modelled and resolved peaks. . . . .	146
7.3	Features of each structure considered. . . . .	155
7.4	The six different types of structure found by the GEP algorithm. The frequencies are for the DNS, FSM-SSG-95-5-DDES and FSM-SSG-95-5-Fz cases — the column headings are abbreviated for space. . . . .	157
8.1	Hybrid RANS/LES periodic hills cases . . . . .	186
8.2	Separation and reattachment points for reference LES and hybrid simulations. The LES simulations are MFR (Fröhlich et al., 2005), TL (Temerman and Leschziner, 2001) and B (Breuer et al., 2009). . . . .	187
8.3	Hybrid RANS/LES tandem cylinder cases . . . . .	196



# Nomenclature

Table 1 is a comprehensive list of symbols used throughout this work. Where appropriate a supplementary equation is provided. Table 2 is a list of abbreviations that are recurrent. Note subscripts and superscripts are often used interchangeably, depending on other required identification (e.g. wall units).

Symbol	Description	Definition
<b>Fluid Mechanics Symbols</b>		
$a_{ij}$	Anisotropy tensor	$a_{ij} = \langle u'_i u'_j \rangle - (2/3)k\delta_{ij}$
$a_{ij}^x$	Extra anisotropy tensor with respect to the Boussinesq approximation	$a_{ij}^x = a_{ij} + 2\nu_t S_{ij}$
$b_{ij}$	Normalised anisotropy tensor	$b_{ij} = (1/2)a_{ij}/k$
$C_f$	Skin Friction Coefficient	$\tau_w / (\frac{1}{2}\rho U_\infty)$
$C_p$	Pressure Coefficient	$(p - p_\infty) / (\frac{1}{2}\rho U_\infty)$
$D$	Cylinder diameter	
$f_b$	Damping function from Menter (1994) SST turbulence model	
$F$	Length scale damping function	
$F_z$	Shielding function	
$F_{f_b}$	Shielding function using $f_b$	
$h$	Fence height	
$H$	Hill / step height	
$II_b$	Second invariant of the anisotropy tensor $b_{ij}$	$(1/2)b_{ij}b_{ij}$
$III_b$	Third invariant of the anisotropy tensor $b_{ij}$	$\det(b_{ij})$
$k$	Turbulent kinetic energy	$(1/2)\langle u'_i u'_i \rangle$
$\ell$	Length scale	
$\ell_k$	Kolmogorov length scale	$(\nu^3/\varepsilon)^{1/4}$
$\ell_t$ ( $\ell^{\text{rans}}$ )	RANS length scale	

	(integral length scale estimate)	$k^{3/2}/\varepsilon$
$\ell_\lambda$	Taylor Micro-scale estimate	$\sqrt{10k\nu/\varepsilon}$
$L_k$	Ratio of grid scale to Kolmogorov length scale	$\Delta/\ell_k$
$L_t$	Ratio of grid scale to integral length scale	$\Delta/\ell_t$
$L_{\text{oes}_S} (L_S)$	OES strain rate normalisation	$kS/\varepsilon$
$L_{\text{oes}_\Omega} (L_\Omega)$	OES rotation rate normalisation	$k\Omega/\varepsilon$
$L_\lambda$	Ratio of grid scale to Taylor Micro-scale	$\Delta/\ell_\lambda$
$L_{\text{trrans}} (L_T)$	TRTRANS length scale ratio	$\max(S/(1.25\Omega), 1)^{-2}$
$p$	Static pressure ( $1/\rho$ absorbed)	
$P_k$	Production of turbulent kinetic energy	$\tau_{ij}^{\text{mod}} S_{ij}$
$Q$	Q-criterion	$(1/2)(\Omega^2 - S^2)$
$r$	Pipe radius	
$\text{Re}$	Reynolds number	$u\ell/\nu$
$\text{Re}_\tau$	Friction Reynolds number	$u_\tau\ell/\nu$
$\text{Re}_\phi$	Reynolds number based on length scale $\phi$	$U_\phi\phi/\nu$
$S_{ij}$	Strain rate tensor for $u_i$	$S_{ij} = (1/2)(\partial_{x_j} u_i + \partial_{x_i} u_j)$
$S$	Strain rate tensor magnitude	$\sqrt{2S_{ij}S_{ij}}$
$u_i$	Velocity (components $u$ , $v$ and $w$ )	
$u_i^+$	Velocity in friction scaling	$u_i/u_\tau$
$u_\tau$	Friction velocity	$\sqrt{\tau_w}$
$u^{\text{rms}}$	Root mean square of the velocity fluctuation	$\sqrt{\bar{u}'^2}$
$U$	Reynolds averaged streamwise velocity (occasionally in place of $\bar{u}$ )	
$U_b$	Bulk velocity	
$\langle u'_i u'_j \rangle$	Exact resolved stress with respect to scale separation (occasionally used in place of $\tau_{ij}^{\text{rans}}$ )	
$y$	Wall normal coordinate	
$y^+$	Wall normal direction in friction scaling	$u_\tau y/\nu$
$\Delta$	Grid scale	
$\Delta_f$	Filter width	
$\Delta_t$	Time step	
$\varepsilon$	Turbulent dissipation rate	$2\nu \langle \partial_{x_j} u'_i \partial_{x_j} u'_i \rangle, \beta^* k\omega$
$\kappa$	von Kármán constant	0.41

$\mu$	Molecular viscosity	
$\nu$	Kinematic eddy viscosity	$\nu/\rho$
$\nu_t$	Eddy viscosity (occasionally sub-grid if in Hybrid RANS/LES)	$C_\mu k^2/\varepsilon$
$\nu^{\text{sgs}}$	Subgrid eddy viscosity	
$\rho$	Density	
$\tau$	Time scale / stress	
$\tau_w$	Wall shear stress	$\mu \partial_y u_i _{y=0}$
$\tau_t$	Integral time scale estimate	$k/\varepsilon$
$\tau_k$	Kolmogorov time scale	$(\nu/\varepsilon)^{1/2}$
$\tau_{ij}^{\text{hyb}}$	Hybrid RANS/LES model	
$\tau_{ij}^{\text{mod}}$	Generalised mathematical model of unresolved stress	
$\tau_{ij}^{\text{rans}}$	Reynolds-Averaged Navier-Stokes model (Reynolds stress tensor)	
$\tau_{ij}^{\text{sgs}}$	Subgrid scale model (LES style model)	
$\omega$	Specific turbulent dissipation rate	$\varepsilon/(\beta^* k)$
$\Omega_{ij}$	Rotation rate tensor for $u_i$	$\Omega_{ij} = (1/2)(\partial_{x_j} u_i - \partial_{x_i} u_j)$
$\Omega$	Rotation rate tensor magnitude	$\sqrt{2\Omega_{ij}\Omega_{ij}}$
$\langle \cdot \rangle$	Generalised scale separation operator / Ensemble average	
$\overline{(\cdot)}$	Reynolds operator/Time average/Structure average	
$\widetilde{(\cdot)}$	Effective filter	
$\phi'$	Fluctuating part with respect to scale separation operator	

### GEP / EA symbols

$c_i$	Cluster centre of $i^{\text{th}}$ group
$c(P_j^i)$	Comprehensibility fitness of individual $P_j^i$
$\mathcal{C}$	Clustering (phenotype in clustering algorithm)
$E^k$	Expected value of $k^{\text{th}}$ data point (training data)
$f(P_j^i)$	Fitness of individual $P_j^i$
$f(P_j^i)^k$	Phenotypic output for $k^{\text{th}}$ data point
$f(P_j^i)_{mn}^k$	Matrix phenotypic output for $k^{\text{th}}$ data point

$f_c$	Connectivity fitness
$f_d$	Distance fitness
$F$	Desired fitness
$\mathcal{F}$	Function set
$h$	Head length, $1D/3D$ used to distinguish as appropriate
$\ell$	Length of simplified phenotype
$l_e$	Length of unsimplified phenotype
$n$	Number of generations / arity of function / number of cluster groups
$N$	Population size (number of individuals)
$N_g$	Number of genes in chromosome
$p_\phi$	Probability of applying genetic operator $\phi$
$P$	Population of individuals / Plasmid arity one symbol
$P^i$	$i^{\text{th}}$ generation of population $P$
$P_j^i$	$j^{\text{th}}$ individual of generation $P^i$
$P_n^j$	$j^{\text{th}}$ best solution after $n$ generations (Chapter 5)
$\mathcal{P}$	Plasmid set
$r_{\min}$	Minimum value of random numerical constants
$r_{\max}$	Maximum value of random numerical constants
$R$	Range of selection
$s$	Tournament size
$\mathcal{S}$	Symbol set
$t$	Tail length <span style="float: right;"><math>h(n - 1) + 1</math></span>
$\mathcal{T}$	Terminal set

### Miscellaneous

$d$	Generalised distance function / Mahalanobis distance	$d(\underline{x}, \underline{y}) = \sqrt{(\underline{x} - \underline{y})\Sigma^{-1}(\underline{x} - \underline{y})}$
$d_e$	Euclidean distance	$d_e(\underline{x}, \underline{y}) = \sqrt{(\underline{x} - \underline{y}) \cdot (\underline{x} - \underline{y})}$
$d_{ps}$	Point symmetry distance	
$I^k$	Scalar invariants with respect to $T_{ij}^k$	
$T_{ij}^k$	Tensor basis, most often invariants of the Reynolds stress tensor	
$\delta_{ij}$	Kronecker delta	$\delta_{ij} = 0$ if $i \neq j$ , $\delta_{ij} = 1$ otherwise

$\Sigma$  Matrix of covariance

Table 1: List of symbols.

Acronym	Definition
(D)DES	(Delayed) Detached Eddy Simulation
DNS	Direct Numerical Simulation
EA	Evolutionary Algorithm
(E)ASM	(Explicit) Algebraic Stress Model
EP	Evolutionary Programming
ES	Evolutionary Strategy
ET	Expression Tree
FSM	Flow Simulation Methodology
GA	Genetic Algorithm
GEP	Gene Expression Programming
GP	Genetic Programming
IS	Insertion Sequence
LES	Large Eddy Simulation
LNS	Limited Numerical Scales
MGEP	Multi-dimensional Gene Expression Programming
(N)LEVM	(Non-) Linear Eddy Viscosity Model
ORF	Open Reading Frame
PANS	Partially-filtered Navier-Stokes / Phase-Averaged Navier-Stokes
PITM	Partially Integrated Transport Model
RANS	Reynolds-Averaged Navier-Stokes
RIS	Root Insertion Sequence
RNC	Random Numerical Constant
RST	Reynolds Stress Transport
SA	Spalart-Allmaras turbulence model
SAS	Scale Adaptive Simulation
SGS	Subgrid Scale
SMC	Second Moment Closure
SR	Symbolic Regression
SSG	Speziale Sarkar and Gatski turbulence model
SST	Stress-Strain Transport model
TRRANS	Turbulence Resolving RANS

TABLE 2: List of Acronyms.



# Chapter 1

## Fundamentals of Turbulence

### 1.1 Introduction

The most common state of fluids in nature and engineering is one of turbulence. Therefore numerical simulations of turbulent flows are of vital interest to the scientist in understanding physical phenomena and also to the engineer in designing objects that must interact with fluids. A definition of turbulence is not easy, but turbulent flows generally exhibit the same features.

Turbulence is highly irregular, yet is fully physicomathematically determinant. However, a complete description of this is too expensive for industrial applications. Turbulent flows are statistically determinant. That is to say statistical properties such as the mean velocity are deterministic and predictions can be made about them. Turbulence is inherently three dimensional, with eddies moving and interacting in all directions. These eddies mix with one another and interact transferring heat and mass. All turbulence is diffusive through friction which acts as a feedback to the mixing of the eddies. These turbulent eddies exist at all scales throughout the flow, both in space and time. This multi-scale nature of turbulence makes it a very challenging problem to consider. Similar scale fluctuations group together to form coherent structures, which make it possible to describe aspects of a turbulent flow. As these structures mix they break down into smaller scales, which happens over and over in what is called the energy cascade. Eventually, at the smallest scale of motion, the energy is lost as heat.

Given the importance, numerical methodologies for predicting fluid flow is a highly active research area which has a large dedicated body of literature. For fundamental introductions to the topic see the works of Tritton (1988), Pope (2000) and Davidson (2004) to name but a few. The wide range of concurrent spatial and temporal scales makes it possible to conceive modelling strategies at all levels of fidelity. It goes without saying that an increase in fidelity comes at a cost and for most industrial applications,

high fidelity methods are simply too expensive. The other side of the coin is that low fidelity methods tend to be insufficient at capturing a given problem. Global large phenomena such as forces around a body depend intrinsically on small scale activities that must be modelled by a low fidelity approach. Correctly modelling turbulence has proven to be a major challenge and as a consequence is an inadequate replacement for resolving it. Striking a balance between computational cost and numerical accuracy is the primary motivation behind this body of work, particularly in developing methodologies that can adapt to a required fidelity, both in space and time. An introduction to existing modelling methodologies will be given in Chapter 2.

Turbulence can be written down as a numerical system by assuming that it is comprised of continuous infinitesimal volumes which can be integrated. These volumes are known as fluid particles and the overall assumption is known as the Continuum Hypothesis (Tritton, 1988) and is therefore a subset of Continuum Mechanics. By resolving forces on a fluid element and integrating over a domain, the equations of motion for a fluid are written as,

$$\begin{aligned}\partial_t u_i + u_j \partial_{x_j} u_i &= -\partial_{x_i} p + \nu \partial_{x_j}^2 u_i \\ \partial_{x_i} u_i &= 0.\end{aligned}\tag{1.1}$$

Equations 1.1 are known as the Navier-Stokes equations for an incompressible, Newtonian fluid.  $\nu$  is the kinematic viscosity of the fluid, whilst  $u_i$  and  $p$  are the velocity and pressure fields respectively. Incompressible means that changes in density  $\rho$  are negligible and note that because of this  $\rho$  in Eq. 1.1 has been absorbed into  $p$ . A Newtonian fluid is one that obeys Newton's laws of viscosity, which relates the viscous stress tensor to the strain rate of velocity — see for example Tritton (1988). A meticulous and well guided proof of Eq. 1.1 and its compressible counterpart is detailed by Anderson (1995).

For a well posed problem, one must provide boundary conditions in space and time. The major difficulty in Eq. 1.1 is the non-linear term  $u_j \partial_{x_j} u_i$ . This term is the product of the rich and complex behaviour exhibited by the system, essentially responsible for the mixing of turbulent eddies. The diffusion term  $\nu \partial_{x_j}^2 u_i$  is the counter balance to this mixing and the ratio between these two quantities is defined as the Reynolds number, denoted by  $\text{Re}$ . The Reynolds number is a parameter that gives the engineer a good impression of the level of turbulence to be expected in a given fluid flow. Convection is a phenomena that can be estimated by  $U_0^2/D$  where  $U_0$  is some large scale reference velocity and  $D$  is a characteristic macro length scale. Similarly the diffusion term can be estimated via  $\nu U_0/D^2$  leaving the Reynolds number to be defined as,

$$\text{Re} = \frac{U_0 D}{\nu}.\tag{1.2}$$

The larger the Reynolds number, the larger the ratio between small and large scales and therefore the broader the spectrum of turbulence as energy must travel further down the energy cascade. Many flows contain a critical Reynolds number, above which the flow

becomes turbulent. A higher Reynolds number thus presents a greater challenge due to the increased number of scales.

## 1.2 Defining Scales of Turbulence

As mentioned it is possible to make statistical statements about a turbulent fluid due to the concurrent nature of eddies. Length and time scales can be defined which describe the local state of turbulence. In order to do this the correlation of the velocity field and the energy spectrum is often used (Davidson, 2004).

The velocity field is split into the mean and fluctuating components,

$$u_i = \bar{u}_i + u'_i, \quad (1.3)$$

where the over-bar denotes an average operator and the prime denotes the fluctuations removed by this. This is a scale separation of the velocity, which has great relevance when constructing the turbulence models discussed in Chapter 2. Considering only the one dimensional case we can measure the correlation of a point  $(x_1, t_1)$  differing from the point  $(x_2, t_2)$  in space and time with the correlation function  $R$  (Sagaut et al., 2013),

$$R(x_1, x_2, t_1, t_2) = \frac{\overline{u'(x_1, t_1)u'(x_2, t_2)}}{\overline{u'(x_1, t_1)u'(x_1, t_1)}}. \quad (1.4)$$

If  $R \approx 1$ , then this implies that over time the two points are quantitatively very similar and we can say they are strongly correlated. If they are very different then the averaging operator will slowly reduce  $R$  to zero, in which case the two points are highly uncorrelated. This concept can be used to determine whether two points are spatially correlated over a distance  $\Delta x$ ,

$$R_x(\Delta x, t_1) = \frac{\overline{u'(x_1, t_1)u'(x_1 + \Delta x, t_1)}}{\overline{u'(x_1, t_1)u'(x_1, t_1)}} \quad (1.5)$$

or whether two times are temporally correlated,

$$R_t(x_1, \Delta_t) = \frac{\overline{u'(x_1, t_1)u'(x_1, t_1 + \Delta_t)}}{\overline{u'(x_1, t_1)u'(x_1, t_1)}} \quad (1.6)$$

We can expect that as we increase the distance, the correlation between two points will approach zero and similarly for very small distances there will be a reasonable correlation. Using this idea, the size of eddies can be estimated via an understanding of the shape of the correlation function throughout the flow field. The integral length and time scales are defined in this way and give an idea of the macro turbulent scales,

$$L(x, t_0) = \int_0^\infty R_x(r, t_0) dr$$

$$T(x_0, t) = \int_0^\infty R_t(x_0, r) dr. \quad (1.7)$$

In order to derive expressions for the smallest scales, characterising the eddies that are at the end of the energy cascade, concepts of dissipation are required. The molecular viscous forces and dissipation happen at the end of the energy cascade, where the turbulent energy no longer dominates. Using the decomposition in Eq. 1.3, the turbulent kinetic energy  $k$  is defined as,

$$k = \frac{1}{2} \overline{u'_i u'_i}, \quad (1.8)$$

and the turbulent kinetic energy dissipation rate  $\varepsilon$  is defined as,

$$\varepsilon = 2\nu \overline{(\partial_{x_i} u'_j)(\partial_{x_i} u'_j)}. \quad (1.9)$$

These two definitions are made clear in Chapter 2. Kolmogorov (1941a) used dimensional analysis on these quantities to define what became known as the Kolmogorov length and time scales that characterise the smallest scales in the flow,

$$\ell_k = \left( \frac{\nu^3}{\varepsilon} \right)^{\frac{1}{4}}, \quad (1.10)$$

$$\tau_k = \left( \frac{\nu}{\varepsilon} \right)^{\frac{1}{2}}. \quad (1.11)$$

Note, dimensional analysis can also be used in this way, by assuming that most of the turbulence exists at large scales  $U_0 = \sqrt{2k}$  and that energy enters the cascade at the same rate it leaves it (Davidson, 2004) so that  $\varepsilon \approx U_0^3/L$ . Using this information, the integral length and time scale can be estimated as,

$$\ell_t = \frac{k^{3/2}}{\varepsilon}, \quad (1.12)$$

$$\tau_t = \frac{k}{\varepsilon}. \quad (1.13)$$

### 1.3 Defining States of Turbulence

The turbulence of a flow is contained in the quantity  $\overline{u'_i u'_j}$ , known as the Reynolds stress tensor. The derivation of the Reynolds stress is discussed in Chapter 2. The anisotropic part of this tensor is given as,

$$a_{ij} = \overline{u'_i u'_j} - \frac{2}{3} \delta_{ij} k. \quad (1.14)$$

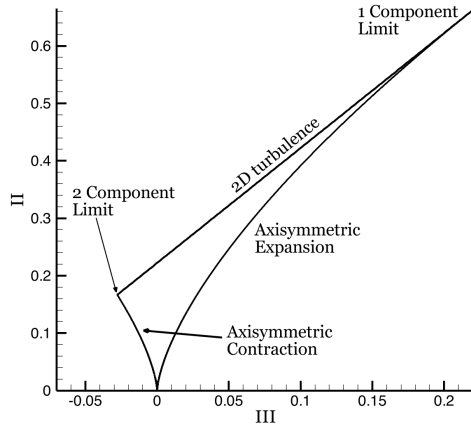


FIGURE 1.1: The Lumley triangle representing all realisable states of turbulence

$a_{ij}$  is often normalised as,

$$b_{ij} = \frac{\overline{u'_i u'_j}}{2k} - \frac{1}{3}\delta_{ij}. \quad (1.15)$$

The anisotropy tensor provides insight into the state of turbulence within a flow field. Solving the characteristic equation for  $b_{ij}$  reveals the direction and magnitude of principal strain. The eigenvectors of  $b_{ij}$  provide the orientation of the anisotropic turbulent stress and the eigenvalues provide respective magnitudes. Using the Cayley-Hamilton theorem, the characteristic equation for  $b_{ij}$  is written as,

$$b_{ik}b_{km}b_{kj} - I_b b_{ik}b_{kj} - II_b b_{ij} - III_b \delta_{ij} = 0. \quad (1.16)$$

$I_b$ ,  $II_b$  and  $III_b$  are invariants of the tensor  $b_{ij}$  and are defined as (Simonsen and Krogstad, 2005),

$$\begin{aligned} I_b &= b_{kk} \\ II_b &= \frac{1}{2}b_{ij}b_{ij} \\ III_b &= \det(b_{ij}). \end{aligned} \quad (1.17)$$

Clearly as  $b_{ij}$  is traceless  $I_b$  is zero, but the values of  $II_b$  and  $III_b$  for a given stress field can shed light on the state of turbulence at a given location. For a given stress field there is not a unique solution, but rather there are bounds upon the possible solutions. This idea was first proposed by Lumley (1979), after whom the bounding triangle is often named after. Figure 1.1 plots the Lumley triangle, where the domain contained within dictates all realisable states of turbulence.

To see why  $II_b$  and  $III_b$  are useful, Simonsen and Krogstad (2005) assumed axial symmetry to express the second and third invariants in cylindrical coordinates,

$$\begin{aligned} II_b &= \frac{1}{2}(b_{rr}^2 + b_{yy}^2 + b_{\theta\theta}^2 + 2b_{ry}^2) \\ III_b &= b_{\theta\theta}(b_{rr}b_{yy} - b_{ry}^2), \end{aligned} \quad (1.18)$$

where the line of symmetry is along the  $y$  axis. When  $II_b = III_b$  the turbulence is isotropic and all diagonal components of  $b_{ij}$  vanish, in other words all diagonal components of  $\overline{u'_i u'_j}$  are equal to  $2k/3$ . Stemming from the origin two different limits are discovered. Assume the flow is axisymmetric, i.e.  $b_{ry} = 0$  and two of the diagonal components of  $b_{ij}$  must be equal. This leads to the relation,  $III_b = \pm 2(II_b/3)^{3/2}$ . For the axisymmetric contraction, the two identical components dominate and the other tends to zero, leading to two component axisymmetric turbulence. For the axisymmetric expansion, the two identical components are dominated and thus tend to zero. This last state is known as the 1-component limit.

The upper limit, joining these two states represents all possible turbulence where only two diagonal components exist, such as in the near wall region where wall normal fluctuations are damped.

The values of  $II_b$  and  $III_b$  therefore give the engineer a picture of the anisotropy of turbulence in the flow field. Maps of the invariants are a popular tool for analysing the state of turbulence after both high fidelity simulations to understand physics and low fidelity simulations to assess validity.

## 1.4 Motivation

The primary objective for this work is to produce turbulence modelling strategies that are reliable, robust and cheap. Both techniques that partially resolve and completely model turbulence are covered. Turbulence resolution methodologies are developed that aim to provide the correct length scale to the model at any level of fidelity. This level of fidelity is instantaneously and spatially assessed by the model itself, alleviating the pressure on engineers.

The secondary objective of what follows is the development of machine learning tools, specifically evolutionary algorithms, that are suitable for the above tasks. The reader will notice that a large portion of this work describes the implementation of novel tools for this purpose. The Venn diagram of fluid mechanics and machine learning is not disjoint. Previous works marry the two — particularly in: aircraft design (e.g. Kipouros et al., 2008), flow control (e.g. Gautier et al., 2015) and work that is close to this thesis has been performed in the past (Dow and Wang, 2011; Duraisamy and Durbin, 2014; Fabritius, 2014; Weatheritt and Sandberg, 2014, 2015; Tracey et al., 2015; Ling and Templeton, 2015). That said, given the respective sizes of the sets of all research in fluid mechanics and machine learning, this intersection of literature is still small. This thesis, along with the work highlighted as similar, represents attempts to bring the power of machine learning to computational fluid mechanics. Please realise, the word *similar* is

relative — should one read these papers then one will realise the *major* differences in both the problems tackled and secondly the method used.<sup>1</sup>

Whilst the development of evolutionary algorithms is paramount, so is increasing the awareness of the turbulence modelling community to machine learning. The power of computers has brought on an age of ‘Big Data,’ where very large data sets are used to help decision making processes. This kind of data driven power can, and in the opinion of this author will, be harnessed by future turbulence modellers to construct descriptions of turbulence. In short, this thesis aims to convince the reader that turbulence prediction strategies can be devised by evolutionary algorithms.

## 1.5 Outline of Thesis

Due to the multidisciplinary nature of this thesis, there is no easy layout that flows from beginning to end. Broadly speaking, there is a split between turbulence modelling and Evolutionary Algorithms (EAs). These two disjoint topics are introduced separately in Chapter 2 and Chapter 3 respectively.

Once these topics have been introduced, the thesis proceeds with contributions to both of these fields. In Chapter 4, implementations of Gene Expression Programming are detailed. This represents the main contribution solely to the field of EAs.

Next, the development of two new turbulence modelling strategies that depend on the EA work are described in Chapter 5 and Chapter 6. The former is a modification of the anisotropy tensor in Reynolds-Averaged Navier-Stokes (RANS) modelling and the latter is the creation of length scale damping functions used within a Hybrid RANS/LES framework. These two chapters represent the main marrying of the two literature reviews in Chapters 2 and 3.

Applications of the Hybrid RANS/LES models devised in Chapter 6 are split into two chapters. Chapter 7 looks at the flow in a turbulent channel. This is mainly to show the deficiencies of the current philosophy of Hybrid RANS/LES and are not comments specific to the models introduced in this thesis. Chapter 8 applies these models to more complex geometries: a vertical fence, periodic hills and inline tandem cylinders. These are flows that all separate from a surface and thus present a challenge more aligned with the modelling philosophy.

Finally, in Chapter 9, the thesis is brought together and an outlook with possible extensions to this work is given.

Due to the wide number of topics considered in this thesis, it is entirely possible that the reader may not be interested in everything. To try to accommodate for this, Fig. 1.2 is

---

<sup>1</sup>Excepting the author’s contribution in the list.

a diagram that shows suggested reading orders. Using either the red path (RANS work) or the green path (Hybrid RANS/LES) work, one can ensure that the correct path is taken through the thesis. Note, all lines are directed downwards which reflects reading the thesis from front to back and that no previous chapter depends on a later one. For example, should one wish to understand the development of anisotropy in RANS, one need read Chapters 2, 3, 4 and 5. Note that chapters on the same level can be read in any order, so alternatively one could read in the order 3, 2, 4, 5.

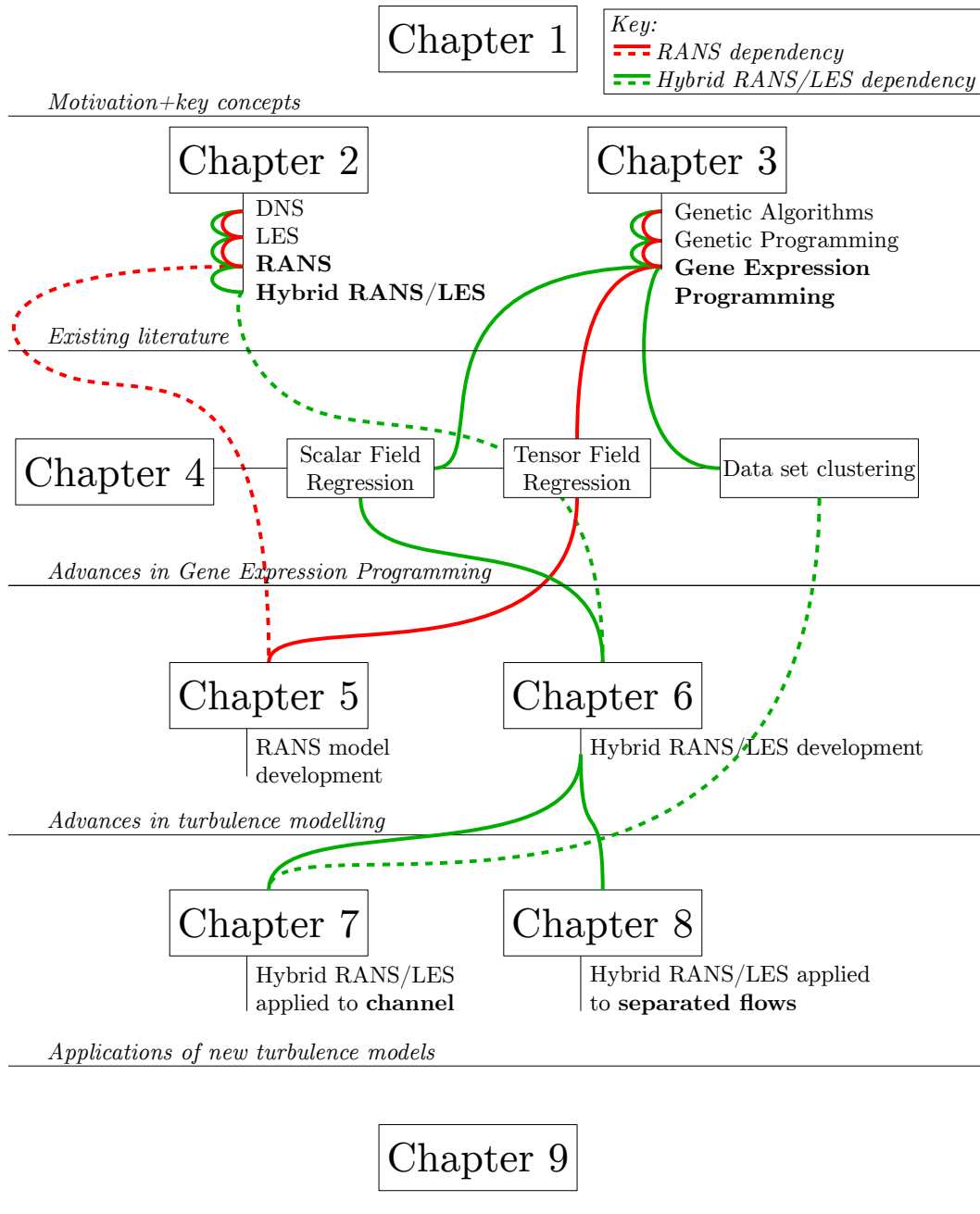


FIGURE 1.2: Dependency diagram of thesis and suggested reading orders. Lines are directed downwards. Solid lines move down one level and dashed lines move down two levels.



## Chapter 2

# Methodologies for Calculating Turbulence

### 2.1 High Fidelity Approach - Direct Numerical Simulation

To directly solve the Navier-Stokes equations, written down for the incompressible case in Eq. 1.1, a considerable computational effort is required. One must solve every single scale from the mean down to the Kolmogorov scale (Eqs. 1.10-1.11). This implies that the grid spacing  $\Delta$  must be on the order of magnitude of  $\ell_t$  and  $\Delta_t$  must be on the order of  $\tau_t$ . If we define the Reynolds number using the integral length scale, then it is easier to show that,

$$\frac{\ell_t}{\ell_k} \approx \text{Re}^{\frac{3}{4}}. \quad (2.1)$$

This has the implication that for the number of points in one coordinate direction  $N_x \propto \text{Re}^{3/4}$ . Therefore the total number of grid points in a full turbulence simulation,

$$N_{xyz} \propto \text{Re}^{9/4}. \quad (2.2)$$

Similar analysis to gain an insight on the scaling of the time step can be performed. The minimum number of time steps necessary to capture the life cycle of one eddy is (taking into account that  $\Delta_t$  must be of the order of  $\tau_k$ ),

$$N_t \approx \frac{\tau_t}{\Delta_t} \approx \frac{\tau_t}{\ell_k/U_0} \approx \frac{\tau_t}{\ell_t/U_0} \text{Re}^{3/4}. \quad (2.3)$$

$U_0$  is some characteristic velocity scale. This provides an estimate on the overall scaling of the full simulation,

$$\text{complexity} \propto N_{xyz} N_t \propto \text{Re}^3. \quad (2.4)$$

The proportionality constant in Eq. 2.4 is the cost of the algorithm employed, which depends on the numerical schemes and the speed of the computer. A high fidelity simulation solving Eq. 1.1 and using the described resolution is known as a Direct Numerical Simulation (DNS).

Note this estimate of computational cost is found by basing the Reynolds number on the integral length scale. If there are walls present in the flow field the smaller structures need to be resolved which leads to an even stronger Reynolds number dependence (Choi and Moin, 2012). In short the cost of DNS quickly removes the possibility of using it for industrial applications. To give an idea of the computational requirements, the DNS studies of Kaneda et al. (2003); Kaneda and Ishihara (2006); Ishihara et al. (2009) looked at isotropic turbulence in a cube at a Reynolds number of 144'000, based on integral length scale.<sup>1</sup> For this low Reynolds number, they used a grid of  $4096^3$  cells on the Earth Simulator which has a peak performance of 40TFlops and main memory of 10TBytes. Clearly these kinds of resources are out of reach of commercial companies. To further reiterate the point, the Reynolds number of typical industrial applications range from  $10^4$  to  $10^8$  and Spalart et al. (1997) estimated that a DNS around the wing of a commercial aeroplane would require  $10^{16}$  points, an order of a million more than the DNS of Kaneda et al. (2003).

## 2.2 Reducing the Cost of Turbulence Calculations

Due to the crippling numerical requirements of DNS, it is necessary to reduce the cost of turbulence simulations. This is achieved by applying some scale separation operator that dictates which scales should be modelled and which scales should be resolved. By modelling the small scales in a flow,  $\Delta$  no longer needs to be of the order of  $\ell_k$  and therefore the computational cost can be greatly reduced. The large scales of practical interest are still resolved whilst the smallest scales are picked up by a mathematical model.

Sagaut et al. (2013) points out that two main types of scale separation have emerged throughout the years. The first uses a statistical description of the flow, in this sense the separation is an averaging procedure. The second is a spatial scale separation between the largest and the smallest eddies. The first operation is primarily used to completely average the flow field and resolve only the mean, which greatly reduces the cost but places enormous pressure on a mathematical model. The second in practice is a low-pass filter in wave space that smoothes the flow field and removes the low energy small scales. These small scales must be picked up by the model, which account for the dissipation of the system, whilst the large energy containing motions are resolved.

---

<sup>1</sup>The original studies cite Reynolds number using the Taylor micro-scale, but this has not been covered - so the Reynolds number scaling between  $\ell_\lambda$  and  $\ell_t$  has been applied. For more on this see for example Sagaut et al. (2013).

Both types of scale separation follow a similar mathematical trend. A variable  $\phi$  can be decomposed by applying the scale separation operator  $\langle \cdot \rangle$  as,

$$\phi = \langle \phi \rangle + \phi'. \quad (2.5)$$

The primed quantity represents everything that is removed by the operator, be it an average or a filter. Therefore  $\langle \phi \rangle$  is the resolved component of  $\phi$  and  $\phi'$  is the unresolved. This operator can be applied to the Navier-Stokes equations to yield equations for the resolved quantities. For this the following assumptions about the separation operator are made (Sagaut et al., 2013),

$$\begin{aligned} \langle a \rangle &= a \\ \langle a\phi \rangle &= a\langle \phi \rangle \\ \langle \varphi + \phi \rangle &= \langle \varphi \rangle + \langle \phi \rangle \\ [\partial_\zeta, \langle \cdot \rangle] \phi &= 0. \end{aligned} \quad (2.6)$$

Where  $a$  is some constant. Using these relations, it is possible to write down equations for the resolved velocity and pressure,

$$\begin{aligned} \partial_t \langle u_i \rangle + \langle u_j \rangle \partial_{x_j} \langle u_i \rangle &= -\partial_{x_i} \langle p \rangle + \nu \partial_{x_j}^2 u_i + \partial_{x_j} \tau_{ij}^{\text{mod}} \\ \partial_{x_i} \langle u_i \rangle &= 0, \end{aligned} \quad (2.7)$$

where  $\tau_{ij}^{\text{mod}}$  is the mathematical model that varies in form greatly depending on the scale separation operator used.

This chapter looks at the major advances in this generalised approach, i.e. the aim to alleviate the cost of DNS. In particular the challenge lies in devising a suitable  $\tau_{ij}^{\text{mod}}$  that is fit for the purpose it is designed for.

### 2.2.1 Large Eddy Simulation

Smagorinsky (1963) in his landmark paper proposed Large Eddy Simulation (LES) which as the name suggests looks at resolving the largest scales in the flow, whilst modelling the smallest. The separation operator applied is a low-pass filter  $G$  for a given filter width  $\Delta_f$ ,

$$\langle \phi(x_i, t) \rangle = \int_0^\infty \int_\Omega G(\Delta_f, x - x^*, t - t^*) \phi(x^*, t^*) dx_i^* dt^* \quad (2.8)$$

that removes the smallest scales in the flow. It is thus the primary role of  $\tau_{ij}^{\text{mod}} = \tau_{ij}^{\text{sgs}}$  to provide turbulent dissipation, whilst  $\langle u_i \rangle$  is a filtered quantity — the resolved flow field — containing the energy carrying eddies (Tennekes and Lumley, 1972). Such low-pass

filters include the Gaussian (Sagaut, 2006),

$$G(x_i - x_i^*) = \left( \frac{6}{\pi \Delta_f^2} \right)^{\frac{1}{2}} e^{\left( \frac{-6|x_i - x_i^*|^2}{\Delta_f^2} \right)} \quad (2.9)$$

and the box filter,

$$G(x_i - x_i^*) = \begin{cases} \frac{1}{\Delta_f}, & |x_i - x_i^*| \leq \frac{\Delta_f}{2} \\ 0, & \text{otherwise.} \end{cases} \quad (2.10)$$

The variable  $\langle \phi \rangle$  is therefore all the scales of a size larger than  $\Delta_f$ . By applying the filter kernel  $G$  to the Navier-Stokes equations, one arrives formally at Eq. 2.7 with the model term taking the form,

$$\tau_{ij}^{\text{sgs}} = -\langle u'_i u'_j \rangle + \langle u'_i \rangle \langle u'_j \rangle. \quad (2.11)$$

This term must be closed in order to form a well posed problem, as primed or subgrid quantities are unknown when solving the resolved equations.

In general LES closures are based on the work of Kolmogorov (1941a) that the small scales are isotropic. As  $\tau_{ij}^{\text{sgs}}$  is primarily designed to model these scales only, generally closures take a form ill-suited to modelling anisotropy. For example the Smagorinsky (1963) model,

$$\tau_{ij}^{\text{sgs}} - \frac{1}{3} \tau_{kk}^{\text{sgs}} \delta_{ij} = -2(C_s \Delta_f)^2 |S| S_{ij} \quad (2.12)$$

uses the eddy viscosity approach discussed in Section 2.2.2.  $C_s = 0.1 - 0.2$  is a tuneable constant and  $S_{ij}$  is the resolved velocity strain rate,

$$S_{ij} = \frac{1}{2} (\partial_{x_j} \langle u_i \rangle + \partial_{x_i} \langle u_j \rangle). \quad (2.13)$$

Equation 2.12 shows that the anisotropic part of the model is proportional to the strain rate only. This is an incredibly poor description of the anisotropy in a turbulent flow field. This will be revisited in detail in Section 2.2.3.1

In practice, LES is performed without an explicit filter or the filter width is set very small. Most often  $\Delta_f = \Delta$ , where  $\Delta$  a characteristic length scale of the grid is used in the interests of efficiency (Fröhlich and Rodi, 2002). This means the grid is explicitly responsible for the scale separation in LES, hence  $\tau_{ij}^{\text{mod}}$  being named  $\tau_{ij}^{\text{sgs}}$  or the subgrid-stress (SGS) tensor. In this case the filtering is considered an implicit operation, a combination of the grid and also the truncation error from the numerical scheme. In this situation, it is impossible to explicitly write down the filter operation for a given flow field (Sagaut et al., 2013). In fact Garnier et al. (1999) reported for isotropic turbulence, and similarly Mossi and Sagaut (2003) for a channel, that low order numerical schemes act like a Smagorinsky SGS model with a higher constant. This led to Implicit LES

(ILES) that does not employ an explicit SGS model, but relies entirely on the numerical scheme for dissipation.

LES provides a robust and useful tool when high fidelity is possible. Indeed throughout this work, LES studies are used to validate lower-fidelity methods because of the high accuracy when the subgrid scale contribution is small. LES however does not provide the answer to industrial computational requirements.

The main drawbacks to SGS modelling are found in wall bounded applications. The small structures near the wall, that must be resolved by traditional LES, require extremely fine grid resolution. Indeed for wall bounded flows, Choi and Moin (2012) showed that the resolution requirements are not significantly better than DNS. This computational expense is extremely crippling and instantly removes the majority of industrial applications from the realm of possibility.

As discussed, the goal of an SGS model is to provide appropriate dissipation of the small scales and as a result, most SGS models are based on the concept that the unresolved scales are isotropic. When pushing the Reynolds number, coarser meshes yield a larger  $\Delta$  that in turn increases the size of the subgrid scales. As the mesh is significantly coarsened, the modelled scales are no longer isotropic and the SGS model provides a poor reflection of this. As a consequence, results from LES can significantly deteriorate (Fasel et al., 2002).

Further, the subgrid dissipation can interact with the numerical dissipation, caused by the truncation error, and contaminate the flow field. This can be extremely damaging to results. Analysis of the discretisation can also show that the numerical dissipation can outweigh the SGS dissipation. In other words, the designed contribution of  $\tau_{ij}^{\text{sgs}}$  is being completely smothered by unintended error.

These problems can be alleviated by using an extremely fine mesh — but then the contribution from the SGS model is negligible. The other option is to use ILES, briefly discussed above. However these are not methods to reduce the cost of turbulence simulation - quite the opposite. Note also that Sagaut et al. (2013) specifically advises against ILES on coarser meshes.

These deficiencies of LES have led to a rather scathing review by Fasel et al. (2002), writing that LES has failed in its task to find a turbulence resolving approach affordable in industry. Instead a new paradigm is required, one which is covered in Section 2.2.4.

## 2.2.2 Turbulence Modelling - Reynolds-Averaging the Navier-Stokes

The spatial scale segregation used in LES does not drastically reduce the cost of turbulence simulations. The other approach to scale separation, the statistical averaging operator, is a much cheaper alternative. The statistical approach leads to turbulence

*modelling* as opposed to *simulation* when applying a filter. In other words, all turbulence must be picked up by  $\tau_{ij}^{\text{mod}}$  and only the mean flow is resolved.

In order to describe only an average state of the flow field, Reynolds (1895) used what have become known as ‘Reynolds operators’ borrowed from invariant group theory. The Reynolds operator  $\langle \phi \rangle = \bar{\phi}$  is assumed to satisfy the conditions of Eq. 2.6, plus the further conditions,

$$\begin{aligned}\bar{\bar{\phi}} &= \bar{\phi} \\ \bar{\phi}' &= 0.\end{aligned}\tag{2.14}$$

By applying the Reynolds operator, the Navier-Stokes reduce to Eq. 2.7 with,

$$\begin{aligned}\tau_{ij}^{\text{mod}} &= \tau_{ij}^{\text{rants}} = \overline{u'_i u'_j} \\ \langle u_i \rangle &= \overline{u_i} \\ \langle p \rangle &= \bar{p}.\end{aligned}\tag{2.15}$$

The quantities  $\overline{u_i}$  and  $\bar{p}$  are now statistical descriptions of the velocity and pressure. This is a conceptual difference to the filtered quantities of LES. The Reynolds decomposition removes all turbulence from  $\overline{u_i}$  and  $\bar{p}$ . This means that the model term, known as the Reynolds Stress,  $\overline{u'_i u'_j}$  must pick up all of the turbulent information, with none explicitly resolved. This quantity was previously defined in Section 1.3 and now the discussion on the anisotropy of turbulence should be clear. Equation 2.7 in this averaged form is known as the Reynolds-Averaged Navier-Stokes (RANS) equations and modelling in this form is known as RANS modelling.

There are many Reynolds operators that average the flow field. For steady flows, the Reynolds operator takes the form,

$$\bar{\phi}_T = \lim_{T \rightarrow \infty} \frac{1}{T} \int_0^T \phi(t^*) dt^*\tag{2.16}$$

which is a complete temporal average and removes all time dependence from  $\bar{\phi}$ . The ensemble average can be thought of as repeating an experiment an infinite number of times and taking the average. The ensemble average therefore takes the form,

$$\bar{\phi}_E = \lim_{N \rightarrow \infty} \frac{1}{N} \sum_{n=1}^N \phi_n(x, t),\tag{2.17}$$

where  $n$  is the experiment number and  $N$  the total. Monin and Yaglom (1971) showed, via the ergodicity principle,  $\bar{\phi}_T$  converges to  $\bar{\phi}_E$  if and only if the ensemble averaged Reynolds stress tensor converges to zero over an infinite time average,

$$\lim_{T \rightarrow \infty} \frac{1}{T} \int_0^T \overline{\phi' \phi'}_E dt^* = 0.\tag{2.18}$$

For steady turbulence, this is valid because  $\overline{\phi' \phi'}_E$  is uncorrelated for large separations in time. If the flow is inherently unsteady, say if it exhibits some periodic motion, then steady approaches are not suitable. In this case a causal operator is defined,

$$\overline{\phi(t)} = \frac{1}{T} \int_{t-T}^{t+T} \phi(t^*) dt^* \quad (2.19)$$

which is the time average in intervals of  $T$ . In effect Eq. 2.19 is a low-pass filter in time, only allowing scales with a turn over time larger than  $T$ . This introduces a time step dependence on the equations, with a smaller  $T$  resulting in more resolution. The lower bound on  $T$  is the characteristic length scale of turbulence, below this value a DNS is being performed as the filter is not active. This approach is Unsteady RANS (URANS) and is generally used for resolving large periodic motions. URANS is an approach that allows for statistical scale separation, whilst still resolving turbulence.

Similarly the phase operator (Cantwell and Coles, 1983),

$$\overline{\phi} = \frac{1}{\Delta\Phi} \int_{t-\Delta\Phi}^t \phi(t) dt, \quad (2.20)$$

where  $\Delta\Phi = T/N$  and  $N$  is the number of phases in a period  $T$ , is a statistical average allowing unsteadiness. This technique is known as Phase-Averaged Navier-Stokes (PANS) and shows that a decomposition of this form is formally equivalent to the steady RANS equations. In these equations  $\tau_{ij}^{\text{mod}} = \tau_{ij}^{\text{pans}} = \overline{u'_i u'_j}$  are the fluctuations present at constant phase.

### 2.2.3 Closures for the Reynolds-Averaged Navier-Stokes Equations

#### 2.2.3.1 Linear Eddy Viscosity Models

##### Theoretical Grounds for the Eddy Viscosity

The primary closure of the RANS equations is known as the Boussinesq approximation after the pioneering work of Boussinesq (1877). Paradoxically this hypothesis closes Eq. 2.7, before Reynolds released his concepts outlined in Section 2.2.2. However, Boussinesq performed erroneous temporal averaging that prevented the explicit discovery of the Reynolds stress tensor (Schmitt, 2007). Boussinesq violated the relations in Eq. 2.6, claiming that his transgression “happens only in a relatively limited region and [is] almost always negligible” which is a highly inaccurate statement. More often than not the opposite is true (Schmitt, 2007). Further his work on theoretical, experimental and numerical grounds is shown to be inadequate for even simple engineering flows. Despite this, he still devised a method popular almost one hundred and fifty years later due to its easy implementation, numerical robustness and low cost.

Boussinesq begins with an analogy to the kinetic theory of molecules (see for example Jeans, 1962). That is a decomposition of the flow velocity  $u = U + u''$ , into an average and random molecular motion. A consideration of the averaged momentum flux  $dP_{ij}$  of all molecules across a differential surface element  $dS$  yields (Wilcox, 1994),

$$\frac{dP_{ij}}{dS} = \rho \langle u''_i u''_j \rangle. \quad (2.21)$$

The total stress on a fluid particle is written,

$$\sigma_{ij} = p\delta_{ij} - \rho\tau_{ij}, \quad (2.22)$$

where  $\tau_{ij}$  is the viscous stress tensor, which is seen to be,

$$\tau_{ij} = \langle u''_i u''_j \rangle. \quad (2.23)$$

The analogy to the Reynolds stress tensor being obvious. Boussinesq's idea is to extend this to turbulent fluctuations,  $u'_i$ , in place of the molecular motion. Boussinesq further included a flow dependent viscosity to relate the turbulent stresses to the mean strain rate, now known as the eddy viscosity or turbulent viscosity  $\nu_t$ . The relation is derived by using a mixing length, analogous to the mean free path of a molecule, coined and formalised by Prandtl (1925), however Boussinesq (1877) had effectively previously stated the same idea. This hypothesis includes a first order approximation of  $\partial_{x_j} \bar{u}_i$  in calculating the momentum flux, see Wilcox (1994) for a full discussion. The resulting relation is known today as the Boussinesq hypothesis,<sup>2</sup>

$$\tau_{ij}^{\text{rans}} = \frac{2}{3}k\delta_{ij} - 2\nu_t S_{ij}, \quad (2.24)$$

where  $\tau_{ij}^{\text{rans}}$  is the Reynolds stress tensor (see Section 2.2.2), the turbulent kinetic energy  $k = \frac{1}{2}\bar{u}'_i \bar{u}'_i$ , is the trace and the mean strain rate,  $S_{ij} = \frac{1}{2}(\partial_{x_j} \bar{u}_i + \partial_{x_i} \bar{u}_j)$ , is the symmetric component of the mean velocity gradient. Note that in this section the notation  $(\cdot)$  is adopted as we mean the Reynolds-average.

However, the further assumptions that must therefore be carried over from molecular kinetics do not hold on this macroscopic scale. Firstly, the mean free path of the molecules is much smaller than the characteristic mean flow length scale and secondly, the distribution of molecular free paths is Gaussian about this mean. These two assumptions are valid for the molecular analogy of Eq. 2.24, however when considering turbulent fluctuations rather than molecular paths both assumptions are violated. Regarding the first, the mixing length is not small compared to the mean characteristic length scale for many engineering flows (Tennekes and Lumley, 1972), therefore the first order Taylor expansion of  $\partial_{x_j} \bar{u}_i$  is not justified, so physically a non-linear relationship between

---

<sup>2</sup>the term 'Boussinesq equation' is avoided, due to arising confusion with the equation describing water waves.

Reynolds stress and mean strain is appropriate. The second requires that the mixing length represents the mean in a Gaussian distribution of free paths of fluid elements. Whilst the mixing length can be found via considerations of correlations, the distribution about this is highly non-Gaussian (Schmitt, 2007).

The linear form of Eq. 2.24 due to the first order truncation within the derivation, gives rise to the classification of such closures as ‘linear eddy viscosity models’ (LEVMs). Despite the above theoretical issues, no model is a less attractive prospect and as such there exists a large and varied set of LEVMs. The main goal of each is to prescribe scales that describe the eddy viscosity. Characteristic scales of turbulence, these can be velocity, length or time are used to set the eddy viscosity. Due to the poorly formed analogy above, Wilcox (1994) describes this process as an exercise in dimensional analysis not fundamental physics. The scales required in recent years are found via two or more transport equations.

### Example Closures - Two Equation Models

An extremely popular and pioneering LEVM is the  $k - \varepsilon$  model.  $\varepsilon$  is the dissipation rate of turbulent kinetic energy defined as,

$$\varepsilon = 2\nu \overline{\partial_{x_j} u'_i \partial_{x_j} u'_i}. \quad (2.25)$$

The mathematical reasoning behind  $k$ ,  $\varepsilon$  and the transport equations is made clear in Section 2.2.3.2, but for now the transport equations used in the example LEVMs are included without explanation purely as a reference. Should the reader wish to understand their beginnings see Section 2.2.3.2.

As the name suggests, the  $k - \varepsilon$  model contains two transport equations, one for the turbulent kinetic energy and one for the dissipation rate  $\varepsilon$ . The beginnings of this turbulence model are found in the work of Chou (1945) and Davydov (1961). However the popularity of the model comes from the work of Jones and Launder (1972); Launder and Sharma (1974). The 1974 version of the model is often cited as the standard  $k - \varepsilon$  model and is by far the most popular version. By transporting  $k$  and  $\varepsilon$ , the eddy viscosity can be found by,

$$\nu_t = C_\mu k^2 / \varepsilon, \quad (2.26)$$

free-stream which closes the collective system of equations consisting of the RANS formulation of Eq. 2.7 and the Boussinesq hypothesis of Eq. 2.24. Note,  $C_\mu = 0.09$  is a constant. The modelled quantities  $k$  and  $\varepsilon$  are found via the transport equations,

$$\begin{aligned} \partial_t k + \bar{u}_j \partial_{x_j} k &= \nu_t S^2 - \varepsilon + \partial_{x_j} \left( (\nu + \nu_t / \sigma_k) \partial_{x_j} k \right) \\ \partial_t \varepsilon + \bar{u}_j \partial_{x_j} \varepsilon &= C_{\varepsilon 1} \frac{\varepsilon}{k} \nu_t S^2 - C_{\varepsilon 2} \frac{\varepsilon^2}{k} + \partial_{x_j} \left( (\nu + \nu_t / \sigma_\varepsilon) \partial_{x_j} \varepsilon \right), \end{aligned} \quad (2.27)$$

where the remaining constants are:  $C_{\varepsilon 1} = 1.44$ ,  $C_{\varepsilon 2} = 1.92$ ,  $\sigma_k = 1.0$  and  $\sigma_\varepsilon = 1.3$  and  $S = \sqrt{2S_{ij}S_{ij}}$ . This model, despite its immense popularity has notable difficulties with regard to stability in the near-wall region (Menter, 1994). Further, Menter (1994) discusses insensitivity to adverse pressure gradients and strong streamline curvature.

Kolmogorov (1941b) and then most notably Wilcox (1988, 1994) transported  $k$  along with the rate of turbulent dissipation  $\omega$  in unit volume and time,

$$\omega = \frac{\varepsilon}{\beta^* k}, \quad (2.28)$$

where  $\beta^* = 0.09$ . The transport equations for what is known as the Wilcox or Standard  $k - \omega$  model are,

$$\begin{aligned} \partial_t k + \bar{u}_j \partial_{x_j} k &= \nu_t S^2 - \beta^* k \omega + \partial_{x_j} \left( (\nu + \sigma^* \nu_t) \partial_{x_j} k \right) \\ \partial_t \omega + \bar{u}_j \partial_{x_j} \omega &= \alpha_k^\omega \nu_t \partial_{x_j} \bar{u}_i - \beta \omega^2 + \partial_{x_j} \left( (\nu + \sigma \nu_t) \partial_{x_j} \omega \right). \end{aligned} \quad (2.29)$$

The remaining model constants are given as:  $\alpha = 5/9$ ,  $\beta = 3/40$ ,  $\sigma = 1/2$  and  $\sigma^* = 1/2$ .

The  $k - \omega$  model alleviates the issue of numerical stiffness in the near-wall region, however sensitivities in the free-stream are induced (Menter, 1994). The model is also reported to perform better in adverse pressure gradients, although often predicting very early separation (Wilcox, 1994).

In order to cure both models, Menter (1993, 1994) combined the two models to use the  $k - \omega$  formulation near the wall and  $k - \varepsilon$  in the free-stream, in what is known as the Shear-Stress Transport (SST) model. A blending function is employed to achieve this, that completes the switch by the edge of the boundary layer. Further the model also includes a limiter on the turbulence level to accurately obtain the separation point, although reduced turbulence levels often lengthen the reattachment length. The transport equations are in their most recent form,

$$\begin{aligned} \partial_t k + \bar{u}_j \partial_{x_j} k &= P_k - \beta^* k \omega + \partial_{x_j} \left( (\nu + \sigma_k \nu_t) \partial_{x_j} k \right) \\ \partial_t \omega + \bar{u}_j \partial_{x_j} \omega &= \frac{\gamma}{\nu_t} P_k - \beta \omega^2 + \partial_{x_j} \left( (\nu + \sigma_\omega \nu_t) \partial_{x_j} \omega \right) + 2(1 - F_1) \sigma_\omega \frac{1}{\omega} (\partial_{x_j} k)(\partial_{x_j} \omega) \end{aligned} \quad (2.30)$$

The terms in Eq. 2.30 are given as,

$$\begin{aligned}
 P_k &= \tau_{ij}^{\text{rans}} \partial_{x_j} \bar{u}_i \\
 \nu_t &= \frac{a_1 k}{\max(a_1 \omega, S F_2)} \\
 F_1 &= \tanh(\Gamma_1^4) \\
 F_2 &= \tanh(\Gamma_2^2) \\
 \Gamma_1 &= \min\left(\max\left(\frac{k^{1/2}}{\beta^* \omega y}, \frac{500\nu}{y^2 \omega}\right), \frac{4\sigma_{\omega 2} k}{CD_{k\omega} y^2}\right) \\
 \Gamma_2 &= \max\left(2\frac{k^{1/2}}{\beta^* \omega y}, \frac{500\nu}{y^2 \omega}\right) \\
 CD_{k\omega} &= \max(2\sigma_{\omega 2}).
 \end{aligned} \tag{2.31}$$

All other terms are constants for the  $k - \omega$  and  $k - \varepsilon$  models, which must be blended via the function,

$$\phi = F_1 \phi_1 + (1 - F_1) \phi_2. \tag{2.32}$$

The values for the constants are,

$$\begin{aligned}
 \gamma_1 &= \frac{\beta_1}{\beta^*} - \frac{\sigma_{\omega 1} \kappa^2}{\sqrt{\beta^*}}, & \gamma_2 &= \frac{\beta_2}{\beta^*} - \frac{\sigma_{\omega 2} \kappa^2}{\sqrt{\beta^*}} \\
 \sigma_{k1} &= 0.85, & \sigma_{k2} &= 1.0 \\
 \sigma_{\omega 1} &= 0.5, & \sigma_{\omega 2} &= 0.856 \\
 \beta_1 &= 0.075, & \beta_2 &= 0.0828 \\
 \beta^* &= 0.09, & \kappa &= 0.41 \\
 a_1 &= 0.31,
 \end{aligned} \tag{2.33}$$

These three examples are celebrated two equation eddy-viscosity models however lower and higher levels of complexity exist, from zero-equation models (or ‘algebraic models’ - see Wilcox (1994)) up to (and beyond) 4-equation models (Durbin, 1991). Full discussions are omitted here, in part due to overall relevance and in part due the highly extensive and detailed literature in existence.

### Practical Failing of Linear Eddy Viscosity Models

As mentioned, the Boussinesq approximation is invalid theoretically. This section looks at the failing on practical grounds. Schmitt (2007) uses the anisotropy tensor,

$$a_{ij} = \overline{u'_i u'_j} - \frac{2}{3} k \delta_{ij}, \tag{2.34}$$

to test the validity of the Boussinesq hypothesis for a given flow. Note Eq. 2.24 reduces the anisotropy tensor to,

$$a_{ij} = -2\nu_t S_{ij}, \tag{2.35}$$

for LEVMs. Boussinesq’s hypothesis can now be thought of as the deviation from isotropic turbulence being proportional to mean strain. This proportionality can be

tested from numerical or experimental values of  $a_{ij}$  and  $S_{ij}$ . This is done via an indicator  $\rho_{RS}$  (Schmitt and Hirsch, 2000),

$$\rho_{RS} = \frac{|a_{mn}S_{mn}|}{\|a_{ij}\|\|S_{ij}\|}, \quad (2.36)$$

where  $\|\cdot\|$  is the contracted norm. This indicator satisfies  $0 \leq \rho_{RS} \leq 1$ ; with values approximately 0 implying complete orthogonality and no proportionality of the two, whereas values approximately 1 suggest one hundred percent validity of the Boussinesq approximation for the given flow. Schmitt (2007) gives a reference value of  $\rho_{RS} = 0.86$  as sufficient evidence for the justified use of Eq. 2.24 and therefore the use of an LEVM.

DNS databases are analysed by Schmitt (2007) for: Couette flow at  $Re = 1300$  and  $Re_\tau = 82$  (Bech et al., 1995), turbulent channel flow at  $Re = 3250$  and  $Re_\tau = 180$  (Kim et al., 1987) and again at  $Re = 10000$  with  $Re_\tau = 590$  (Moser et al., 1999), zero pressure turbulent boundary layer flow at  $Re = 2 \times 10^5$  and  $Re_\theta = 1410$  (Spalart, 1988) and finally flow in an annular pipe at  $Re = 2800$  and  $Re_\tau = 180$  (Quadrio and Luchini, 2002). These flows are chosen due to their one dimensional flow field; this corresponds to  $S_{ij}$  containing just two non-zero components,  $S_{12} = S_{21} = d_y \bar{u}(y)/2$ . In order for Eq. 2.35 to be satisfied,  $\text{diag}(a_{ij}) = 0$ , which is not necessarily the case. Consider that for these flows  $a_{ij}$  reduces to,

$$a = \begin{pmatrix} \overline{u'u'} - 2k/3 & \overline{u'v'} & 0 \\ \overline{u'v'} & \overline{v'v'} - 2k/3 & 0 \\ 0 & 0 & \overline{w'w'} - 2k/3 \end{pmatrix} \quad (2.37)$$

and so,

$$\rho_{RS} = \frac{|\overline{u'v'}|}{|a_{ii}^2 + 2\overline{u'v'}|^2}. \quad (2.38)$$

$\rho_{RS} \xrightarrow{\overline{u'v'} \rightarrow \infty} 0$  and further since the normal stresses are not equal (Nisizima and Yoshizawa, 1986; Speziale, 1987),  $a_{ii}$  tends to be large. Therefore it is difficult to see, even for these simple flows, justification for the linear eddy viscosity closure. Schmitt (2007) evaluates  $\rho_{RS}$  as a function of  $y^+ = u_\tau y/\nu$  and discovers that in the region  $3 \leq y^+ \leq 70$ , which is roughly the buffer layer, the Boussinesq approximation is entirely inadequate. Further, for the annular pipe, only the region where viscous stress dominates the total stress ( $y^+ \leq 3$ ) is the Boussinesq approximation valid.

These flow set-ups are impossibly simple relative to the plethora of relevant engineering configurations. With the above failure of the Boussinesq hypothesis on practical and theoretical grounds; it is clear that engineers in many applications require a more sophisticated approach. Note, that in many applications a RANS model may well give a sufficient solution. The work of Schmitt (2007) discussed above assesses the validity of the Boussinesq approximation. This is just one of the assumptions that go into RANS

modelling. In a more general sense, Hunt and Savill (2005) outlined a map of where and when *specific* models are valid. This work covers not just the linear models introduced above, but also the more complex closures discussed below where one would assume that a generalised version of  $\rho_{RS}$  takes a higher value.

### 2.2.3.2 Reynolds Stress Modelling

Instead of assuming a linear relation between mean strain and Reynolds stress which is shown to be physically inadequate above, six extra equations are introduced to close Eq. 2.7. Each equation governs the transport of an independent component of  $\overline{u'_i u'_j}$  and so Reynolds Stress Transport (RST) modelling is known as a Second Moment Closure (SMC). An extra six transport equations is expensive but is in principle more physically grounded and should yield better results; the Reynolds stress convection, diffusion, production and redistribution are all accounted for.

Apart from the extra expense, RST closures do have another major drawback. The derivation of Eq. 2.7 introduces the six unknown components of  $\overline{u'_i u'_j}$  but inevitably deriving transport equations for each of these produces further unknowns. These need to be modelled in order to close the equation set. Early work in this field began with Rotta (1951), whom successfully modelled every term in the transport equations, based on some of Kolmogorov's work (Kolmogorov, 1941a) supplemented by new ideas (Speziale, 1991). The first RANS calculation, based on Prandtl's mixing length, did not happen until the 1920's; but the extra effort required for RST calculations delayed implementation until the 1970's at the onset of more powerful computers. Particular works of Daly and Harlow (1970); Reynolds (1970); Naot et al. (1972); Hanjalic and Launder (1972); Lumley and Khajeh-Nouri (1974) represent the efforts of independent research groups, but Launder et al. (1975) aggregated the then current models into a hierarchy (Al-Sharif, 2011). The basic model presented by Launder et al. (1975) had the advantage of being simple, yet more capable than eddy-viscosity closures and upon contraction the  $k-\varepsilon$  closure of Hanjalic and Launder (1972) is obtained, displaying unusual but welcome consistency (Speziale et al., 1991). This is another reason why the Launder et al. (1975) model is very popular today.

A full review of RST models is not required here, however important aspects of the exact equations are covered. For a full comprehensive review of available SMC closures read Al-Sharif (2011). In order to derive the RST equations, the Reynolds operator is applied to the Navier-Stokes Eq. 1.1,

$$\overline{u'_i N(\bar{u}_j + u'_j)} + \overline{u'_j N(\bar{u}_i + u'_i)} = 0, \quad (2.39)$$

where  $N(\cdot)$  is the Navier-Stokes operator.<sup>3</sup> The result is six transport equations, one for each component of Reynolds stress,

$$\begin{aligned} \partial_t \overline{u'_i u'_j} + \bar{u}_k \partial_{x_k} \overline{u'_i u'_j} &= - \left( \overline{u'_i u'_k} \partial_{x_k} \bar{u}_j + \overline{u'_j u'_k} \partial_{x_j} \bar{u}_i \right) + \overline{u'_i \partial_{x_j} p'} + \overline{u'_j \partial_{x_i} p'} - 2\nu \overline{\partial_{x_k} u'_i \partial_{x_k} u'_j} \\ &\quad + \partial_{x_k} (-\overline{u'_i u'_j u'_k}) + \nu \partial_{x_k} \partial_{x_k} \overline{u'_i u'_j} \\ &= +P_{ij} + \Pi_{ij} - \varepsilon_{ij} + D_{ij}^t + \nu \partial_{x_k} \partial_{x_k} \overline{u'_i u'_j}. \end{aligned} \quad (2.40)$$

The second line represents the more compact notation; each term appears in respective order, with the sign added for clarity. These are: production of Reynolds stress  $P_{ij}$  due to mean velocity gradients, velocity-pressure gradient diffusion  $\Pi_{ij}$ , the dissipation rate  $\varepsilon_{ij}$ , turbulent transport  $D_{ij}^t$  and viscous diffusion  $\nu \partial_{x_k} \partial_{x_k} \overline{u'_i u'_j}$ . Only production and molecular diffusion are closed, the remaining terms require modelling as they include single fluctuations or triple correlations. Modelling these terms is not straightforward and especially vital to do correctly. For example the velocity-pressure gradient diffusion is,

$$\begin{aligned} \Pi_{ij} &= \overline{p' (\partial_{x_j} u'_i + \partial_{x_i} u'_j)} - \partial_{x_k} (\overline{p' u'_i} \delta_{jk} + \overline{p' u'_j} \delta_{ik}) \\ &= \Phi_{ij} + D_{ij}^p. \end{aligned} \quad (2.41)$$

The first term on the right hand side of Eq. 2.41 is the pressure-strain correlation and is traceless so has no effect on the normal stresses and therefore turbulent kinetic energy. However it has huge consequences for the anisotropy of the flow field by redistributing energy due to pressure and strain rate fluctuations. This redistribution is vital and as a result  $\Pi_{ij}$  receives a lot of attention (Al-Sharif, 2011). It is this kind of anisotropy, if modelled correctly will provide greater predictive power over LEVM. The second term,  $D_{ij}^p$  is responsible for the transport of fluctuations due to pressure, which also contains an anisotropic modelling element — but is not as strong at redistribution.

The added complexity of RST modelling induces several numerical challenges absent from eddy-viscosity modelling. Large source terms generally dominate the equations, which result in numerical stiffness; the equation set is highly non-linear and extremely coupled (Leschziner and Lien, 2002; Lien and Leschziner, 1994) and when using a collocated grid a ‘checkerboard’ velocity field due to odd-even decoupling is often observed (Al-Sharif, 2011).

From Eq. 2.39, it is now clear that LEVM transport equations can be derived in a similar process. Recall that  $k = \frac{1}{2} \overline{u'_i u'_i}$  and  $\epsilon = 2\nu \overline{\partial_{x_k} u'_i \partial_{x_k} u'_i}$ . In this way the  $k$  transport equation can be derived by,

$$\overline{u'_i N(\bar{u}_i + u'_i)} + \overline{u'_i N(\bar{u}_i + u'_i)} = 0, \quad (2.42)$$

---

<sup>3</sup> $N(u_i) = 0$  is Eq. 1.1

which is a contraction of Eq. 2.39. The transport for  $\varepsilon$  is derived from,

$$\overline{2\nu(\partial_{x_j} u'_i)\partial_{x_j} N(u'_i)} = \partial_t \varepsilon, \quad (2.43)$$

which is a contraction of a more general transport equation for  $\varepsilon_{ij}$  that appear in Eq. 2.40.  $\omega$  is then further derived from Eq. 2.43 by transforming  $\varepsilon$ . The exact equations also contain unclosed terms, the discrepancies in turbulence closures arise from modelling these terms.

### 2.2.3.3 Explicit Algebraic Stress Modelling

The two extremes of RANS closure have been covered. The Boussinesq hypothesis is a stable yet overly simplistic option. RST modelling captures as much physics a RANS closure can, whilst remaining practical — yet is not without weakness. The following sections outline a methodology that aims to take aspects from both, namely the robust nature of the eddy viscosity and the anisotropic qualities from having individual Reynolds stress equations. An algebraic stress relationship is derived from Eq. 2.40. The resulting closure is an Algebraic Stress Model (ASM), which in the following formulation is combined with a Non-Linear Eddy-Viscosity Model (NLEVM).

### Implicit Methodology

Rodi (1972, 1976) promoted a weak equilibrium hypothesis which states that all variations in the components of  $\overline{u'_i u'_j}$  are due to variations of the trace only. Therefore,

$$\overline{u'_i u'_j} \sim k. \quad (2.44)$$

This has an impact on the convection and diffusion terms,

$$D_t \left( \overline{u'_i u'_j} \frac{k}{k} \right) - D_{ij} \approx k D_t \left( \frac{\overline{u'_i u'_j}}{k} \right) + \frac{\overline{u'_i u'_j}}{k} D_t k - \frac{1}{2} \frac{\overline{u'_i u'_j}}{k} D_{ll} = \frac{\overline{u'_i u'_j}}{k} (D_t k - D_k). \quad (2.45)$$

$D_{ij}$  is the combination of turbulent transport terms,  $D_{ij}^t$ ,  $D_{ij}^p$  and molecular diffusion  $\nu \partial_{x_k} \partial_{x_k} \overline{u'_i u'_j}$ .  $D_k = \frac{1}{2} D_{ii}$  is the transport and diffusion of turbulent kinetic energy. The anisotropy tensor Eq. 2.34 normalised,

$$b_{ij} = \frac{\overline{u'_i u'_j}}{2k} - \frac{1}{3} \delta_{ij} \quad (2.46)$$

is seen to be approximately constant, implying that the material derivative vanishes. This material derivative of  $a_{ij}$  can be split into a Reynolds stress and a turbulent kinetic energy component, meaning both transport equations can be utilised by considering Eq. 2.45.  $D_t k$  and  $D_k$  can be used to substitute in  $\frac{1}{2} P_{ii} = P_k$  and  $\varepsilon_{ii} = (2/3)\varepsilon$ . The

result is the algebraic relation (Grundestam et al., 2005),

$$\left( a_{ij} + \frac{2}{3} \delta_{ij} \right) \left( \frac{P_k}{\varepsilon} - 1 \right) = \frac{1}{\varepsilon} \left( P_{ij} - \varepsilon_{ij} + \Phi_{ij} \right). \quad (2.47)$$

The dissipation rate  $\varepsilon_{ij}$  and the pressure-strain  $\Phi_{ij}$  need to be modelled, usually via combinations of mean rates of strain  $S_{ij}$  and rotation  $\Omega_{ij}$ ; so that the anisotropy tensor depends on these two quantities and the ratio of production to dissipation  $P_k/\varepsilon$  (e.g. Launder et al., 1975; Speziale et al., 1991; Wallin and Johansen, 2000). Equation 2.47 is now an implicit equation for  $\overline{u'_i u'_j}$  which can be solved via an iterative process. Turbulent kinetic energy is required to make up the anisotropy tensor and the dissipation rate is required to solve Eq. 2.47. The traditional method to supply them is via the transport equations for turbulent kinetic energy and a transport equation to provide a length scale, usually dissipation rate.

In the process of transporting Reynolds stress, streamline curvature effects are accounted for. In the derivation of Eq. 2.47 this is naturally lost; the resulting ASM techniques are inferior due to the disregard of the anisotropy material derivative (Rumsey et al., 1999, 2000). Instead a transformation,  $T_{ij}$ , to a coordinate system that follows the flow field can yield better results (Rodi and G., 1983; Girimaji, 1997), yet it is not trivial to find  $T_{ij}$  (Hellsten, 2002). Invoking the weak equilibrium hypothesis loses significant history effects, although some are retained via the two supplementary equations. As a result, ASMs are only valid when convection and transport do not dominate terms in Eq. 2.40, i.e. a slowly evolving system which is close to equilibrium. ASMs were born from RST models and so retain many of the weaknesses, primarily numerical stiffness from the nature of dominating source terms and the highly nonlinear formulation. Finally, a numerical problem is induced via the implicit formulation: complex geometries may require too many iterations to be practical and uniqueness of the equations is no longer guaranteed, which could result in convergence to unphysical solutions (Speziale, 1997).

## Explicit Methodology

To overcome the numerical issues of the implicit approach, an explicit formula for the anisotropy tensor can be derived, by considering the dependencies of Eq. 2.47. Assuming that,<sup>4</sup>

$$a_{ij} = a_{ij}(S_{ij}, \Omega_{ij}), \quad (2.48)$$

the solution has ten independent dimensions (Pope, 1975),

$$a_{ij} = \beta_k T_{ij}^k, \quad k = 1, \dots, 10. \quad (2.49)$$

---

<sup>4</sup>currently ignoring the ratio  $P_k/\varepsilon$

Where  $\Omega_{ij} = \frac{1}{2}(\partial_{x_j}\bar{u}_i - \partial_{x_i}\bar{u}_j)$  is the rotation rate tensor. The coefficients  $\beta_i$  are scalars that depend on invariant combinations of  $S_{ij}$  and  $\Omega_{ij}$  contractions. For the limit of two-dimensional mean flow the number of required basis vectors is reduced to three,

$$T_{ij}^1 = S_{ij}, \quad T_{ij}^2 = S_{ik}\Omega_{kj} - \Omega_{ik}S_{kj}, \quad T_{ij}^3 = S_{ik}S_{kj} - \frac{1}{3}S_{lk}S_{kl}\delta_{ij}. \quad (2.50)$$

The substitution of these two-dimensional mean flow assumptions into Eq. 2.47, yields a set of equations which can almost be solved explicitly in terms of  $\beta_i$  (Pope, 1975). The relationship<sup>5</sup>  $P_k/\varepsilon = -a_{ij}S_{ij}$  stills introduces non-linear behaviour removing this possibility. A consistent approach<sup>6</sup> that performs well in non-equilibrium zones is to use the  $a_{ij}$  solution and solve a separate polynomial (Girimaji, 1996). With this tweak, the system of equations becomes fully explicit and is called an Explicit Algebraic Stress Model (EASM).

EASMs are categorised as NLEVMs due to the relationship Eq. 2.49 inducing a non-linear stress-strain relationship on the Reynolds stress. The coefficient  $\beta_1$  is found via a Boussinesq-like approximation and so the equation is written in terms of an EASM eddy viscosity prescribed via characteristic length and time scales,

$$\overline{u'_i u'_j} = \frac{2}{3}k\delta_{ij} - 2\nu_t S_{ij} + a_{ij}^x. \quad (2.51)$$

The anisotropy has been decomposed into  $-2\nu_t S_{ij} = \beta_1 T_{ij}^1$  and  $a_{ij}^x = \beta_2 T_{ij}^2 + \beta_4 T_{ij}^4$ . This formulation of Reynolds stress modelling offers the compromise between the robust nature of the linear eddy viscosity and superior physics of RST modelling. Whilst many aspects of the latter have been lost, so has much of the computational requirement and numerical difficulties.

The weak equilibrium hypothesis can also be understood by considering a transformation of Eq. 2.40 to a transport equation for anisotropy,

$$kD_t a_{ij} - kD_{ij}^a = \frac{\overline{u'_i u'_j}}{k}(P_k - \varepsilon) + P_{ij} - \varepsilon_{ij} + \Phi_{ij}. \quad (2.52)$$

$D_{ij}^a$  are the diffusion and transport terms. By modelling the pressure-strain correlation  $\Phi_{ij}$  with a quasi-linear form (Lauder et al., 1975; Gibson and Launder, 1978; Speziale et al., 1991), the transport equation for  $a_{ij}$  becomes,

$$\begin{aligned} \frac{\tau_t}{A_0}(D_t a_{ij} - D_{ij}^a) &= \left(A_3 + A_4 \frac{P_k}{\varepsilon}\right)a_{ij} + A_1 S_{ij} - (a_{ik}\Omega_{kj} - \Omega_{ik}a_{kj}) \\ &+ \left(a_{ik}S_{kj} + S_{ik}a_{kj} - \frac{2}{3}a_{ik}S_{kj}\right). \end{aligned} \quad (2.53)$$

Grundestam et al. (2005) details the formulation of Eq. 2.53 and then applies Rodi's weak equilibrium hypothesis to remove convection, diffusion and transport terms. The

---

<sup>5</sup>found by normalising  $P_{ij}$  with  $\varepsilon$ , considering symmetric and anti-symmetric components of  $\partial_{x_j}\bar{u}_i$  and finally taking the trace.

<sup>6</sup>assuming  $P_k \sim \varepsilon$  has been studied (e.g. Taulbee, 1992)

	$A_1$	$A_2$	$A_3$	$A_4$
LLR	1.54	0.37	1.45	2.89
SSG	1.22	0.47	0.88	2.37
WJ	1.20	0	1.8	2.25

TABLE 2.1: Table of model constants for EASM models.

result is the equation,

$$Na_{ij} = -A_1 S_{ij} - A_2 \left( a_{ik} S_{kj} + S_{ik} a_{kj} - \frac{2}{3} a_{ik} S_{kj} \right) + (a_{ik} \Omega_{kj} - \Omega_{ik} a_{kj}). \quad (2.54)$$

$N$  is given as,

$$N = A_3 + A_4 \frac{P_k}{\varepsilon}. \quad (2.55)$$

$A_i$  are constants that must be specified. Three different sets are available in the literature, Launder et al. (1975) (LRR), Speziale et al. (1991) (SSG) and Wallin and Johansen (2000) (WJ). The values of these coefficients are specified in Table. 2.1. Equation 2.55 is still an implicit polynomial that needs to be solved iteratively. In order to make this explicit, Weinmann and Sandberg (2009) used the same pressure-strain model of Speziale et al. (1991) to formulate an expression for  $a_{ij}^x$ . The result is,

$$a_{ij}^x = \beta_2 (S_{ik} S_{kj} - \frac{1}{3} II_S \delta_{ij}) + \beta_4 (S_{ik} \Omega_{kj} - \Omega_{ik} S_{kj}), \quad (2.56)$$

where,

$$\beta_2 = 2 \frac{A_1 A_2}{Q},$$

$$\beta_4 = -\frac{A_1}{Q},$$

$$Q = N^2 - 2II_\Omega - \frac{2}{3} A_2^2 II_S, \quad (2.57)$$

$$N = A_3 + A_4 \frac{P_k}{\varepsilon}$$

$$II_S = S_{ij} S_{ij}.$$

The resulting eddy viscosity is given as,

$$\nu_t = C_\mu^\nu k \tau, \quad (2.58)$$

where  $C_\mu^\nu = 0.22$  and

$$\tau = \max \left[ \min \left( \frac{k}{\epsilon}, \frac{0.6}{\sqrt{6} C_\mu |S_{ij}|} \right), C_\tau \sqrt{\frac{\nu}{\epsilon}} \right]. \quad (2.59)$$

The remaining coefficients are given as  $C_\mu = 0.09$  and  $C_\tau = 6$ . To close the equation set, Eq. 2.30 are solved. As such,

$$\varepsilon = C_\mu k \omega. \quad (2.60)$$

Equation 2.54 is quadratic in the velocity gradient tensor, however Eq. 2.49 allows higher powers. The model by Craft et al. (1996) is an example of a cubic model, that was designed to better capture streamline curvature. This section is closed by noting that one is not limited to raising the power of the stress-strain relationship to improve the anisotropy. Durbin (1991) added two extra transport equations to account for near wall damping of the eddy viscosity. One transport equation accounts for a quantity closely related to the wall normal stress and another accounts for an elliptic relaxation function. Because of the numerical stiffness of the original approach, Laurence et al. (2004) modified the form of the equations into what is known as  $\varphi\text{-}\alpha$  elliptic blending.

## 2.2.4 Hybrid Modelling

Two methods for reducing the cost of turbulence simulation have been presented. The first used a scale separation  $\langle \cdot \rangle$  that filtered scales fundamental to LES. The second, applied a statistical separation  $\overline{\langle \cdot \rangle}$  that averaged scales fundamental in the RANS approach. LES is not a significant cost saving relative to industrial flow. RANS has been discussed as largely inaccurate, although computational affordable. Hybrid RANS/LES modelling aims to combine the two philosophies to provide a middle ground. A more accurate, unsteady description of turbulence is required for industry purposes. In recent years there has been a shift in application, from on-design conditions which contain little separation and is mostly steady, to off-design conditions, noise control and dynamic load calculations. These applications require three dimensional unsteady turbulence resolution (Spalart and Bogue, 2003; Sagaut and Deck, 2009). Because LES is simply too expensive — Spalart et al. (1997) predicted LES of a full wing configuration will not be possible until 2045 — the compromise Hybrid RANS/LES offers is very seductive.

The general philosophy is to resolve some turbulence where possible, but to use RANS where this is not. The combination of LES and RANS is made possible by the generalised derivation of Eq. 2.7. As both the statistical average and the low pass filter arrive at structurally similar equations, methods can be devised that solve a single set of equations based on a generalised scale separator. The scale separator acts as a low pass filter in regions of turbulence resolution and as a statistical average in regions of turbulence modelling. Solving the same set of equations everywhere in this manner is known as Global Hybrid RANS/LES and is covered in Section 2.2.4.1.

Another option is to segregate the domain into an LES region and a RANS region. This is known as zonal RANS/LES and broadly describes approaches that deploy at least two sets of fundamentally different equations that must be coupled across an interface.

This interface is the major challenge for segregated modelling, not only does it have to be prescribed in a location that will not affect the quality of the solution, but it must provide realistic fluctuations in the RANS to LES direction and this is not a trivial task. Further, the coupling of two different equation sets that transport different quantities is not easy and boundary conditions must be applied that preserve continuity and at the same time do not affect the quality of the solution.

Work on Hybrid RANS/LES began because of the crippling near wall grid requirements discussed in Section 2.2.1. Schumann (1975) reduced the cost of LES by modelling at the wall. It was not until Speziale (1997) and Spalart et al. (1997) independently released conceptually similar methodologies that hybrid modelling gained serious weight. After this a plethora of methodologies circulated the literature, so many so that Sagaut et al. (2013) describes the current state of the literature as a ‘jungle.’ The upcoming sections describe important breakthroughs in Hybrid RANS/LES modelling.

#### 2.2.4.1 Global Methodologies

Global methodologies apply a generalised scale separator that acts in an ambiguous way. The operator, from this point forward denoted via  $\widetilde{(\cdot)}$ , acts as a statistical average in regions of low resolution and as a low pass filter in regions of high resolution. There is a controversial grey area in the between where many would argue that the scale separator is acting as neither.

In practical situations this scale separator is not explicit (Sagaut et al., 2013), instead the generalised filter is implicit in the numerical procedure with the grid width  $\Delta$  acting as an effective filter. Therefore  $\tau_{ij}^{\text{mod}}$  must pick up all the unresolved scales that are removed by the effective grid filter.

In the fine grid limit, the grid filter acts well as a low pass filter removing scales in much the same way as classical LES. In fact this is how most LES is carried out, because explicit filtering is such an expensive operation. In the coarse limit, the grid filter has sufficiently removed enough scales such that the resolved time scale  $\tau \rightarrow \infty$ , implicating a statistical approach is being performed. In between, the filter is neither classical LES resolution nor (U)RANS resolution. It is argued that the approach is consistent in this grey area because the filter is removing spatial and time scales and whilst is neither a statistical nor spatial separator, time and length scales of turbulence are intrinsically linked to one another. As such arguing a scale separation operator is statistical or low-pass is not really relevant as they act upon both time and length scales. The only real difference is that traditionally the statistical operator is applied much more aggressively. As an example, consider the URANS operator in Eq. 2.19. As  $T \rightarrow 0$  the operator removes less and less *spatial* scales and as such with a small enough period, classical

LES resolution would be achieved. In the converse situation, as  $T \rightarrow \infty$ , the steady statistical average is achieved.

Magnient et al. (2001); Magnient (2001) carried out studies on the effective filter for several different types of subgrid model. The conclusion was that the effective filter depended strongly on the length scale present in the (subgrid) eddy viscosity and the subgrid viscosity definition itself. Therefore RANS/LES methods that force a change in the subgrid length scale, induce a change in the local grid resolution. This behaviour is utilised by global RANS/LES methods. The challenge of a global approach is therefore to provide an appropriate length scale to  $\tau_{ij}^{\text{mod}}$  that provides the correct amount of modelling and and by extension the correct amount of dissipation.

Broadly speaking there are two types of global hybrid methodology, initially categorised by Spalart (2000) and extended by Fröhlich and von Terzi (2008). Either a methodology does not depend explicitly on the grid scale or it does. The first type aims to provide the appropriate subgrid length scale without any explicit information on the effective filter, whilst the second utilises  $\Delta$  to assist in the prescription of the correct length scale. A methodology without any explicit dependence on the grid is commonly referred to as URANS and with an explicit dependence the methodology is referred to as LES. This classification is not a reflection of the relative resolutions of the methodologies, but merely a historical convention that arose from the nature of RANS and LES closures. The classification does not necessarily dictate what type of underlying subgrid model is used. A RANS closure can be used in an LES environment to produce a hybrid closure that does not employ a classical LES model. This is a point of discussion and debate. RANS models such as those introduced in Section 2.2.3.1 are derived assuming a steady resolved flow field by applying statistical averaging operations to the Navier-Stokes, such as Eq. 2.42. Hybrid RANS/LES assumes the effective filter satisfies the relations of Eq. 2.6 and it is argued that the turbulence closures of the same form can be derived using the generalised filter. In other words the functional form of RANS closures make sense in an unsteady environment. The issue remains of coefficients however, as these are calibrated for a steady environment. These should be adjusted relative to the level of filtering. This is not done in this body of work, but it is acknowledged that this should be performed to provide a more consistent methodology.

In the next two sections, global methodologies that aim to adjust the subgrid length scale are explored in detail. Section 2.2.4.2 discusses advances in the URANS classification, whilst Section 2.2.4.3 discusses advances in the LES classification. It should be noted that there is a lot of crossover in methodologies, but each presented offers a unique way of providing their model contribution. Further, each methodology is introduced with the RANS and/or SGS model that it was originally or most popularly used with. But it should be noted that most methodologies are easily formulated using a different

RANS and or SGS model. This kind of flexibility makes global Hybrid RANS/LES easily implementable into any existing RANS solver.<sup>7</sup>

#### 2.2.4.2 Global URANS Closures

This section describes global Hybrid RANS/LES formulations that do not explicitly depend on  $\Delta$ . This makes a methodology free from explicit grid dependencies and therefore extremely easy to incorporate into an existing RANS solver. However without an explicit grid dependency, the control of  $\tau_{ij}^{\text{mod}}$  is harder with respect to the effective filter. This could result in model contribution vastly different from that which is required to supplement the resolved flow field. For example, see Section 8.4 where Scale-Adaptive Simulation is used to predict the flow field around inline tandem cylinders. The flow-field did not respond to the grid resolution and  $\tau_{ij}^{\text{mod}}$  was significantly smaller than required. Scale-Adaptive Simulation was compared against methodologies that did contain explicit grid dependence and the latter philosophy proved to be far superior.

#### Classical URANS

The URANS filter expressed in Eq. 2.19 is probably the simplest method of performing time-dependent RANS calculations. As mentioned the averaging period  $T$  must be larger than  $\tau_k$ . In order for URANS to be successful,  $T$  must also be smaller than the period of the large scale motions. URANS can be useful for predicting flows with large scale forcing where there is a spectral gap between the large scale motion and the smallest turbulent scales. In other words the turbulent instabilities are not the driving force behind the global flow field. Classical URANS is sometimes referred to as Transient-Reynolds-Averaged Navier-Stokes (TRANS) (Hanjalić and Kenjeres, 2000). PANS introduced in Section 2.2.2 also falls into this category of Hybrid RANS/LES, where a phase average is applied. If large scale periodic motions exist, then PANS can give good results — for example Renaud et al. (2012) used the phase induced by rotor blades to perform PANS on a full helicopter configuration. Due to the similarity between PANS and TRANS these are often considered the same technique.

#### (Original) PANS: Partially-Filtered Navier-Stokes<sup>8</sup>

Partially-Filtered Navier-Stokes (PANS), introduced by Girimaji (2006), is a URANS closure that effectively damps the coefficient appearing in the eddy viscosity equation

---

<sup>7</sup>Providing appropriate finite difference stencils are available. Too much numerical dissipation can seriously hurt hybrid methodologies.

<sup>8</sup>This is not the same as the Phase-Averaged Navier-Stokes. Both are abbreviated to PANS. Further, URANS and LES types of the methodology exist. Both are covered in the respective sections. The term original corresponds the URANS Partially-Filtered Navier-Stokes methodology.

for a classical RANS model. The PANS approach uses *a priori* and *ad hoc* damping of the turbulent variables to represent the unresolved scales. For example, a  $k - \varepsilon$  PANS approach would define  $\nu^{\text{sgs}}$  as,

$$\nu^{\text{sgs}} = C_\mu^* \frac{k^{\text{sgs}}}{\varepsilon^{\text{sgs}}} = C_\mu \frac{f_k^2 k}{f_\varepsilon \varepsilon}. \quad (2.61)$$

$f_k^2/f_\varepsilon$  represents the constant damping of the RANS model. The RANS transport equations are for the subgrid quantities  $k^{\text{sgs}}$  and  $\varepsilon^{\text{sgs}}$ . The transport equations are derived consistently, but require an extra modelling term — suggestions are made by Girimaji (2006). The coefficients are damped using ratios of  $f_k$  and  $f_\varepsilon$  which represent the ratios of subgrid to total quantities. This alleviates the problem of applying a RANS model in an unsteady environment.

The potential and possibly alarming issue, is that  $f_k$  and  $f_\varepsilon$  are user prescribed and constant. This places a lot of pressure to not only understand beforehand what is the appropriate amount of damping, but also the grid must respect a constant ratio of unresolved to resolved scales. This is highly unlikely for industrial flows, where mesh quality is likely to be suboptimal and *a priori* knowledge of turbulent length scales is not possible. The methodology should be considered though, because it has addressed the issue of coefficient damping of a standard RANS model. Note the criticisms here for PANS are for this URANS implementation. PANS has been developed to include a specific dependency on  $\Delta$ . Because the methodology has effectively switched classification, the LES-PANS closure is covered in Section 2.2.4.3.

Whilst PANS damps the coefficients of the turbulent transport equations, these equations of motion are derived by assuming that the material derivatives of total to unresolved are self-similar. For example the  $k^{\text{sgs}}$  transport equation is derived assuming,

$$\partial_t k^{\text{sgs}} + \tilde{u}_j \partial_{x_j} k^{\text{sgs}} = f_k (\partial_t \bar{k} + \bar{u}_j \partial_{x_j} \bar{k}). \quad (2.62)$$

Equation 2.62 is fine in the RANS limit, as  $f_k = 1$  and no scales are resolved. Also in the DNS limit  $f_k = 0$ , so the relation trivially holds. However outside of these limits it seems implausible that the small scales mimic the total scales. Consider in the LES regime, the small scales are considered isotropic, whilst the large scales should exhibit strong macro dependencies induced by the geometry. Because this assumption is invalid, it is unclear as to whether the coefficient damping is providing better solution control.

### SDM (OES): A Semi-Deterministic Approach (Organised Eddy Simulation)

The Semi-Deterministic Methodology (SDM) approach first introduced by Ha Minh and Kourta (1993), also known as Organised Eddy Simulation (OES) (Braza, 2000), is a URANS approach that differs in philosophy from the scale separations already

introduced. The phase-averaged Navier-Stokes equations are solved, so the method is independent of any spatial scale separator (i.e. grid filter) that is applied. The scale separator, is one that splits a component  $\phi$  into its coherent part  $\langle \phi \rangle$  and incoherent part  $\phi'$ . In other words the determination of the scales to be resolved is not based on physical size, but rather on their actual physics.  $\phi'$  picks up the chaotic, uncorrelated motions. Being a URANS methodology, a RANS model is employed to model this chaotic motion. The RANS equations are formally similar to the classical URANS approach, however the time and lengths scales of the transported variables are different as they represent fundamentally different quantities. Sagaut et al. (2013) points out that the phase-averaged SDM turbulent stress plus the energy from the resolved phase flow field is analogous to the steady RANS turbulent energy. As a consequence the following inequality is observed  $\tau_{ij}^{\text{sdm}} < \tau_{ij}^{\text{rans}}$ . In order to account for this, the eddy viscosity relation is damped in a very similar way to PANS. Ha Minh and Kourta (1993) suggested using  $C_\mu = 0.05$  for an SDM based on the  $k - \varepsilon$  model. It should be noted that this kind of constant damping suffers from the same drawbacks as the PANS methodology.

The problem with lowering  $C_\mu$  in the attached boundary layer is that it was derived to ensure appropriate log-law scaling near the wall. As a consequence Deprés (2003) performed SDM which used  $C_\mu = 0.09$  in attached boundary layers, but lowered the value to  $C_\mu = 0.02$  for flow separation.

Kourta (1999) devised a temporally and spatially dependent value of  $C_\mu$  by providing explicit dependence on the velocity gradients,

$$C_\mu(S^*, \Omega^*) = \frac{2}{3} \frac{1}{A + S^* + \gamma \Omega^*}. \quad (2.63)$$

The star represents a normalisation of the strain and rotation tensor magnitudes,

$$S^* = \frac{\langle k \rangle}{\langle \varepsilon \rangle} |S_{ij}| \quad \Omega^* = \frac{\langle k \rangle}{\langle \varepsilon \rangle} |\Omega_{ij}|. \quad (2.64)$$

$A = 1.25$  and  $\gamma = 0.9$  are constants.

SDM suffers from an overestimation of the coherent structures (Kourta, 1999; Deprés, 2003), which affects the quality of the solution. That said, the advantage of SDM is that grid refinement does not introduce new resolved flow physics — due to the phase-average. This means the grid does not need to be finer than for RANS, which means grid convergence can be achieved. That said, without being able to respond to finer grids, additional structures cannot be resolved — which makes the method unsuitable when a lot of grid points are available. One could theoretically reduce the period  $T$  in Eq. 2.20, but then one must know the number of phases  $N$  in this period. As a result, SDM is best suited to only resolving the large coherent motion for which the number of phases is more easily known.

## TRRANS: Turbulence Resolving RANS

Travin et al. (2004) introduced the URANS approach Turbulence-Resolving RANS (TRRANS). The original formulation was based on the  $k - \omega$  model introduced in Section 2.2.3. The modification is to the  $k$  destruction term,

$$D_k^{\text{trrants}} = F_{\text{trrants}} \cdot \beta^* k \omega, \quad (2.65)$$

where  $F_{\text{trrants}}$  is defined as,

$$F_{\text{trrants}} = \left[ \max \left( \left( \frac{S}{C_{\text{trrants}} \Omega} \right), 1 \right) \right]^2. \quad (2.66)$$

$C_{\text{trrants}}$  is a constant larger than 1. In shear layers  $S \approx \Omega$  and in vortices  $S < \Omega$ , implying classical RANS in these regions. However when the flow is dominated by strain  $D_k^{\text{trrants}} > D_k^{\text{rants}}$ , so the value of  $k$  drops resulting in a drop of eddy viscosity. This in turn allows the simulation to go unsteady and the possibility to resolve turbulence.

For the flow around a high-angle of attack aerofoil, TRRANS gives LES-like resolution (Travin et al., 2004), however it failed entirely to resolve turbulence for the backward facing step. The ability of TRRANS to act as an LES should be questioned. There is no explicit dependence on the effective filter, only sensitivities to velocity gradients. For two different flow fields it performed entirely differently and therefore the URANS approach should be brought into question.

## SAS: Scale Adaptive Simulation

Scale Adaptive Simulation (SAS) is a similar approach to TRRANS. SAS was originally derived as a one-equation model for the transport of eddy viscosity (assuming equilibrium of production and dissipation rate) (Menter, 1997). An inverse dependence on the von Kármán length scale (Menter et al., 2003),

$$\ell_{vk} = \kappa \sqrt{\frac{\partial_{x_j} u_i \partial_{x_i} u_j}{\partial_{x_m}^2 u_l \partial_{x_l}^2 u_m}}, \quad (2.67)$$

was introduced in the destruction term for  $\nu_t$ .  $\ell_{vk}$  is effectively a measure of unsteadiness outside the boundary layer. The more unsteady the flow field, the smaller  $\ell_{vk}$  thus increasing destruction of  $\nu_t$  in a similar way to TRRANS.

Menter et al. (2003) extended the model to the  $k - \omega - \text{SST}$  model formulation of Eq. 2.30. The approach saw a modification to the  $\omega$  equation,

$$D_t \omega_{\text{sas}} = D_t \omega + Q_{\text{sas}}, \quad (2.68)$$

where  $Q_{\text{sas}}$  is,

$$Q_{\text{sas}} = \left[ \zeta_2 \kappa S^2 \left( \frac{\ell_m}{\ell_{vk}} \right)^2 - C_c \frac{2}{\sigma_\phi} k \max \left( \frac{1}{\omega^2} |\partial_{x_i} \omega|^2, \frac{1}{k^2} |\partial_{x_i} k|^2 \right) \right], \quad (2.69)$$

where the constants are  $\zeta_2 = 1.47$ ,  $C_c = 2$ ,  $\sigma_\phi = 2/3$ .  $\ell_m$  is the length scale of the modelled turbulence defined as,

$$\ell_m = \frac{\sqrt{k}}{C_\mu^{0.25} \omega} \quad (2.70)$$

The  $Q_{\text{sas}}$  term goes large in the presence of unsteadiness, so acts as a destruction mechanism for turbulent kinetic energy. SAS is possibly the most popular hybrid URANS approach. It shows promising results Menter (1997); Menter et al. (2003), however the discussions made in the TRRANS approach apply here. Further, Fröhlich and von Terzi (2008) discusses a strong time-step dependence and also a force feedback loop on the production of  $\nu_t$  that can undesirably force the model steady.

#### 2.2.4.3 Global LES Closures

Global Hybrid RANS/LES methodologies that exhibit an explicit grid-dependence are in the opinion of this author more appropriate. An explicit dependence on  $\Delta$  should in theory provide a better and more physical interpretation of the scale separation. Whilst the URANS approach aims at resolving turbulence in the presence of unsteadiness, there is not much control of the level of model contribution. Comparing turbulent length scales to  $\Delta$  should provide a more accurate description of the required length scale in the subgrid model.

#### FSM: Flow Simulation Methodology

Speziale (1997, 1998) developed a Hybrid RANS/LES methodology that would become known known as Flow Simulation Methodology (FSM) (Zhang et al., 2000; Fasel et al., 2002). The basic concept is to damp the Reynolds stress from a RANS closure,

$$\tau_{ij}^{\text{mod}} = F(\Delta, \dots) \tau_{ij}^{\text{rans}}. \quad (2.71)$$

The FSM subgrid model therefore consists of two components,  $\tau_{ij}^{\text{rans}}$  that models the turbulence and  $F(\Delta, \dots)$  that damps this contribution to be an accurate representation of the subgrid scales.  $F$  is bound between 0 and 1. When  $F \rightarrow 0$  the model switches off and DNS is performed. When  $F \rightarrow 1$  the scale separator is acting aggressively enough for the methodology to act as RANS. Speziale aimed to provide one technique that automatically offered anywhere between DNS to RANS resolution. Clearly the success of the method relies on the construction of the contribution function  $F$ .

To create a more consistent approach, consider that the Boussinesq approximation of Eq. 2.24,  $\tau_{ij}^{\text{mod}}$  can be rewritten as,

$$\tau_{ij}^{\text{mod}} = \frac{2}{3} F k \delta_{ij} - 2 F \nu_t S_{ij}. \quad (2.72)$$

Weinmann (2011) argues that the first term of Eq. 2.72 on the right does not need to be damped, provided an appropriate length scale is used in the  $k$  equation. The second term suggests a damping of the turbulent length scale in  $\nu_t \sim \ell_t u_t$ , arguing that the velocity scale  $u_t$  is already correct due to the effective filter. This reduces FSM to a damping of the turbulent length scale and is how the methodology is currently applied throughout this thesis,

$$\ell^{\text{fsm}} = F(\Delta, \dots) \ell_t. \quad (2.73)$$

This is still not a fully consistent set of equations, as it is built by reasoning that increased dissipation lowers SGS contribution. By simply changing the length scale you are forcing the model unsteady, hopefully in a controlled way, depending on the definition of  $F$ . However, the equations of  $\tau_{ij}^{\text{rants}}$  have been rescaled but each individual term has a physical meaning regarding RANS. Either equation coefficients should be damped in a way that is not dissimilar to PANS<sup>9</sup> or new transport equations should be derived based on Eq. 2.71. Deriving new transport equations is highly involved and yields equations with the second derivatives of  $F$ , so has not yet been explored. Based on the standard  $k - \varepsilon$  model, the transport equation for  $k^{\text{sgs}}$  would contain sixteen terms. This is derived from the modelled equations, not an SGS environment or even the exact equation for  $k$ . That is not to say it is not worth exploring, as the equations would be closed and could potentially yield benefits. It is hypothesised that the transport equations derived by considering Eq. 2.71 would be more consistent than the PANS approach, because spatial and temporal gradients of  $F$  would not be ignored, nothing is assumed about the shape of  $F$  and the derivation starts from a principle that the resolved energy is less than the total energy — seen by first taking the trace — which is fundamentally correct (as opposed to starting a derivation from an assumption). Clearly the construction of  $F$  is still absolutely vital. Without a physical and realistic model damping term, the benefits of painstakingly deriving transport equations is largely lost.

Whichever formulation of FSM you prefer, the methodology relies on  $F$  and so most of the research has centred around this. Speziale (1997) originally suggested,

$$F(\Delta, \ell_k) = \left(1 - e^{-\beta \frac{\Delta}{\ell_k}}\right)^n, \quad (2.74)$$

where  $n = 1$  and  $\beta = 0.001$ . These constants are calibrated to cope with the DNS limit.  $\beta$  effectively dictates what is DNS resolution, whilst  $n$  controls how fast this limit is approached. Equation 2.74 therefore is valid in the DNS limit, but much beyond this

---

<sup>9</sup>See Sections 2.2.4.2 and below. For neither the URANS or the LES breed of PANS do you get consistent equations.

there is little hope of providing the appropriate model contribution.  $F$  of this form reacts far too slowly to local grid coarsening and it is hypothesised that the RANS limit would never be reached. This is because  $\Delta/\ell_k$  is not a useful measure of the largest scales of motion. That said Eq. 2.74 has been successfully applied on fine meshes — see Sandberg and Fasel (2004); Fasel et al. (2006).

The coarse limit has been recognised as a problem by several researchers and much effort has gone into changing  $F$ . Zhang et al. (2000) changed the coefficient  $\beta$  effectively making it an *ad hoc* adjustment for each flow configuration. Magnient et al. (2001) used an equilibrium assumption to derive a contribution function based on the integral length scale,

$$F(\Delta, \ell_t) = \frac{\Delta^{\frac{4}{3}}}{\ell_t^{\frac{4}{3}}}, \quad (2.75)$$

where coefficients are changed in the definition of  $\nu_t$ , not explicitly added to Eq. 2.75. This contribution function is likely to be very good for flows in equilibrium on coarser meshes, but is likely to fall down far from equilibrium and in the DNS limit. This dependence was also explored by Weinmann (2011), but  $F$  was a linear function with respect to  $\Delta/\ell_t$ . The overall function  $F = F(\Delta, \ell_t, \ell_k)$  contained DNS and LES regime control. Despite being constructed on an *ad hoc* basis, FSM based on this contribution function performed well on a range of flow fields.

Germano (1998) also derived a contribution function,

$$F = 1 - \frac{\overline{\tau_{ij}^{\text{rans}}} \cdot \overline{\tau_{ij}^{\text{res}}}}{\overline{\tau_{mn}^{\text{rans}}} \cdot \overline{\tau_{mn}^{\text{rans}}}} \quad (2.76)$$

where  $\tau_{ij}^{\text{res}}$  is the resolved turbulent stress. Note that  $(\bar{\cdot})$  is added to the equation to reinforce that Germano's derivation required a time average. Thus Eq. 2.76 is unsuitable for practical simulations, despite providing a very sensible and intuitive shape for  $F$ .

### LNS: Limited Numerical Scales

Limited Numerical Scales (LNS) (Batten et al., 2000, 2002) is based on FSM, but with a slightly different philosophy on  $F$ ,

$$F = \frac{\min(\nu_t^{\text{rans}}, \nu_t^{\text{les}})}{\nu_t^{\text{rans}}}. \quad (2.77)$$

If LNS is formulated with an LEVM,  $F$  forces LNS to act as RANS-limited LES, in other words  $F$  simply picks RANS or LES modelling depending on which is smaller. In theory any turbulence model can be used and the equation set does not need any further constants — simply taking the ones from  $\nu_t^{\text{rans}}$  and  $\nu_t^{\text{sgs}}$ . Note that LNS is a LES-hybrid due to  $\tau_{ij}^{\text{les}} = \tau_{ij}^{\text{les}}(\Delta, \dots)$ .

### (Modified) PANS: Partially-Averaged Navier-Stokes — the LES version

PANS has already been introduced as a URANS methodology in Section 2.2.4.2. However, Girimaji (2006) modified PANS such that,

$$f_k = \frac{1}{\sqrt{C_\mu}} \left( \frac{\Delta}{\ell_t} \right)^{\frac{2}{3}}, \quad (2.78)$$

which was derived using similar considerations as Magnient et al. (2001) in Eq. 2.75.  $f_\varepsilon = 1$  assuming that all dissipation is picked up by the model. Using Eq. 2.78 is like a double edged sword. Firstly, the model is now adaptive to local changes in grid-turbulence ratios — which is vital for a successful turbulence model. Secondly however, the model does not account for this dependence on space and time in the transport equations. There derivations are based assuming  $f_k$  is constant, but now derivatives in space and time cannot be ignored.

It is worth mentioning the Partially-Integrated Transport Model (PITM) of Chaouat and Schiestel (2005). PITM is effectively the same as PANS but has been constructed in a different way. The amount of subgrid stress is controlled via the model constants, but Sagaut et al. (2013) expresses that this is not done in a physical way and the ratio of modelled to total energy in practical situations is not the expected one.

### DES/DDES: Detached Eddy Simulation

Detached Eddy Simulation (DES) of Spalart et al. (1997) is the most popular hybrid methodology in industry. This is in part due to its age and its success of flow prediction around massively separated surfaces. The original DES involved a modification to the one-equation model of Spalart and Allmaras (1992), however Strelets (2001) also formulated DES with the  $k - \omega$  SST turbulence model.

The change, as with many of the methodologies outlined above, involves altering the turbulent length scale in the dissipation equation,

$$\ell^{\text{des}} = \min(C_{\text{des}}\Delta, y), \quad (2.79)$$

where  $C_{\text{des}} = 0.65$ . The wall distance  $y$  insures that DES runs in RANS mode near the wall, then the model moves to LES in separated boundary layers. The main issue with DES is the so called grey area. This is true of all the hybrids mentioned above, but the form of Eq. 2.79 best highlights the problem. The switch between RANS and LES mode is inherently grid dependent and the location where  $y = C_{\text{des}}\Delta$  hugely affects overall results. If this switch occurs inside the buffer layer, then resolved eddies will lack the required amount of energy. The result is an artificially low eddy viscosity which in some cases can cause premature separation (Menter et al., 2003). These eddies in the

boundary layer are characterised as long stream-wise structures that have unphysically long time steps. To partly overcome this issue, Spalart et al. (2006) proposed the following modification, known as Delayed Detached Eddy Simulation (DDES),

$$\ell^{\text{ddes}} = y - f_b \max(0, y - C_{\text{des}}\Delta), \quad (2.80)$$

where  $f_b$  is,

$$f_b = 1 - \tanh\left(8 \frac{\nu^{\text{sgs}} + \nu}{\sqrt{S_{ij} S_{ij} \kappa y^2}}\right), \quad (2.81)$$

where  $\kappa = 0.41$ .

The second and unsolved issue with DES is the value of  $C_{\text{des}}$ . It was initially calibrated by considering isotropic turbulence, for LES like resolution. However, consider that for the RANS limit (away from the wall),  $C_{\text{des}}\Delta = \ell_{\text{rans}}$ . This implies that the grid spacing must be bigger than the integral length scale before the RANS mode is recovered. This is hugely undesired, as the viscosity field is severely under predicted. In many cases there is not enough dissipation to ensure a physical solution. This is especially noticeable for attached boundary layers running in RANS mode.

#### 2.2.4.4 Issues with and Ongoing Development of Global Methods

There are several issues with the unified hybrid approach. The first, Model Stress Depletion, discussed above, is revisited in Chapter 7. Even more fundamental than that is the way in which an approach goes unsteady and resolves turbulence. There are two broad methodologies — URANS and LES — both of which have been introduced. But within these categories, we have seen a highly diverse approach to damping the turbulence contribution. Effectively, each method boils down to providing a form for  $F$  where  $\ell^{\text{hyb}} = F\ell_{\text{rans}}$ . There seems to be reasonable convergence in the literature towards this (with methods like PANS providing extra damping for coefficients to ensure production balances dissipation in equilibrium zones). However, there is very little agreement on what the shape of  $F$  should be or even the variables it should depend on. This is because derivations of  $F$  are hard (if not impossible) due to the unknown effect of the turbulence model and the filter on an arbitrary mesh. As a consequence, each unified closure outlined in this chapter has been largely constructed *ad hoc* and most have serious undoings for given flow problems. The most challenging test case currently encountered by this author is the tandem cylinder configuration in Chapter 8.4. For this problem, the original FSM (Speziale, 1997) did not provide model dissipation to be stable, the FSM of Weinmann (2011) depended strongly on the SGS closure for stability, whilst LNS and SAS gave very poor results.

This thesis focusses on introducing new techniques that can be employed to change the way turbulence models are constructed. This approach is introduced throughout the

remainder of this work and applied in the studies of Chapter 6. This is primarily an outline of the methodology to refine  $F$  and ascertain a sensible shape for it, however what is presented can easily be applied to assist with other questions also — namely MSD and the correct form of the subgrid model. The latter is the most fundamental question that remains unanswered regarding unified approaches. Many people have an issue with using RANS models in an unsteady environment, however the approach requires that the model reverts to RANS mode near solid walls and in the presence of poor resolution. The easiest way to achieve this RANS limit is to use it as a subgrid model, but maybe some changes are required to make it more SGS friendly. A more modest question is to simply ask which RANS model should be used. DES is traditionally used with the one-equation Spalart-Allmaras or the two-equation SST. This highly confuses the author because the near wall region is undoubtedly important and surely using the best available equipment in this region is preferable.

## 2.3 Summary

### 2.3.1 Choice of Prediction Strategy

The full spectrum from complete turbulence simulation through to complete turbulence modelling has been discussed. Choosing the correct strategy for one's needs is not always trivial.

DNS is the obvious choice in terms of accuracy, but is almost always out of reach in terms of computational demands. This leaves broadly two choices, (some) turbulence resolving as described in Sections 2.2.1 and 2.2.4 or turbulence modelling as described in Sections 2.2.2 and 2.2.3. LES is a more expensive resolution approach than Hybrid RANS/LES which has aimed to bridge the cost gap to RANS. This leaves a hierarchy of turbulence prediction strategies. This hierarchy is well laid out by Sagaut et al. (2013) into a pyramid representing the number of applications possible at each cost level.

There are some applications that simply must be done via turbulence resolving approaches. These are problems where the inherent unsteady nature of the flow plays a critical role in the parameter of interest. For example, acoustic predictions rely on the unsteady surface pressure data which is most accurately obtained via a turbulence resolving approach. Weinmann et al. (2014) used a Hybrid RANS/LES approach for acoustic predictions around an inline tandem cylinder geometry. The fluctuating pressure caused by the impinging wake on the downstream cylinder was excellently predicted. Consequently, main contributing factors to the acoustics were captured and yielded good results.

Other applications simply must be performed with RANS due to project time-frames (Hanjalic, 2005). This is not always a major cause for concern, if one only demands lift

and drag coefficients then steady RANS computations would often suffice. As alluded to in Section 2.2.2, there are a wide range of RANS models available, a sub-hierarchy within the overall picture of turbulence prediction strategies. Turbulence models generally have their merits and faults, often stemming from their original field of application. Hunt and Savill (2005) provides a detailed guide with regards to model choice and qualitative advice on selection.

In summary, there is (currently) no universal approach that can solve all problems. Each level of closure has its place in academic literature and in industry. This is unlikely to change for some time, with the advent of faster computers the relative problem size of each strategy will remain unchanged. Instead, we will begin to attack bigger problems that were previously completely impossible.

### 2.3.2 Avenues of Exploration for Current Research

This chapter has spoken briefly on the full hierarchy of modelling strategies available. There are several points in this spectrum that this thesis tries to address. Firstly, on theoretical and practical grounds, linear eddy viscosity modelling was discussed as inadequate (for many applications). Therefore this thesis attempts to address modifications to the linear stress strain model in Chapter 5. These modifications are similar to the models of Section 2.2.3.3.

The other entry point into this hierarchy is the problem of Unified Hybrid RANS/LES. There is already a plethora of models available, however with the tools discussed in the next few chapters, this thesis aims to build a hybrid formulation that is less *ad hoc* than those discussed in Section 2.2.4. Therefore, making it more applicable to a wider range of problems and better bridging the gap between LES and RANS.

# Chapter 3

## Evolutionary Algorithms

### 3.1 A Brief Note on Other Optimisation Strategies

Before proceeding with the namesake of this chapter, a mention to other optimisation processes is given. The field of optimisation is huge and covers a very broad range of topics. A review of very basic optimisations (e.g. minimisation of single valued functions), gradient based methods, simulated annealing through to Genetic Algorithms mentioned in this work is given, with engineering design in mind, by Deb (2012); Keane and Nair (2005). A full review of the topic is out of the scope of this work, instead a brief note on the choices made in this thesis is given.

The main advantage of evolutionary methods is their ability to operate on many different solutions at once (called the population), whilst other optimisation techniques generally only operate on one. This lack of diversity often means a poorer searching of the problem space and consequently a local optima is often reached. The freedom of expression in problem formulation is another attractive feature, evolutionary methods therefore have a very wide range of problem domains meaning they benefit from advances in many different fields of study. They are highly unconstrained in their problem definition, in contrast to classical techniques and are amongst the algorithms given the highest level of freedom to obtain a solution.

### 3.2 Overview of Evolutionary Algorithms

Evolutionary Algorithm (EA) is a generic term describing an artificial system that has been inspired by biological processes that adapt according to some metaheuristic. EAs define some high-level heuristic or procedure, designed to search a solution space for a low-level heuristic (hence the meta- prefix). For example, one may devise an algorithm

that searches for the safest path through a minefield, the low-level rule, according to how many mines are on said path, the high-level rule.

Specifically EAs are inspired by Darwin's (1859) ideas of natural selection. An artificial system consisting of a population of candidate solutions is evolved iteratively, according to survival of the fittest. An EA represents a simplified version of Darwin's ideas with imitations of physical biological processes. Reproduction, replication, mutation (both simple and relatively complex) and genetic crossover appear in these artificial mimicries. The terminology used is borrowed from genetics and ecology. The list of candidate solutions is denoted as the population and each candidate is an individual/organism/chromosome/gene depending on the application. Each iteration of the simulation is called a generation. The observable characteristics of an individual is its phenotype, for example a mathematical expression in regression problems or an actual path through a minefield. This phenotype is the interpretation of the individual's genotype which following the same examples would be a list of mathematical symbols ( $\times, +, -, x, y, \dots$ ) or a set of instructions for navigation (`left, right, stop, forwards, ...`).

By using these ideas, an EA is designed to be at heart a probabilistic search algorithm that performs better than random, by slowly accumulating beneficial variations over successive generations. This trial and error process keeps individuals that perform well and forces poorer ones to die out. This performance, known as the fitness of an individual, is a measure of its phenotype's suitability to the predefined high-level heuristic's fitness function. For example, in regression one may use the least square error from some training data or in the minefield example how many times an agent blows up.

EAs surfaced in the literature as early as the 1950s (Friedberg, 1958; Friedberg et al., 1959), as an improvement over existing optimisation and search methodologies. Non-evolutionary algorithms (see for example Steeb, 2011; Brownlee, 2011) often struggle on complex fitness landscapes that contain a vast amount of local optima. EAs aim to randomly search the space as with traditional approaches — but crucially they also contain the memory aspect inherent in the evolutionary process. Friedberg's initial work barely mentions evolution or natural selection, however the parallels are obvious — in the words of Friedberg (1958), 'Machines would be more useful if they could learn to perform tasks for which they were not given precise methods.' This is an early formulation of a metaheuristical philosophy. Despite the novelty, these ideas lay largely dormant for over ten years (Steeb, 2011), possibly because advances in computational power were required. Work throughout the 1970's by Rechenberg (1973) and Schwefel (1977) popularised EAs as an optimisation technique for complex problems in engineering. This approach was termed Evolutionary Strategies (ESs) designed to optimise real-valued function parameters as the primary application. Independently, the subclass of EAs known as Evolutionary Programming (EP) was also devised with the aim of parameter optimisation, pioneered in the 1960s and 1970s by David and Lawrence Fogel (see - Fogel, 1995, 1999). Both ESs and EPs perform biological processes directly on

the parameter values themselves. An individual consists of a vector and the genetic operators manipulate these values — most often using multivariate Gaussian distributions. The main difference between these two approaches is their abstraction of the evolutionary concepts. EPs deal with reproductive populations and thus the recombination metaphor does not make sense between two different species. The main agents in ESs are reproductive individuals and so a recombination of genetic material is a valid operation.

A far more versatile EA was formulated by Holland (1962, 1975) to study the processes of natural evolution computationally, keeping the work largely theoretical. Holland's work, known as Genetic Algorithms (GAs), gained serious weight and remain a popular optimisation choice today, assisted by the landmark text of Goldberg (1989). An individual is represented as a bit-string which due to its generality and freedom can be applied to an extremely wide range of optimisation and search problems. A further and major generalisation to this methodology is the Genetic Programming (GP) concept of Cramer (1985), expanded by Koza (1992). GPs evolve a population of tree structures, which greatly improves the freedom of what can be represented by an individual, widening the breadth of EA applications.

The final major expansion of EAs is that of Gene Expression Programming (GEP) (Ferreira, 2001). GEP combines both GAs and GPs and the result is the first EA with a true genotype-phenotype system. Genetic material is stored in strings which are expressed as tree structures. This distinction between the genotype and phenotype allows for a more varied expression because the genetic operations are not applied to the observable characteristics of an individual. As a result the whole genetic information need not necessarily be expressed. Further, the framework automatically produces syntactically correct phenotypes — a major issue with GPs. The guarantee of correct phenotypes drastically increases the number of available genetic operators. This enables the algorithm to keep a larger amount of variation in the population, reducing the probability of converging to a locally optimal solution.

In the following sections GEP is detailed as a tool for regression analysis. The preceding elements from GAs and GPs that form GEP are covered in Sections 3.3 and 3.4. Section 3.5 looks at the marrying of these elements and discusses the benefits and issues of using GEP primarily as a regression tool.

### 3.3 Genetic Algorithms

#### 3.3.1 Overview

Genetic Algorithms (GAs) are the most common branch of Evolutionary Algorithms. GA is a broad term that refers to too many strategies to list, but all follow the same

general structure — namely the Mendelian description of population evolution. This is the use of chromosomes, genes and alleles. As well as the landmark texts of Holland (1962, 1975) and Goldberg (1989) mentioned above, Mitchell (1995, 1999) introduces the topic very well. In what follows, the original form of the algorithm is presented; should the reader wish to see more complicated versions and modern interpretations of the basic GA, then proceed to the book by Goldberg (2002). Note, whilst the algorithm has changed over the years, the fundamentals introduced below still apply.

Each individual (chromosome) is usually encoded as a fixed-length binary string. Each position in the string is known as the gene, whilst the given value (0 or 1) is its allele. For example the chromosome,

101101100001011011001101

is a typical member of a GA population. A chromosome of length  $n$  using binary alleles allows for a total of  $2^n$  possible solutions. So one can see that for problems that can be formulated in this way that contain just a few parameters — i.e.  $n$  is small, a GA is not a worthwhile methodology.

The basic flow of the algorithm is described in Fig. 3.1. To solve an optimisation problem using a GA, one must first be able to describe the problem in GA terms. The problem must be decomposable into a fixed-length chromosome, with each gene containing specific information about the problem at hand. Also one must devise a fitness function  $f$ , the measure of an individual's chances of survival. The more optimal a solution is, the better the chance the individual will survive.

A population  $P^0 = \{P_1^0, \dots, P_N^0\}$  of  $N$  individuals is randomly created at generation  $i = 0$ . The fitter chromosomes are allowed to survive and then replicate using one of the strategies outlined in Section 3.3.2. Then with a certain probability each individual in the new generation will be subject to the genetic transformations of Section 3.3.3. This is then repeated many times over, creating the new generation  $P^{i+1}$  from  $P^i$  until the population converges to a solution (optimal or not), or the wall-time is exceeded. An optimal solution is found when the desired fitness  $F$  and maximum fitness of the population are within some tolerance  $\epsilon$ . A suboptimal solution is reached when the variance of the population's fitness values are smaller than some value  $\Sigma$  and the previous condition is not met.

### 3.3.2 Replication

Replication is a varied process in most EAs and GAs are no different. Depending on the application a certain kind of replication makes more sense. The most basic form of

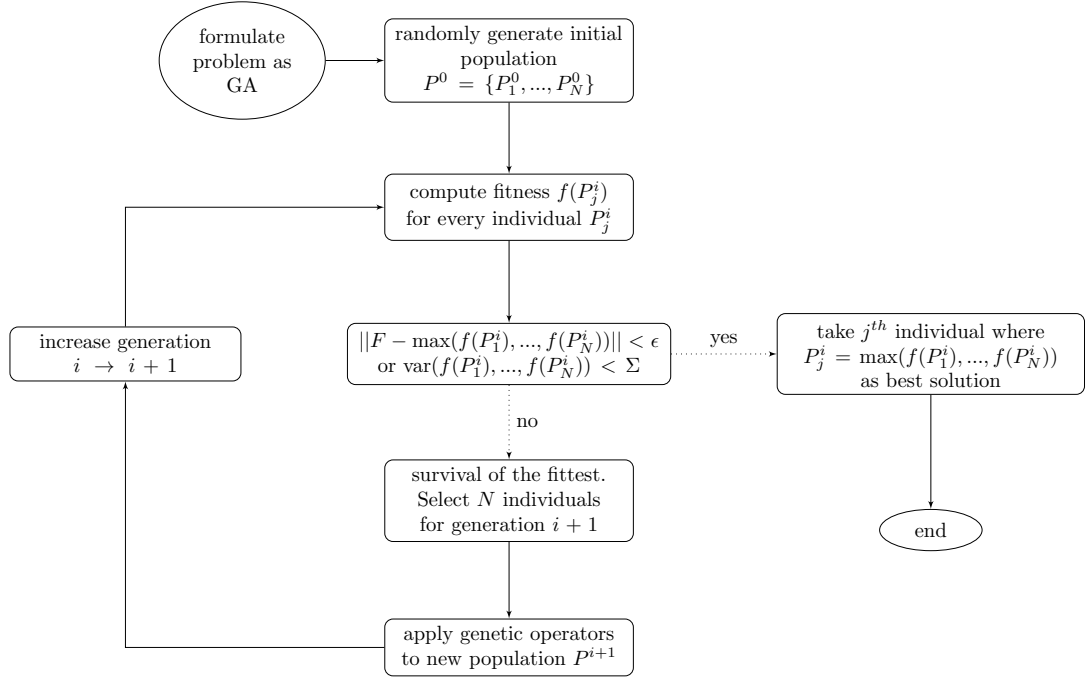


FIGURE 3.1: The flow of a typical Genetic Algorithm. This simplified diagram is the structure of almost all Evolutionary Algorithms.

replication (Koza, 1992), which is just copying an individual,

$$P_j^{i+1} = P_j^i \quad \forall j \quad (3.1)$$

analogous to asexual reproduction in microorganisms without any selection pressure. With this reproduction no genetic drift occurs as the fitness function is not employed. In this way, GAs act effectively as a random search of the solution space by relying solely on genetic operators.

In order to use the powerful memory component of evolution, the fitness function must be exploited to decide which weaker individuals should die out. The fitness function is entirely problem dependent — for two examples see Section 4.3 and Section 4.4.

Two of the most common methods for selection of individuals from generation  $i$  into generation  $i + 1$  are roulette wheel and tournament selection. Both are widely used due to their easy implementation. Roulette wheel selection can be thought of as spinning a roulette wheel  $N$  times with a box for each member of  $P^i$ . Each box is of a differing size based on the fitness of individual  $P_j^i$ . Should the ball land in the box for  $P_j^i$  then it is selected for the population  $P^{i+1}$ . The probability of an individual being selected  $p_r(P_j^i)$  upon each spin, is proportional to its fitness  $f(P_j^i)$ ,

$$p_r(P_j^i) = \frac{f(P_j^i)}{\sum_{j \leq N} f(P_j^i)}. \quad (3.2)$$

So the fitter the individual, the bigger its number on the roulette wheel and thus the larger the chance the ball will finish up in this box. In this sense, perhaps a wheel of fortune analogy is more appropriate, not the equally sized bays of a roulette wheel in casinos. Note that each individual is selected with replacement — in other words, if the roulette ball stops on  $P_j^i$  more than once during the  $N$  spins then it will appear multiple times in the next generation.<sup>1</sup>

The major issue with the roulette wheel is the often hugely varying or highly skewed fitness of individuals, such that a small set of a few individuals  $\mathcal{P} = \{P_l^i, \dots, P_{l+m}^i\}$  where  $m \ll N$  dominate the roulette wheel,

$$\begin{aligned}\sum_{P_j^i \in \mathcal{P}} p_r(P_j^i) &\approx 1 \\ \sum_{P_j^i \notin \mathcal{P}} p_r(P_j^i) &\approx 0.\end{aligned}\tag{3.3}$$

Therefore the same few individuals are repeatedly chosen resulting in convergence that is extremely quick and towards a suboptimal solution.<sup>2</sup>

The popular alternative to the roulette wheel is tournament selection. A predefined tournament size  $s$  is set. Then upon selection,  $s$  individuals are chosen (with replacement)  $N$  times from generation  $i$  to compete in tournaments for the  $N$  places in generation  $i+1$ . The fittest from each of these tournaments is selected to survive and thus take the position in the new population. The parameter  $s$  is an effective selection pressure. For larger values of  $s$  there is a much greater chance of each tournament containing a strong individual, and for smaller values of  $s$  surviving the tournament is easier as competition is between fewer randomly selected individuals. Therefore by tuning  $s$ , one can achieve the desired amount of variation for a given problem.

More complex variations of tournament selection exist, created by redefining the tournament process. One could implement any kind of tournament they desire, be it a round robin or a knockout competition decided by successive mini roulette wheels. However in practice, the standard of allowing the fittest out of the  $s$  individuals to survive is most often used as it is much easier to implement and more complex tournaments give questionable gains.

Sometimes, during these selection processes the best individual or even the top few are not selected for the next generation — resulting in a loss of good solutions. This could be from either the roulette ball never landing on the fittest individuals or they could not get selected to compete in any tournaments. Further, even if selected, the genetic operators outlined in Section 3.3.3 may randomly be applied and could seriously affect the quality of a desirable solution. Whilst these outcomes are present in the blind evolution of nature, they can be seriously harmful to algorithmic performance. A simple

---

<sup>1</sup>Selection without replacement clearly does not make sense.

<sup>2</sup>Note:  $p_r(P_j^i) \approx 1 \nRightarrow f(P_j^i) = \sup\{f(\sigma) | \sigma \in \Sigma^n, \Sigma = \{0, 1\}\}$  as  $p_r$  is proportional to the members of the population at generation  $i$ , not the overall global optima of the solution space.

measure to counter this is elitist selection. The basic principle of elitism is to ensure that the best solutions are carried forward into  $P^{i+1}$ . At the very least, one should store in a separate location the best individual for all times so that should it die out and leave the gene pool you at least still have access to it.

De Jong (1975) did the first major work on the study of selection in GAs. Several methods were introduced as alternatives to the processes above, but elitist modelling (now called simple elitism) was the first method to preserve good solutions. Simple elitism is just the act of preserving the best individual, which can also be removed from the list of candidates for crossover (see Section 3.3.3) or made available. In the latter option, the best is copied and if chosen for crossover its genetic material is effectively duplicated in any children it will have.

Countless variations on the selection theme exist throughout the literature. Examples include: selection with reducing fitness once an individual has been mutated or has mated to reduce stochastic sampling error (De Jong, 1975), ranking individuals from  $1, \dots, N$  and using these values in a roulette wheel to avoid the skewness mentioned above, roulette wheel selection with a single spin of  $N$  equally spaced balls (Baker, 1987) and selection based on the expected number of a certain individual appearing at generation  $i + 1$  (Brindle, 1981). For a comprehensive review of selection methods see Michalewicz (1996).

### 3.3.3 Genetic Operators

After the individuals for  $P_j^{i+1}$  have been selected from  $P_j^i$ , they are each subject to genetic operators with a given probability. Generally, each chromosome may undergo multiple operations but in order to protect them from too much genetic destruction, one can limit each individual to at most one genetic operation. The order in which they are implemented then becomes important, as those which are applied first are more likely to happen.

There are two main genetic operators in GAs — mutation and recombination. If a chromosome is selected for mutation, then this is simply a random change of a random gene's allele. For example,

```
100011100010101101
101011100010101101
```

an individual's third gene is mutated from 0 to 1. Recombination requires two or more parent individuals from the previous generation. Although two parents is the most biologically inspired, a greater number may provide better quality children (Eiben et al.,

1994; Ting, 2005). Recombination, also known as crossover, is the process of making cuts in the parent individuals and then swapping portions to make new children for the next generation. One-point and two-point recombination are the most popular, where the number reflects how many cuts are made. The cuts are made at the same random position on all parents in order to preserve the length of the chromosomes and thus the meaning of the phenotype for the given problem. For example the parents,

```
100011110001010110101111
101101100001011011001101
```

may undergo one-point recombination with a cut made between the seventh and eighth position to form the children,

```
101101110001010110101111
100011100001011011001101
```

by swapping these first seven genes. Two-point recombination can easily be imagined by making two cuts and swapping the middle portion. Or if more than two parents are involved, then some kind of permutation process is required — as fanciful as one dares encode. Once the parents have mated and formed offspring for generation  $i+1$ , they die out and their children take their place in  $P^{i+1}$ . If some individuals do not mate, then they are just copied to the next generation — in doing so preserving  $N$ .

### 3.3.4 Limitations

In GAs, the genotype and phenotype are both represented by the bit-string, meaning the chromosomes in GAs are equivalent to simple replicators in biology. One may argue that the phenotype of a chromosome is what it physically represents. For example, a chromosome may be split twice,

```
10110110 00010110 11001101
```

to represent three floating point numbers for a parameter optimisation problem. Or each gene may represent the switching of some binary operation — say left or right through a maze and the resulting path could be argued as the phenotype. However this is purely semantical, the key point is that the genotype and phenotype consist of entirely the same information — nothing more and nothing less. The chromosome is both the genotype and phenotype, both the genetic material and functionality of an individual.

This seriously hampers a GAs performance. It is not possible for a phenotype to be only a partial expression of the genotype. Firstly, the implications of this is that an individual must live with all of its genetic information — the good and bad. An individual that may contain highly useful genetic material that should be passed onto future generations may die out because of a few adverse alleles. Secondly, it is not possible for genetic material to lie dormant. Potentially beneficial combinations of genetic material will never be found unless the previous individuals manage to survive, which is unlikely with only partially good genes. Because of this nakedness of the chromosome, the major benefit of recombination — the process of merging pieces of useful genetic material is lost.

Another major constraint of GAs is the fixed-length nature of its chromosomes. This restricts the list of problems that can be formulated as a GA. Obviously some problems suit this, such as the Knapsack Problem (e.g. Khuri et al., 1994), where there is a finite and fixed number of parameters to the problem. But if we do not know the number of parameters that should be expressed and indeed if there is an interaction between the genes, then a GA is not a suitable approach. For example, regression problems where the functional form is unknown are highly unsuitable. Whilst we could conceivably use a non-binary dictionary, the fixed-length chromosome is difficult to use as we do not know whether the functional form is short or long and as an aside, the mathematical syntax of an individual is likely to be far from correct. Consider the next example of optimising a path through a maze. The dictionary is easy enough to construct as `{left, right, forwards, ...}` and the fitness function can be defined as the distance from the goal to the finishing point of a path. But because the chromosome is a fixed-length, each solution is restricted to *exactly* the same number of moves. This will hardly produce the varied and diverse solutions we desire.

## 3.4 Genetic Programs

### 3.4.1 Overview

Genetic Programs (GPs) were devised by Cramer (1985) and heavily expanded by Koza (1992) as a solution to the limitations inherent with the GA fixed-length individual. Instead, each individual exists as a non-linear structure — known as a Parse Tree. Further the language of these Parse Trees is far more varied than the standard binary alphabet used in most GAs. These factors add up to a much broader range of problems that can be tackled using evolutionary methods.

Symbolic Regression (SR) is one such extra possibility. As the name suggests, SR is a regression analysis where, unlike traditional methods, no functional form is required *a priori*. Instead the user merely supplies a list of symbols, which are the allele's in the GP process, akin to the 1's and 0's of GAs. These symbols form parts of a mathematical

expression. For example the symbols  $\mathcal{S} = \{+, -, /, *, \log, x, y, 1\}$  can be arranged in Parse Trees, which in turn can be read as mathematical expressions. For this to happen  $\mathcal{S}$  must be split into a function set  $\mathcal{F}$  and a terminal set  $\mathcal{T}$ . Elements from the function set,  $\mathcal{F} = \{+, -, /, *, \log\}$ , exist as branches in the Parse Tree, whilst elements from the terminal set  $\mathcal{T} = \{x, y, 1\}$  exist as leaves. Figure 3.2 is an example member of a GP population using these symbols. Note that not every symbol must be used by

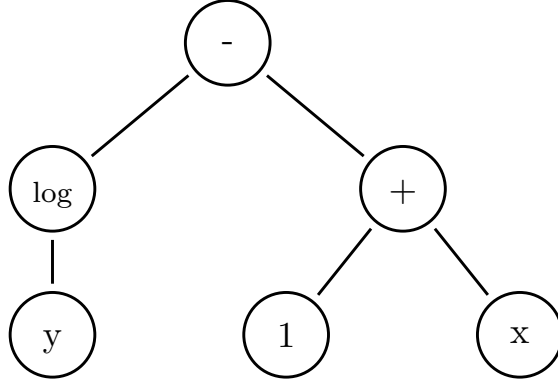


FIGURE 3.2: Parse tree individual. Terminals exist on leaves, functions as branches.  
The mathematical expression of this individual is  $\log(y) - (1 + x)$ .

each individual. The difference between functions and terminals, as their names should suggest, is that functions depend on arguments to make sense whilst terminals must not take arguments. Hence terminals exist at the extremities of the tree. The tree is read top down in a recursive nature with each node, known as a gene, having as many branches as required arguments. So the  $+$  takes the two arguments 1 and  $x$ , but  $\log$  only takes  $y$ . The number of required arguments is known as the arity  $n$  of a function, e.g. the arity of  $+$  is 2 and the arity of  $\log$  is 1. Reading from left to right and from top to bottom, the individual of Fig. 3.2 is precisely,

$$\log(y) - (1 + x). \quad (3.4)$$

A GP follows the same structure as Fig. 3.1 and so the overall feel is very similar to a GA. Replication can be carried out in precisely the same way — one may use tournament selection, roulette wheel selection, etc. The major differences lie in the individuals (outlined above) and as a result the genetic operators.

### 3.4.2 Genetic Operators

Genetic operators act on the Parse Trees themselves and as a result are quite distinct from their GA counterparts. The two main operations are crossover and mutation, but sometimes a third known as permutation is used.

GA mutation is a simple binary switch of a gene's allele. This is not possible with GPs due to the tree-like structure of an individual. One may not randomly mutate

a function freely because this will have implications lower down the structure. For example, mutating a  $\log$  to a  $+$  results in a differing arity and as a result the tree is missing a branch and the expressed function is no longer syntactically valid. To account for this, mutation is carried out by choosing a random gene, as with GAs, then replacing this gene and everything below it with a randomly generated tree structure. This is highlighted in Figs. 3.3 and 3.4. Notice that this mutation does not affect the overall

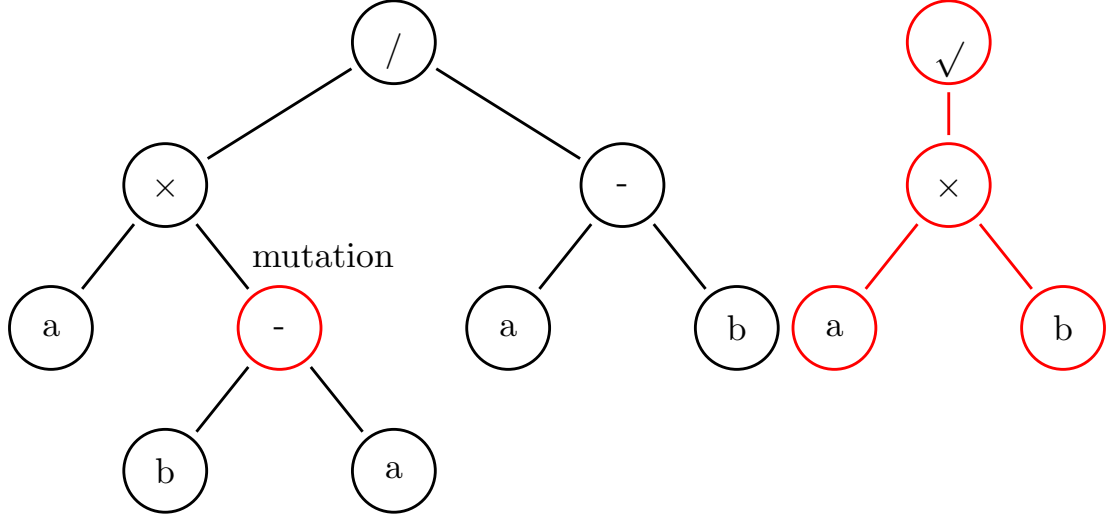


FIGURE 3.3: Individual before mutation. The randomly generated tree to be inserted is red as is the mutation location.

structure of the individual that much. Further, the random creation of the replacement tree structure can introduce serious overheads as the syntax of the tree must be valid.

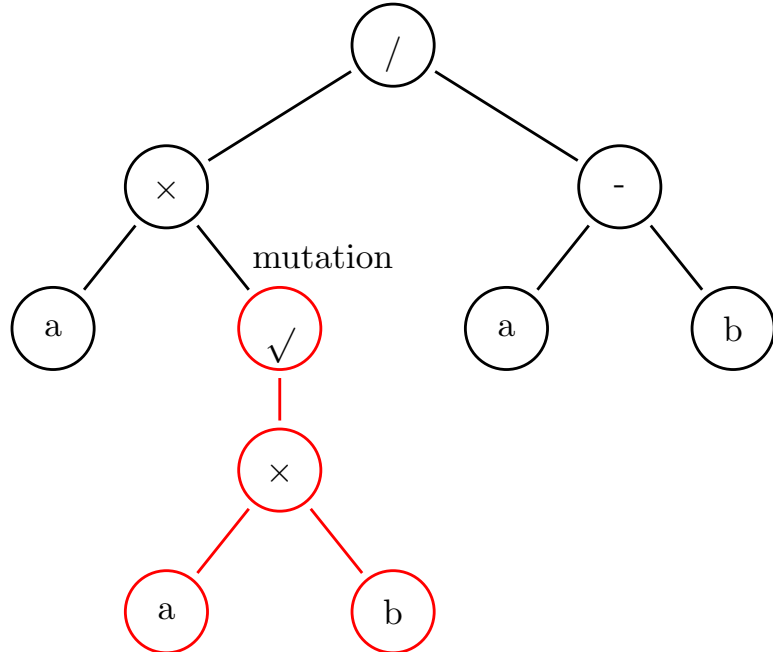


FIGURE 3.4: The resulting individual of the above mutation. The mutated structure is shown in red.

Permutation is a genetic operator that does not make much sense in a GA environment, but is well suited to Parse Trees. For permutation a random gene is chosen and its branches are switched, as in Fig. 3.5. This operator is the most conservative of those used in GPs; permutation has no effect on terminals, arity one symbols or symmetric operators. Even when it does have an effect, the shape of an individual is barely altered.

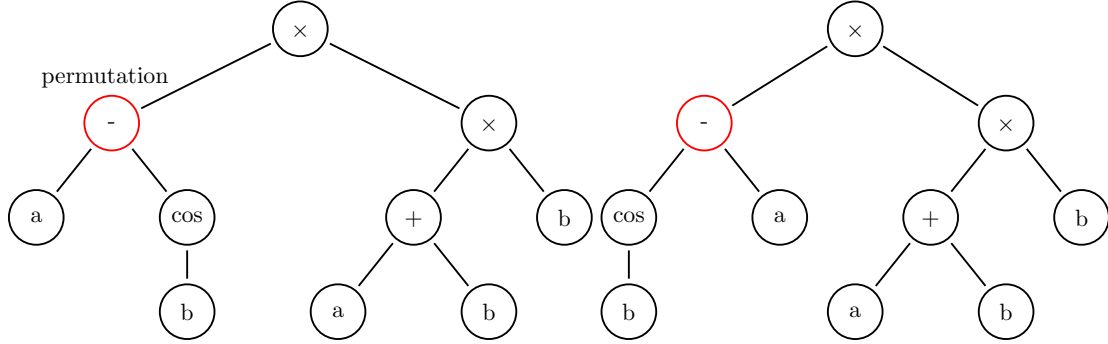


FIGURE 3.5: Before (left) and after (right) the permutation operator.

The final operator is crossover, an example of which can be seen in Figs. 3.6 and 3.7. If two Parse Trees are selected for crossover, then a random branch must be chosen on each individual. This position can be distinct on both trees, unlike with GAs, as the length of the tree is not fixed. The genetic information is then switched below these points to create the new children.

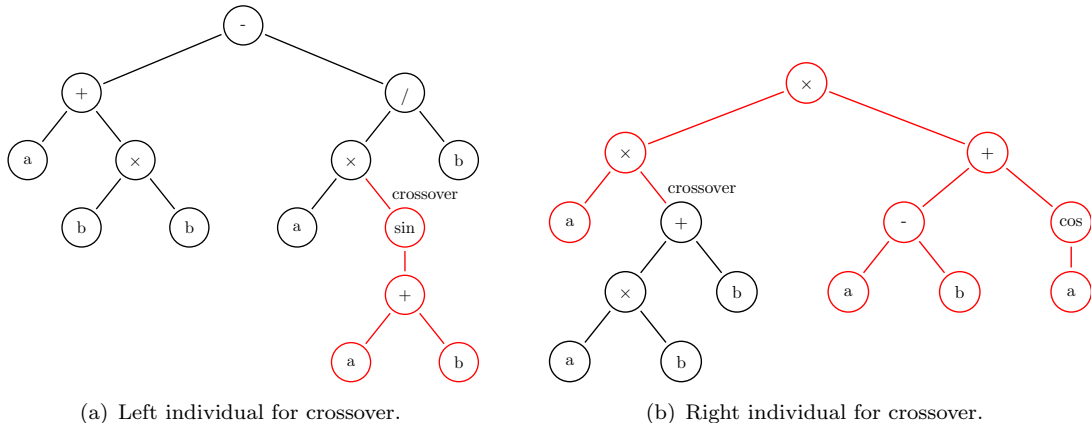


FIGURE 3.6: Individuals before crossover. The material to be swapped is shown in red and black colours and the point is marked as crossover.

Crossover is by far the most common operator as it does not require the complications of mutation and is far more capable at producing varied individuals than permutation. In a lot cases it is the only operator used (Koza, 1992, 1994; Koza et al., 1999). This means that throughout the entire process, no new genetic information is produced. This could have severe consequences if the population has been seeded poorly or if a subset of the symbols are far more important. It means that the individuals have to share these useful

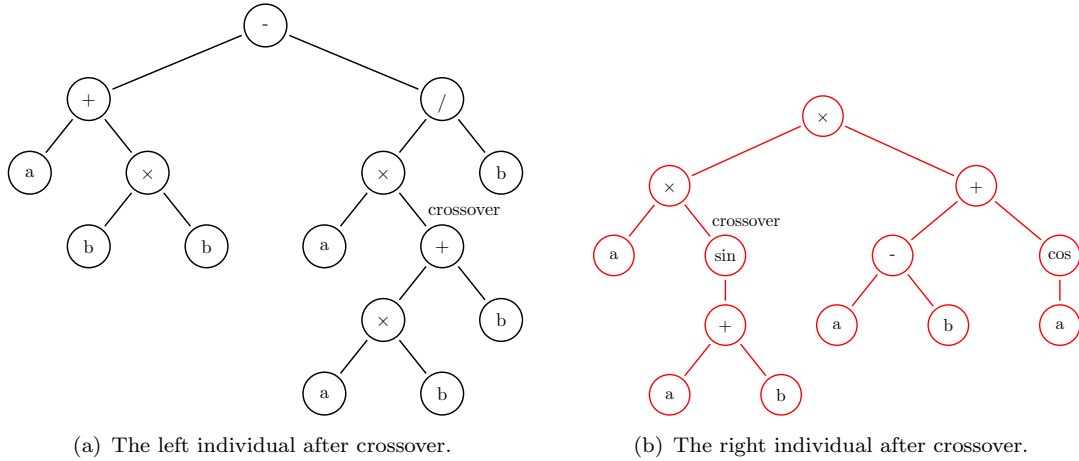


FIGURE 3.7: The children of the above crossover. All red genetic material constitutes the right individual whilst all the black genetic materials constitutes the left.

symbols, placing an upper boundary on the average fitness of the population which can only be overcome with genetic drift via selection. This leads to less diverse populations.

The Parse Tree makes it difficult to apply varied genetic operators like those presented in Section 3.5.6. Even mutation is not trivial. As a result, the available genetic operators of GPs feel more like a careful mathematician than blind evolution (Ferreira, 2006).

### 3.4.3 Limitations

Whilst the fixed-length limitation of GAs is overcome by representing individuals as Parse Trees, there are still many issues present in the GP framework. GPs are a step forward in terms of expressible individuals. The resulting individual is varied in length, making SR a possibility. However, the Parse Tree is both the genotype and phenotype as with GAs — all genetic material is expressed. All the problems outlined in Section 3.3.4 with this are therefore still present.

The limitations of the genetic operators have been documented in Section 3.4.2. The constraints placed on these operators reduces the evolutionary efficiency of GPs because of their simplicity and the high probability of producing invalid Parse Trees through mutation.

GPs can also fall victim to bloated individuals. Individuals can possibly grow cumbersome and unwieldy through repeated crossover. This is a major problem in GP algorithms as there is a tendency for the overall size of individuals to increase (Langdon, 2000). These large individuals become hard to interpret as their complexity increases. Bloated Parse Trees also increase storage requirements and execution time.

## 3.5 Gene Expression Programming

### 3.5.1 Overview

Gene Expression Programming (GEP) (Ferreira, 2001), is an extension to GAs and GPs in the sense that a population of individuals is evolved over many generations. Individuals are selected according to their fitness and genetic variation is introduced through the random application of genetic operators. In fact, due to the modularity of EA design, the overall structure of the algorithm is largely unchanged from Fig. 3.1. GEP is in essence a combination of the best aspects from GAs and GPs. Individuals in GAs are linear fixed-length strings and in GPs are non-linear Parse Trees. Because these individuals are both the genotype and phenotype, when compared with natural evolution their differences are only superficial. GAs are limited by their expression, their functional complexity, but are easy to manipulate, whereas GPs have a high functional complexity but it is extremely difficult to induce variation.

The fundamental advantage of GEP lies in the construction of the individual, known as the chromosome. Each chromosome has a *distinct* genotype and phenotype. To reiterate, the purpose of the genotype is to store genetic information that can be evolved, whilst the phenotype is the functional expression of this code. Ideally an individual should have a linear genotype and non-linear phenotype. This combines ease of evolution with functional complexity — the two respective advantages of GAs and GPs. GEP chromosomes do precisely this, the genotype is encoded as a fixed-length string made up of some alphabet (a function and terminal set), whilst the phenotype is a non-linear Expression Tree (ET).

Dawkins (1995) speaks of evolutionary thresholds being vital to the explosion of variation and adaptability in life on Earth. The first is the replicator threshold, which is a system of self replicating individuals which survive as a direct consequence of their properties. This implies that GAs and GPs have crossed this barrier. The second is the phenotype threshold, for this to be crossed, individuals must survive by some implications of their properties — in other words they possess some kind of phenotype. So GAs and GPs have not crossed this threshold. The DNA/protein system is such an example and has created hugely successful and varied life on Earth. Dawkins (1995) and Smith and Szathmáry (1995) enforces the idea that life should cross the phenotype threshold in order for true complexity. GEP crosses this barrier and as a consequence marks a major step in the long term advancement of evolutionary computation.

One of the consequences of complex evolution paired with phenotype expression is a richer imitation of evolutionary processes. In natural evolution a given organism can be functionally broken down into component parts which have some *other* purpose — this is an argument against the irreducible complexity of intelligent design. This is not to say the product of evolution is necessarily the sum of its parts, evolution is blind

and cannot just add components to yield a desired purpose. But, each component previously had some (unrelated) function and the random act of mutation brings lesser components together to produce functionality *more* than the sum of its parts. This is perhaps most notably seen in Flagellum (Dembski and Ruse, 2004).<sup>3</sup> The Flagellum is an appendage present on certain cells as a means for locomotion, however a subset of its genetic information is precisely that required for secretory proteins designed to attack host bodies. This latter functionality is clearly not required for locomotion, but displays evolution's random mash up of functionally independent components to produce something entirely unrelated. This phenomena is present in GEP and is extremely useful, not only does it produce complex expressions during the algorithm unforeseen by an ‘intelligent designer,’ but each sub-component is potentially useful for something, with respect to the fitness landscape, unbeknown upon the conception of the project.

GEP is an extremely versatile machine. Applications include: Symbolic Regression (SR) ((Ferreira, 2001; Karakasis and Stafylopatis, 2006; Eldrandaly and Negm, 2008)) - which implicates any mathematical operation; image clustering and general data clustering techniques (Zheng et al., 2012); discovery of complex (chaotic) functions; the construction of neural networks (Ferreira et al., 2004) and decision trees (Ferreira, 2014); simulating evolutionary processes (Ferreira, 2002a); parameter optimisation (Xu et al., 2009) and density-classification rules (Ferreira, 2002c) to name a few. For an idea of potential performance gains, GEP outperforms GP by four orders of magnitude in the last example (Ferreira, 2001).

As mentioned the structure of GEP is similar to all EAs. Figure 3.8 expands on the basic algorithm of Fig. 3.1. The clear expansion of GEP lies in the number of genetic operators, outlined in Section 3.5.6. The increase from the standard mutation and recombination provides a major impact on the ability to increase variation in a population. The additional operators are simply not implementable in GPs due to the non-linear structure of chromosomes and in GAs make no sense. Due to the lack of a non-linear expression, more complex operators in GAs do not create meaningful changes — which is why only mutation and recombination are predominantly used. Figure 3.8 presents the algorithm employed by this author and so decisions behind the implementation will be explained in Section 4.2.

### 3.5.2 The Genome

The individuals, named chromosomes, of GEP are encoded as fixed-length linear strings. Each chromosome consists of one or more genes,<sup>4</sup> that are linked together in some arbitrary way. For multigenic individuals see Section 3.5.3. The function of the chromosome

---

<sup>3</sup>This is perhaps an unfortunate example, as it was originally thought to be so complex by creationists that it couldn't possibly have naturally evolved.

<sup>4</sup>The term gene has a distinct meaning from that in GPs.

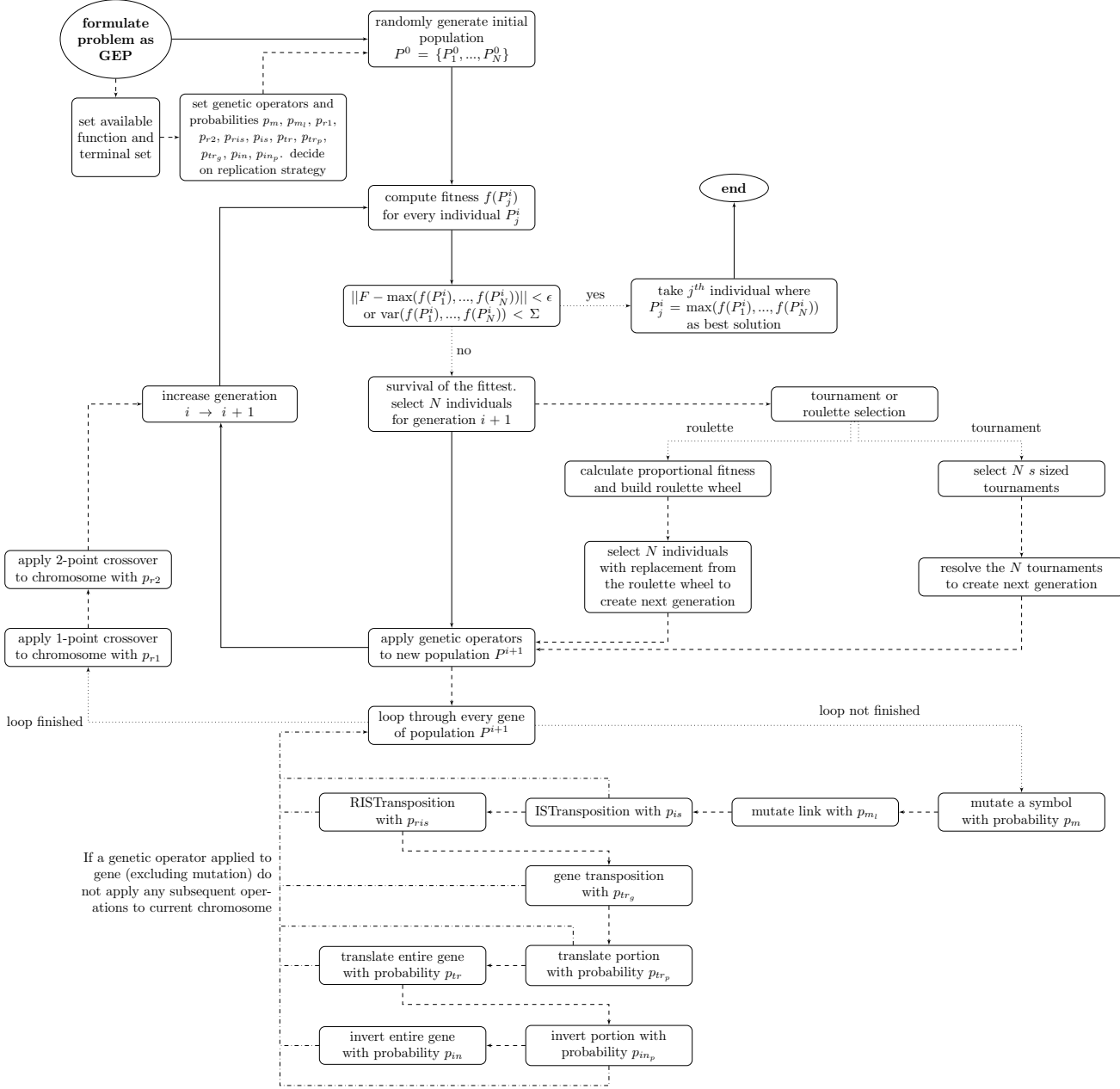


FIGURE 3.8: Detailed look at a GEP implementation. (—) represents overall direction, (— —) the additional details behind the main process and (.....) conditional statements.

is the Expression Tree (ET), which can vary in size despite the fixed-length nature of the genotype. This is an important point to reiterate: the phenotype is not fully restricted in size by the length of the genotype. Rather, the length of the genotype merely places an upper bound on the size of the phenotype.

Open reading frames (ORFs) are the biological mechanism for interpreting the genome. One can consider a gene having a frame over the top,

`abcd|bbcdaabddaaab`

where the box represents the ORF. From this gene the only genetic material expressed is in the ORF, so the phenotype is constructed from `bbcdaabd`. The upstream portion `abcd` and the downstream portion `daab` are not coded into the expression, but are still present in the genotype, so that should the ORF move over them, they will become functionally active. This concept is applied in GEP, although the ORF is restricted to start at the first position. It may still vary in length however, such that the ORFs over two example genes are valid in the GEP framework,

`abcdbbcdaa|bddaab`

`adcdaaadbcbaadc|ab`

It is in this way that the phenotype varies in length.

Currently,  $\{a, b, c, d\}$  is an arbitrary alphabet, but now consider SR as a concrete example. The possible alleles are similar to those in GPs, the set of symbols  $\mathcal{S}$  is decomposed into a function set  $\mathcal{F}$  and a terminal set  $\mathcal{T}$ . For the GP analogy see Section 3.4.1. Let's consider the alphabet  $\mathcal{F} = \{+ : +, - : -, * : \times, / : /, c : \cos\}$  and  $\mathcal{T} = \{x : x, y : y\}$ . The left symbol is the coding in the genotype and the right is the coding in the phenotype. Consider the mathematical expression,

$$\cos(x - y) \times (x + y). \quad (3.5)$$

The corresponding ET is shown in Fig. 3.9. So far this is the same as the GP Parse Tree, however in GEP there are also two more levels of abstraction to the gene. The first is the ORF,

`*c-xy+xy`

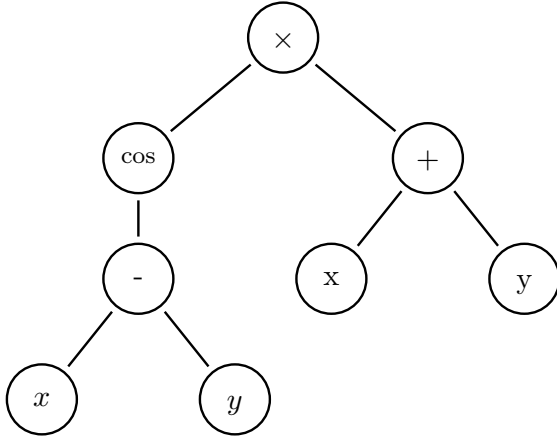


FIGURE 3.9: Example Expression Tree corresponding to Eq. 3.5.

The ORF is read recursively to produce Fig. 3.9. Note this is different from the original Karva-notation of Ferreira (2001). But this only affects implementation, a recursive procedure is easier to handle objectively and produce versatile software.

The final level of abstraction is the chromosome itself, which we consider single-genic for now. From the above information we cannot say what is downstream of the ORF, but remember that the ORF does not necessarily span the total length of the gene. For example the gene that is expressed as Fig. 3.9 and Eq. 3.5 may be,

\*c-xy+xy|yy\*-xy

The beginning of the ORF, always corresponding to the beginning of the gene, is known as the root position. Clearly the root is the most important position as it is the only position to be guaranteed expression. Then moving from left to right each position decreases in importance. Many of the genetic operators introduced in Section 3.5.6 are methodologies for moving coding regions to the root position.

The reason why the ORF ends in the above gene is because the tree is completely full in the reading of the genotype — no more branches can be added to Fig. 3.9. The ORF is not explicitly set in length, it is governed by the reading of the gene — once the ET is full, the ORF closes. Currently there is nothing to stop the ORF extending beyond end of the gene. Consider the following,

c++-yx ...

This does not produce a syntactically correct ET, as shown in Fig. 3.10, so that the corresponding mathematical expression is garbage. The red nodes cannot be filled as

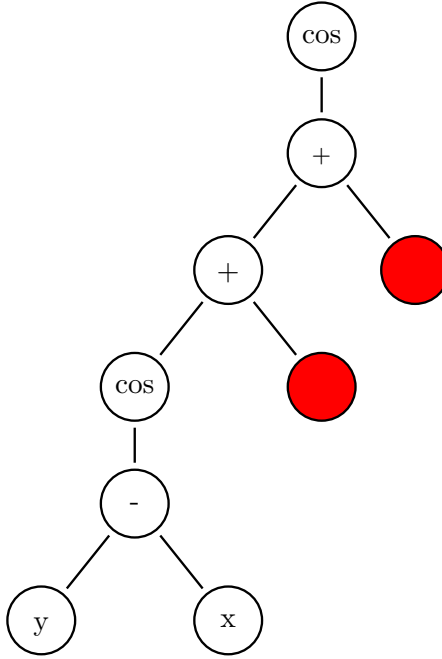


FIGURE 3.10: Incorrectly specified genes result in incomplete ETs. Nodes are left empty due to a lack of genetic information in the genotype.

there is not enough information encoded in the gene. A minimum of two symbols are required to complete the ET — but importantly there has to be at least two symbols from  $\mathcal{T}$ , as only terminals can exist at the extremities.

To counter this problem and indeed ensure correctness in the phenotype, a constraint is placed on the gene. The genome is split into a head and tail with respective lengths  $h$  and  $t$ . The head length is specified as  $h$ , but the tail length is found via,

$$t = h(n - 1) + 1 \quad (3.6)$$

where  $n$  is the largest arity in the function set  $\mathcal{F}$ . Each position in the head may be chosen from the function and terminal sets, whereas the tail may only be comprised of terminals. Therefore the worst case scenario, where each symbol in the head is a function with arity  $n$ , there is guaranteed to be enough terminals to close the ET and avoid situations like Fig. 3.10.

In our current example function set,  $\mathcal{F}$  has maximum arity  $n = 2$  and so a gene with  $h = 8$  would have a tail length of  $t = 9$ , For example,

/+-xycy-|xyyyyyxyy

is a valid genotype, where the  $|$  represents the split between the head and tail regions. The ORF currently terminates in position 10 and so two tail symbols are required to close the ET. Note, were the head a chromosome in GP, the individual would not be a

valid Parse Tree. The mathematical expression looks as follows from reading the ET of Fig. 3.11,

$$\frac{(x - y) + \cos(y)}{x - y} \quad (3.7)$$

The presence of the tail makes genetic operators very powerful in GEP. As long as a function never appears in the tail, one is free to use any operator without restriction. This makes for some interesting operations outlined in Section 3.5.6.

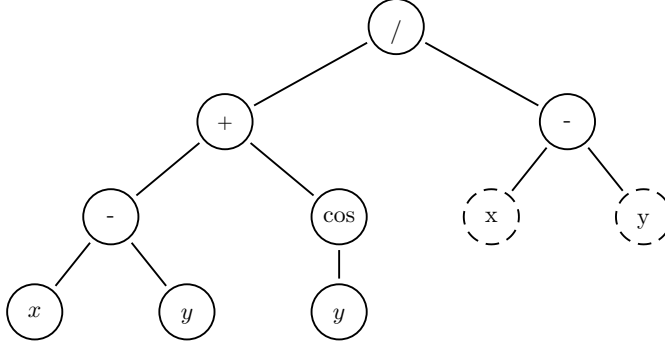


FIGURE 3.11: Example Expression Tree corresponding to Eq. 3.7.

As a preliminary example, imagine an operator changes the  $y$  in the fifth position to a  $*$ ,

$/+-x*c y - | x y y y x x y$

Then the resulting expression, Fig. 3.12 has changed somewhat — even from such a simple operator.

The resulting equation,

$$\frac{x - \cos(y)(x - y) + y}{y} \quad (3.8)$$

is also markedly different. The ORF (not shown) has moved from the tenth position to the twelfth. At this point, one may be fooled into thinking that the genetic operators are too destructive — such a small change had huge implications on the structure of the expression. However, the fifth position carries relative importance compared to lower down the gene and the example changed the symbol's arity by the maximum possible ( $0 \rightarrow 2$ ) causing the biggest shift in genetic material. Were the operation lower down the gene, the resulting ET would not be significantly changed, and in fact any symbol change in the tail does not alter the tree structure — true also with any like for like arity swaps.

The ORF does not always have to increase in size. Should a symbol be swapped for one of lower arity, then the ORF would reduce. As an example consider the above case in reverse. Trivially also, the changing of the first position to a terminal would result

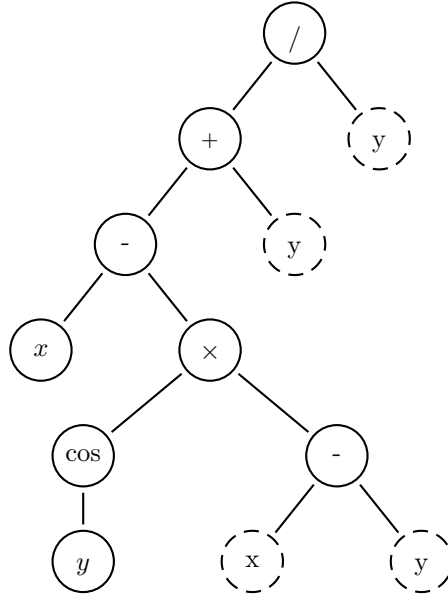


FIGURE 3.12: Example Expression Tree corresponding to Eq. 3.8. Dashed nodes correspond to symbols from the tail.

in an ORF of length one. The ORF concept is the beauty of GEP. The lack of restriction afforded by the head and tail give much more freedom in operators to manipulate genotypes and produce more meaningful variations. The non-mapped regions outside of the ORF are also vital to the GEP philosophy. Not only do they allow a linear genetic makeup to be mapped to a non-linear expression, but the dormancy of this material increases the chance of survival, via the promotion of more useful alleles. In general it increases the algorithm’s ability to tinker as a more physical evolutionary imitation.

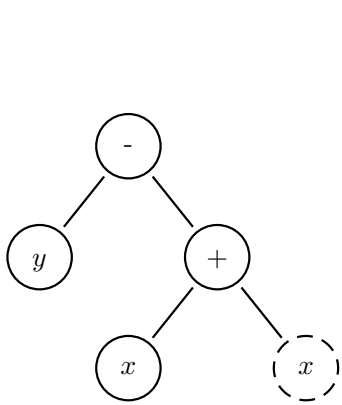
### 3.5.3 Multigenics

In realistic optimisation problems, chromosomes are going to consist of more than one gene. This may be due to multiple outputs — each gene in the individual controls a single output. The other reason for multigenic chromosomes is for an extra degree of non-linearity in the expression. Each gene encodes a sub-ET which when combined forms a single expression. In the former, each gene survives entirely on its own merit, each has a fitness measured against one of the outputs. In this case an individual is made of varying quality chromosomes, each optimised for a particular purpose. Multiple regression problems are well suited to this where the independent variables  $x_i$  satisfy  $x_i \in \mathbb{R}$ . The second purpose for multigenics, to increase the overall non-linearity between genotype and phenotype, is incredibly important for the optimisation of complex problems.

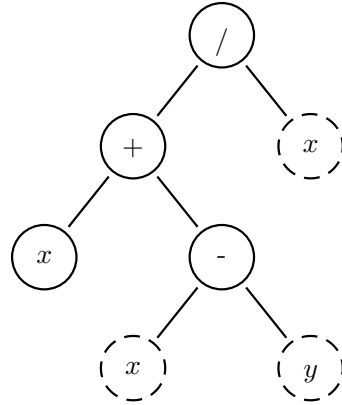
Each gene encodes a sub-ET which must be connected via some linking function. Ferreira (2001) suggests using an *a priori* defined link. For example the individual,

$$\boxed{-y+x|xyxyx} \leftrightarrow \boxed{/+x-|xyxyy}$$

consists of two genes linked via multiplication. The  $\langle \rangle$  denotes the linking function. Whilst Ferreira (2001) claims this situation works very well, it is easy to introduce the linking function into the genome — thus allowing it to evolve also. Note, clearly the individual contains two ORFs.



(a) The sub-ET formed from translating the right gene.



(b) The sub-ET formed from translating the left gene.

FIGURE 3.13: The two sub-ETs formed from the above multigenic chromosome.

The above individual contains the two sub-ETs shown in Fig. 3.13. The mathematical expressions of these genes are given as,

$$y - (x + x) \quad (3.9)$$

and

$$\frac{x + (x - y)}{x} \quad (3.10)$$

respectively. The two sub-ETs form the single expression shown in Fig. 3.14 using the linking function  $*$ .

Obviously, one is not restricted to chromosomes with two genes — the process is easily generalised. Either by higher arity linking functions, more linking functions or a combination of both.

Multigenic chromosomes are vital to the evolution of complex programs. This is because they allow for the development of modular sections of code, each evolved separately (and thus independently) from one another. In this way each gene is responsible for a small coding section. The number of genes in a chromosome has been explored by this author and seriously affects the chances of finding good solutions.

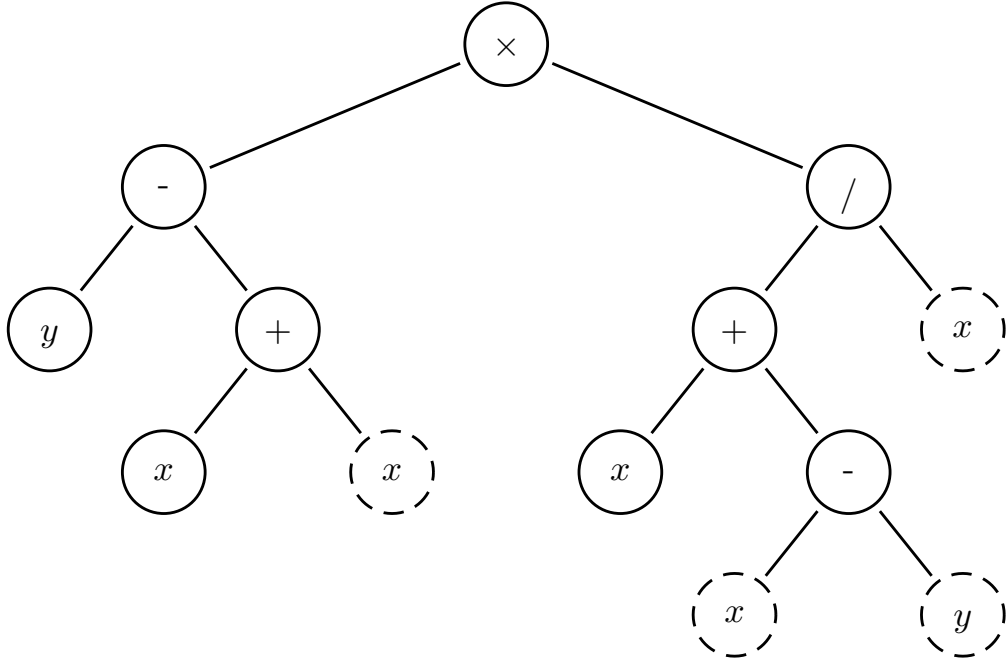


FIGURE 3.14: Full expression of multigenic chromosome.

### 3.5.4 Fitness and Selection

As with GAs and GPs, covered in Sections 3.3.2 and 3.4.1, individuals are selected for generation  $P^{i+1}$  from  $P^i$  by testing its suitability according to some fitness function. The fitness function is vital to the success of the optimisation and is extremely varied from problem to problem. A well defined fitness function directs the evolution of the program towards the desired goal. Often the fitness function is the hardest component of a GEP optimisation to implement.

Ferreira (2001) introduces two fitness functions, clearly identifying the original intended applications of the GEP philosophy. The first, is designed to be used with SR applications. One can use either the absolute error of individual  $P_j^i$ ,

$$f(P_j^i) = \sum_{k=1}^m (R - |f(P_j^i)^k - E^k|) \quad (3.11)$$

or the relative error,

$$f(P_j^i) = \sum_{k=1}^m \left( R - \frac{100 \cdot |f(P_j^i)^k - E^k|}{E^k} \right) \quad (3.12)$$

as the fitness function.  $f(P_j^i)$  is a measure of the distance from  $m$  expected values  $E^k$  otherwise known as training data or target values.  $f(P_j^i)^k$  is the evaluation of individual  $P_j^i$  at the  $k^{\text{th}}$  data point.  $R$  is the range of selection, a tuneable parameter that allows the user to impose a pressure on the selection procedure much in the same way as  $s$  in

Section 3.3.2. When using either Eq. 3.11 or Eq. 3.12, the optimal solution will have a fitness  $f(P_j^i) = mR$ . This definition makes the fitness of a program only relevant to the problem at hand. In order to normalise the fitness one should divide by  $mR$ , this makes the fitness of  $P_j^i$  relevant to other optimisation studies. In particular if the number of data points is reduced then the range of possible fitness values changes with  $m$ . Further, if one wishes to measure the impact of the variation of  $R$ , then two solutions are more comparable under normalisation (although still not directly comparable).

$R$  is an extremely important component and critically determines the performance of an optimisation. Severe narrowing of the selection window, corresponding to a small  $R$ , results in extremely slow evolution and premature convergence. However a large  $R$  also results in a hampered performance as too much diversity will be present in the population and convergence will again be very slow. It is very difficult to determine the optimal value for the range of selection *a priori* and often a parameter study is vital for complex problems.

The second type of fitness function introduced by Ferreira (2001) is for use with boolean concept learning (see for example Koza, 1992). For this application, an individual  $P_j^i$  is assessed on how many fitness cases it performs correctly for. In such problems, an individual has a 50% likelihood of correctly evaluating a boolean problem and so any individual below this mark should be punished severely. Above 50%, the number of cases can easily be used as a fitness measure,

$$f(P_j^i) = \begin{cases} n, & n \geq \frac{1}{2}m \\ C, & n < \frac{1}{2}m, \end{cases} \quad (3.13)$$

where  $C$  is some constant (e.g. 1 or 0) which acts as a punishment for poor performance.

These examples are fitness functions that work well in a GEP environment, however can easily be incorporated into a different EA. The reverse is also true, many optimisation problems can easily be adapted for GEP — for example chaotic sound signal generation (Zelinka et al., 2010). The fitness function is a way to order all chromosomes present in the population. The actual matter of selecting new individuals by forcing them to compete based on their fitness is a process that is borrowed from pre-existing EAs. The main selection procedures used in GEP are tournament and roulette wheel selection along with their variants covered in Section 3.3.2.

Since the introduction of GEP, many other applications have been conceived and result in varied fitness functions, but the discussion is restricted in order to avoid tangential topics. One more example included in this body of work is data clustering, outlined in Section 4.4.

### 3.5.5 Multi-Objective Fitness Criteria

With the natural multigenic framework, without linking functions, introduced in Section 3.5.3 it becomes simple for multi-objective optimisation (Zhou et al., 2011). Fitness functions such as Eq. 3.11, Eq. 3.12, Eq. 3.13 are all examples of single-objective fitness functions  $f(P_j^i)$ . In realistic problems there may well be many optimisation goals. The most obvious example is multivariate regression analysis, where one requires simultaneous optimisation of many dependent variables. Another common purpose of multi-objective optimisation is to force chromosomes to satisfy certain constraints whilst fitting training data. The length of the expression, despite being naturally bounded because of the fixed head length of the genotype, can become unwieldy and too long — effectively overfitting the data. This problem, whilst discussed as a major problem of GP may still be an issue for GEP. So one may want to introduce an extra objective to minimise the length of the chromosome. This can be done by minimising the length and breadth of the expression tree or more simply the number expressed symbols.

If there are multiple objectives then the fitness of a chromosome  $P_j^i$  is defined as some map  $\Pi$ ,

$$\Pi : f(P_j^i)^1 \times \cdots \times f(P_j^i)^p \rightarrow f(P_j^i) \quad (3.14)$$

for  $p$  fitness criteria. This implies that the fitness of  $P_j^i$  is now some measure that exists in a space of dimensionality  $p$  or less. For example, the easiest multi-objective fitness map is simply the weighted average of each criteria,

$$f(P_j^i) = \sum_{k=1}^p w_k f(P_j^i)^k \quad (3.15)$$

where each weight  $w_k$  can be predefined. So the map  $\Pi : \mathbb{R}^p \rightarrow \mathbb{R}$  effectively reduces the multi-objective nature into a single criteria.

Equation 3.15 is simple to implement, especially into single-objective codes. Further, it is quick to evaluate which is important in large optimisations where computational performance is critical. Each fitness criteria  $f(P_j^i)^k$  can be individually given more or less importance by tuning  $w_k$ .

There are issues with Eq. 3.15. Firstly, determining the influence of each  $f(P_j^i)^k$  on evolutionary performance is not necessarily easy. If each component of the fitness vector are not independent then it is unclear of the influence of each  $w_k$ . The path the best chromosome takes through the solution space may be hampered or terminate in a local optimum by the excessive favouring or neglecting of one criteria. Secondly, this kind of linear weighting will allow individuals, whose fitness is dominated by one or two components, to easily survive. These specialist individuals score highly for say  $f(P_j^i)^l$  but very poorly for  $k \in [1, l] \times (l, p]$ . These specialists are generally not desirable compared to individuals that perform better across all criteria, however they will be

strongly favoured in the selection process. One potential solution is to use a ranking system for each  $f(P_j^i)^k$ . For each fitness criteria, the best member is given  $f(P_j^i)^k = N$  where  $N$  is the population size and the worst  $f(P_j^i)^k = 1$ . Therefore the fitness of each chromosome is a vector of ranks, which can then be summed. This does not alleviate the problem entirely but can remove the heavy skew present in the raw fitness values.

Because the components  $f(P_j^i)^k$  are often conflicting, an increase in one can cause a decrease in another. Therefore a more sophisticated definition of the fitness is often required. With multi-objective optimisations there will inevitably be a trade-off between each  $f(P_j^i)^k$ . To deal with this balancing of criteria, concepts from game theory have been incorporated into EAs. Namely the idea of Pareto fronts and Pareto domination (e.g. Zhou et al., 2011; Zheng et al., 2012).  $\Pi$  once again ranks the components, but without the summation of Eq. 3.15. Instead a comparison is made between two individuals by determining which *dominates* the other.  $P_j^i$  is said to dominate  $P_q^i$  if for every  $k$  fitness criteria,  $P_j^i$  at least outranks  $P_q^i$  and definitely outranks for at least one fitness criteria,

$$\begin{aligned} f(P_j^i)^k &\geq f(P_q^i)^k, \quad \forall k \\ f(P_j^i)^l &> f(P_q^i)^l, \quad l \in [1, p]. \end{aligned} \quad (3.16)$$

The Pareto optimal set is the set of all chromosomes that are not *strictly* dominated by any other member of the population, i.e for every Pareto optimal individual there is no individual for which  $f(P_j^i)^k > f(P_{p\text{-opt}}^i)^k, \quad \forall k$ . The Pareto Front is the image of this set, an example of which is highlighted in Fig. 3.15. For this 2-objective example the Pareto front is a line in the fitness space. All individuals on the Pareto front should be thought of as feasibly optimal and because of this, elitism with Pareto Multi-objectivity usually involves keeping the entire Pareto Front during selection of  $P^{i+1}$ .

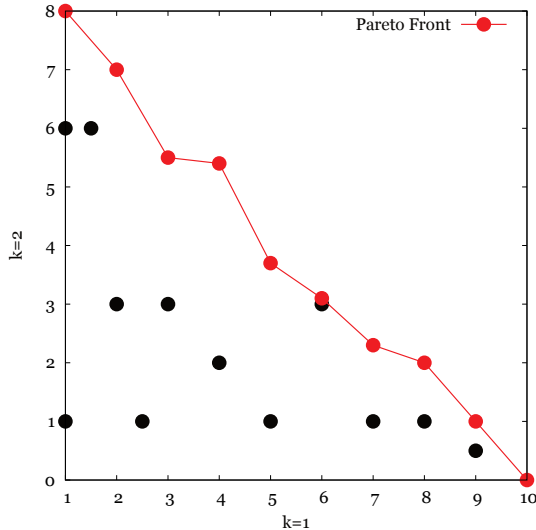


FIGURE 3.15: Pareto front for 22 individuals being subjected to the fitness criteria  $f(P_j^i)^k, \quad k = 1, 2$ . The Pareto front represents the individuals not strictly dominated by any other and so are feasible solutions to the optimisation problem.

### 3.5.6 Genetic Operators

As with GAs and GPs, GEPs are incapable of producing genetic diversity without genetic operators. With just the ‘asexual replication’ of tournament and roulette selection, i.e. copying without mistake, there is no room for new genetic information. Instead the genetic operations introduced here are used in conjunction with some selection process to introduce the blind tinkering of evolution.

Overall, the genetic operators of GEP have the same feel as with the methodologies that preceded it. Section 3.3.3 and Section 3.4.2 introduce mutation and crossover (multiple parent reproduction) for GAs and GPs. Mutation and crossover have been implemented into GEP, but due to the sophistication of the chromosome there is much more freedom to implement new operators. As long as the tail of the genotype only ever contains symbols from the terminal set, the phenotype will always be correctly expressed. This means that genetic operators in the GEP framework can be much more varied and far more powerful.

Below GEP genetic operators are introduced using SR applications. For this purpose the arbitrary terminal and function sets of  $\mathcal{T} = \{x : x, y : y, 1 : 1\}$  and  $\mathcal{F} = \{* : \times, / : \div, + : +, - : -, c : \cos, s : \sin, e : e\}$  respectively are used.

#### 3.5.6.1 Mutation

Mutation is the most common genetic operator in GEP (Ferreira, 2001). The implementation is similar to GA mutation (Section 3.3.3), but there are a few differences. If a gene is selected for mutation then it must preserve the structure of the chromosome. This is achieved by allowing symbols in the head to be mutated to any symbol from  $\mathcal{F}$  and  $\mathcal{T}$ , whilst only allowing symbols in the tail to be mutated to any symbol from  $\mathcal{T}$ . For example if the chromosome,

$-y+ex|xy1yxy$

is selected for mutation, then the following are valid mutations,

$-y+sx|xy1yxy$   
 $-y-ex|xy1yxy$   
 $-x+ex|xy1yxy$

$-y+ex|yy1yxy$   
 $-y+ex|xyyyxy$   
 $-y+ex|xy1yx1$

Note by the arguments of Section 3.5.2, then mutation can be quite destructive to the genome depending on the position and arity change of the mutation. Non destructive mutations, i.e a like for like arity swap or mutations that occur in the non-coding region, are relatively common in nature but this is not necessarily the case for GEP. Mutations can be much more destructive.

### 3.5.6.2 Crossover

GEP recombination is identical to GA and GP crossover (see Section 3.3.3 and Section 3.4.2). It exists as 1-point recombination, 2-point recombination, etc. Unlike with mutation, crossover does not need any constraint to ensure correct implementation with respect to the head and the tail. For example the two chromosomes,

```
-y+ex|xy1yxy
+x/ys|xxx1yy
```

can recombined using a position in the head,

```
-y+ys|xxx1yy
+x/ex|xy1yxy
```

or just as easily a position from the tail,

```
-y+ex|xyx1yy
+xs/ys|xx1yxy
```

to produce two syntactically correct offspring. The bold sections correspond to the swapped regions. In practice if two chromosomes are selected for crossover then the positions where the cuts are made is entirely random.

Further to this crossover there is also gene recombination. This is, as the name suggests, recombining entire genes. For example the two multigenic chromosomes,

```
-y+x|xyxyx <*> /sx-|x1xyy <+> e+xx|1y1xx
*se-|x1y1x <-> //x+|yyy11 <*> -xy1|xx11y
```

can be recombined to give,

---

```
-y+x|xyxyx <*> //x+|yyy11 <+> e+xx|1y1xx
*se-|x1y1x <-> /sx-|x1xxy <*> -xy1|xx11y
```

Whilst not necessarily a strong source of genetic variation, gene recombination is an extremely powerful tool allowing strong genes to be paired together. Note, when gene recombination is the only source of genetic variation, extremely large population sizes are required (Ferreira, 2001).

### 3.5.6.3 Transposition

Transposition is an extremely powerful genetic operator that comes in several forms. The basic principle is to move fragments, called insertion sequences, of genetic material to other locations. This kind of operation is not trivial in GPs due to the inevitable syntax problems that will arise.

There are three main transpositions: insertion sequence (IS) transposition, root insertion sequence (RIS) transposition and root gene insertion. Ferreira (2001) implemented transposition contained within the chromosome, i.e. insertion sequences cannot leave their own chromosome, however Steeb (2011) takes the approach that insertion sequences can jump to anywhere in the population. This variation of transposition is known as insertion or root insertion.

Placing an insertion sequence into the head, but not the root position, of a chromosome is IS transposition. In the implementation of Ferreira (2001) the insertion sequence is generated from another portion of the chromosome which is then copied and inserted into the head. For example suppose  $-xy$  in position 5 of gene 2 was randomly chosen for insertion into gene 1 at position 3 in the following chromosome,

$$x+y\text{cy}|11yxx1 <+> +--+|x\text{yyyy}1 <-> \text{cxyx}1|yy\text{yxx}1$$

then the chromosome would look as follows,

$$x+-\text{xy}|11yxx1 <+> +--+|x\text{yyyy}1 <-> \text{cxyx}1|yy\text{yxx}1$$

However, in the methodology of Steeb (2011) the IS is randomly generated.

RIS transposition is identical to IS transposition except for the fact that the insertion sequence is always inserted to the root of a randomly chosen gene and must start with a function symbol. This last point is a relic of single-gene chromosome environments.

Because in this case a chromosome that expresses only a terminal is not much use, however in multigenic chromosomes this additional overhead is not important and can be dropped.

The last kind of transposition differs slightly. The gene transposition operator chooses a gene at random and places it at the root of the chromosome. The original copy of the transposon is deleted to avoid either excessive duplication of genetic material or variable length chromosomes. For example if the second gene of the chromosome,

$$x+ycy|11yxx1 \leftrightarrow +---|xyyyy1 \leftrightarrow cxyx1|yyyxx1$$

was chosen for gene transposition, then the following chromosome would be produced,

$$+---|xyyyy1 \leftrightarrow x+ycy|11yxx1 \leftrightarrow cxyx1|yyyxx1$$

Note how the linking function is associated with the gene to the left. In SR, this particular form of transposition is not very useful as all genes have equal importance due to the nature of the linking functions. However in other applications, say boolean logic where the linking function may be an IF, gene transposition is more useful. In order to make gene transposition more useful for SR applications an external gene may be randomly generated similar to the insertion techniques of Steeb (2011) or taken from another chromosome (Section 4.2).

### 3.5.6.4 Inversion

Inversion was originally a GA mutation operator (Michalewicz, 1996), but because the bonds between genes did not always translate to an arrow of information, inversion did not receive much attention. It cannot be used at all with GPs, due to the structure of the individual. With GEP inversion is possible and although still not necessarily a popular operator in the literature, it does have uses.

The basic premise is to take two points at random in the head of a chromosome and invert everything in between. The same can be done for two points in the tail. By keeping entirely in the head or tail, the inversion operator is guaranteed to produce an individual with an expressible phenotype. An example inversion in the head is given below,

$$\begin{aligned} &**xy1s|yxxxxyy1 \\ &+1yx*s|yxxxxyy1 \end{aligned}$$

index	0	1	2	3	4	5	6	7	8	9
value	0.01	0.87	0.68	0.44	0.99	0.04	0.54	0.37	0.11	0.27

TABLE 3.1: Generated Random Numerical Constants are stored with an index, so that chromosomes make use of them during the evolutionary process.

Inversion is generally performed in two ways. Either by taking two points and inverting the subset in between, or inverting the entire head (or tail). The former is denoted portion inversion and the latter inversion.

With GEP this is an extremely powerful source of variation (Ferreira, 2002b). Because the ORF is decoded in a particular direction, any allele affected has its degree of importance greatly changed (recall that the root is the most important position with subsequent positions having a decreased importance). Inversion, because it is so invasive, should be used quite sparingly, i.e. a low probability of occurrence.

### 3.5.7 Random Numerical Constants

Regression analysis undoubtedly requires some form of constants available in order to be effective. For example, imagine GEP applied to the simple regression problem,

$$f(x) = 1000 - x^3, \quad (3.17)$$

with the function and terminal sets,  $\mathcal{F} = \{ * : \times, + : +, - : -, / : \div \}$  and  $\mathcal{T} = \{x, 1\}$  respectively. Equation 3.17 is unknown at runtime and in general it is not clear what constants should be included in  $\mathcal{T}$ . The chosen terminal set is clearly very bad for this problem, and a complex ET is required just to fit the y intercept.

Instead of attempting to guess appropriate constants *a priori*, Random Numerical Constants (RNCs) can be added to the optimisation problem. For an example of this see the SR problems of Ferreira (2006). In these applications, Ferreira (2006) strangely uses integer random constants and limits the number allowed per gene (< 6% of the chromosome length). This does not need to be the case however and indeed Ferreira (2001, 2003) outlines a method for dealing with RNCs.

The premise is to explicitly set them at the outset. One can choose a minimum  $r_{min}$  and maximum  $r_{max}$  for the RNC values. Then before the creation of  $P^0$ , a user specified number of RNCs are generated in this range and stored for use throughout the optimisation. Generally throughout the literature an extra terminal, represented as ?, is used to represent an RNC. Further, there is an extra portion of the chromosome of length  $t$  allocated to decide which of the user defined RNCs are expressed.

For example, say the user defined  $r_{min} = 0$  and  $r_{max} = 1$  and generated the RNCs in Table 3.1, Then these constants can be referenced by a chromosome if and when a ? is

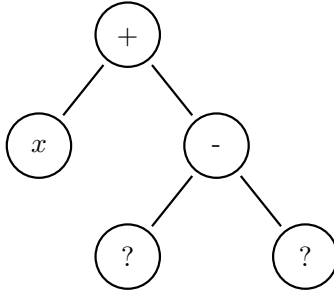


FIGURE 3.16: Expression Tree before interpreting RNCs.

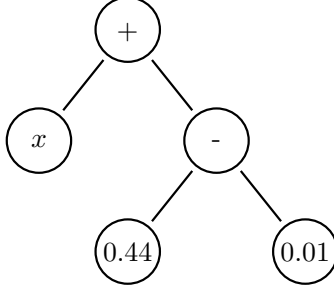


FIGURE 3.17: Expression Tree after interpreting RNCs.

decoded in the ET. Consider the individual,

$$+x-??|y?yxx1$$

who is expressed in Fig. 3.16.

Now there are two expressed RNCs that need to be given a value. This is done via a second tail of length  $t$  which stores the chromosome's indices, say for example this could be,

$$+x-??|y?yxx1|301239$$

These numbers represent look up indices. Using Table 3.1, the resulting ET is shown in Fig. 3.17 and the resulting mathematical expression is,

$$(x + (0.44 - 0.01)) = x + 0.43. \quad (3.18)$$

This extra tail is also free to evolve just like the rest of the chromosome, allowing for gradual drift towards more appropriate constants. In fact, a study by Ferreira (2003) shows that manipulating the RNCs a chromosome can access greatly improves algorithmic performance.

### 3.5.8 Limitations

Whilst GEP is a clearly advantageous over GP, it is not without limitations that a user should be aware of. The length of the phenotype is now bounded by the length of the genotype. This is not a major issue, as increasing the head length will alleviate it, but it is possible that individuals are too short to express the complexity of a given problem.

Now that the phenotype length is not rigidly related to the genotype length, this does decrease the number of problems to consider. For example fixed-length phenotypes are not possible.

## 3.6 Summary

This chapter has presented recent developments in rich language EAs, focusing on SR as the primary application. In particular the most recent branch of evolutionary computation has been the primary object of concern. GEP theory has been thoroughly detailed, without too much concern for complete examples, applications will come in Chapters 5 and 6. The pre-existing ancestors of GEP have also been outlined with their inherent limitations discussed — the reasoning behind the extensions present in GEP should now be clear.

In Section 4.2, the implementation of the above theory is described and in Chapter 6, this is applied to Hybrid RANS/LES. In Section 4.3 a new framework for high-dimensional problem solving is detailed, which is then applied to RANS modelling in Chapter 5.



# Chapter 4

# Implementation of Gene Expression Programming Environments

## 4.1 Introduction

This chapter outlines all implementations of Gene Expression Programming (GEP) used throughout this work. Each implementation performs a significant role in what follows. Chapter 5 uses the novel tensor regression algorithm highlighted in Section 4.3 for the improvement of anisotropy prediction in RANS modelling. The scalar field implementation, described in Section 4.2, is applied in Chapter 6 for the development of length scale damping functions in Hybrid RANS/LES. Finally in Chapter 7, the clustering algorithm, described in Section 4.4, is applied to analyse the resolved structures in DNS and Hybrid RANS/LES.

## 4.2 Scalar Field Regression

All of the discussions in Chapter 3 focussed on scalar field regression, with all examples using this language. This section therefore is a short accumulation of these ideas into the implementation used within this work.

Essentially, the implementation of GEP for scalar fields follows that of Ferreira (2001), with minor extensions to the original algorithm. Figure 3.8 describes the overall flow of the algorithm. In validation studies, tournament selection was found to be far superior to using the roulette wheel and so is adopted as the only method of selection in this work.

The individuals are fully multigenic (Section 3.5.3) with random numerical constants (Section 3.5.7). Validation studies of the implementation showed a significant improvement over single gene chromosomes (see also - Ferreira, 2001). This is because segregating code into packets allows for more control with specific genetic operators that act on whole genes. The links are also encoded such that they too can evolve via mutation and are not fixed. Note, the links exist separate to the genes and are not affected by other genetic operators.

In the fitness step, all members of the population are assigned a fitness,

$$f(P_j^i) = \frac{1}{mR} \sum_{k=1}^m \left( R - |f(P_j^i)^k - E^k| \right). \quad (4.1)$$

This fitness function measures the distance between the value of the function and the expected value at each of the  $k$  data points. By summing these distances one gets an objective view of how good or bad a solution is. The further from the training data a function is, the more it is penalised. The range of selection  $R$  is used to scale the fitness value and skew the distribution of the chromosomes' fitness. By tuning this parameter one can drastically change the effectiveness of an optimisation. High values of  $R$  skews the fitness values towards 1, whilst low values skews towards 0. As a rule of thumb, raise  $R$  if you are not currently happy with a solution of a high fitness. In the reverse situation, lower  $R$  if the algorithm is struggling to evolve at all. Note these comments are only applicable if some type of fitness proportional selection is used,  $R$  has no impact in a ranking based system. This author uses tournament selection almost exclusively to reduce this degree of freedom that can often be very hard to set.

Equation 4.1 uses the absolute value over the sum of square error because the latter can often be heavily influenced by outliers. The equation also uses vertical offset as the distance measure, i.e. the distance is only a function of the dependent variable deviation. Another option would be to use perpendicular offsets, which can be thought of as the *actual* distance the training data and the function deviate by. The latter, whilst a more accurate representation of distance, is less desirable for symbolic regression. This is because as a chromosome evolves, so would the fitness function — requiring many more overheads — especially when the shape of the function is very complex. Also, as the fit becomes better, the difference between perpendicular and vertical offset is small.

Equation 4.1 is a formula similar to Eq. 3.11, but with the extra factor  $1/mR$ . Recall that for Eq. 3.11,  $\max(f(P_j^i)) = mR$  and  $m$  and  $R$  are parameters that the user is likely to change during an optimisation study. So bounding  $0 < f(P_j^i) < 1$  makes each successive optimisation more comparable.

Beyond the basic measure of distance from training data, one may also use other criteria to form a multi-objective simulation.

Attention is paid to avoiding bloat with several exchangeable measures. The first is a measure of the number of expressed symbols,

$$c(P_j^i) = \frac{N_g(h+t) - l_e}{N_g(h+t)}. \quad (4.2)$$

$l_e$  is the number of nodes in the Expression Tree (ET),  $N_g$  is the number of genes in the chromosome and  $h+t$  is the length of a gene.  $c(P_j^i)$ , the comprehensibility of  $P_j^i$ , is therefore a measure of the number of nodes in the ET.  $c(P_j^i)$  is bounded  $0 \leq c(P_j^i) < 1$  such that the lower bound means the ET uses the entire genotype and the upper bound corresponds to a tree with just a root node.

Slightly more sophisticated options are the average depth of the ET. The average depth of the tree is the sum of the depths of each node divided by the number of nodes. The depth of a node is the distance from the root node. The higher the average depth of the ET, the more nested the mathematical operations are. This is often desirable to minimise, as for many realistic situations an equation such as  $\exp(\exp(\exp(\exp(\varphi(\mathcal{F}, \mathcal{T}))))$  is not very useful.

The depth measure  $d(P_j^i)$  is,

$$d(P_j^i) = 1 - \frac{2}{l_e(l_e - 1)} \sum_{n=1}^{l_e} d_n \quad (4.3)$$

where  $d_n$  is the depth of node  $n$ . The depth of the root node is set to  $d_0 = 0$ .  $0 \leq d(P_j^i) \leq 1$ , making it easily incorporable into a multi-objective simulation with Eq. 4.1 and Eq. 4.2. Zero corresponds to the least desirable ET, one that consists of  $h$  arity one symbols and one tail symbol. One corresponds to an ET consisting of just the root node.

These three objectives can be combined using any of the methods discussed in Section 3.5.5.

The genetic operators outlined in the original GEP work of Ferreira (2001) and in Section 3.5.6, plus the inversion operator of Michalewicz (1996) outlined in Section 3.5.6.4 are all used. Each operator is assigned a particular probability of occurrence during the genetic operator step.

The transposition type operator, discussed in Section 3.5.6.3, is similar to the insertion operator of Steeb (2011), except that the insertion sequence (IS) is not randomly generated but is taken from another chromosome in the population. This is the case for RIS, IS and gene transposition. Taking the IS from another gene promotes sharing of genetic material in a similar way to crossover. As a simulation progresses, the shared genetic material will become more and more useful. Having an extra operation like crossover is incredibly useful, especially as transposition in this form is less destructive

than crossover, so an individual has the chance to keep the majority of its structure whilst adding a useful piece of genetic code. Sharing is better than randomly generating genetic material, which destroys the improvement by gradual change ethos of GEP.

The genetic operator step is applied after selection (see Fig. 3.8). But, if after a genetic operator has been applied, the fitness  $f(P_j^{i+1})$  has dropped below a threshold value, say  $0.5f(P_j^i)$ , then the change is reversed when the individual is copied into  $f(P_j^i)$ . This is useful to stop too much variation being present in the population, and provide a gentle force pushing the population towards convergence.

During each generation, every chromosome is subjected to genetic operators with given probabilities. The probability of mutation is denoted,  $p_m$  ( $p_{ml}$  for links) whilst  $p_{r1}$  and  $p_{r2}$  are the probabilities of 1-point and 2-point crossover.  $p_{ris}$ ,  $p_{is}$  and  $p_{tr_g}$  denote RIS, IS and gene transposition probabilities.  $p_{in}$  and  $p_{in_p}$  are the probabilities for full inversion or portion inversion and finally  $p_{tr}$  and  $p_{tr_p}$  denote full translation or portion translation probabilities.

The order of application is very specific. Every gene in the population may mutate with  $p_m$  ( $p_{ml}$  for links), so the probability of mutation for a given chromosome is higher than this nominal value, depending on the number of genes. The other genetic operator probabilities are each defined as the probability of application to the chromosome. They are also the probability of occurrence given the previous genetic operators have not been applied, see Fig. 3.8. If a previous operator is applied, then no further operators are applied to the chromosome. Therefore, at most one operator can be applied to a chromosome per generation. The exception to this is mutation. It is a vital operator — being the only way of introducing new random symbols into the genome — so its probability is relatively high. But it also has a reasonable chance of being ineffective, say if the mutation occurs low down the ORF or even outside of it. To frequently not apply any other operator is effectively blocking some of the power of GEP. So if a mutation occurs, other operators are still allowed to be applied. After mutation, the first operator to be considered is transposition, then translation and finally inversion. This goes roughly in order of their destructive nature. This also implies that the probability of transposition is precisely  $p_{is}$ , but the actual probability of inversion is lower than the one supplied by the user  $p_{in}$ , based on the conditional events before. At most one of these operators can be applied to ensure that too much randomness is avoided. The order is chosen so that more preserving operators are given preference, with the more destructive operators providing a small chance of large change.

Crossover is also kept separate from this genetic operator step. This is because crossover is a biologically inspired reproduction operator and so recombination is treated fundamentally different from genetic mutations. There are several ways to implement this. For lacking better terminology, crossover can either be monogamous or polygamous. In the former, individuals assigned to crossover are paired off to create children. In the

latter, each individual assigned to crossover is randomly assigned a mate with replacement. The polygamous option is chosen, mainly for its ease of implementation and its slightly reduced overheads, but it also adds a little more randomness into the procedure. Especially for later generations when good individuals can mate multiple times, each with a different recombination point and a different individual.

Because the transposition operator is significantly different from the original version (Ferreira, 2001), a translation operator is implemented. The idea of the original transposition operator is to move genetic material around within in a chromosome. This strategy of providing variation is not strongly available by only using the operators outlined above, so a translation operator is provided.

Translation, as the name suggests, is a permutation operator. Two forms are implemented, portion translation and root translation (or just denoted translation). It takes two random points in either the head or tail and permutes each symbol by a random amount. For example take the chromosome,

```
/a+bc*1bb|b1dbbacaa1
```

the positions 2 and 6 and the random number 3. Then the chromosome becomes,

```
/bc*a+1bb|b1dbbacaa1
```

Root translation is identical except that the first position always corresponds to the root. Whilst not the same as the original transposition operator, the focus of trying different parts of the genotype in different locations (especially the root position) is still the motive.

With regards to the specific value of each genetic operator and crossover probability, a good deal of trial and error is required. Because each problem is very specific, there is no one size fits all with regards to algorithm set up. There are a few rules of thumb however and some important trends found in a range of validation studies (not included within this thesis). Generally, the probability of each operator should be in the range  $1/N, 1/(N_g(h + t))$ . The overall probability of a crossover operation is often set in the region of 0.4-0.7 (Koza, 1992; Ferreira, 2001).

For each genetic operator, one can think of a higher probability as a quicker means of traversing the search space. This is because the rate of change of the population is much higher. However this comes at the price of less direction. The higher the probabilities are set, the closer to random search the algorithm becomes. It is often a careful balancing act to get the right level of search and direction, which is achieved by adjusting the probability of each operator.

## 4.3 Beyond scalar fields

### 4.3.1 Motivation

The ideas presented in Chapter 3 and applied in Chapter 6 are extremely useful for Symbolic Regression (SR) of scalar fields, that is finding a functional form such as,

$$\varphi : \mathbb{R} \times \cdots \times \mathbb{R} \rightarrow \mathbb{R}. \quad (4.4)$$

However, the Gene Expression Programming (GEP) system becomes entirely useless when considering functions that map to higher dimensional spaces. Should a regression problem that requires the optimisation of a function  $T$ ,

$$T : V^1 \otimes \cdots \otimes V^n \rightarrow W^1 \otimes \cdots \otimes W^m, \quad (4.5)$$

where each  $V^i \subset \mathbb{R}^n$  and each  $W^i \subset \mathbb{R}^m$  is a variable in some higher dimensional space, the standard GEP algorithm cannot be neatly applied. This is because the independent variables are now linked, so individual scalar field regressions for each component cannot be applied. Further, one single regression encompassing all independent variables does not work either. This is because incorrectness of the phenotype is almost always guaranteed. For example, imagine that finding a functional form for the tensor  $T \subset \mathbb{R}^3$  is required, which is related to the independent variables  $a, b \in \mathbb{R}$  and  $X, Y \subset \mathbb{R}^3$ . Clearly a solution such as,

$$T = aX + bY \quad (4.6)$$

is a correct expression. This could be represented by the Open Reading Frame (ORF),

`**aX*bY`

But during the course of a genetic mutation, the genome could be modified to give,

`**aX*bb`

which represents the expression,

$$T = aX + bb. \quad (4.7)$$

Equation 4.7 is poorly formed due to the ambiguity of the particle  $bb$ . Either  $bb \in \mathbb{R}$  which invalidates the dimensionality of the operator  $+$  and therefore the dimensionality of  $T$ , or one could define  $*$  polymorphically depending on its arguments.  $bb$  could be evaluated to  $bbI$  or some other equivalent. This is inelegant and it is difficult to see how this would be productive as large portions of the population would be wasting its time

on genetic fragments defined in these unusual and undesired ways. In the worst case, the genotype could contain no appearance of  $X$  or  $Y$  and one has entirely lost all of the multi-dimensional non-linear nature of the system.

Using this method of polymorphic operators is very clunky, one would have to define operators for every possible combination of variable type. With the above example, this would require three different operators for each of  $+$ ,  $-$  and  $*$ . Also, operators such as  $/$  makes no sense mathematically for tensors, so one would be required to make another alteration. Clearly the resulting number of operators worsens if one were to introduce vector variables.

By the end, one would be left with an algorithm where the mapping of the genotype to phenotype produces an unnatural and quite probably unreadable expression. This is due to the increased number of operators that are only included to enable the algorithm to work but are not intended for use and harm the resulting individual's fitness. As a result the best individual is likely to be very poor.

Another solution to the phenotype syntax problem would be to continually check for correctness and replace any wrong code with some that produces a valid expression. To be deterred away from this consider the simple case of an ORF consisting of,

$+aY$

using the same language as above. To correct this expression one must be able to either find the source of the dimensionality issue and choose a code fragment with the correct dimensions or replace the entire genotype. The former option is highly non-trivial as the remaining ORF is dependent on the replaced code, so a further validation is likely required. The second option requires brute force generation of random code as with Genetic Programming (GP) mutations — see Section 3.4.2. This overhead is undesired in GPs, but in the higher-dimensional problem it would cause catastrophic overheads. For the simple piece of code above, assuming there is only  $+$ ,  $*$ ,  $X$ ,  $Y$ ,  $a$  and  $b$  available, the probability of correct replacement is only  $\frac{160}{729}$ , assuming the multiplication of a scalar and tensor commutes. When one starts lengthening the gene and increasing the population to relevant sizes the problem is hugely compounded. The concept of a GEP tail is not introduced as this further complicates the issue. Any strategy employing this method is no longer a GEP and loses all of its advantages.

Instead another method of combining multi-dimensional terminal symbols is required to formulate a tensorial regression GEP framework. Such an implementation is outlined in the following sections. The methodology uses components that share an analogy with a biological structure known as a plasmid. The plasmid is first described in Section 4.3.2 as a biological entity and then the full methodology is detailed in Section 4.3.3.

### 4.3.2 Concept of a Plasmid

#### 4.3.2.1 Plasmids in Biology

Endosymbiotic theory, regarding organisms existing within organisms was popularised by Margulis and Fester (1991). Endosymbiosis was at the time a reasonable departure from mainstream biology — but has been shown to be incredibly powerful in nature.

One such example, a plasmid, is a small DNA molecule that resides most commonly in bacterial molecules (Lederberg, 1952), but have also been found in the cells of archaea and eukaryotic organisms (Lipps, 2008). A plasmid is a separate entity but not considered a life form in its own right (Sinkovics et al., 1997). Plasmids replicate independently from the DNA chromosomes of the organism and carry their own DNA sequence which may be beneficial to their host, such as antibiotic resistance. Plasmids alter the host gene expression to give this competitive advantage.

As mobile genetic elements they frequently travel from bacteria to bacteria via horizontal gene transfer. As a result, the number of plasmids per organism varies by up to three orders of magnitude. When a plasmid carrying organism divides each plasmid is copied and is present in each child. Plasmids also reproduce in their own right and may migrate to other organisms.

#### 4.3.2.2 Plasmids in Evolutionary Computation

Plasmid like structures have been used throughout Evolutionary Computation, although for differing purposes. In some sense the name is just a placeholder for genetic code that exists separately to the main individuals, or in some cases is just a name for the transferring packets of genetic material. More often than not, the term horizontal gene transfer is used to keep in line with the biological inspiration.

The simplest implementation of an Evolutionary Algorithm (EA) deploying the concept of a plasmid is the Genetic Algorithm (GA) of Harvey (2001). The concept is hardly different from the GA outlined in Section 3.3, the notion of plasmid and horizontal gene transfer is just used semantically to define the elements of genetic material that is transferred between individuals. In this way the conjugation operator replaces crossover. The idea of coexisting independent and importantly coevolving genetic material is not utilised. Admittedly Harvey (2001) states the algorithm is not functionally different from and certainly does not outperform the original GA. The simplicity of the biological ideas however are argued to increase his algorithms teachability.

Plasmids have been utilised in a very different way in a GP to keep evolutionary fragments separate. Yamamoto (2008) created a GP that rewrites its own code. The plasmid is the only type of molecule present in the GP; plasmids ‘react’ together and reside in

'reactors,' to keep to an artificial chemistry metaphor, which is quite different from the artificial evolution philosophy adopted in this work. The reactor is analogous to an individual in the population, whilst the plasmids contain the information on how to generate and modify the reactor via their interactions. The result is a decentralised GP, where genetic operators are contained within the individual. The phenotype is now the outcome of the plasmid reactions, whilst the genotype is created from instructions contained within the plasmids. This signifies a partial separation of genotype and phenotype.

The bi-objective minimum spanning tree problem is NP-hard. Monteiro et al. (2009) applied a transgenetic algorithm (TA) to find solutions to this problem. A TA is a branch of evolutionary computing that use plasmids to transfer genetic material, in a subtly different way to the regular genetic operators covered here. Endosymbiosis is partly achieved via the concept of plasmids, but these are the only way of producing variation. Host chromosomes do not crossover or mutate by themselves. In this sense endosymbiosis is not fully achieved.

The Travelling Purchases Problem (Ramesh, 1981) is a generalisation of the Travelling Salesman Problem (see e.g. - Applegate, 2006) that includes the notion of markets into the classical network theory benchmark. An agent must traverse along weighted edges representing travel costs to nodes representing markets. The agent has a list of products to purchase. Both the travel costs and purchasing costs must be minimised. Almeida et al. (2010) implemented a TA to solve this problem. The plasmid once again was the only means of genetic transfer but there is distinction between it and the chromosome. This is still only really superficial however, as the chromosome itself does not appear to evolve, rather it contains genetic information that is changed in the presence of plasmids and also contains information regarding the problem. The plasmid is a more mobile evolutionary method, but true endosymbiosis is not fulfilled due to the lack of coevolution.

The plasmid TA implementations briefly described above show recent endosymbiotic ideas. However because the plasmid contains genetic information that could be carried by the host chromosome itself, there is little point in applying further genetic operators. In these cases, if one wished to apply mutation and crossover operators to the chromosome *as well as* employ the plasmid concepts outlined above, then you might not use the language of plasmid and horizontal gene transfer. Instead one may use the more modest terminology in terms of a new translation operation.

Because the host does not evolve independently of plasmid interaction, the endosymbiotic idea is not fully realised. The idea of a plasmid is just largely a semantic argument to describe the sole variation in chromosomes, probably used because a chromosome lacks true expression in GAs and GPs. By terming the mutation vectors as plasmids, a separate entity, the genetic variation is kept separate from the phenotype. This is not quite genotype/phenotype distinction but it is halfway towards the idea. Note, in

GEP the genotype and phenotype are distinct so the above notion of endosymbiosis is irrelevant. One may just define the plasmid interactions described in the above papers as a new genetic operator.

### 4.3.3 A New Plasmid Implementation

#### 4.3.3.1 Endosymbiotic Genomes

In order to truly involve endosymbiosis in an EA, the plasmid must contain an evolutionary advantage, contain distinct genetic information to its host and evolve separately from an already evolving chromosome. The GEP framework can be modified to fulfil these transgenic criteria to perform symbolic regression of varying dimensionality.

The modified framework, Multi-dimensional GEP (MGEP), consists of chromosomes and plasmids. For simplicity, the discussion below will be limited to considering functional forms of  $3 \times 3$  matrices which depend only on  $3 \times 3$  matrices and scalar variables. Say  $T_{ij}$  of Eq. 4.5 is unknown and given some data set of expected values of  $T_{ij}$ , the known tensor variables  $A_{ij}$ ,  $B_{ij}$  and the known scalar variables  $a$  and  $b$ , a functional form is required.

An individual in MGEP consists of only symbols with the right dimensionality, in both the arguments and the function output. In this case,  $A_{ij}$ ,  $B_{ij}$ , any matrix operation that maps matrices to  $\mathbb{R}^3$  and any (random) constants that belong to  $\mathbb{R}^3$  would be allowed. So a valid function and terminal set would respectively be,

$$\mathcal{F} = \{+ : +, - : -, * : F(A_{ij}, B_{ij}) \rightarrow A_{ik}B_{kj}, T : F(A_{ij}) \rightarrow A_{ji}\} \quad (4.8)$$

and

$$\mathcal{T} = \{\mathbf{A} : A_{ij}, \mathbf{B} : B_{ij}, \mathbf{I} : \delta_{ij}, ? : RNC_{ij}\}. \quad (4.9)$$

From this valid individuals can be constructed and solutions can be found to the given problem. Note  $RNC_{ij}$  denotes a randomly created constant consisting of nine independent components. Information regarding  $a$  and  $b$  has not been passed onto the individual as the current chromosome has no way of processing scalars. This means the algorithm will struggle to find the global optimum, especially if the actual functional form of  $T_{ij}$  is strongly dependent on  $a$  and  $b$ .

To overcome this hurdle, plasmid individuals are also created that contain only symbols relevant in a scalar context. So valid plasmid function and terminal sets are, for example, respectively,

$$\mathcal{F}_P = \{+ : +, - : -, * : \times, \mathbf{s} : \sin, \mathbf{e} : \exp\} \quad (4.10)$$

and

$$\mathcal{T}_P = \{\mathbf{a} : a, \mathbf{b} : b, \mathbf{1} : 1, ?: ?\}. \quad (4.11)$$

Plasmids using these symbols can live in a higher dimensional individual via the arity one symbol  $P$ . An individual in MGEP makes use of the complete function set  $\mathcal{F} \cap \mathcal{P}$ , where  $\mathcal{P}$  is the set of all symbols that connect to each different type of plasmid. In this case  $\mathcal{P}$  only consists of  $P$  — the arity one symbol that connects three dimensional chromosomes to scalar field plasmids. In other applications one may need further types of plasmids, say ones that consist of matrix arguments mapped to scalars, allowing operations such as the determinant.

$P$  is the symbol that allows a chromosome to connect to a plasmid and the connection is made via a scalar multiplication of the argument of  $P$ . For example consider the chromosome,

**P+AB|AIBBI**

which can be expressed as,

$$P(a, b)(A_{ij} + B_{ij}) \quad (4.12)$$

Notice the plasmid scalar field function  $P(a, b)$ . Each plasmid symbol contains its own genotype, made up of symbols from  $\mathcal{F}_{\mathcal{P}}$  and  $\mathcal{T}_{\mathcal{P}}$ , and by extension, its own phenotype. This plasmid may evolve independently of the host chromosome and interact with other plasmids in the gene pool.  $P$  effectively acts as a connection point, that allows a plasmid to latch onto a chromosome and affect the host's expression.

To complete the example above, the chromosome **P+AB|AIBBI** contains one plasmid which could have its own genotype, say,

**\*asb1|??ab1b**

leaving the final expression,

$$a \sin(b)(A_{ij} + B_{ij}). \quad (4.13)$$

Note there is no restriction, except for the head length, on the number of plasmids allowed in a chromosome and, as  $P$  is treated as an arity one symbol, the syntax of the expression is always guaranteed. In order to write down the full genotype, the following notation is used,

**P(\*asb1|??ab1b)+AB|AIBBI**

where the plasmid genotype is recorded inside the brackets. In terms of expression, the mathematical formulation is given easily as Eq. 4.13 but the ET is now not so

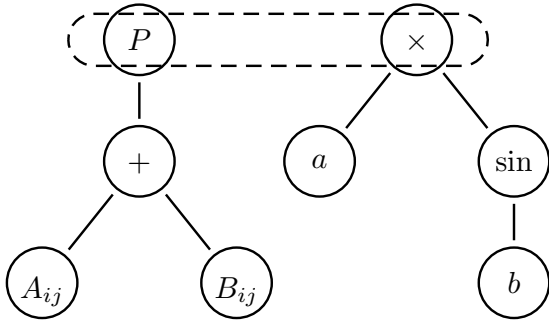


FIGURE 4.1: The individual and plasmid ET for Eq. 4.7. The left is the higher dimensional chromosome, whilst the right is the scalar field plasmid. The link shows the point where the plasmid expression latches onto the host.

straightforward. The host chromosome and plasmid should be expressed as two distinct trees, depicted in Fig. 4.1. This makes sense because the chromosome and the plasmid are two separate entities.

#### 4.3.3.2 The MGEP Algorithm

There is a multitude of different ways of handling plasmid evolution. MGEP handles plasmids simply, but potentially in such a manner that adversely affects overall algorithm performance. Upon the creation of a  $P$  symbol, a plasmid is created by MGEP and similarly, upon destruction, the plasmid scalar field is removed from the gene pool. This implies a variable population size of plasmids. This population evolves in the same way as the host chromosomes, by using genetic operators and a selection process. The genetic operators for plasmids are the same as those detailed in Section 3.5.6 and Section 4.2. The selection process can either be roulette or tournament selection, where the fitness is based on the host fitness score. Each plasmid survives by the virtue of its host and is more likely to survive by providing an evolutionary advantage. Elitism in the selection process corresponds to keeping any plasmids that are associated with the best individual, this could mean keeping multiple, one or no plasmids.

MGEP is an identical procedure to GEP, with the addition of a plasmid step. Figure 4.2 shows this added step. Firstly the plasmids are gathered together into a plasmid population by extracting them from their hosts.<sup>1</sup> This population then undergoes genetic operators and selection, before being redistributed back amongst the host chromosomes. The gather and redistribution is a first in first out system, to ensure that each  $P$  symbol receives the correct plasmid — which may be significantly changed via the genetic operators.

This implementation could potentially suffer from an overly large plasmid population, massively increasing overheads. Another downside of this approach is the relative

<sup>1</sup>In MGEP, this is done by keeping an array of pointers so there are no major memory overheads

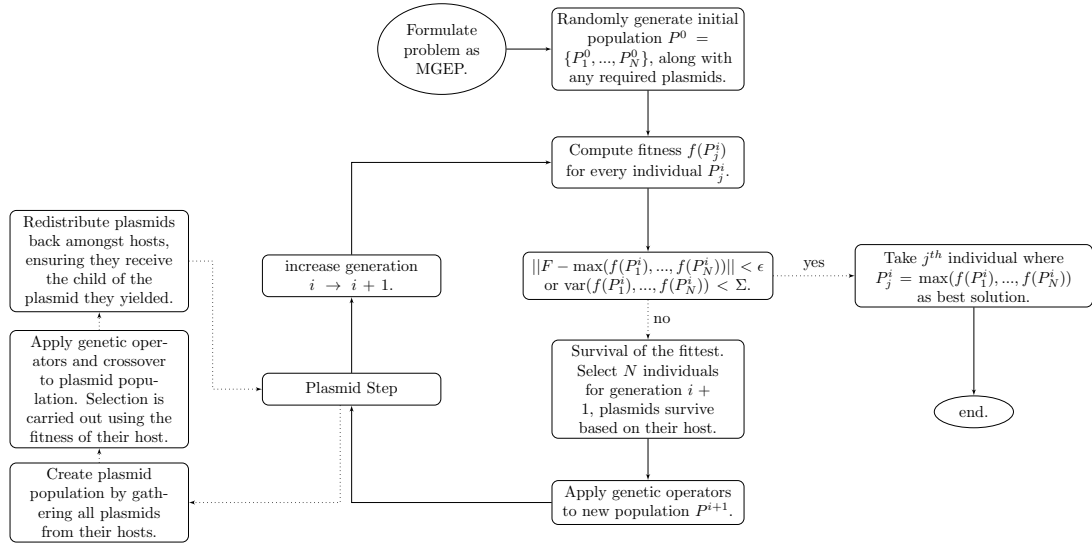


FIGURE 4.2: The general flow of the MGEP algorithm, with the plasmid step detailed.

ease with which good plasmids could fall out of the genome. This could be because their host does not make it through selection, or the  $P$  symbol is changed via a mutation. To combat this, other methodologies could be implemented. One possibility is to have a fixed size population of plasmids, where one of which is chosen at random when a chromosome has an active  $P$  symbol. This population can evolve in the same way, but the fitness would now be based on how many generations the plasmid has been active for. So if a plasmid is more frequently expressed, it has a higher chance of being selected for the next generation plasmid gene pool. This second approach is not as easy to implement and as of yet has not been explored.

Horizontal gene transfer has not been explicitly utilised in MGEP because of the already rich set of genetic operators available to the plasmids. One possible implementation of horizontal gene transfer would be to replace the translation and crossover operators with a swap like operation, however it does not seem necessary to just to satisfy the metaphor.

In summary, MGEP is a fully endosymbiotic system. The plasmid organism fulfils the criteria expressed in Section 4.3.3.1. The plasmid provides an evolutionary advantage by changing the expression, but not the genotype, whilst living in but evolving independently, of its host chromosome.

#### 4.3.3.3 Higher Dimensional Fitness

Now each chromosome has more than one component, some form of multi-objective fitness is required. Multi-objective fitness was introduced in Section 3.5.5, which could either take the form of a weighted average, Eq. 3.15, or a Pareto front, Eq. 3.16. Both

have their merits, but in the opinion of the author, neither fully grasp the goal of tensor regression.

In practical optimisations of physical phenomena, say the components of a stress tensor, each component is highly coupled. As such, preliminary implementations utilising a Pareto front did not yield good results. Further tests showed that assessing the magnitudes of each component combined with a weighted average was not a useful objective. This is because too much focus is placed on the magnitude of low gradient regions and the desired shape of the training data is not found.

Instead, this work applies a fitness function of the form,

$$f(P_j^i) = \sum_{k=1}^m \frac{f(P_j^i)_{pq}^k E_{pq}^k}{\sqrt{f(P_j^i)_{rr}^k E_{ss}^k}} \quad (4.14)$$

which is a test of the local alignment with the expected values  $E_{ij}^k$ . Note Einstein summation on  $p, q, r$  and  $s$ .  $f(P_j^i)$  is bound between -1 and 1, for complete misalignment and alignment respectively.  $E_{rs}^k$  is the expected value (the training data) at the  $k^{\text{th}}$  data point.  $f(P_j^i)_{mn}^k$  is the evaluation of the individual  $P_j^i$  at the  $k^{\text{th}}$  data point.

Equation 4.14 was found under testing to be effective at finding a tensor  $f(P_j^i)_{rs}$  that contains the correct relationship between components. However, it does not specify anything regarding the magnitude. This can be circumvented, as in Chapter 5, by careful scaling of the independent variables and allowed constants. If this kind of problem would persist in an application, there is always the possibility of a multi-objective fitness that combines Eq. 4.14 with a Lebesgue norm to appropriately scale the output.

## 4.4 Clustering Algorithm

So far GEP has been discussed in a language that describes regression. It is the easiest way in which to introduce the evolutionary concepts. A second and completely different application is now described. This is the clustering or grouping of data points into distinct groups. Essentially the same features of the algorithm discussed in Chapter 3 apply; the main difference is the list of symbols, through the function  $\mathcal{F}$  and terminal  $\mathcal{T}$  sets, available to chromosomes.

Effectively, finding a clustering  $\mathcal{C}$  is the act of assigning a label to unsorted data.  $\mathcal{C}$  can be thought of as a list of labels and an instruction on how to assign labels to data points, either from the training data or from a new set. There are many different ways to cluster a data set and as with all machine learning algorithms, there is no free lunch. Data clustering is a task that many disciplines require and as such, there are numerous and diverse methods available. A full review is out of the scope of this work, but for

full reviews see Xu et al. (2005); Han et al. (2011). Broadly speaking the two most famous methods of clustering are k-means (Lloyd, 1982) and hierarchical clustering (e.g. Kaufman and Rousseeuw, 2009). The k-means clustering algorithm can be summarised as: choose the number of clusters  $k$ , choose  $k$  data points as the cluster centres, assign each data point to the cluster with the closest centroid, calculate the new centroids as the mean of all data points within each cluster. The assign and calculate steps are repeated until the data points no longer change clusters. Despite being reasonably quick to run, one can see that a user must prescribe  $k$  which is often unknown. Hierarchical clustering circumvents to an extent the prescription of  $k$ . The algorithm either comes in a top-down or bottom-up flavour. For the top-down, all data points begin in one cluster and then this is split recursively based on some splitting criteria. For the bottom-up, each data point begins in its own cluster and these are then merged based on some merging criteria. In both cases a hierarchy of potential clusterings are returned. Therefore a range of clusterings are returned at different resolutions and it is not always clear which is best. Another drawback is the slow runtime due to the merging/splitting decisions that must be made. Instead, this work uses the advantage of the GEP chromosome for a framework that can build variable length phenotypes and consequently a variable number of labels. Therefore there is no prescription of the number of centres and the algorithm decides what resolution level is appropriate.

The first usage of a GEP framework by Chen et al. (2007) captured the essence of producing variable length  $\mathcal{C}$ , yet did not preserve the syntax of the individual. Many individuals, much like in GP, had to be rejected on the grounds of an invalid phenotype. Zheng et al. (2012) further developed this algorithm to preserve the syntax, however their paper leaves ambiguities for certain situations that do not explain this feature of their algorithm. However, they tested GEP for clustering on real data sets and it performed admirably against existing deterministic methodologies.

The easiest way to define  $\mathcal{C}$  is as a list of centroids,

$$\mathcal{C} = \{c_i | c_i \in \mathbb{R}^m, i = (0, 1, \dots, n - 1)\}, \quad (4.15)$$

where  $c_i$  is a vector of the same dimensionality as the data set and defines the centre of the  $i^{\text{th}}$  group. For example, suppose we have a data set comprised of  $m$ -dimensional data points  $x_j \in \mathbb{R}^m$ . Each  $x_j$  can be assigned to one of the  $n$  groups by ascertaining, via the use of a distance metric, which  $c_i$  is closest. For example, consider Fig. 4.3, that contains 1000 data points  $x_j \in \mathbb{R}^2$ . The data is arbitrary for the purpose of point and it is coloured by the desired grouping. There are two example clusterings  $\mathcal{C}$  shown in the plot, both produce the desired grouping when using the Euclidean distance to evaluate the closest  $c_i$  for each  $x_j$ . The orange clustering however is clearly a less robust definition of  $\mathcal{C}$  by the virtue that should we wish to group the large green circle, a new data point that is previously unseen, it will belong to the red group not the intuitive blue.

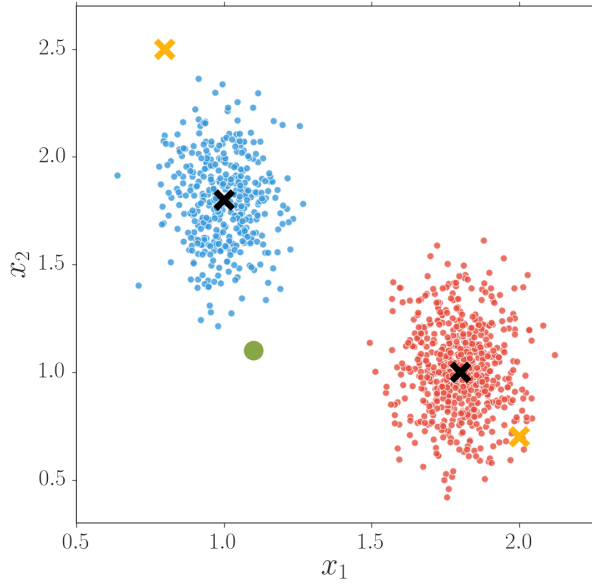


FIGURE 4.3: Example clustering. Red and blue scatter: data points  $x_i$  distinguished by the desired grouping. Black crosses: example of a good  $\mathcal{C}$ . Orange crosses: example of a bad  $\mathcal{C}$ . Green circle: previously unseen data point.

It is therefore the job of a clustering algorithm to provide a good set of centres that define each type of group in a data set. Further, with the GEP framework we do not have to specify the number of groups beforehand. In this section properly defined function and terminal sets are outlined that guarantee preservation of phenotypic syntax. A multi-objective fitness framework is proposed that is simple and prioritises efficiency and quality of the clustering.

#### 4.4.1 Individuals in GEP Clustering

Each individual encodes a possible  $\mathcal{C}$ . The individual consists of a head and a tail, exactly as described in Section 3.5. The phenotype however is now not a mathematical expression but a list of centres, one for each group in the clustering.

The terminal set  $\mathcal{T}$  is precisely the  $m$ -dimensional data set one wishes to cluster,

$$\mathcal{T} = \{x_j \mid x_j \in \mathbb{R}^m\}. \quad (4.16)$$

This implies that individuals are functions of the training data and also that the degrees of freedom in an individual is very large. To use the data set makes intuitive sense and many clustering algorithms rely on this dependence (e.g. Jain et al., 1999). Largely however, these algorithms encode an individual as long as the data set. For very large training sets this becomes undesirable. Because the GEP framework allows for variable

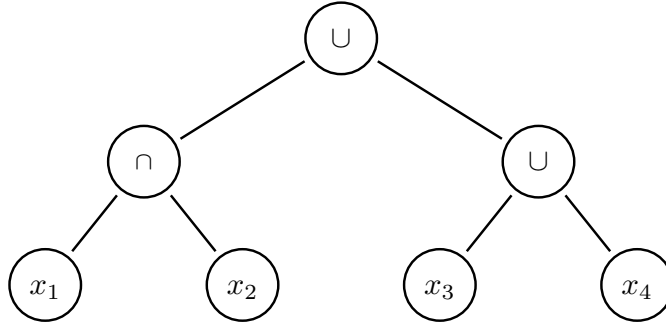


FIGURE 4.4: Example Cluster ET

length phenotypes, an individual can have access to the entire data through  $\mathcal{T}$  but its maximal size is determined by the predefined head length.

The function set, originally proposed by Chen et al. (2007) and modified by Zheng et al. (2012), does not preserve the syntax of the phenotype. Note, Zheng et al. (2012) claims this problem is solved, however their paper does not address all possible situations. There are some notable exceptions to the list of phenotypes and how their function set would resolve this. Presented below is a function set very similar to that proposed, but ensures correctness in the list of cluster centres it describes.

There are two main functions, a union operator  $\cup$  and an intersection operator  $\cap$ . Both are arity two symbols that inspect their arguments and return either the combination of their arguments ( $\cup$ ) or the intersection of their arguments ( $\cap$ ). In simplistic terms,  $\cup$  adds a cluster to the grouping  $\mathcal{C}$  and  $\cap$  combines its arguments into one cluster. The number of  $\cup$ 's in the phenotype defines the number of groups in the clustering.

Before the formal definition of each symbol, the centroid function between two  $m$ -dimensional data points  $x_i$  and  $x_j$  is introduced,

$$\zeta(x_i, x_j) = \left( \frac{x_{i1} + x_{j1}}{2}, \frac{x_{i2} + x_{j2}}{2}, \dots, \frac{x_{im} + x_{jm}}{2} \right), \quad (4.17)$$

which defines the midpoint between  $x_i$  and  $x_j$ . This is the  $\cap$  symbol. The original functions as defined by Chen et al. (2007) are,

$$\{x_1, x_2, \dots, x_n\} \cup \{y_1, y_2, \dots, y_m\} = \{x_1, x_2, \dots, x_n, y_1, y_2, \dots, y_m\} \quad (4.18)$$

and

$$x_i \cap y_j = \{\zeta(x_i, x_j)\}. \quad (4.19)$$

Using these symbols, we can read for example the Expression Tree (ET) in Fig. 4.4 as the list of centres,

$$\mathcal{C} = \{(x_1 + x_2)/2, x_3, x_4\}. \quad (4.20)$$

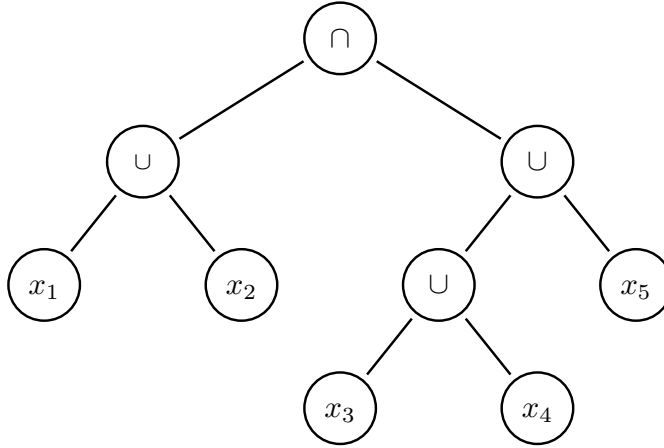


FIGURE 4.5: Example Cluster ET that is invalid with the original specification of Chen et al. (2007)

Equation 4.20 describes a clustering over the data using 3 groups: the first is the midpoint between data points  $x_1$  and  $x_2$ , the second is the data point  $x_3$  and the third is the data point  $x_4$ .

This definition however is not complete – consider the ET in Fig. 4.5. Equation 4.19 does not provide us with details on how to treat mixed length arguments, which would be very common at runtime. Chen et al. (2007) chose to throw these out and repeatedly generate new individuals until this problem was solved. This is fine on small arbitrary test data sets as the head length is very small, however this author applies the clustering algorithm to very large data sets. In this case, the head length can be as high as 50 or 100.

To overcome this issue, two symbols are introduced to replace  $\cap$ . The first is the left intersection  $\cap_L$ ,

$$\{x_1, x_2, \dots, x_n\} \cap_L \{y_1, y_2, \dots, y_m\} = \\ \left( \bigcup_{i=1, \dots, N} \{\zeta(x_i, y_i)\} \right) \cup \{x_N, x_{N+1}, \dots, x_M\} \cup \{y_N, y_{N+1}, \dots, y_M\}, \quad (4.21)$$

where  $N = \min(n, m)$  and  $M = \max(n, m)$ .  $\cap_L$  calculates the centroids of its arguments one at a time, by treating the sets as an ordered list. Then when one of the sets has no more remaining arguments the remainder in the other set is appended. Therefore, at least  $\{x_N, x_{N+1}, \dots, x_M\} = \emptyset$  or  $\{y_N, y_{N+1}, \dots, y_M\} = \emptyset$ . The second symbol introduced is the right intersection  $\cap_R$ ,

$$\{x_1, x_2, \dots, x_n\} \cap_R \{y_1, y_2, \dots, y_m\} = \{x_n, x_{n-1}, \dots, x_1\} \cap_L \{y_m, y_{m-1}, \dots, y_1\}, \quad (4.22)$$

to account for the asymmetry of  $\cap_L$ .

Fig. 4.5 can now be decoded by replacing  $\cap$  with, for example,  $\cap_{\mathcal{L}}$  and read to be,

$$\mathcal{C} = \{(x_1 + x_2)/2, (x_2 + x_4)/2, x_5\} \quad (4.23)$$

Note, if it was replaced by  $\cap_{\mathcal{R}}$  then  $\mathcal{C}$  would be defined differently.

To summarise, the function set in the GEP clustering algorithm used in this thesis is,

$$\mathcal{F} = \{\cap_{\mathcal{L}}, \cap_{\mathcal{R}}, \cup\}. \quad (4.24)$$

#### 4.4.2 Fitness Function and Metric

Whilst the trivial example above, Fig. 4.3, uses the Euclidean distance,

$$d_e(\underline{x}, \underline{y}) = \sqrt{(\underline{x} - \underline{y}) \cdot (\underline{x} - \underline{y})}, \quad (4.25)$$

there are more useful distance functions. Issues with the Euclidean distance become apparent when data sets are hugely skewed and may contain clusters of more complex shapes or each dimension in the data set takes values over varied domains. This is because Euclidean geometry is defined via an isotropic metric. In other words, Eq. 4.25 is only suitable for clusters of shapes near to hyper-spheres. Several proposals have tackled this issue and shall now be assessed. To take care of higher dimensional complex shapes, the so called point-symmetry distance (Su and Chou, 2001) can be used,

$$d_{ps}(\underline{x}_i, \underline{y}) = \min_{j=1, \dots, m, i \neq j} \frac{d_e(\underline{x}_i + \underline{x}_j, 2\underline{y})}{d_e(\underline{x}_i, \underline{y}) + d_e(\underline{x}_j, \underline{y})}. \quad (4.26)$$

Equation 4.26 defines the point-symmetry distance of the data point  $\underline{x}_i$  to the point  $\underline{y}$ . Equation 4.26 evaluates distance based on whether any other data point is a similar (Euclidean) distance from  $\underline{y}$  as  $\underline{x}_i$ . The distance is lower if this is the case and is minimised if the mirror image point  $\underline{z} = 2\underline{y} - \underline{x}_i$  exists in the data set. The denominator is a normalisation to ensure that the relative Euclidean distance  $d_e(\underline{x}_i, \underline{y})$  does not matter, only that there is a similarly relative point. This allows for complex shapes to be found in the data set.

There is a major flaw with Eq. 4.26 however, namely that it can be minimised by maximising the denominator. That is, if  $\underline{x}_i$  is almost equally symmetrical with two cluster centres, say  $c_1$  and  $c_2$ , then  $\underline{x}_i$  would be assigned to the further cluster centre. This can have the effect of merging the data set into one large cluster around  $c_k$  whilst the remaining  $n - 1$  cluster centres are not assigned to any data points. To overcome this, Chou et al. (2002) proposed the distance measure,

$$d_{ps2}(\underline{x}_i, \underline{y}) = d_{ps}(\underline{x}_i, \underline{y})d_e(\underline{x}_i, \underline{y}), \quad (4.27)$$

however this too can simply be shown to fail. Just consider  $d_{ps}(\underline{x}_i, \underline{y}) = 0$  and the Euclidean distance plays no role in determining the point-symmetry distance.

Notice that Eq. 4.26-4.27 requires information on all other  $m$  data points in the training data. Considering that GEP requires many individuals and generations and the training data may be very large, Eq. 4.26-4.27 are entirely unacceptable in terms of overheads. For example, the clustering in Chapter 7 is on a training data set of  $10^5$  points.

Bandyopadhyay and Saha (2007) proposes a more sensible measure,

$$d_s(\underline{x}_i, \underline{y}) = \frac{d_e(\underline{z}, \underline{z}_1) + d_e(\underline{z}, \underline{z}_2)}{2} \cdot d_e(\underline{x}_i, \underline{y}), \quad (4.28)$$

where  $\underline{z}$  is again the symmetry point of  $\underline{x}_i$  (although not necessarily in the data set) and  $\underline{z}_1$  and  $\underline{z}_2$  are the two nearest neighbours of  $\underline{z}$  (from the data set). Whilst this significantly reduces the overheads, it is not sufficient for consideration here as in general  $\underline{y}$  changes many times at runtime, requiring a recalculation of  $\underline{z}_1, \underline{z}_2$  for every evaluation of an individual. To see this, imagine as an individual evolves,  $\mathcal{C}$  changes and so therefore does evaluating  $d_s(\underline{x}_i, c_j)$ .

Instead, in this work, the Mahalanobis distance is utilised as the distance function,

$$d(\underline{x}_i, \underline{y}) = \sqrt{(\underline{x}_i - \underline{y})\Sigma^{-1}(\underline{x}_i - \underline{y})}. \quad (4.29)$$

$\Sigma$  is the covariance matrix of the data set. This has been used many times as a clustering distance function and was first proposed by Mao and Jain (1996). It effectively is able to find hyper-ellipsoid shaped clusters. The only additional overhead to Eq. 4.25 is the initial calculation of the inverse covariance matrix. Note the inversion can be overcome by simply normalising each dimension by the standard deviation. In this case  $d_e = d_s$ .

To reduce the occurrence of situations such as the poor clustering example in Fig. 4.3, a multi-objective framework to evaluate fitness is devised as follows. For a clustering  $\mathcal{C}$  on  $m$  data points  $x_i$  (underscores are now dropped) defined by an individual as described in Section 4.4.1, the distance fitness is defined as,

$$f_d(P_j^i) = \sum_{k=1}^m \sum_{l=0}^{n-1} d(x_k, c_l) s_{kl}, \quad (4.30)$$

where  $s_{il}$  is 1 if  $x_k$  belongs to cluster  $l$  and 0 otherwise. The aim of the optimisation is to minimise Eq. 4.30. During tournament selection (the only time that the evaluation occurs, see Section 4.4.3), if an individual scores lower than its opponent, it gets 1 point. It gets a further point if its  $f_d$  is 70% that of its opponent.

The next step is to calculate the connectivity of the clustering (Zheng et al., 2012),

$$f_c(P_j^i) = \sum_{k=1}^m \sum_{l=1}^L \Gamma_{k,n_{kl}}, \quad (4.31)$$

where,

$$\Gamma_{k,n_{kl}} = \begin{cases} 1/l, & \text{if } \nexists c_q \mid x_k \in c_q \wedge n_{kl} \in c_q \\ 0, & \text{otherwise.} \end{cases} \quad (4.32)$$

$n_{kl}$  is the  $l^{\text{th}}$  nearest neighbour of  $x_k$ . Equation 4.31 is calculating a score based on how many nearest neighbours, up to some predefined number  $L$ , exist in the same cluster (defined as  $c_q$ )<sup>2</sup> as  $x_k$ . In this work  $L$  is set to 5. If the nearest neighbour of  $x_k$  is not in the same cluster then 1 is added to the connectivity score  $f_c$ , if the second nearest neighbour is not in the same cluster  $1/2$  is added to the score and so on. This type of fitness criteria has the added benefit of favouring clusterings that are not close to each other (imagine a clustering in Fig. 4.3 where two centres describe each group, thus there are a surplus of groups and the algorithm has intuitively failed).

In the tournament selection process, an individual gains a further point if its connectivity score is lower than its opponent. This gives an individual a maximum score of 3 (2 for  $f_d$  and 1 for  $f_c$ ) and in this case it would win the tournament. If the score is tied, then the one with the lowest  $f_c$  wins. This scoring system allows for individuals that minimise Eq. 4.30, but if two individuals are closely matched in this regard, then the scoring favours the more connected individual.

#### 4.4.3 Full Algorithm

The full algorithm is very similar to that of Fig. 3.8, with a few changes to account for scalability. The fitness step is no longer calculated, rather this is absorbed into the selection step. There are only 2-3 tournaments per generation, the rest of the population is left unchanged. This is known as a steady state Evolutionary Algorithm (Syswerda, 1989, 1991). This means that there are many members of the population with an unknown fitness, making elitism and a stopping criteria difficult. An imperfect option is taken, such that a record of the best known individual (the one with the lowest known  $f_d$ ) is protected from changes and it is to this individual that the stopping criteria is applied. This incompleteness of information is preferred to the overheads induced by evaluating the total population at each generation, given that the data set contains tens of thousands of data points. If the stopping criteria is not met after the specified number of generations, then a full sweep of all individuals is performed to find the best scoring as determined by  $f_d$ .

---

<sup>2</sup>This is a momentary abuse of notation:  $c_q$  really defines a centroid, however writing Eq. 4.32 in terms of distances is quite disgusting.

The final change to the main flow of the algorithm is the reduction in the number of genetic operators. Only mutation and 1- and 2- point crossover is used, again in the interest of scalability.

## 4.5 Summary

Three implementations of the GEP framework have been outlined. Scalar field regression closely following the original algorithm of Ferreira (2001) was detailed in Section 4.2. A novel tensor field regression, that utilises a symbiotic relationship between host chromosomes and plasmids, was described in Section 4.3. Finally a clustering algorithm, similar to the work by Zheng et al. (2012) is detailed in Section 4.4.

Each of these algorithms finds a place in later chapters of this thesis. The scalar field GEP is used in Chapter 6 to find functional forms for length scale damping functions. The original framework is well suited to this problem, due to the freedom of expression and minimisation of assumptions. This framework however, as discussed in Section 4.3, is not suited to problems of many dimensions. Therefore, the development of the stress-strain relationship in Chapter 5 utilises the tensor regression framework. Finally, the clustering framework is used to analyse Reynolds stress structures from a channel flow in Chapter 7. Because the number of clusters is not needed *a priori* and the high dimensionality of the data set, this clustering algorithm is very useful.

The main novelty of this chapter is the tensor regression algorithm outlined. In its current form it is useful for finding relationships between tensors and scalars. This has obvious applications in physical modelling, indeed it is used for turbulence modelling in this thesis. It is hoped however that the general framework can be expanded upon to achieve a more general matrix/array framework that is able to utilise arguments of differing dimensions. The symbiotic relationship used in this thesis has not been deeply explored. Future studies should test the optimality of the algorithm flow and also the evolutionary concepts employed.

# Chapter 5

## Evolutionary Optimisation of the Anisotropy Tensor

### 5.1 Introduction

In a lecture series over forty years ago, Launder and Spalding (1972) stated ‘several thousand man hours’ have been spent developing Reynolds-Averaged Navier-Stokes models (RANS) to describe turbulence. Today it is hypothesised, with a reasonable level of confidence, this number has risen considerably. In short, RANS modelling is a hard problem. In this chapter a novel approach is taken to building mathematical models of turbulence that utilise data over mathematics.

RANS models have known deficiencies in separated flows, this comment extends from linear constitutive relationships through to full second order closures (Wilcox, 1998). The common Shear-Stress Transport (SST) two-equation model (Menter, 1994), which uses a linear stress-strain relationship, is modified such that its prediction in a separated flow is greatly improved.

The linear constitutive relationship is modified by adding terms that account for the anisotropy in the Reynolds stress in the presence of slowly changing mean strain (Rodi, 1972, 1976; Pope, 1975). This branch of RANS is labelled Explicit Algebraic Stress Modelling (EASM) and there are many successful closures currently available (e.g. - Speziale et al., 1991; Wallin and Johansen, 2000; Abe et al., 1997, 2003; Hellsten, 2005). Each model has a portfolio of cases where it is a good predictor but it is unknown *a priori* whether a model will be able to add a new case to its résumé. This is primarily because models are calibrated/derived for equilibrium conditions and industrial reality is anything but (Speziale, 1997; Murakami, 1998).

Despite these shortcomings, RANS has and will remain the mainstay of turbulence prediction for the majority of flow types in industry (Pope, 1999; Hanjalic, 2005). An

increase in computational power is not a ticket to performing Large Eddy Simulation (LES), but rather a ticket to reducing the design cycle in competitive markets.

This work details the use of Direct Numerical Simulation (DNS) data to sensitise RANS models to the physics present in a separated flow. This is done non-deterministically and is at heart a closure calibration to a particular flow type. Coefficients in models are routinely calibrated using DNS, typically of a channel or other simple wall bounded flow, but the term closure calibration is a generalisation. The DNS used to sensitise RANS models in this study is of a backward facing step geometry. The anisotropy tensor itself is created by symbolically regressing an algebraic equation. The Gene Expression Programming (GEP) framework discussed in Section 4.3 is used for this task. This minimises the number of assumptions made and creates a tensor expression without the user supplying any functional form.

Optimisations of this type are beginning to emerge for the improvement of closures. Currently, there is a movement in *replacing* model terms with an Artificial Neural Network (ANN). An ANN is the ultimate black box, it consists of an input, output and a host of hidden highly interconnected nodes (Haykin et al., 2009). An ANN must be trained on a data set beforehand, much like the evolutionary algorithms presented throughout this text. Once trained, the ANN can be used in place of model terms. The input is some trustworthy information about turbulence, say from DNS or experiment and the output is the *result* of a model. The hidden layers are in place of the model terms and cannot easily be reconstructed into an analytical form. For example, Yarlanki et al. (2012) used an ANN for the optimisation of  $k - \varepsilon$  turbulence model coefficients. The procedure consisted of experimentally measuring values and then building a parameter space by running CFD simulations of the same configuration (a data centre) by changing the values of the coefficients. These results were then approximated by an ANN, which was used as an objective function for a minimisation of the error. This approach however requires many CFD runs to build the parameter space. Similar to this work, Fabritius (2014) used a Genetic Algorithm to tune the coefficients of the  $k-\varepsilon$ ,  $k-\omega$ -SST and Spalart Allmaras turbulence models. Further to just coefficient tuning, Tracey et al. (2015) replaced known model terms in the Spalart-Allmaras with an ANN and tested the ability to reproduce RANS calculations. Whilst the ANN successfully trained to RANS flow fields (the ANN reconstruction of the training flow field was remarkable), as more of the model was handed to the ANN, the performance became unpredictable. This unpredictability is extremely difficult to diagnose due to the black box nature of the ANN. One cannot simply look at terms in an equation and understand the cause of issues. This is compounded when the number of hidden layers is increased. This hurdle must be overcome before an ANN can be trusted to predict previously unseen flow fields.

Zhang and Duraisamy (2015) focussed on machine learning tools for improving RANS. An inverse modelling approach (e.g. Dow and Wang, 2011; Duraisamy and Durbin, 2014)

was taken to determine an adjustment parameter to be inserted into the RANS equations. This parameter was then learned by an ANN and also two variants of Gaussian Processing. All methods were shown to be extremely powerful regression tools, however the models depend explicitly on the training data. Further, Gaussian Processing assumes a joint Gaussian distribution between training samples. The accuracy of this assumption is questionable and may have consequences when used in a predictive setting.

In this chapter, the models for anisotropy are transparent and tangible which can be implemented directly into CFD codes painlessly. GEP is not only able to reproduce the anisotropy, but is able to give us *how* it got there and therefore we can use it as a predictive tool. The work flow is summarised as follows:

- Calculate the anisotropy tensor from the DNS of the backward facing step case.
- Use GEP to create algebraic forms for this anisotropy based on scalar  $I^k$  and tensor  $T_{ij}^k$  variables, using the *a priori* form  $a_{ij} = a_{ij}(T_{ij}^1, T_{ij}^2, \dots, I^1, I^2, \dots)$ .
- Insert the new algebraic form into the baseline SST model.
- Make observations about the model by testing *a posteriori* on the periodic hills geometry.

In total, 50 models are created in this way. The production of 50 models is purely for the statistical analysis of the GEP methodology and is not a practical example of how the methodology should be used. Clearly, the combination of 50 models is not a useful method of prediction. In practice, one may be able to develop a relationship between the fitness of a class of GEP solutions and their predictive capability *a priori*. As the number of these solutions increases, the confidence in the ensemble solution should increase. If the number of solutions required for a confident ensembled prediction is small, then the presented methodology could become viable.

Section 5.2 describes the baseline SST model to be modified. Section 5.3 details the methodology and the performance of GEP when regressing solutions of the *a priori* form. Section 5.4 discusses the ability of the new algebraic expressions to improve the prediction of the periodic hills test case. A link is then made between the *a priori* optimisation and *a posteriori* observation in Section 5.5 by using the point of reattachment as a metric for performance. In this sense, *a priori* refers to the assumption that sensitising a model to DNS data will improve it and *a posteriori* refers to the CFD testing of this assumption. The chapter is closed with a summary in Section 5.6. A list of the created algebraic forms of the anisotropy tensor can be found in Appendix A.

## 5.2 Baseline Model

The RANS model chosen for modification is a slight variant of the SST (Menter, 1994). The SST is known to overpredict the size of recirculation regions making it an ideal target for improvement. For example, the predicted separation bubble for the periodic hills case, used throughout this chapter, is plotted in Fig. 5.2.

The model is very robust and easy to use, the result is ubiquity throughout CFD codes such that modifications presented in this chapter have a reasonable chance of being implementation ready. The baseline<sup>1</sup> model transport equations are,

$$\partial_t k + U_j \partial_{x_j} k = P_k - \varepsilon + \partial_{x_j} [(\nu + \sigma_k \nu_t) \partial_{x_j} k] \quad (5.1)$$

$$\partial_t \omega + U_j \partial_{x_j} \omega = \gamma \frac{\omega}{k} P_k - \beta \omega^2 + \partial_{x_j} [(\nu + \sigma_\omega \nu_t) \partial_{x_j} \omega] + \sigma_d CD_{k\omega}^+. \quad (5.2)$$

The Reynolds stress  $\overline{u'_i u'_j}$  is defined,

$$\overline{u'_i u'_j} = \frac{2}{3} \delta_{ij} k - 2\nu_t S_{ij} + a_{ij}^x, \quad (5.3)$$

where  $a_{ij}^x$ , the extra anisotropy with respect to the linear Boussinesq approximation, is set to zero for the SST. This is the subject of modification via optimisation. Auxiliary relations to close the transport equations are,

$$\begin{aligned} CD_{k\omega} &= \partial_{x_j} k \partial_{x_j} \omega, & CD_{k\omega}^+ &= \max [CD_{k\omega}, 0], \\ \varepsilon &= \beta^* k \omega, & P_k &= -\overline{u'_i u'_j} \partial_{x_j} U_i, \\ \nu_t &= \frac{k}{\omega}. \end{aligned} \quad (5.4)$$

Note the eddy viscosity  $\nu_t$  or production  $P_k$  are not limited as suggested by Menter (1993). This is primarily because the goal is to assess the performance of GEP as a tool for model improvement. As  $a_{ij}^x$  is strongly linked to both, it is the opinion of this author not to obfuscate findings by attempting to give a helping hand.

Finally the coefficients  $\psi$  of the model are blended using the function  $F_1$ , such that  $\psi_1$  is active near the wall and  $\psi_2$  in the far field,

$$\begin{aligned} \psi &= \psi_2 + F_1(\psi_1 - \psi_2), & F_1 &= \tanh(1.5\Gamma^4) \\ \Gamma &= \min \left[ \max \left[ \frac{k^{\frac{1}{2}}}{\beta^* \omega y}, \frac{500\nu}{y^2 \omega} \right], \varphi \right], & \varphi &= \frac{20k}{\max [y^2 CD_{k\omega}, 200k_\infty]}. \end{aligned} \quad (5.5)$$

---

<sup>1</sup>Baseline with respect to modifications to  $a_{ij}^x$ , it does not refer to the BSL-SST model.

The function  $F_1$  is the modified version of Hellsten (2005). The full set of coefficients are,

$$\begin{aligned}\gamma_1 &= 0.518, & \gamma_2 &= 0.44, & \beta_1 &= 0.0747, & \beta_2 &= 0.0828, \\ \sigma_k &= 1.1, & \sigma_{\omega 1} &= 0.53, & \sigma_{\omega 2} &= 1.00, & \beta^* &= 0.09, \\ \sigma_{d1} &= 1.0, & \sigma_{d2} &= 0.4.\end{aligned}\quad (5.6)$$

### 5.3 Methodology

The modified Gene Expression Programming (GEP) environment detailed in Section 4.3 is utilised to regress the tensor  $a_{ij}^x$ . The full anisotropy,

$$a_{ij} = \overline{u'_i u'_j} - \frac{2}{3} \delta_{ij} k \quad (5.7)$$

is calculated from a DNS and serves as training data. The result is then inserted into  $a_{ij}^x$  without any explicit coefficient calibration and the periodic hills case is used as an *a posteriori* test. Therefore a given model for  $a_{ij}^x$  must survive by its own virtue and is not protected via manual modifications. This is the harshest way to test GEP and allows for complete automation of the process.

The reader may be concerned by the consistency issue of regressing  $a_{ij}^x$  with  $a_{ij}$ . This is perceived as the most practical and simple method, because  $S_{ij}$  from DNS is not aligned with  $a_{ij}$  which results in the regression being overly sensitised to the strain and not the anisotropy of turbulence. Using  $S_{ij}$  in the Eq. 5.3 at all is an artifact of two-equation models assuming a linear approximation in their derivation and therefore must be included in the modified Reynolds stress tensor. Failure to do so strongly increases the likelihood of divergence in *a posteriori* testing. It should be noted however, that in preliminary tests to confirm this statement, GEP often found models of the form  $a_{ij} = -C\nu_t S_{ij} + \dots$  where  $C$  is constant and approximately 2.  $a_{ij}^x$  is necessarily traceless and by sensitising it to the DNS  $a_{ij}$ , the total turbulent kinetic energy is unchanged and the model acts as a further redistribution of this energy.

Models for  $a_{ij}^x$  are built assuming,

$$a_{ij} = a_{ij}(k, \varepsilon, S_{ij}, \Omega_{ij}), \quad (5.8)$$

following the analysis of Pope (1975), a starting point for deriving Explicit Algebraic Stress Models. This is equivalent to an implicit assumption of the weak equilibrium hypothesis (Rodi, 1972, 1976) in the regression. Normally this would imply bad prediction in strong convection regions because the material derivative is lost, but GEP does not care about physics and suitable training data would circumvent this weakness.

Pope (1975) derives a linearly independent basis for  $a_{ij}$  through the Cayley-Hamilton theorem and assuming a functional dependence on  $S_{ij}$  and  $\Omega_{ij}$  only. For this study the first four are used along with the two scalar invariants,

$$\begin{aligned} T^1 &= S_{ij} & T^2 &= S_{ik}\Omega_{kj} - \Omega_{ik}S_{kj} \\ T^3 &= S_{ik}S_{kj} - \frac{1}{3}\delta_{ij}S_{mn}S_{nm} & T^4 &= \Omega_{ik}\Omega_{kj} - \frac{1}{3}\delta_{ij}\Omega_{mn}\Omega_{nm} \\ I^1 &= S_{mn}S_{nm} & I^2 &= \Omega_{mn}\Omega_{nm}, \end{aligned} \quad (5.9)$$

this implies resulting models are quadratic in tensor products.

To preserve physical dimensions in models for  $a_{ij}^x$ , all variables must be non-dimensional.  $a_{ij}$  is divided by  $k$  and each instance of the velocity gradient is multiplied by  $2\beta^*\tau = 0.18k/\varepsilon$ . The coefficient for gradient non-dimensionalisation is chosen such that when re-multiplying through by  $k$ , the eddy viscosity falls out and the optimisation is at least given a chance of producing terms with the right magnitude.

### 5.3.1 Training Data

The mean quantities of a DNS<sup>2</sup> of the backward facing step geometry are chosen as inputs to the process. The Reynolds number based on step height  $H$  is  $\text{Re}_H = 3000$ . Equation 5.7 and Eq. 5.9 are calculated along the profile  $x/H = 5.7$  — see Fig 5.1. At the selected location  $\overline{v'v'} \sim \overline{u'u'}$  and a successful regression should pick up on the evident curvature effects.

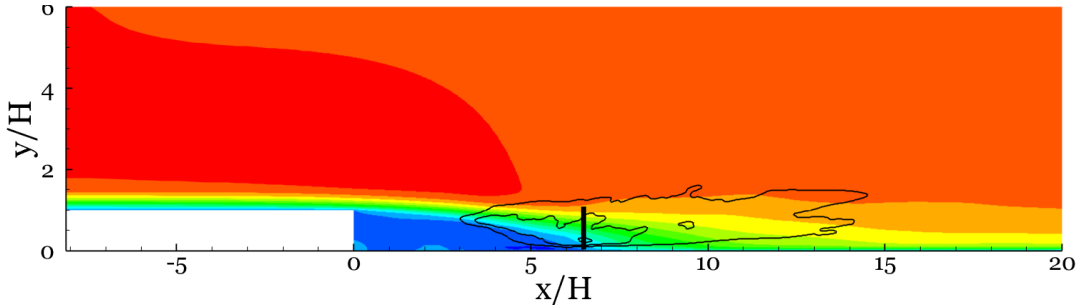


FIGURE 5.1: Training data location from DNS. Filled by mean streamwise velocity  $U$ , lines are the ratio of  $v^{\text{rms}}/u^{\text{rms}}$  (contour levels : 0.4, 0.6, 0.8).

This case is ideal for a DNS-RANS comparison. Parneix et al. (1996) highlighted the good agreement of the RANS  $\varepsilon$  — and by association  $\omega$  — with the DNS quantity. The backward facing step is therefore a good test case as no treatment of the DNS quantities is required in order to make them consistent with a RANS prediction. This is not in general true and relaxation of DNS quantities is necessary (Dow and Wang, 2011; Duraisamy and Durbin, 2014).

<sup>2</sup>Courtesy of Javier Otero, University of Southampton.

### 5.3.2 *A Posteriori* Test Case

In order to test the efficacy of GEP it is vital to actually use created models as predictive tools. The similar, yet crucially different, periodic hills geometry is chosen to validate the methodology. The flow travels over a series of continuously differentiable constrictions, or ‘hills’ in a two dimensional channel. The separation from a curved surface is inherently unsteady, induced via the action of the adverse pressure gradient, with the instantaneous point of zero wall shear stress fluctuating significantly along the domain (Fröhlich et al., 2005). Once the flow reattaches, the upstream side of each hill offers a strong favourable pressure gradient. This flow regime is markedly different from the training data and the ability of each  $a_{ij}^x$  can be observed in off-design conditions.

The unsteadiness of the separation line has implications in the shear layer; generally, additional large structures of a turbulent nature, often periodic, are present which increases mixing and thus reduces the reattachment length (Jakirlić et al., 2002). This unsteady nature of the flow field is a particular challenge to RANS modelling; indeed flows of a similar type (Rodi et al., 1995) are poorly and inconsistently captured by such techniques; even the same closure exhibits a wide range of performance for different geometries (Jang et al., 2002; Manceau and Bonnet, 2003; Wang et al., 2004). A full spectrum of RANS closures were applied to the periodic hills case for the 9th (Jakirlić et al., 2002) and 10th (Manceau and Bonnet, 2003) ERCOFTAC-SIG15 workshops. A wide range of reattachment lengths were reported ranging from severe overpredictions to moderate underpredictions. The large structures missing in the shear layer resulted generally in too long reattachment regions. The shear stress component was almost ubiquitously underpredicted, along with the overall turbulent kinetic energy. In the worst cases the reattachment was not accounted for by the model at all, with the flow reattaching on the upstream side of the next hill. In this case, the separation region is too long by at least 58%.

The LES of Temmerman and Leschziner (2001), denoted here as LES-TL, serves as reference data. The mean streamlines are plotted for the Spalart and Allmaras (1992), SST and SSG (Speziale et al., 1991) models in Fig. 5.2. The latter is a cubic Explicit Algebraic Stress Model, to highlight that additional terms do not necessarily correspond to improved performance. The streamlines are compared with an FSM simulation (Weatheritt and Sandberg, 2015) that closely matches the reference LES-TL.<sup>3</sup>

The Reynolds Number, based on hill height  $H$  and averaged bulk velocity  $U_b$  from hill crest to upper surface is  $\text{Re} = 10'595$ . Streamwise periodic boundary conditions are imposed, with a pressure gradient to ensure the correct mass flow rate. The grid, displayed in Fig. 5.3, consists of  $120 \times 130 = 15'600$  cells. Plots of  $y^+$  and grid convergence (using a mesh of 27'000 cells) are shown in Fig. 5.4. The initial condition is calculated from the converged solution for the SST model ( $a_{ij}^x = 0$ ) described in Section 5.2. Each

---

<sup>3</sup>Data in the  $x$ - $y$  plane is not available for LES-TL.

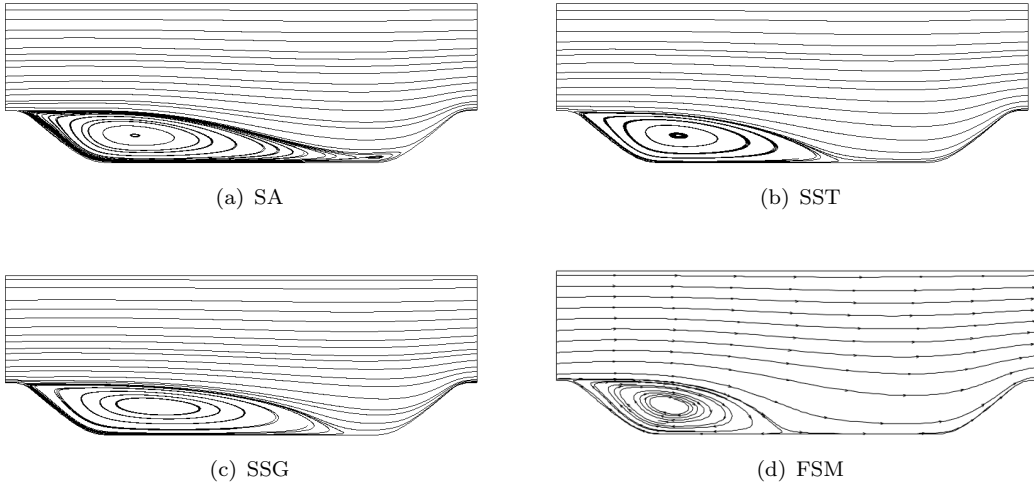


FIGURE 5.2: Streamlines for RANS closures, compared to Hybrid RANS/LES.

model is run for 500 time units  $H/U_b$ . Time convergence is shown in Fig. 5.4. Both convergence studies and  $y^+$  are shown using Eq. A.1, the first model for  $a_{ij}^x$ .

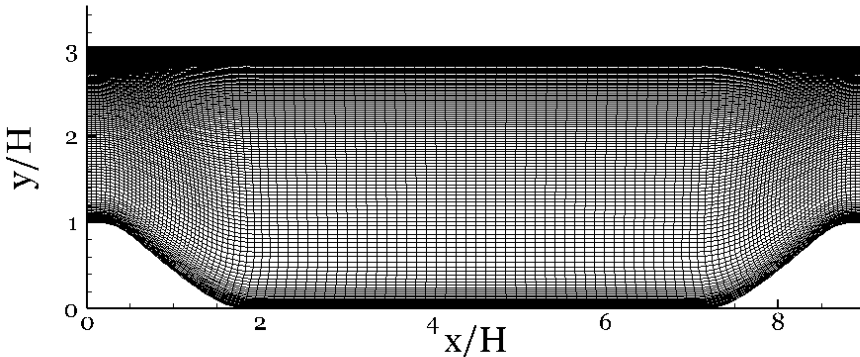


FIGURE 5.3: Computational grid.

### 5.3.3 *A Priori* Optimisation

All parameters for the GEP optimisation are listed in Table 5.1. A head length  $h_{3D} = 3$  is such that the longest possible tensor phenotype is 36. This number can grow as individuals include plasmid scalar fields into their expression, which have the upper bound of 24 on their phenotype.

The bounds on random constants ( $r_{\min}$ ,  $r_{\max}$ ) dictate a possible magnitude of 0.2, as this is close to  $2\beta^*$ , individuals can play with constants similar to the initial rescaling. To complement, 1 and 0.01 are made explicitly available such that the magnitude can be overridden, either by addition of 1 or multiplication with 0.01. This allows coefficients ranging three orders of magnitude, but higher orders are difficult to obtain.

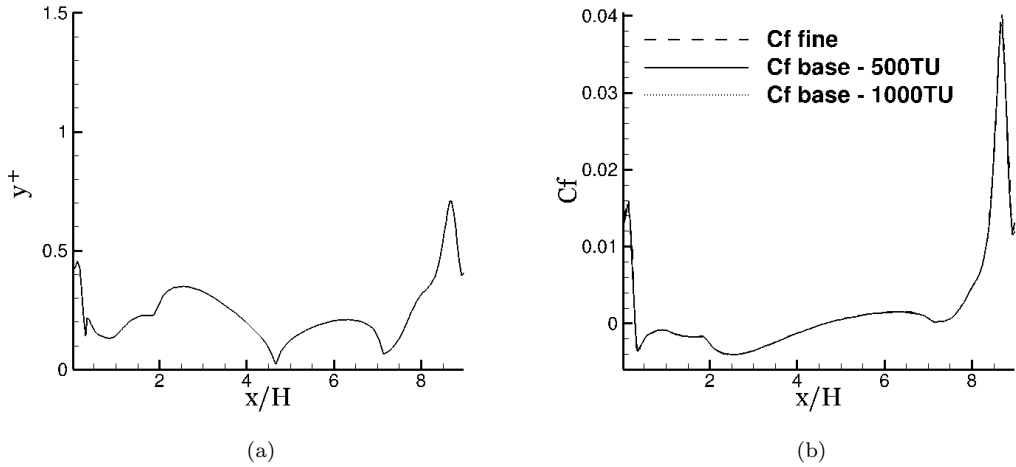


FIGURE 5.4: First cell centre wall distance  $y^+$  (left). Grid and time convergence of the skin friction along the lower surface  $C_f$ . TU denotes time units  $H/U_b$ .

Parameter	Value	Notes
$N$	200	Population size
$n$	300	Number of generations
$n_{g3D}$	3	number of genes in 3D chromosome
$n_{g1D}$	2	number of genes in plasmid chromosome
$h_{3D}$	3	head length in 3D gene
$h_{1D}$	3	head length in plasmid gene
$r_{\min}$	-0.2	random constant minimum
$r_{\max}$	0.2	random constant maximum
$s$	2	tournament size
$\mathcal{T}$	$T_{ij}^1, T_{ij}^2, T_{ij}^3, T_{ij}^4, P$	3D chromosome terminal set
$\mathcal{T}_{1D}$	$I^1, I^2, ?, 1.0, 0.01$	1D chromosome terminal set: ? is a random constant
$\mathcal{F}_{3D}$	$+, -, P$	3D chromosome function set: $P$ is plasmid arity one symbol
$\mathcal{F}_{1D}$	$+, -, \times$	plasmid chromosome function set
$p_m$	0.05	probability of mutation
$p_{tr_g}$	0.001	probability of root gene transposition
$p_{ris}$	0.001	probability of root insertion sequence transposition
$p_{is}$	0.001	probability of insertion sequence transposition
$p_{tr_p}$	0.005	probability of sequence translation
$p_{tr}$	0.001	probability of entire gene translation
$p_{inv_p}$	0.005	probability of sequence inversion
$p_{in}$	0.005	probability of entire gene inversion
$p_{r1}$	0.65	probability of one-point recombination

TABLE 5.1: Values of all parameters used in GEP optimisation.

Inversion and translation are powerful genetic operators, so their probability is reasonably high. To compensate for this, the probability of recombination is reduced from the standard 0.7. The population is reasonably small to keep simulation time down, therefore the tournament size is small to prevent premature convergence.

The objective function, or fitness of an individual  $P_i^j$ , is defined

$$f(P_i^j) = \frac{a_{mn}^{DNS} a_{nm}^{GEP/DNS}}{(a_{pp}^{DNS})^{1/2} \cdot (a_{qq}^{GEP/DNS})^{1/2}}, \quad (5.10)$$

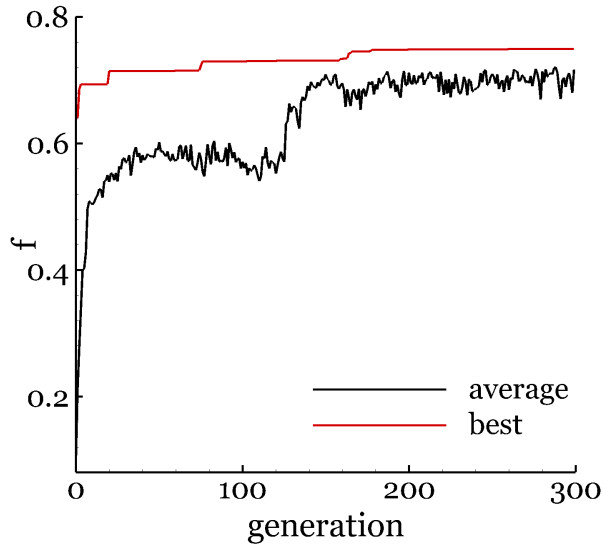
which is bound between -1, complete misalignment and 1, complete alignment.  $a_{ij}^{DNS}$  is the raw DNS anisotropy and  $a_{ij}^{GEP/DNS}$  is a model for anisotropy (an individual's phenotypic expression) evaluated using the DNS. The higher the value of Eq. 5.10 for an expression, the better it is deemed to be and the more probable it will survive in the evolutionary optimisation.

The optimisation is run 50 times and the best closure for  $a_{ij}^x$  is recorded from the final generation  $n = 300$ , denoted  $P_n^j$ ,  $j = 1, \dots, 50$ . Simple elitism is applied to ensure the best individual is immutable. The phenotypic output, simplified into representative equations, for  $a_{ij}^x/k$  is found in Appendix A. The superscript  $\tau$  denotes a scaling with  $2\beta^*k/\varepsilon$ . To use an expression in Eq. A.1-A.50, first multiply by  $k$  and insert into Eq. 5.3.

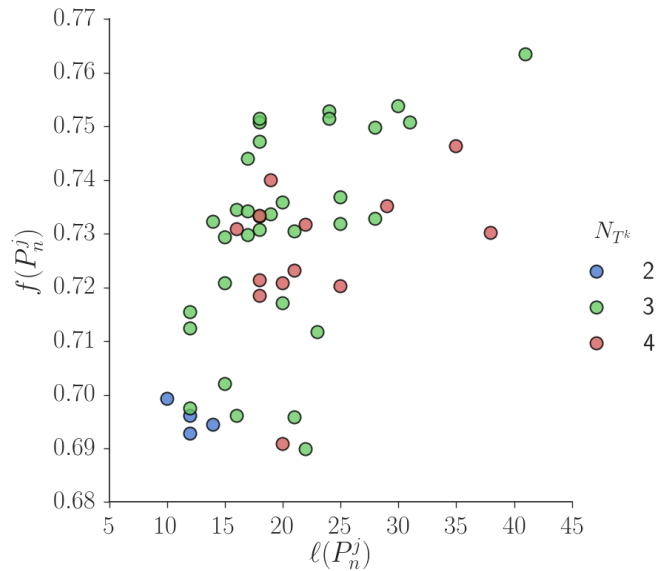
A typical fitness versus generation plot is displayed in Fig. 5.5. This particular run is for the output Eq. A.2. There are 15 increases in best fitness that span a range of only  $\sim 0.1$ . This seems like a small window, however we should not expect a linear response to the entire range of possible values of Eq. 5.10 and this is confirmed in Section 5.5. The average fitness fluctuates heavily as new individuals are created and the large increase in average fitness after 100 generations is probably due to the best individual propagating through the population. This kind of explosion is detrimental to the evolutionary system and as such we do not see many more major improvements as the population begins to converge.

Figure. 5.6 is a plot of the fitness of the 50 final solutions  $f(P_n^j)$  against the length of the simplified expression  $\ell(P_n^j)$ . The length is incremented by 1 for every symbol,  $\times, +, -, T_{ij}^k, I_{ij}^k, \dots$ . Only brackets do not contribute to this score. Each model is coloured by the number of distinct tensors  $N_{T_k}$  appearing in their expression. There is a strong correlation between the length and fitness of a model, yet the colouring shows that using the full basis set can be detrimental. Rarely a model only includes two of the tensor bases as the phenotype is highly truncated and these models are amongst the least fit.

The fitness and length of an individual given it uses symbol  $S^k$  is plotted in Fig. 5.7, where the boxes delimit the 25% and 75% quartiles, the median is also shown and the scatter is individual data points. Unsurprisingly the scalars  $I^k$  appear in longer

FIGURE 5.5: Typical plot of population and best fitness  $f$ .

equations — the inclusion of scalars necessarily increases the possible length.  $T_{ij}^4$ , which depends only on the rotation rate, lowers the fitness somewhat generally appearing in marginally shorter individuals. This hints at an incompatibility, at least in the regression process, with the first three — this is possibly because  $T_{ij}^4$  is the first tensor not linearly independent in two dimensional flow. The other tensor bases appear to have very similar performance.

FIGURE 5.6: Individual  $P_n^j$  fitness  $f$  against expression length  $\ell$ , coloured by the number of distinct tensor bases  $N_{T^k}$ .

Finally, a comment is made about the efficiency of the algorithm. Clearly, there is a probability of finding fit solutions completely by random. In order to persuade the reader that ‘evolution’ is indeed taking place, Fig. 5.8 is a histogram of the fitness of

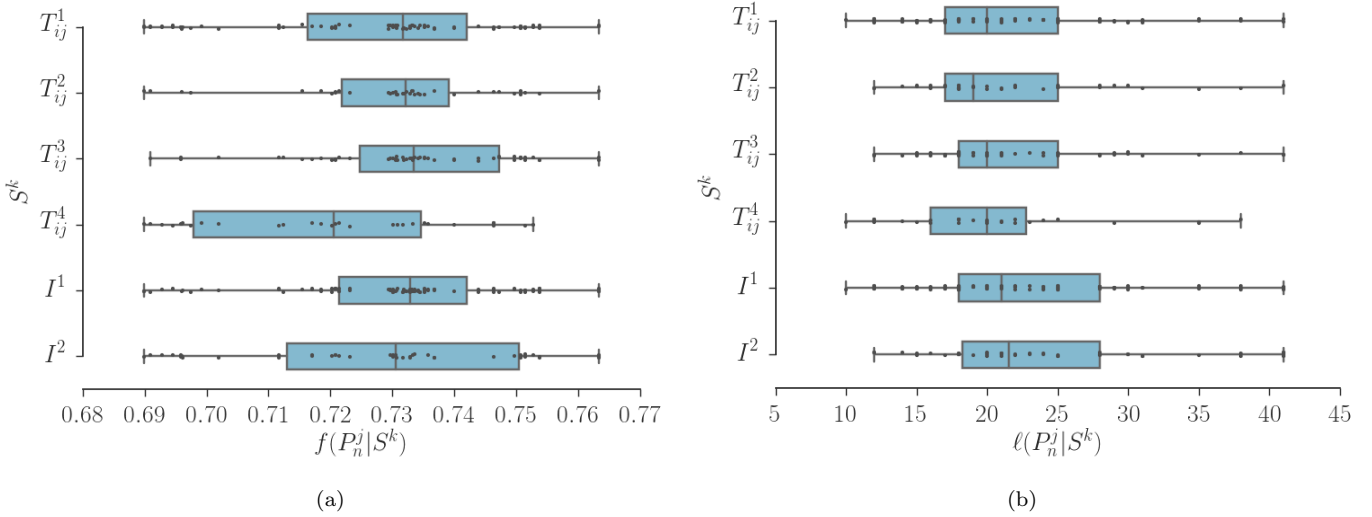


FIGURE 5.7: Effect of terminal  $S^k$  on individual  $P_n^j$  fitness  $f$  and length  $\ell$ .

randomly generated individuals. The same GEP chromosome is utilised to avoid the tedium of invalid solutions and make the comparison fair. The green bar is the region of the 50 best solutions obtained by GEP as a comparison. As the reader can see, there is an overlap between blue and green implying that fit solutions can be found by chance. Yet the number of evaluations required increases by 3 orders of magnitude. In 300'000 random individuals, one was better than the median GEP solution. The strong peaks in the histogram plot are made up of simple linear combinations of three tensor bases only, an artifact of  $n_{g3D} = 3$ .

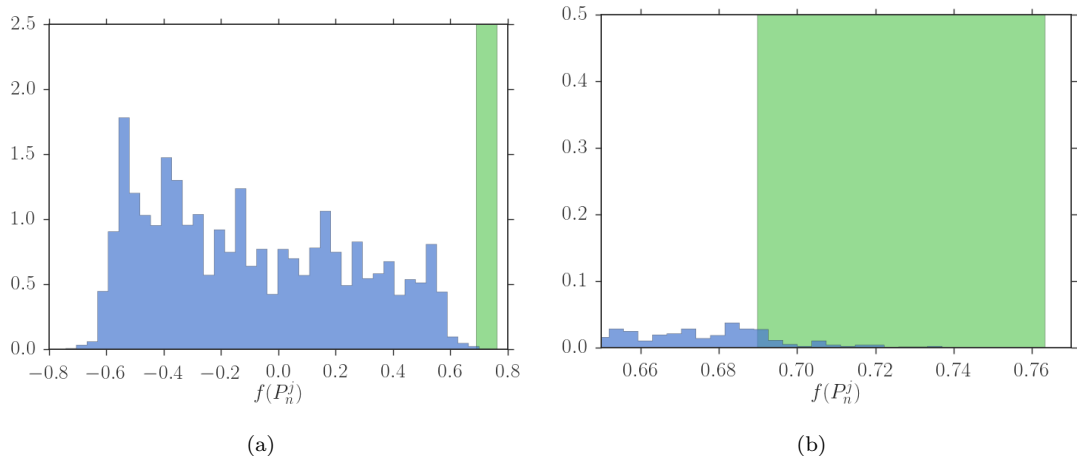


FIGURE 5.8: Normalised histogram of the fitness of chromosomes obtained completely at random. Green band is a normalised histogram of the best solutions from GEP (y-axis extends to 24.5). Left: full fitness domain. Right: closeup of highest values of fitness.

## 5.4 A Posteriori Results

Of the fifty models, Eq. A.1-A.50, none diverged when applied to the setup described in Section 5.3.2, although there is a known small chance of divergence. The ensemble skin friction of every model along with a 99% confidence interval is plotted in Fig. 5.9. The reverse flow region is remarkably predicted, with the small confidence interval showing a similar performance by each model. Compare this with the report by Jakirlić et al. (2002), which shows in general poor agreement and a high variation between existing closures. The crest of the hill is largely overpredicted, but this is quickly forgotten as the flow convects downstream. The ensemble reattachment point is  $x = 4.806/H$ , with a standard deviation of 0.2955. This is an error in the point of zero skin friction  $C_f^{err}$ , when compared to LES-TL, of 1.8%. This error is smaller than the difference between the reference LES simulations of Temmerman and Leschziner (2001); Fröhlich et al. (2005); Breuer et al. (2009). Over the baseline model, each anisotropy tensor produced by GEP reduced the error in reattachment point by approximately 94%.

Profiles of streamwise velocity and Reynolds stress along the domain are plotted in Figs. 5.10-5.18. The stress components are labelled in Fig. 5.10 and the other locations match this labelling. Each of the largest peaks are the streamwise normal component, the exception to this is the GEP profile at  $x/H = 8.0$ . Here the inner peak is  $\overline{u'u'}$  and the bigger outer peak is  $\overline{v'v'}$ , in contrast to the reference LES.

Small confidence interval bars in velocity indicate that despite each model has a different formulation of  $a_{ij}^x$ , the velocity is uniformly predicted well. Understandably the Reynolds stress has a wider confidence interval, most prominently seen in the  $\overline{u'u'}$  component. All models underpredict  $\overline{u'u'}$  where the unsteady content in the free shear layer is missed by the steady closure. The shear-stress  $\overline{u'v'}$  predicted by each model in the reverse flow region, a known issue with RANS (Jakirlić et al., 2002), is excellent. A similar sentiment can be expressed regarding the wall-normal stress.

The evolutionary algorithm is trained on an adverse pressure gradient whilst the region  $x/H > 6.0$  is a strong favourable pressure gradient. This region is predicted very poorly, the shear stress is approximately three times too large. At the location  $x/H = 8.0$ ,  $\overline{v'v'} > \overline{u'u'}$  in the bulk region. The consequence of these facts is a high probability of non-realisability exhibited by both the Cauchy-Schwarz inequality and negative stress. Contours of the probability density function for the violation of these realisability constraints are plotted in Fig. 5.19. Despite a 70% chance of negative  $\overline{u'u'}$ , the magnitude is only 6% of the profile maximum. This departure from the reference indicates a moderate sensitivity to the training data and supports the notion of future models being trained simultaneously on different flow types or being utilised only locally on complex geometries.

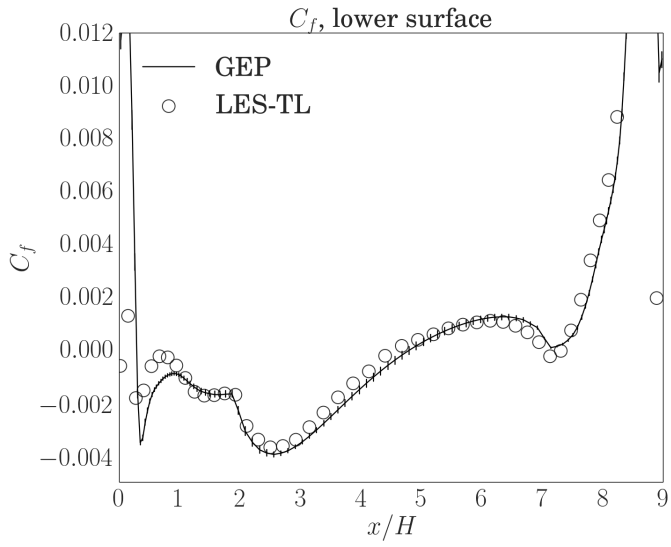


FIGURE 5.9: Ensemble skin friction coefficient  $C_f$ . Bars are 99% confidence interval.

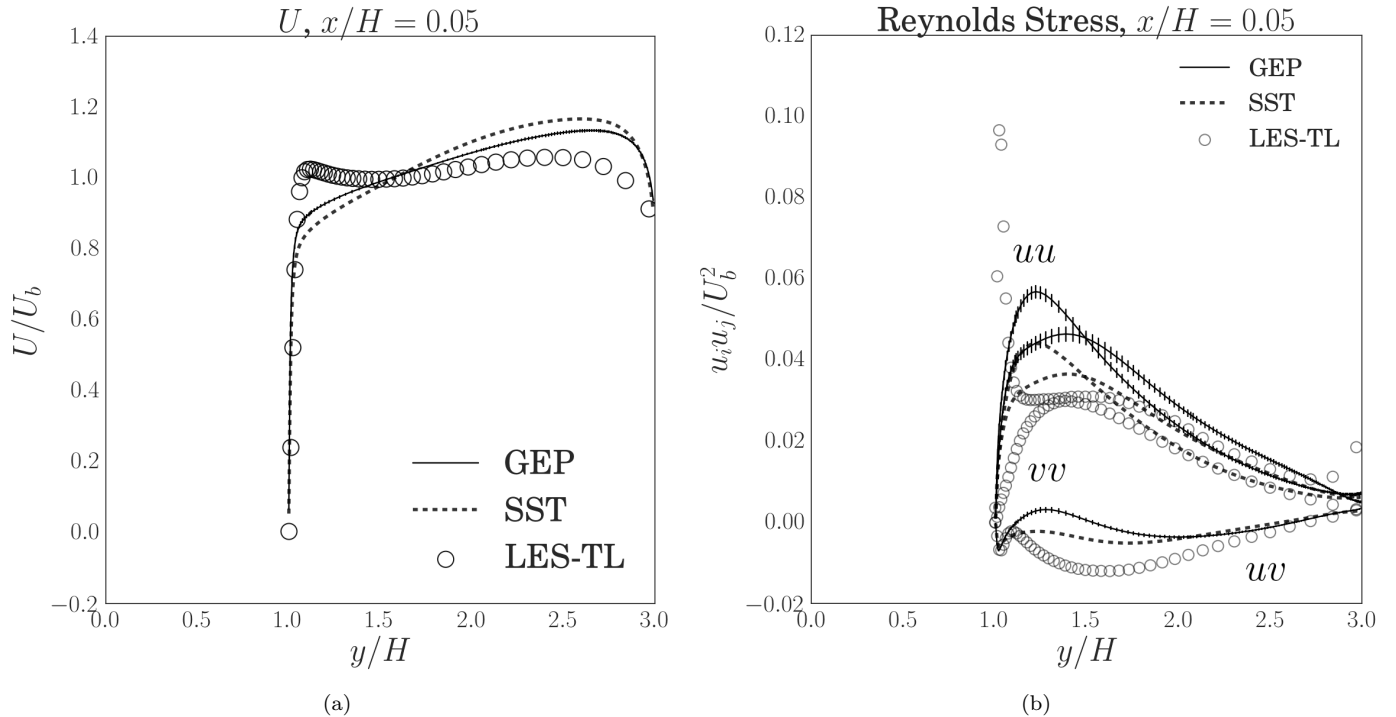


FIGURE 5.10: Ensemble velocity and Reynolds-stress at  $x/H = 0.05$ , bars represent 99% confidence interval. Each stress component is labelled, the highest peak of each modelled line is  $\overline{u'u'}$ .

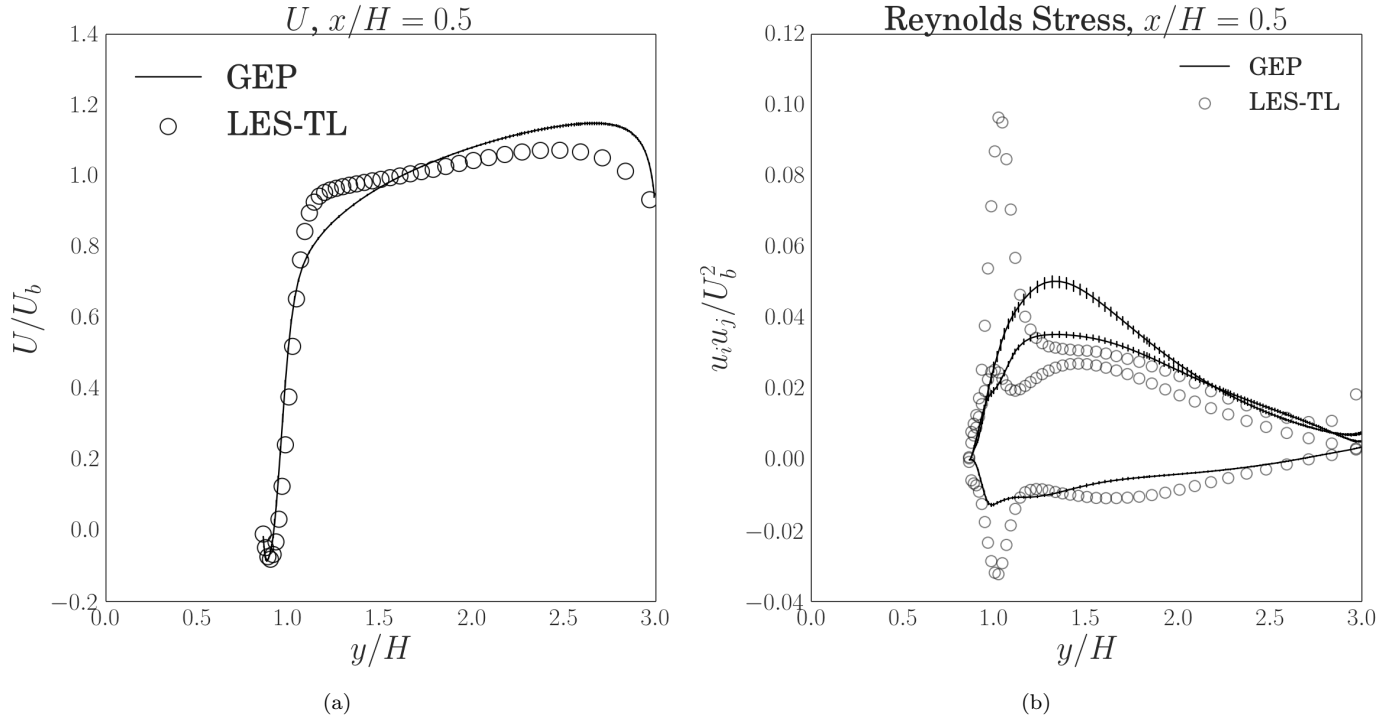


FIGURE 5.11: Ensemble velocity and Reynolds-stress at  $x/H = 0.5$ , bars represent 99% confidence interval.

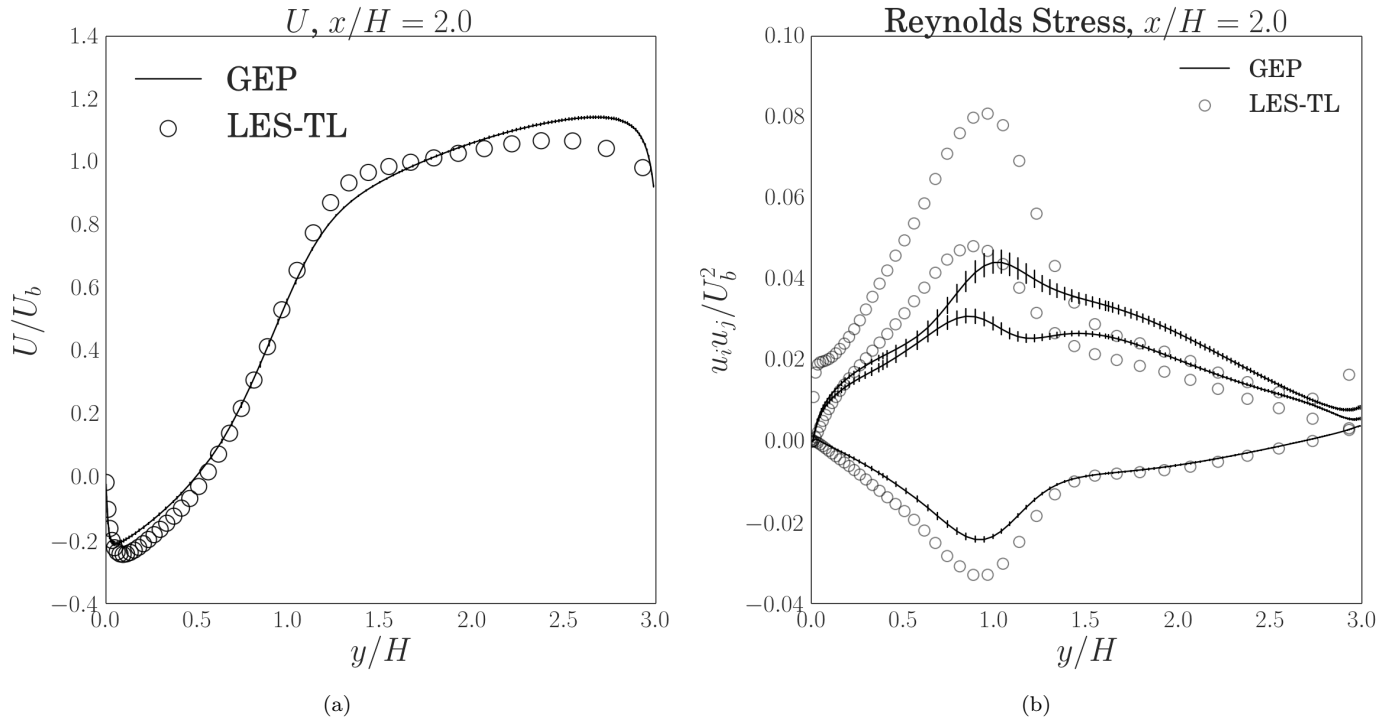


FIGURE 5.12: Ensemble velocity and Reynolds-stress at  $x/H = 2.0$ , bars represent 99% confidence interval.

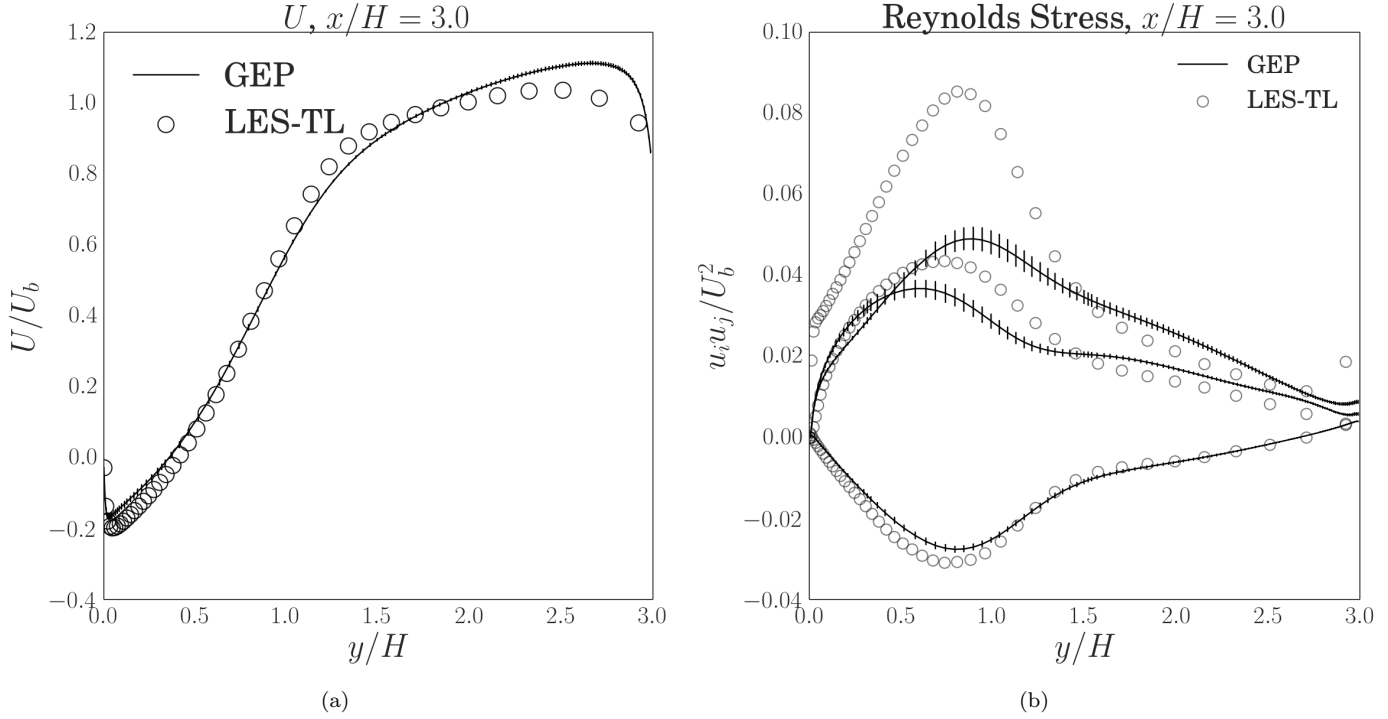


FIGURE 5.13: Ensemble velocity and Reynolds-stress at  $x/H = 3.0$ , bars represent 99% confidence interval.

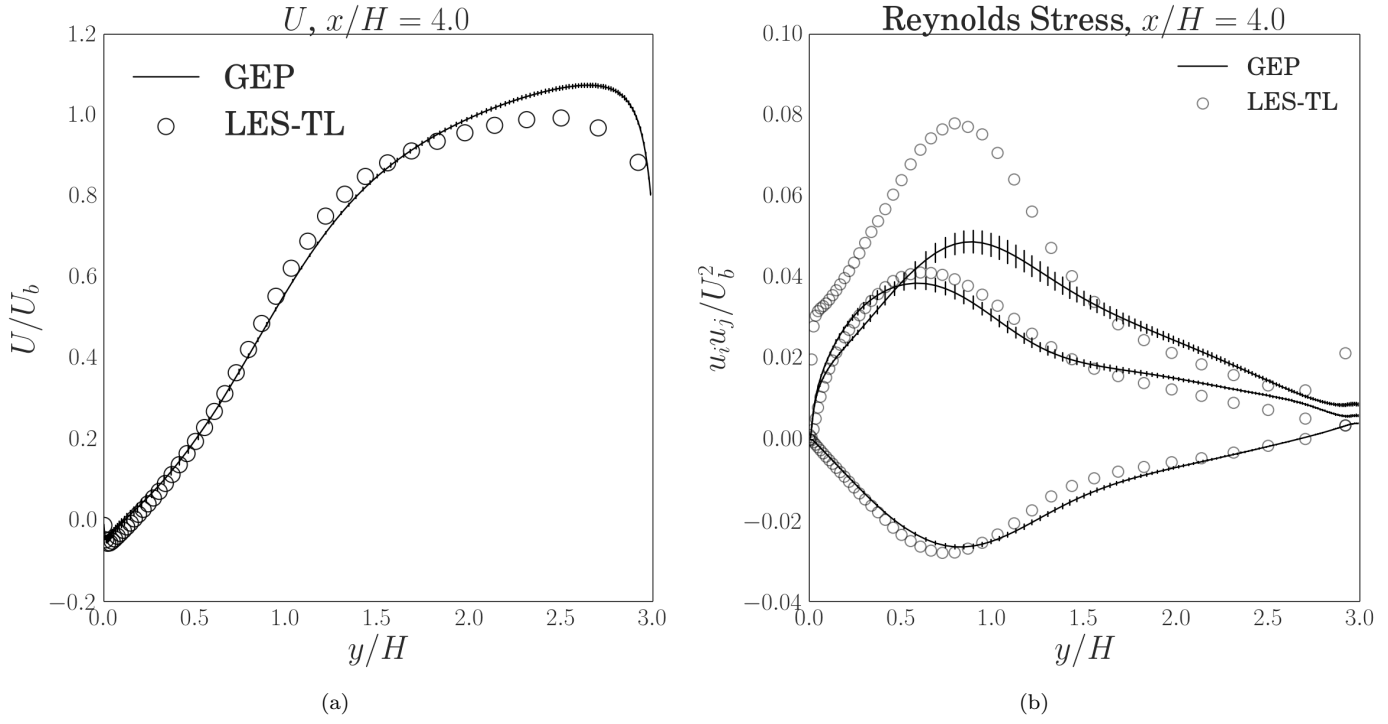


FIGURE 5.14: Ensemble velocity and Reynolds-stress at  $x/H = 4.0$ , bars represent 99% confidence interval.

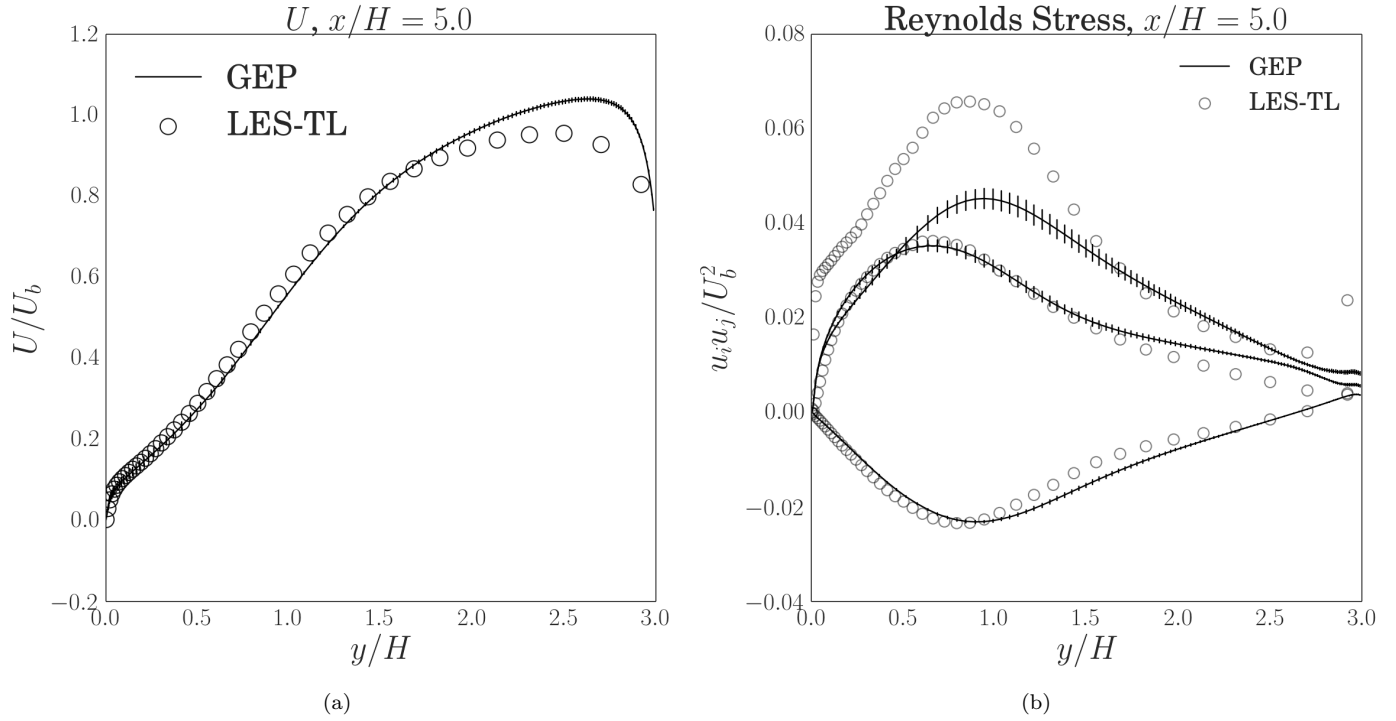


FIGURE 5.15: Ensemble velocity and Reynolds-stress at  $x/H = 5.0$ , bars represent 99% confidence interval.

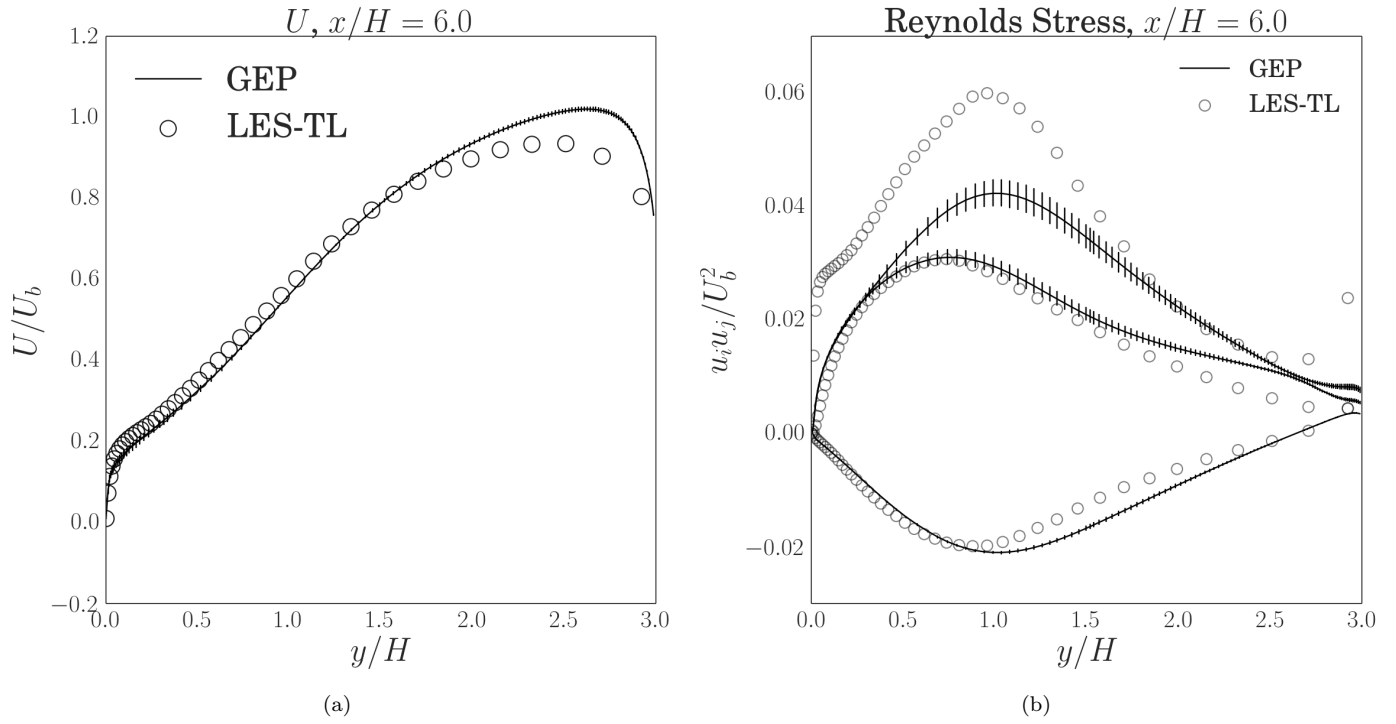


FIGURE 5.16: Ensemble velocity and Reynolds-stress at  $x/H = 6.0$ , bars represent 99% confidence interval.

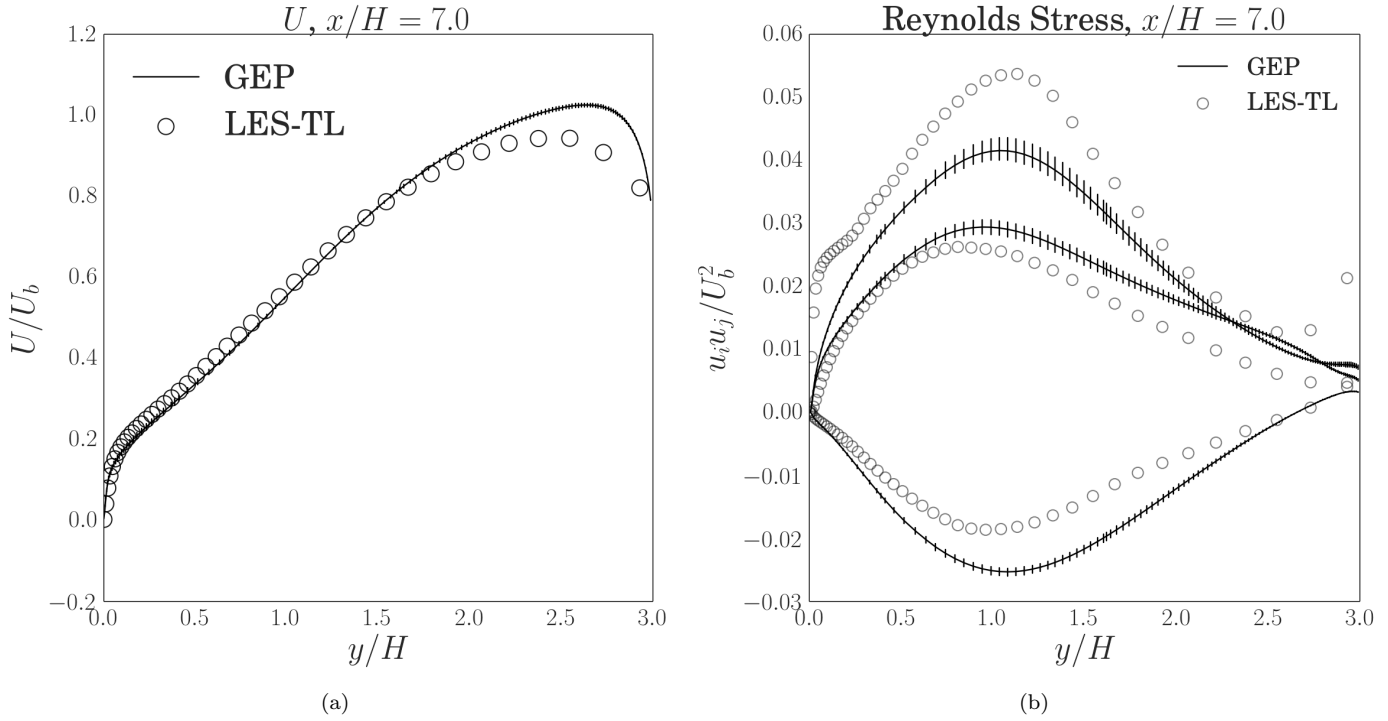


FIGURE 5.17: Ensemble velocity and Reynolds-stress at  $x/H = 7.0$ , bars represent 99% confidence interval.

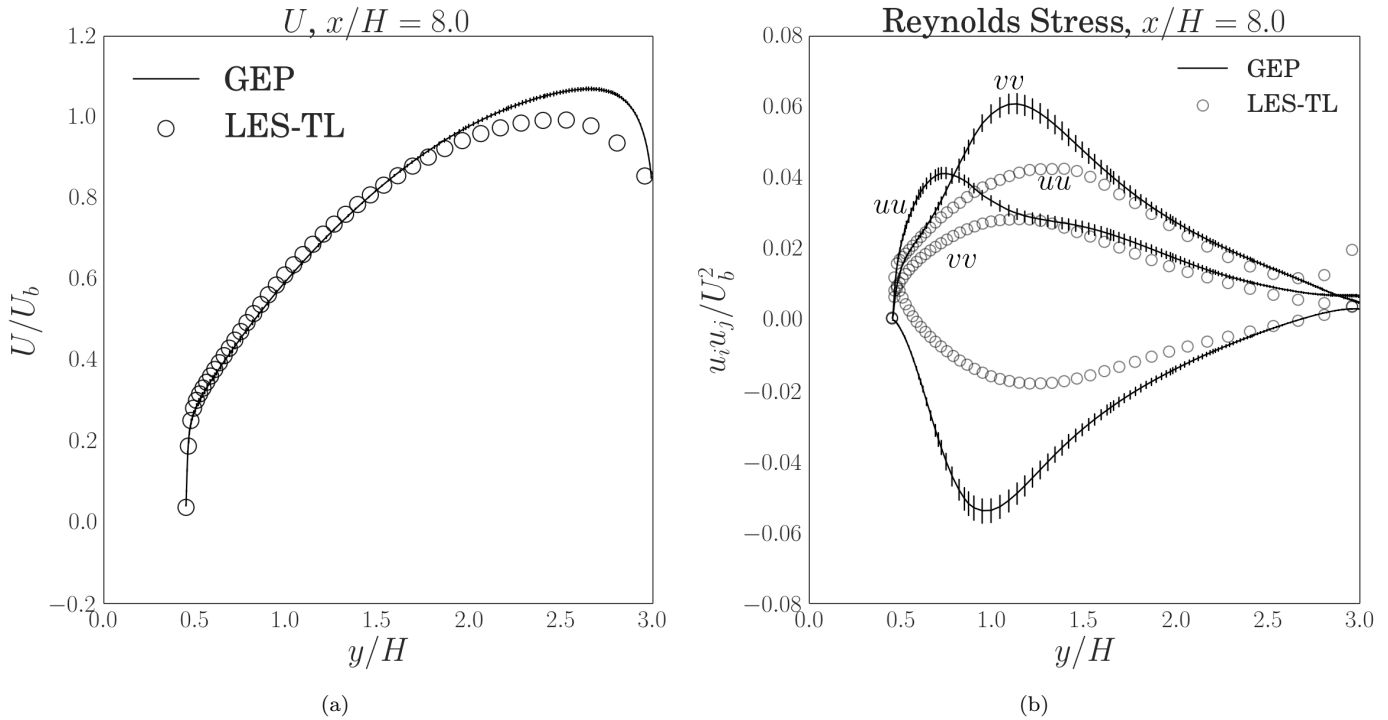


FIGURE 5.18: Ensemble velocity and Reynolds-stress at  $x/H = 8.0$ , bars represent 99% confidence interval. Notice the labelled switch between the normal stress component magnitudes.

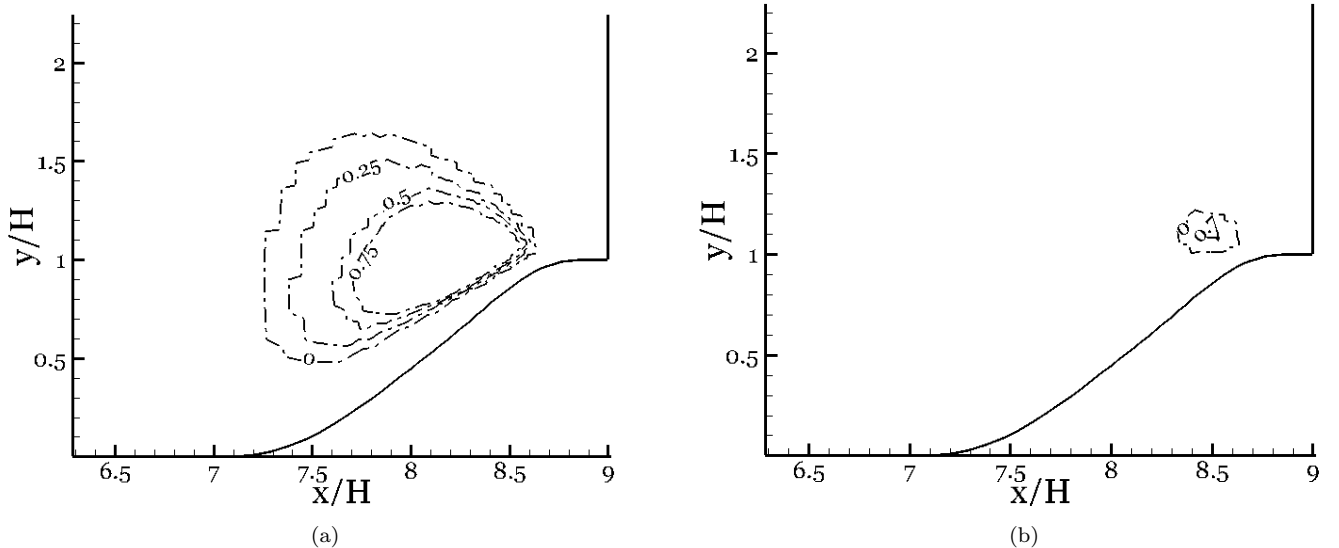


FIGURE 5.19: Probability density function for breaking realisability,  $\bar{u}'v' < \bar{u}'u' \cdot \bar{v}'v'$  (contour levels : 0.0, 0.25, 0.5, 0.75) (left) and  $\bar{u}'u' < 0$  (contour levels : 0.0, 0.7) (right).

## 5.5 The Link Between the Two Environments

The relationship between *a priori* optimisation and *a posteriori* result is vital for the novel GEP process to be taken seriously. This section comprehensively concludes that GEP is successfully training model anisotropy tensors and *crucially*, the better the algorithm performs, the better the model is as a predictive tool on a similar flow type. Further, it is shown that GEP can be used as a tool for analysis. By establishing a relationship between Eq. 5.10 and *a posteriori* performance, one can then look at the performance of existing closures or terms within closures.

The metric for *a posteriori* performance is the error in the point of zero skin friction  $C_f^{err}$  for each model  $P_n^j$ .  $C_f^{err}(P_n^j)$  is easy to calculate and is a global quantity that strongly depends on global solution quality making it an ideal indicator.

Figure 5.20 is a plot of  $C_f^{err}$  against the fitness, Eq. 5.10, of each  $P_n^j$ . Also included is a linear regression<sup>4</sup> and the residuals when removing this regression line. The error in the linear model is reasonably uniform in  $f$ , producing reasonable confidence in interpretations. The p-value of non-zero Pearson correlation coefficient ( $r = -0.4$ ) is 0.043, suggesting that at a 95% significance level we can accept the negative correlation. The conclusion is a higher alignment of an anisotropy tensor  $a_{ij}^x$  with the DNS anisotropy, the higher chance of better prediction of similar flow fields. Equation 5.10 is therefore

<sup>4</sup>The irony of using linear regression to evaluate a more complex regression tool is not lost. However for this application linear regression suffices.

a good objective function for GEP and the better the algorithm can perform, the more useful the model is for a similar flow field. In the regression, there is one clear outlier, with the worst fitness and reattachment error. This is Eq. A.39, which is highly non-linear by its use of the scalar invariants and contains the harmful  $T_{ij}^4$  term. Note, this model is still better than the baseline. For reference, the most successful model *a posteriori* (Eq. A.36) is not the best model *a priori* (Eq. A.3).

Figure. 5.21(a) is a linear regression of the number of distinct tensors  $N_{T_k}$  in the phenotype as a predictor of  $C_f^{err}(P_n^j)$ . Note that for  $N_{T_k} = 2$  there are only 4 data points, so this value has not influenced the regression line. The line shows that if the model uses all available tensors, then the error in reattachment position for the periodic hills is larger. This is probably just because the model is using the detrimental  $T_{ij}^4$  symbol and extrapolations of this regression line are unlikely to be of any use. Figure 5.21(b) shows the detrimental effect of  $T_{ij}^4$  on  $C_f^{err}$ . Each box is a 25-75% quartile box plot with the dividing line the median. This plot of reattachment error for each individual given it contains the input symbol  $S^k$  can be compared with Fig. 5.7(a). Both plots largely arrive at the same conclusions meaning that the relationship between *a priori* fitness and *a posteriori* prediction extends beyond individual equations to each input variable  $S^k$ . This allows GEP to be used as a tool to make predictions about terms in equations. Whilst the rank ordering of the median  $C_f^{err}$  and  $f(P_n^j|S^k)$  values are preserved, the relative quartile sizes between the scalars  $I^k$  and  $T_{ij}^2$  with the other tensors are not. It would be interesting to increase the number of models to see if this disparity vanishes or whether outliers are always to be expected.

Finally, a multiple linear regression plot of  $C_f^{err}$  against  $f$  for each tensor  $T_{ij}^k$  is shown in Fig. 5.22. Each line is a linear regression of the models containing the indicated basis. Hollow circles mark the 50 individuals and colours contained within show the tensors used by each. The tensor  $T_{ij}^2$  is shown to be most strongly linked *a priori* and *a posteriori*, whilst  $T_{ij}^4$  is very unconvincing. Fig. 5.22 shows that the variance of  $C_f^{err}(P_n^j|T_{ij}^4)$  in Fig. 5.21(b) is down to noise, but for the other  $T_{ij}^k$  it can be largely attributed to individual fitness  $f$  in Fig. 5.7(a).

## 5.6 Summary

In this chapter Gene Expression Programming has been explored as a tool to create algebraic expressions for the anisotropy tensor of Reynolds stress. Evidence has been presented to support its use as a methodology for assisting in the development of RANS models. It should be said that claims in this chapter apply to a particular flow field using a particular training set and should not be generalised to arbitrary cases. However these modest steps towards applying machine learning to turbulence closures have proven promising.

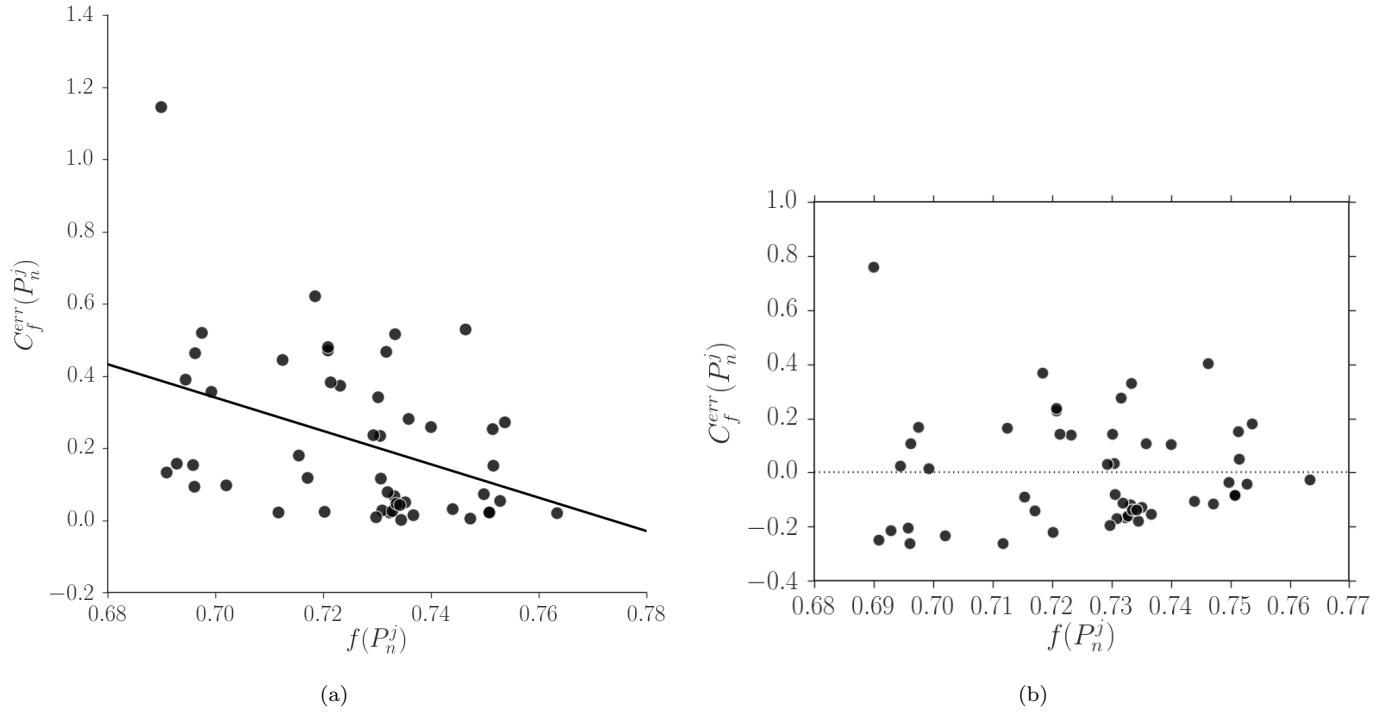


FIGURE 5.20: Linear regression of individual fitness  $f(P_n^j)$  as a predictor for error in reattachment location  $C_f^{err}(P_n^j)$  (left) and residual plot for regression.

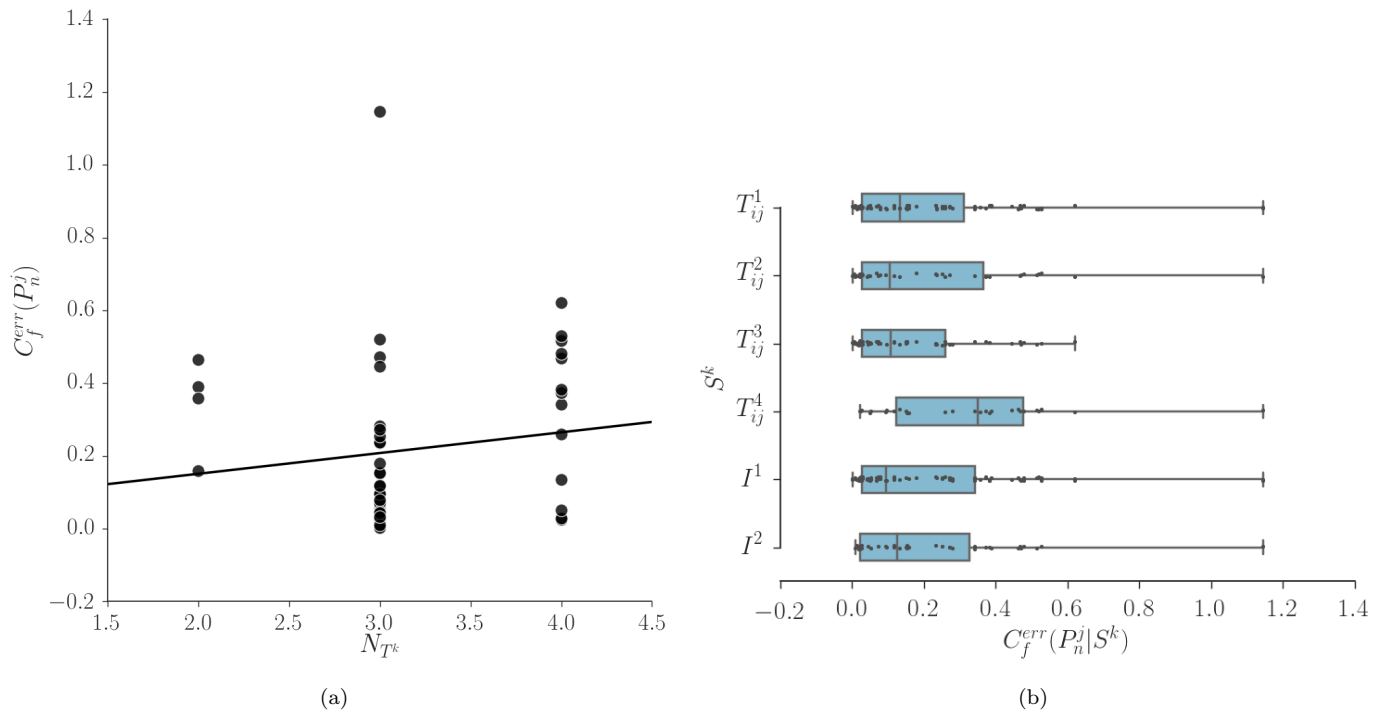


FIGURE 5.21: Linear regression of the number of distinct tensors  $N_{T_k}$  in individual  $P_n^j$  as a predictor for error in reattachment location  $C_f^{err}(P_n^j)$  (left). Influence of symbol  $S^k$  on an individuals skin friction coefficient  $C_f^{err}(P_n^j)$  (right).

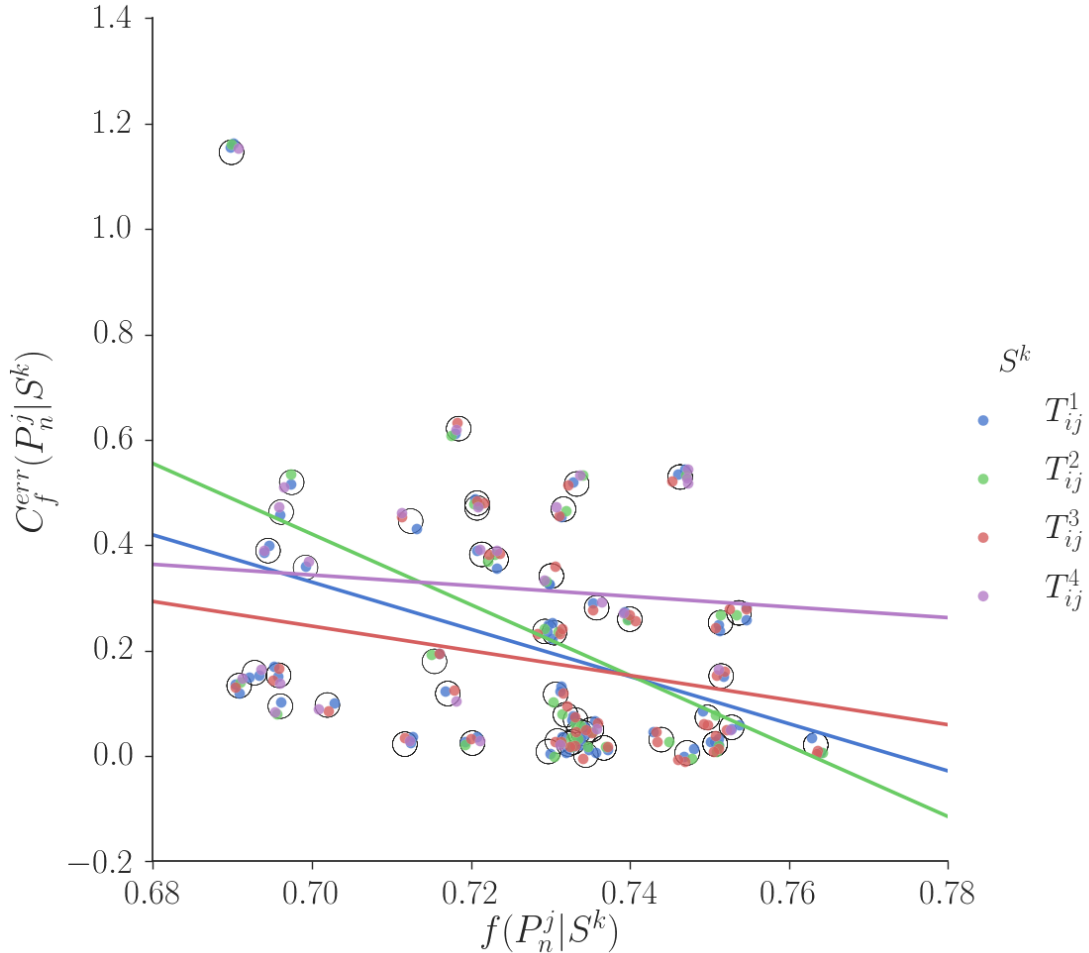


FIGURE 5.22: Linear regression of the fitness of an individual given tensor basis  $f(P_n^j | S^k)$  as a predictor of the individuals error in reattachment location  $C_f^err(P_n^j | S^k)$ . Hollow circles are the individuals  $P_n^j$  and coloured circles contained within show symbols  $S^k$  present in given solution.

The periodic hills, a difficult case for RANS, has been predicted very well by 49 of the 50 evolved anisotropy tensors inserted in Eq. 5.3. On average an improvement of 94% over the baseline SST was observed in the point of reattachment behind the hill. This is an error from the reference LES-TL of only 1.8%. The wall normal and shear stress were predicted with a high level of accuracy, however the  $\overline{u'u'}$  component was still short of the peak in the free shear layer.

Despite each output from the evolutionary algorithm, Eq. A.1-A.50, being structurally different, the second order statistics were predicted reliably. This *a posteriori* similarity can be considered as an extension of each individual's phenotype. In other words, the way in which each equation interacts with its environment – in this case the periodic hills geometry — is the same, even if the instructions on how to get the answer are different. The fact that the algorithm does not produce the same result is testament

to the difficulty of the problem and this very essence makes it a suitable problem for non-deterministic approaches.

A link has been established between the objective function Eq. 5.10 and CFD performance. The evidence that better fitness directly translates into a better closure lends credibility to the methodology. The evolutionary system is aggregating towards solutions that are useful predictive tools to an engineer. Whilst again it should be reiterated that this is only one specialised case, the potential for use in a design loop using high fidelity data to feed RANS models which then in turn feed the direction of future high fidelity tests is apparent. As a consequence, it would be a natural progression to test on complex geometries. The poor performance in the favourable pressure gradient region is a hurdle to overcome in this regard. Whether multiple data sets can be used to alleviate this remains to be seen. Maybe features from different data sets would cancel each other out. Perhaps intelligent choice in independent variables is required, expanding Eq. 5.9 to include damping functions sensitive to pressure gradients and rotation (e.g. Abe et al., 2003). There always remains the option of using different sets independently,

$$a_{ij}^x = f^{\text{rot}} a_{ij}^{\text{rot}} + f^{\text{pg}} a_{ij}^{\text{pg}} + \dots \quad (5.11)$$

where each term is sensitised to a representative data set of, for example, rotational and adverse pressure gradient flows. The damping functions  $f$  would be devised to become active in such regions. Another option would be to use indicators similar to that described by Hunt and Savill (2005) which could activate certain terms in a model for  $a_{ij}^x$ . Future tests of this kind will include the poorly predicted asymmetric diffuser flow (El-Behery and Hamed, 2011) and aerofoil geometries using DNS data of Vinuesa et al. (2014).

It is doubtful the methodology can be expected to produce one unified model for anisotropy. Currently the set of inputs is too narrow and insufficient to capture physics. The implicit weak equilibrium hypothesis assumption aside, each variable permitted for use is scaled by  $k$  which is 0 at solid boundaries. The consequence is 0 anisotropy for  $a_{ii}$  components at the wall in simple turbulent boundary layers. A different treatment of units is therefore required, potentially using a viscous time scale limit or using velocity gradients to obtain a scaling with friction units. Potentially allowing individuals freedom of units and only accepting dimensionally valid individuals may suffice. This is a suspect claim however, the probability of preserving units of energy is minimal.

The other issue is a lack of a realisability measure in the algorithm. Whilst quite a simple condition to enforce, say by rejecting solutions that violate negative stress or Cauchy-Schwarz constraints, this is very damaging. Over constraining individuals results in destroying the evolutionary process, personal experience has shown simpler objectives with less direction for harder problems is much more fruitful than trying to play intelligent design.

As a final note, aside from the CFD in this chapter, the performance of the novel GEP algorithm has been observed. Purely as an optimisation problem, the algorithm cannot be validated *per se* because the optimal solution is unknown. However there are clear signs of evolutionary advantage over random search. This was the main reason for producing so many RANS models. It should be reiterated that 50 models were created purely for statistical analysis. In order to lend support to the GEP framework, many models were tested to show that successful *a posteriori* predictions were not chance. On this last point, it is highly interesting that 50 runs of the GEP algorithm produced structurally different equations that all performed to a similar level. The simultaneous optimisation of six components was well handled by the objective function and the structural output of the mathematical expressions is tangible enough to be implemented.

## Chapter 6

# Gene Expression Programming Applied to Flow Simulation Methodology

### 6.1 Motivation

Flow Simulation Methodology (FSM) was introduced in Section 2.2.4.3, with many of the length scale damping functions  $F$  present in the current body of literature. With the exception of the functional form of Magnient, Eq. 2.75, all practical contribution functions are constructed in an *ad hoc* fashion. This is potentially damaging and non-physical. Note, Eq. 2.75 is derived assuming  $P_k = \varepsilon$ , which is heavily violated in relevant applications of FSM.

Further improvements on the approach of Magnient may be difficult via analytic means. Assumptions about the flow field may be crippling to the resulting contribution function. Instead, in this chapter, an alternative methodology is proposed using Gene Expression Programming (GEP), detailed in Chapter 3. Training data is constructed from Direct Numerical Simulations (DNS) representing the idealised form of the contribution function. The proposed methodology allows an assumption free construction of  $F$  and is easily generalisable to other hybrid models.

In order to use a regression analysis, training data is required to fit potential solutions. DNS data can be used to calculate the idealised contribution function, then this functional form can be fit via Symbolic Regression (SR). In order to evaluate the idealised form, the DNS flow field must be made to represent Hybrid RANS/LES. Hybrid RANS/LES flow fields are under-resolved due to the effective filter created by large grid scales  $\Delta$  and time steps  $\Delta_t$ . In order to mimic this, filters are applied to the fully resolved flow field that remove the small scales. The large scales are those that would be still

resolved by a hybrid model and the small scales that are removed by the filter are those that must be picked up by the hybrid closure term  $\tau_{ij}^{\text{hyb}}$ .

This decomposition creates a hybrid flow field without having to perform an under resolved DNS. This is undesirable not just for time constraints but also for non-physical dissipation levels which would impact on results and numerical stability. Filtered DNS (FDNS) also allows for the creation of a pseudo hybrid flow field without having to run any hybrid model. This is beneficial for several reasons. Firstly, FDNS is free from any model assumptions. Any model used is likely to be reflected in the results from a regression process, introducing bias. Secondly, FDNS allows for a test bed without having to repeatedly run hybrid simulations to assess potential candidates. Thousands of candidate contribution functions can be tested, a conservative estimation implies  $8 \times 10^8$  contribution functions can be tested in the time it takes to perform actual CFD once.<sup>1</sup> This kind of time saving is extremely useful, not least that it allows for detailed statistical analysis of independent variables. The length scales required for different filtering levels, flow structures, etc can be easily tested and accounted for. This is simply not possible via traditional methods.

The flip side of FDNS is the limited Reynolds number incurred by using a DNS flow field. This removes the possibility of considering high Reynolds number flows. Whilst the process is free from the assumptions of using a model or derivation, assumptions are implicit from the FDNS field considered. The flow structures present will implicitly introduce assumptions that affect the GEP analysis. For example, considering a simple equilibrium flow will produce a contribution function well suited to this. So many different types of flow fields need to be considered to reduce the amount of extrapolation required and give a wider operating range. That said, considering complex flow structures is possible with a little more rigour than traditional methods and by considering training data with a wide range of features should allow for a versatile and highly useful functional form of  $F$ .

The second criticism of the method is that filtering a DNS field does not correspond to the effective filter of Hybrid RANS/LES. This is true, however one should note that in the regression process there is no dependence on the grid coordinates. There is only a dependence on the input and output variables, see Section 6.2. In other words the training data is a portfolio of example filtering levels and how much contribution to provide for these cases. Therefore, the filtering operation removes scales from the DNS and the resulting function  $F$  is sensitised to these particular values independent of the physical point in space. So when the new  $F$  is used in CFD and sees a particular resolution level, induced by the effective filter, it will draw on its training in the correct way.

---

<sup>1</sup>Based on the convergence time of the periodic hills case in Section 8.3.

## 6.2 Process

Once a DNS field or fields have been chosen, they must be filtered. This is done using traditional filters from DNS and LES. The filtering is performed locally, such that the strength of the filter depends on the grid size of DNS. The number of points used in the filter is kept constant, so that the filter width varies locally. In other words the pseudo hybrid grid is still fine near solid boundaries and in coarser regions the filter is stronger. This is desired because the training data comprises of a wide range of filtering levels. The challenge is to relate the actual filter to the effective grid filter width from hybrid simulations. The transfer function  $T$  is inspected for a given filter and the hybrid grid width is defined by the point where  $T = 0.5$ . Ideally one would like the shape of the transfer function to yield a sharp cut-off of small scales, whilst heavily coarsening the FDNS field.

Lowering the order of explicit filters from DNS provides a quick and simple way of removing scales. The downside is that the transfer function is not easy to shape. To get a sharp cut-off, a high order is required resulting in a weak filter. To get a strong filter, the cut-off is not as sharp. Both scenarios do not represent the grid filter of hybrid methodologies.

The other option is to use LES filters, two of which are the box and Gaussian filters — see Section 2.2. For the box filter, heavy coarsening is possible but the treatment of the small scales is non-physical. The Gaussian filter appears to contain the best compromise between small scale removal and strength of the filter.

From the FDNS data, an idealised contribution function can be derived. Germano (1998) starts from the relation,

$$\tau_{ij}^{\text{rans}} = \tau_{ij}^{\text{hyb}} + \overline{\tau_{ij}^{\text{res}}}, \quad (6.1)$$

where  $\tau_{ij}^{\text{res}}$  is the resolved stress,  $\overline{(\cdot)}$  is homogeneous coordinate and time averaging. Note that  $\tau_{ij}^{\text{rans}}$  is the total stress, which in theory a RANS model should correctly account for. Now,

$$\tau_{ij}^{\text{hyb}} = F\tau_{ij}^{\text{rans}}, \quad (6.2)$$

holds for FSM and is implicitly true for many of the hybrid approaches introduced in Section 2.2.4.3. This last point can be seen by introducing the Boussinesq approximation into Eq. 6.2. By substituting Eq. 6.1 into Eq. 6.2 and a contraction with  $\tau_{ij}^{\text{rans}}$ ,

$$0 = \tau_{ij}^{\text{rans}}\tau_{ij}^{\text{rans}} - F\tau_{ij}^{\text{rans}}\tau_{ij}^{\text{rans}} - \tau_{ij}^{\text{rans}}\overline{\tau_{ij}^{\text{res}}}. \quad (6.3)$$

is obtained. Rearranging this equation leads exactly to,

$$F = 1 - \frac{\tau_{ij}^{\text{rans}}\overline{\tau_{ij}^{\text{res}}}}{\tau_{mn}^{\text{rans}}\tau_{mn}^{\text{rans}}}. \quad (6.4)$$

As already discussed this equation is impractical in actual simulations due to the infinite time average required, but is the ideal form of the contribution function. Note that  $\tau_{ij}^{\text{rans}}$  contains an average itself. This function can be evaluated for FDNS data, using a series of snapshots to build a picture of the contribution function for a range of flow fields. Equation 6.4 contains a time average and as a result it is unclear as to how this will affect the effective filter of the FDNS field. Consequently a calibration procedure will be required to readjust any coefficients that fall out of the GEP process.

Equation 6.4 is also free from any explicit length scale dependence so the modeller is free to test many different length scales as independent variables throughout the regression analysis. These are also calculated from the FDNS flow field. One should take care to only use variables that are available to a RANS model at runtime. This increases the portability of FSM and also considers the computational cost of the algorithm. The length scales chosen reflect those presently used in damping functions in the literature, covered in Section 2.2. Also, the Taylor micro-scale is added, as this is the length scale of the smallest resolved eddies (Sagaut et al., 2013). It is easily calculated and has not been previously considered. The length scales studied are defined as,

$$\begin{aligned}
 L_k &= \frac{\Delta}{\ell_k}, & \ell_k &= \left( \frac{\nu^3}{\varepsilon} \right)^{\frac{1}{4}} \\
 L_t &= \frac{\Delta}{\ell_t}, & \ell_t &= \frac{k^{\frac{3}{2}}}{\varepsilon} \\
 L_\lambda &= \frac{\Delta}{\ell_\lambda}, & \ell_\lambda &= \sqrt{\frac{10k\nu}{\varepsilon}} \\
 L_{\text{trans}} &= \max \left( \frac{S}{1.25\Omega}, 1 \right)^{-2} \\
 L_{\text{oes}_S} &= \frac{kS}{\varepsilon} \\
 L_{\text{oes}_\Omega} &= \frac{k\Omega}{\varepsilon} .
 \end{aligned} \tag{6.5}$$

Equations 6.5 represent traditional LES-like hybrid length scales and also URANS-like hybrid length scales. Note, that the notation  $L_{\text{trans}} = L_T$ ,  $L_{\text{oes}_S} = L_S$  and  $L_{\text{oes}_\Omega} = L_\Omega$  is used interchangeably. See Section 2.2 for their original uses in TRRANS, OES, FSM, PANS and DES.

All six scales are non-dimensional, which means that there is no restriction in a regression analysis. The modeller is free to pick the optimal solution without having to worry about dimensional analysis. Once these length scales are calculated one is ready to perform GEP in order to optimise  $F$  for a given flow field.

To summarise the process,

- Filter a DNS flow field or many flow fields to create pseudo hybrid data — denoted as FDNS.
- Evaluate the effective grid filter by relating to the transfer function.
- Evaluate Eq. 6.4 for the FDNS flow field, along with the length scales Eq. 6.5.

- Perform GEP analysis to yield an optimal functional form  $F = F(L_k, \dots, L_\Omega)$  that fits the idealised contribution function.
- Calibrate the coefficients to take into account the time average of Eq. 6.4.

## 6.3 GEP Studies

### 6.3.1 Preliminary Study - Pipe Flow

As a preliminary study, a turbulent pipe flow<sup>2</sup> was considered at a Reynolds number  $Re_r = 3350$  (Weatheritt and Sandberg, 2015). Due to the pressure gradient driving the flow and the axial symmetry of the geometry, only a one-dimensional profile of Eq. 6.4 is relevant. The pipe geometry represents a simple shear flow void of complex flow features induced by the geometry.

Only the variables  $L_k$  and  $L_t$  are considered to keep matters simple. The filter is a 2<sup>nd</sup> order explicit filter induced by truncating the Taylor expansion of each variable. This produces a moderately filtered flow field from the DNS data. One snapshot of the DNS streamwise velocity fluctuation can be see in Fig. 6.1.

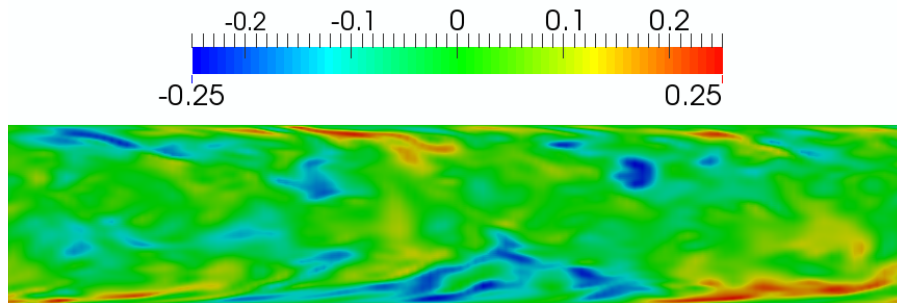


FIGURE 6.1: Instantaneous snapshot of  $u'/\bar{u}$  for the pipe flow. Streamwise direction is left to right, vertical direction is the pipe diameter.

Two hundred snapshots are used in the calculation of Eq. 6.4,  $L_k = \Delta/\ell_k$  and  $L_t = \Delta/\ell_t$ . This is not enough for convergence due to the larger eddy turnover time in the bulk, however the same oscillations are observed in both the independent and dependent variables. As a result, smooth damping functions are still producible by the evolutionary algorithm. Equation 6.4,  $L_k$  and  $L_t$  are plotted in Fig. 6.2. The strength of the filter is apparent from this plot —  $L_k$  is of the order of  $10^1$ , implying that the grid spacing is ten times bigger than the Kolmogorov scale. The integral length scale is approximately 10 times bigger than  $\Delta$  by a similar argument. The filter therefore represents a reasonable coarsening of this low turbulent case, evident also by the greater rate of change of  $L_t$

<sup>2</sup>In house study, conducted by Patrick Bechlars.

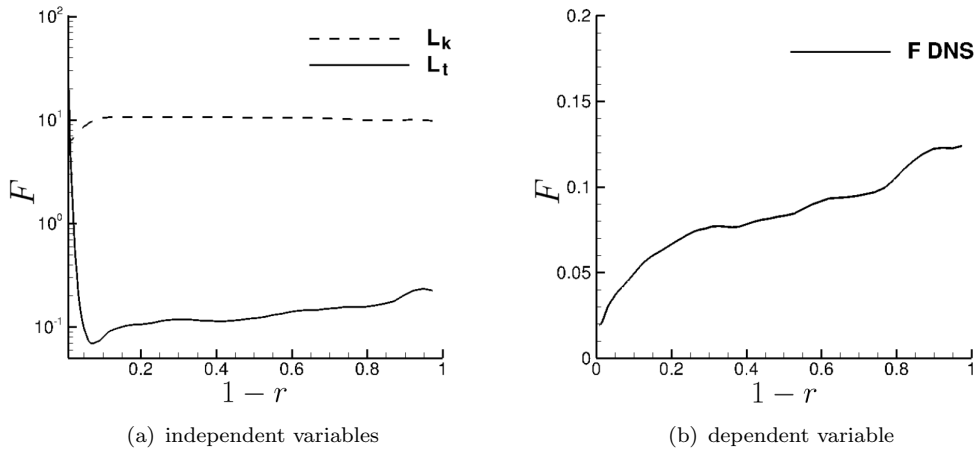


FIGURE 6.2: The idealised contribution function and the length scales calculated for the pipe flow.

with respect to its magnitude than  $L_k$ . Therefore we may expect  $\Delta/\ell_t$  to be a better indicator of variation in  $F$  and indeed by visual inspection this appears to be the case. The algorithm is highly likely to favour  $L_t$  as this closely resembles  $F$ , in terms of both gradient and magnitude. The exception to this is the near wall region. This does not matter because in the boundary layer we desire a switch to RANS mode forced by a near wall shielding function (see Section 7).

To make individuals, the complete function  $\mathcal{F}$  and terminal  $\mathcal{T}$  sets are,

$$\begin{aligned}\mathcal{F} &= \{+ : +, - : -, * : \times, / : \div, \text{e} : \exp, \text{L} : L(x) = \log(1+x), \wedge : q(x, y) = x^y\} \\ \mathcal{T} &= \{\mathbf{a} : L_k, \mathbf{b} : L_t, 1 : 1, ? : ?\}.\end{aligned}\quad (6.6)$$

Link functions are  $+$ ,  $-$  and  $\times$ . Notice that  $L$  is not the standard logarithmic function, as this could easily induce negative or undefined expressions. Instead the function  $L$  provides the logarithmic operator, but the addition of 1 allows for a smooth transition to 0 as  $L_k$  and  $L_t$  are positive. The random numbers are limited between 0 and 1, as this is the desired limits of the damping function. Constants larger can still appear in the evolutionary process as compounds of smaller constants and mathematical operators. There is an obvious bias against this though, as more space in the gene is required.

A population of five hundred individuals with four genes of length five were evolved for two thousand generations. The probability of mutation was set to 0.01, one point crossover set to 0.7 and all the other genetic operators outlined in Section 4.2 were set to 0.002. These model parameters were set by considering precursor validation and parameter studies. Note, these studies have been removed from this thesis in the interests of space.

The fitness of each individual is measured as a linear weighting of relative fitness denoted in Eq. 4.1 and the comprehensibility denoted in Eq. 4.2. The weighting is 90% in the

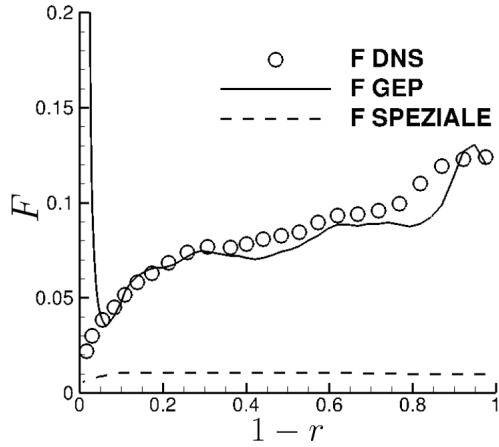


FIGURE 6.3: Results from GEP process compared with FDNS data and Speziale's original function, Eq. 2.74.

favour of Eq. 4.1, because the chromosome length is relatively short and acts to some degree as a natural truncation of functional complexity.

The fittest individual to result from the process had the phenotype, where  $C_i$  and  $n$  are constants,

$$F = C_1 \left[ \log \left( 1 + C_2 \frac{\Delta}{\ell_k} \right) \right]^n \frac{\Delta}{\ell_t}. \quad (6.7)$$

This is very pleasing result. Firstly, the similarity to existing techniques such as DES (Spalart et al., 1997) and the FSM of (Weinmann et al., 2014) serves as validation for the methodology of model formulation. Equation 6.7 is plotted against Eq. 6.4 and Speziale's original function, Eq. 2.74, in Fig. 6.3. Note, all plots in Fig. 6.3 are created using the FDNS data, so the time average of Eq. 6.4 may be working against its true performance. However, that said, it is unlikely to give the right order of magnitude of  $F$  given the value of  $\beta$  and this plot just serves to reinforce that issue.

The functional shape of  $F$  has picked up the linear dependence on  $L_t$  strongly suggested by the data. Further there is a second factor dependent on  $L_k$ . This is the unique part of the functional form that has occurred from the process. Instead of the exponential favoured by Speziale (1997) and Weinmann et al. (2014) the logarithmic has been preferred. This results in higher length scale damping for larger values of  $L_k$  than the exponential and further moves from the DNS limit faster.

### 6.3.2 Backward Facing Step Flow

The flow behind a backward facing step<sup>3</sup> is considered for a more in depth study of the shape of the function  $F$  (Weatheritt and Sandberg, 2014). For this study, a non-equilibrium flow is considered that presents a more difficult challenge as the turbulence

<sup>3</sup>In house study, by Javier Otero.

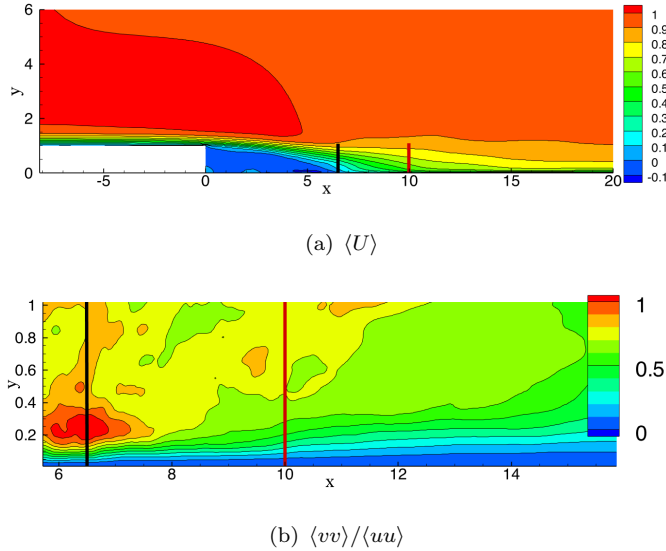


FIGURE 6.4: Mean statistics from the backward facing step DNS.

displays non-local effects induced from the step geometry. The evolutionary system produced in this study, with all six independent variables from Eq. 6.5, is highly dependent on initial conditions and the functional complexity required to exactly match the idealised contribution function is high. As a result, the main body of this study is about ensemble and transient statistics from the evolutionary system. Evolutionary runs are repeated and statistics about the final population are recorded and ensembled, much like the reasoning for a physically deterministic system — for example the reasoning behind the RANS operator applied to the Navier-Stokes. One may argue that the outcome of an evolutionary system is not deterministic, however this is not the case. The contingency of the initial population and fitness environment are the only freedom and given these two parameters, determinism ensues. The population should converge from its initial state to fit the environment presented, if given enough time. This author argues the outcome is determined as long as the initial conditions allow for it. Note, biological evolution is considered deterministic (see for example - Kiontke et al., 2007) and evolutionary algorithms are after all mimics of this.

The Reynolds number  $Re = 3000$  is based on step height. The previous study in Section 6.3.1 looked at a simple shear flow, this study is aiming to look at algorithm performance for a non-equilibrium separated flow, so consider the two locations in Fig. 6.4. Figure 6.4(b) is a plot of the averaged Reynolds stress ratio  $\langle vv \rangle / \langle uu \rangle$  downstream of the step, Fig. 6.4(a) is a plot of mean streamwise velocity included as a visual reference.  $x/h = 6.5$  is a region where the normal stresses are significant, just before reattachment, and  $x/h = 10$  is a slice of the recovering boundary layer.

These two locations present a reduction in the number of data points to consider for the evolutionary process, yet still capture in essence the features of the flow field. As a

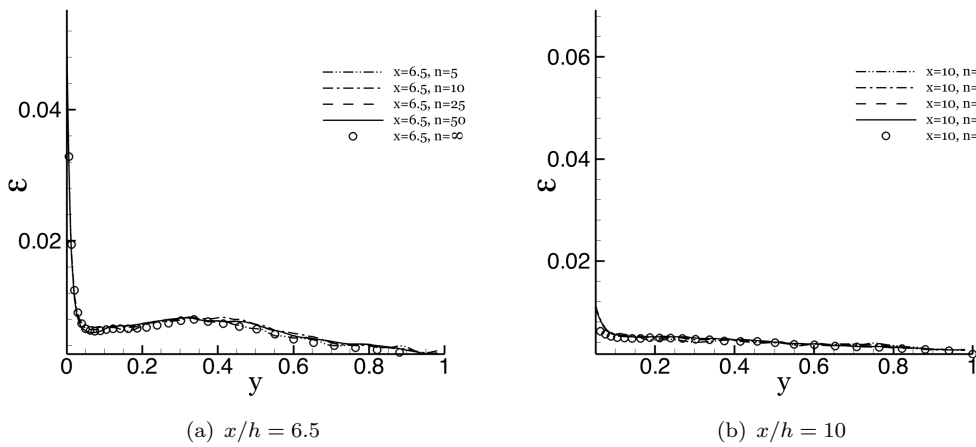


FIGURE 6.5: Convergence of  $\varepsilon$ .

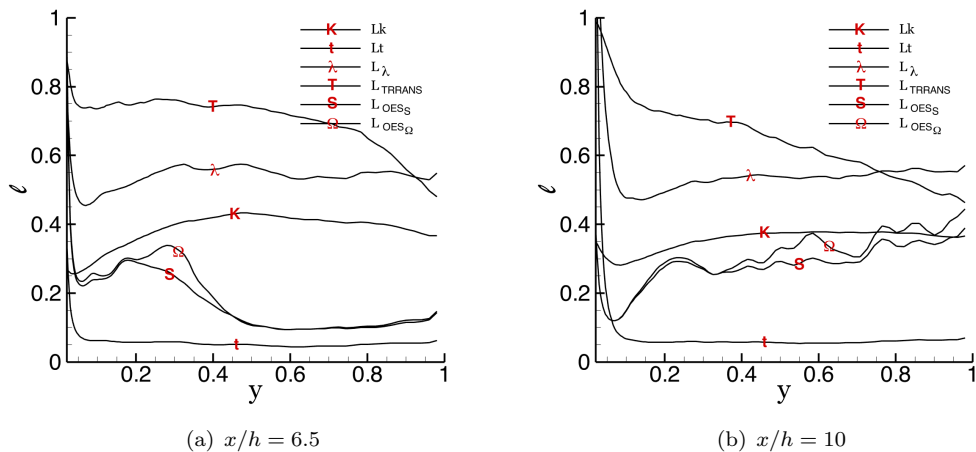


FIGURE 6.6: Length scales for the backward facing step flow.  $L_k$  has been factored by 0.04 in order to fit conveniently into the plots.

result, the training data for the problem is precisely these two locations, representing a significant saving in overheads.

The convergence of the statistics when averaging over snapshots and the spanwise direction is studied via  $\varepsilon$ . Figure 6.5 are the results from this convergence study. One can see that ultimate convergence has not been achieved, but  $n = 50$  snapshots presents a good approximation to the statistical mean of the DNS data ( $n = \infty$ ). Therefore fifty snapshots are used with confidence of producing reliable results in the calculation of Eq. 6.4.

Figure 6.6 shows the plots of the length scales at the locations  $x/h = 6.5$  and  $x/h = 10$  using fifty snapshots and spanwise averaging. Note  $L_k$  has been factored by 0.04 in order to fit conveniently into the plots.  $y/h = 0$  corresponds to the lower surface and  $y/h = 1$  is the height of the hill.

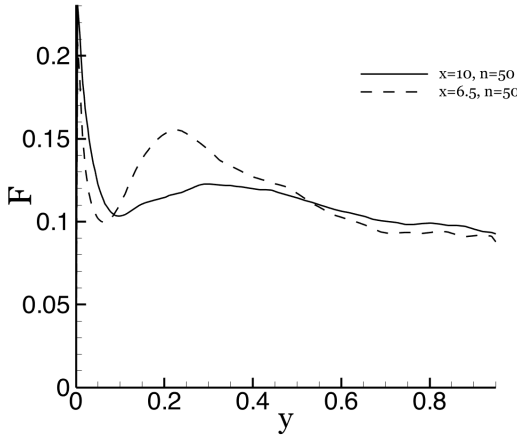


FIGURE 6.7: Idealised contribution function calculated for the backward facing step FDNS data.

Figure 6.7 is a plot of the idealised contribution function at  $x/h = 6.5$  and  $x/h = 10$ . This represents the training data for the regression. The echo of the shear layer can be seen — the location where  $F$  reaches its peak for the  $x/h = 6.5$  profile. This peak has gone from the profile at  $x/h = 10$  as the boundary layer has undergone some recovery. Above  $y/h = 0.5$ , the flow is effectively the top half of a free shear layer and as a consequence it is expected to exhibit similar behaviour to the pipe flow of Section 6.3.1.

Considering the plots of Fig. 6.6 and Fig. 6.7 it is clear that this is a much harder problem than the pipe flow above. There is no clear independent variable that matches the contribution function at any streamwise location. Only the variable  $L_T$  even has the right overall gradient, but completely lacks any information that could be used to predict the peak in  $F$  at  $x/h = 6.5$ . Instead, multiple length scales are required for any useful fit of the FDNS data.

The overall algorithm set up is the same as that of Section 6.3.1. The main difference are the symbol sets,

$$\begin{aligned} \mathcal{F} &= \{+ : +, - : -, * : \times, / : \div, \text{e} : \exp, \text{L} : L(x) = \log(1 + x), \wedge : q(x, y) = x^y\} \\ \mathcal{T} &= \{\text{a} : L_k, \text{b} : L_t, \text{c} : L_\lambda, \text{d} : L_T, \text{e} : L_S, \text{f} : L_\Omega, 1 : 1, ? : ?\}. \end{aligned} \quad (6.8)$$

Note the name clash between the genotype symbols for  $\exp$  and  $L_S$  is not an issue within the code — they exist as objects not merely as strings.

To gather ensemble statistics, thirty independent runs of one hundred generations are performed for each statistic. The exception is when considering the combined data set of  $x/h = 6.5$  and  $x/h = 10$ . Due to the increase in the number of data points, three hundred generations were required.

A look at the transient nature of the evolutionary system is possible by looking at the relative frequency of each length scale throughout the top ten percent of the population.

Figure 6.8 is precisely this for each streamwise location and then the combination of both.

Clear, particularly at  $x/h = 10$  (highlighted in red), the ratio of the grid to integral length scale  $L_t$  initially is the most popular variable as a descriptor of  $F$ . This implies that before the functions are well formed, existing as primitive and sub-optimal organisms that do not contain the inherent history of evolution, the integral length is the most useful. Once functions can form over time and produce meaningful relationships through the evolutionary process, the integral length scale becomes far less popular.

$L_\lambda$  is popular individually, however when considering the locations together it occurs with the second lowest frequency. This is puzzling, perhaps because the frequencies were only collected up to 100 generations, when 300 were required and recorded for all other statistics. Therefore the results of Fig. 6.8(c) should be taken with a pinch of salt, perhaps many more generations were required or indeed the individual uses  $L_\lambda$  differently at each spatial location, which are incompatible with each other.

Another interesting feature of the transient data, is the relative smoothness of  $x/h = 6.5$ , whilst the transient of  $x/h = 10$  contains many oscillations. This is an inherent feature of the complexity of the curve fit at each location. The dependent variable at  $x/h = 10$  is easier to fit, so small changes are reflected as small changes in fitness. The presence of the detached shear layer at  $x/h = 6.5$  makes it a much trickier location to fit. This means that small changes in genotype manifest themselves as big changes in fitness. These changes are normally negative and so will not be visible in Fig. 6.8(a). Changes to fitness during the curve fit at  $x/h = 10$  are relatively more likely to be beneficial and are visible in Fig. 6.8(b).

The range of frequencies is much wider for the location  $x/h = 6.5$ . This is also a feature of the complexity of the curve fit at this location; the algorithm greedily uses  $L_\lambda$  as it has found early, after about 15 generations, a benefit to using this variable and it propagates through the population. The other independent variables and combinations of the other variables are not able to improve on this. If the profile was easy to fit, then you would expect uniform usage of independent variables as many different functional forms would adequately approximate the training data.

The average fitness (Eq. 4.1) of the initial population and final population are plotted for the locations  $x/h = 6.5$ ,  $x/h = 10$ ,  $x/h = 10$  with  $y/h > 0.5$  and finally the combination of streamwise locations in Fig. 6.9. The threshold is increased from 90% in the above statistics, to 98%. This means that only the top 2% of the population is included in Fig. 6.9. The frequency of each length scale is included in the plot.

The increase in fitness from the initial population is evidence that EVE is working correctly. Further, it is clear that all independent variables are capable of producing fit solutions, but their occurrence is much more varied. Due to the uniform high fitness,

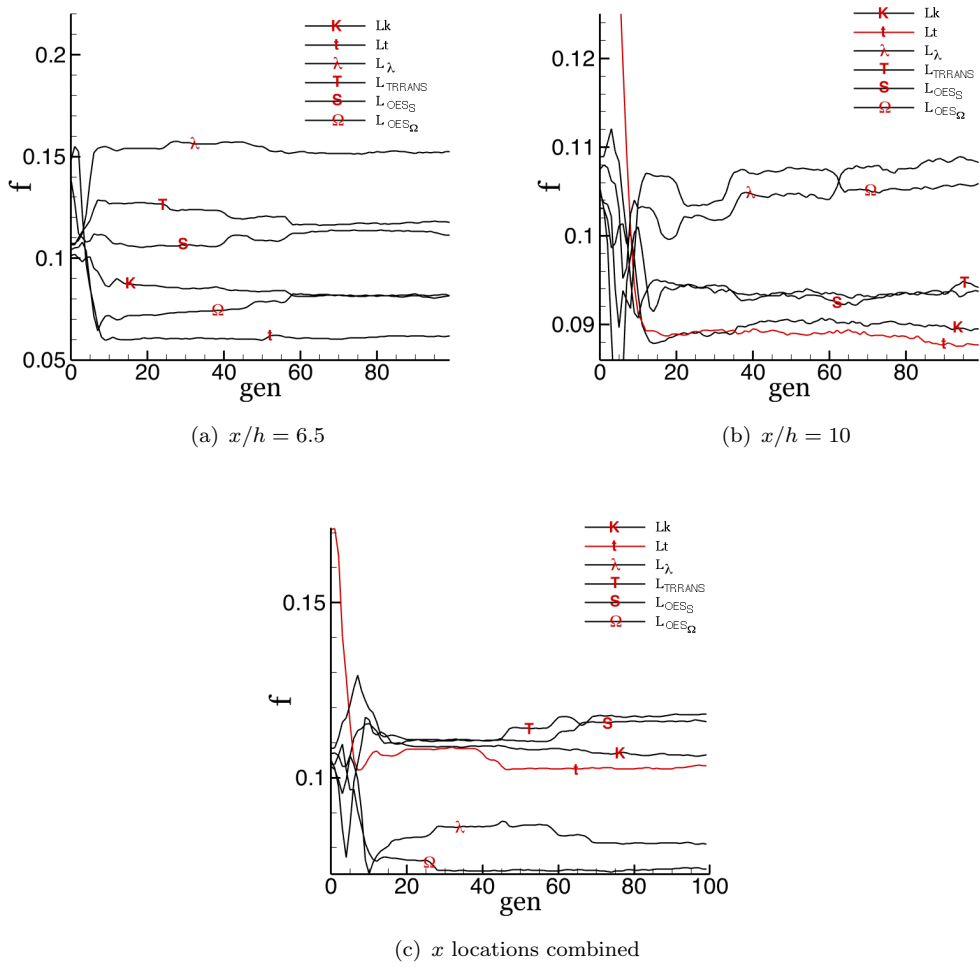


FIGURE 6.8: Average frequency of length scales throughout the top 10% of the population given generation (Transient probability of occurrence).

the frequencies provide a more useful indication of appropriate independent variables. Consistently across all locations,  $L_T$  and  $L_\lambda$  are the most frequent amongst the top organisms.

A few ‘obvious’ results (with hindsight) are now discussed. For the location  $x/h = 10$ ,  $y/h > 0.5$ , that is the most similar to the pipe flow of Section 6.3.1,  $L_t$  is relatively much more frequent. At this same location, over half the members of the population include  $L_T$ . This is because both have a roughly negative linear gradient and so a curve fit with this variable is much simpler.  $L_k$  is rare with the individuals. This is because it differs from  $F$  by two orders of magnitude and so an evolving individual must be able to take this into account *and* use  $L_k$  in a meaningful way.

The average comprehensibility, Eq. 4.2, is recorded in Fig. 6.10 for locations  $x/h = 6.5$ ,  $x/h = 10$ ,  $x/h = 10$  with  $y/h > 0.5$  and the combination of these. One can see that the length of the top solutions is on average increasing, indicating that more complexity is required on average. The simplest solutions are produced by  $L_T$  and  $L_\lambda$  with the

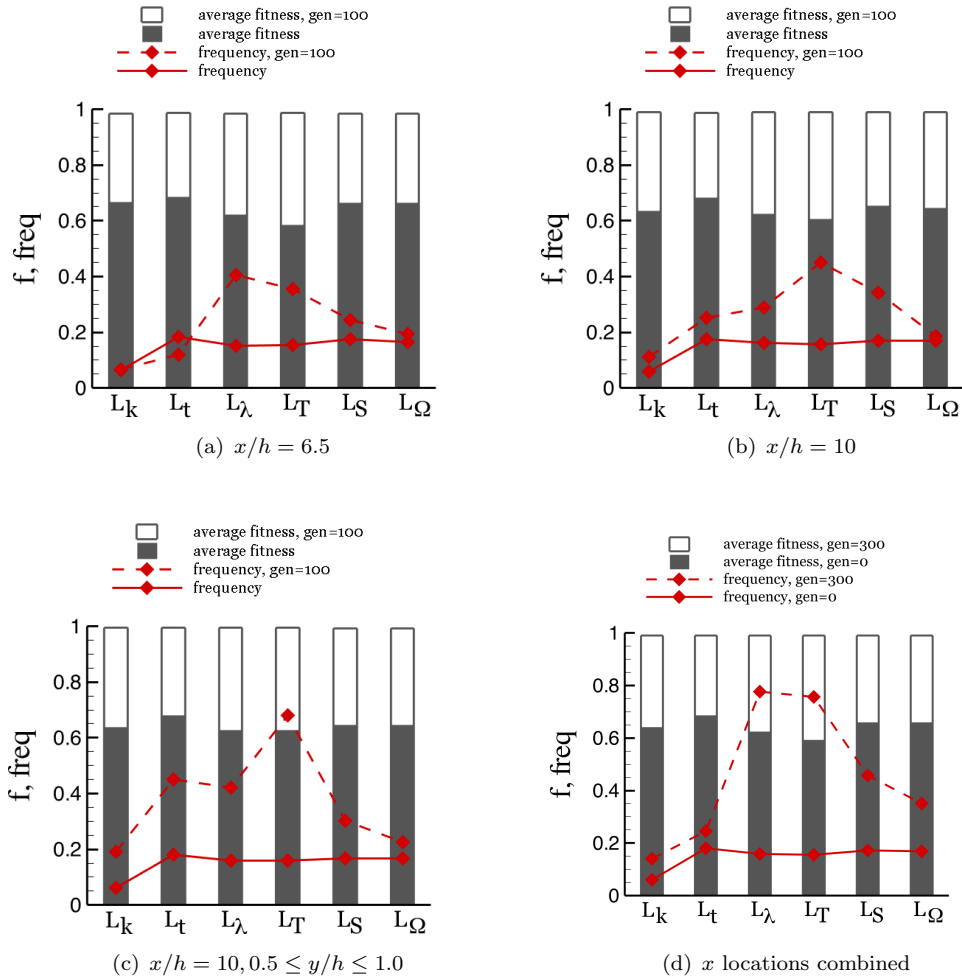


FIGURE 6.9: Average fitness (Eq. 4.1) of the top 2% of the population given a length scale present. Average frequency of each length scale of the top 2% of the population given a length scale present. Ensemble statistics are gathered for the beginning and end of each simulation.

exception of rarely occurring good solutions containing  $L_k$ . These should be explored, but their rarity implies that they could be an over specialisation of this data or some interaction with another variable. More likely however, the differing order of magnitude issue mentioned above is the culprit.

This large amount of ensemble data must be digested and from these human decisions must be made. For this problem, human intervention is really the only option. One instance of the population after 100 generations is very different to another (from a differing starting population). Further, complete automation of *a posteriori* testing, as in Chapter 7 is not possible due to the long simulation times required for Hybrid RANS/LES.

In conclusion, this ensemble data has shown that any length scale is capable of giving a good solution, but the functional complexity is vastly different in order to produce

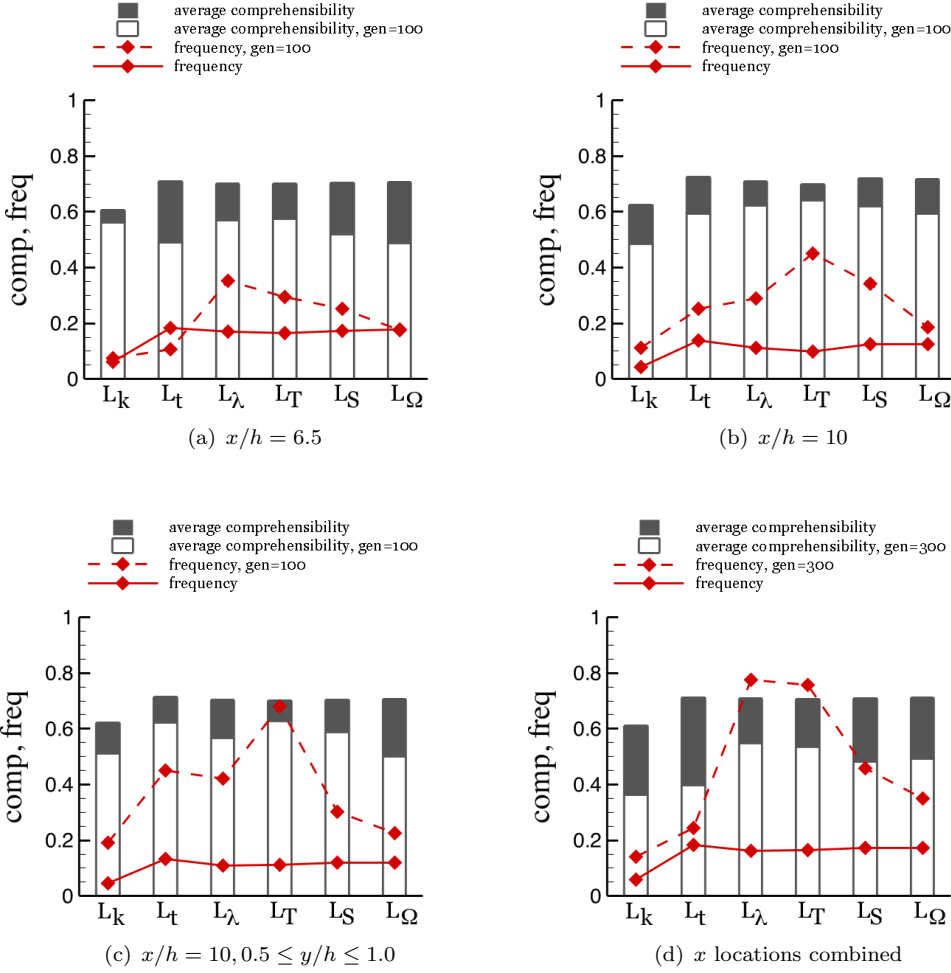


FIGURE 6.10: Average comprehensibility (Eq. 4.2) of top 2% of population given length scale present. Average frequency of each length scale of top 2% of population. Ensemble statistics are gathered for the beginning and end of each simulation.

this. The relative frequency of each variable's occurrence also echoes the functional complexity required. The anomaly to this is  $L_k$ , which because of its large order of magnitude, is much rarer.

In order to build an optimal contribution function, it is decided that  $L_T$  and  $L_\lambda$  are the most significant variables and are used below in an optimisation. This decision is made due to the frequency of occurrence. Their high frequencies mean that  $L_T$  and  $L_\lambda$  can explain the data in a more robust fashion. The implication is that there is an insensitivity in performance using these variables and this robustness is a highly desirable trait. Obviously a robustness in functional form does not translate directly to a robustness with respect to the environment, but it is hypothesised there will be some correlation between these two traits. The comprehensibility is also a good indicator of robustness to environment. As mentioned,  $L_k$  performs best for this trait, but the order of magnitude difference is likely to be too insensitive to changes — much like the

problems with the original formulation of Speziale (1997) discussed in Section 2.2.4.3. For this reason  $L_k$  is not included in the final analysis.

The best result from evolutionary runs including only  $L_T$  and  $L_\lambda$  as independent variables is given as,

$$F = C \frac{\Delta}{\ell_\lambda} \max \left[ \left( \frac{S}{1.25\Omega} \right), 1 \right]^{-2}, \quad (6.9)$$

where  $C$  is a constant that must be calibrated. This is not the final form every time, but often a function is produced that easily simplifies to this form by cancelling negligible terms.

## 6.4 Creation of Full Hybrid Models

In order to turn Eq. 6.7 and Eq. 6.9 into fully working hybrid models, they must be modified to ensure proper boundedness between 0 and 1. The lower bound is trivially maintained, providing  $C_i$  are positive.

In order to ensure  $F \leq 1$ , the following respective modifications are made. First to Eq. 6.7,

$$F = \min \left( C_1 \left[ \log \left( 1 + C_2 \frac{\Delta}{\ell_k} \right) \right]^n, 1 \right) \min \left( \frac{\Delta}{\ell_t}, 1 \right) \quad (6.10)$$

and the second to Eq. 6.9,

$$F = C \min \left( \frac{\Delta}{\ell_\lambda}, 1.0 \right) \max \left[ \left( \frac{S}{1.25\Omega} \right), 1 \right]^{-2}. \quad (6.11)$$

Notice that each factor that could exceed unity is given its own limiter. This is because it could interfere with the predictive capability of another factor. For example in Eq. 6.9, if  $\ell_\lambda < \Delta$  then some of the unsteadiness detected in the organised motions by  $L_T$  would be lost.

Before the calibration of the coefficients, the near wall treatment of Weinmann et al. (2014) is added to each model,

$$F = \min \left( \frac{F_{\text{damp}}}{1 - f_b}, 1 \right), \quad (6.12)$$

where  $F_{\text{damp}}$  is the damping function from either Eq. 6.10 or Eq. 6.11.  $f_b$  is the damping function from the Menter (1994) SST turbulence model designed to be 0 in the outer layer and 1 at the wall. Using this in the manner of Eq. 6.12, it is possible to achieve RANS at the wall and LES outside of the boundary layer. This is vital to the success of the hybrid simulation, not only for near wall cost requirements, but also on predictive performance (Sagaut et al., 2013). This particular wall switching method, along with

the Delayed Detached Eddy Simulation Spalart et al. (2006), is investigated in detail in Chapter 7.

The coefficients for each model were calibrated for a channel flow of friction Reynolds number 550, using a blended convection scheme (Weinmann et al., 2014). By matching the shear stress component, the coefficients are found to be  $C = 0.8$ ,  $C_1 = 2.1$ ,  $C_2 = 0.75$  and  $n = 4$ . These coefficients are found using the SSG (Speziale et al., 1991) turbulence model. Each turbulence model and numerical scheme used should have its own calibration procedure however, in the interests of time, this is not performed.

Note, due to the chronology of this research, cases referred to as FSM in the subsequent Chapters use Eq. 6.10. Equation 6.11 is denoted as HYB in order to distinguish.

## 6.5 Summary

In this chapter two new Hybrid RANS/LES formulations have been proposed, both variants on the FSM framework detailed in Section 2.2.4.3. These closures are put through their paces for a channel flow in Chapter 7 and for separated flow applications in Chapter 8.

The novelty lies in their creation. Using the GEP framework outlined in Section 4, Eq. 6.10 and Eq. 6.11 were found by looking at simulation data. This minimised assumptions and *ad hoc* formulations in the hope that the new damping functions are more applicable to a wider range of flows.

The DNS data considered was first filtered to mimic Hybrid RANS/LES. Then, using Eq. 6.4, new versions of the damping function were found by the GEP algorithm. This kind of process is applicable to a wide range of turbulence resolving approaches. In particular it is easy to see how this kind of approach could be repeated for modifications to specific terms in the RANS equations, such that they become suitable for Hybrid RANS/LES. Further, extra components of the damping function can be created, such as a component to deal with transition. This could be easily performed by calculating the intermittency factor and creating a coefficient such that  $F \rightarrow 1$  in turbulent regions and  $F \rightarrow 0$  in laminar regions. This would be useful in high Reynolds number flows when transition is not automatically accounted for by the turbulence model.

## Chapter 7

# Application of Hybrid RANS/LES to the Planar Channel

### 7.1 Hybrid RANS/LES at Solid Boundaries

The original concept behind combining Reynolds-Averaged Navier-Stokes (RANS) modelling with Large Eddy Simulation (LES) is to ease the near wall grid requirements of the latter. This is achieved by treating the boundary layer with RANS and switching to LES in the outer layer. Chapman (1979) estimated that an LES of a flat plate boundary layer requires a total number of grid points  $N$  proportional to the Reynolds Number  $\text{Re}_{L_x}$  via the relation

$$N \sim \text{Re}_{L_x}^{9/5}, \quad (7.1)$$

which is only marginally better than Direct Numerical Simulation (DNS). The exponent was later revised by Choi and Moin (2012) to be 13/7.  $L_x$  is the length of the flat plate. Strong dependence on and poor scaling with Reynolds number puts the majority of industrially relevant geometries out of reach for LES.

Work on wall modelled LES started with the seminal work of Deardorff (1970); Schumann (1975) who derived equilibrium laws to relate the wall shear stress with the velocity in the core, assuming a universal law of the wall. These laws made it possible to relax the near wall grid requirements and the good results of Schumann (1975) showed the feasibility of wall modelled LES. Note that Deardorff (1970) used a resolution much too low in the outer layer, reducing the solution quality.

This kind of wall model is only possible when a universal law of the wall (e.g. Townsend, 1961, 1976) can be assumed such that the only feasible applications are simple geometries like pipes and channels. Despite this shortcoming, near wall models did not get an

overhaul until Spalart et al. (1997) and Speziale (1997) essentially devised the same philosophy of damping the length scales in a RANS model as the wall normal direction is traversed. These two methodologies became known as Detached Eddy Simulation (DES) and Flow Simulation Methodology (FSM). DES contains an explicit switch between the RANS and LES modes,

$$\ell^{\text{des}} = \min(d, C_{\text{des}}\Delta) \quad (7.2)$$

where  $\ell^{\text{des}}$  is the dissipation length scale in the Spalart and Allmaras (1992) turbulence model,  $\Delta$  is the grid length scale,  $d$  is the wall distance and  $C_{\text{des}} = 0.65$ . This idea is easily generalisable to other turbulence models,

$$\ell^{\text{hyb}} = \min(\ell_t, C_{\text{des}}\Delta), \quad (7.3)$$

where  $\ell_t$  is the RANS length scale. FSM on the other hand did not have such a treatment and the switch was made continuously by damping the RANS length scale.

Equation 7.3 works well when  $\Delta_x$  and  $\Delta_z$  are much bigger than the boundary layer thickness  $\delta$ . Such a constraint forces the closure to act in RANS mode near the wall, through the sensitivity in  $\Delta$ . Even with a  $\Delta_x^+ > 8000$ , Nikitin et al. (2000) showed that turbulence is sustained in the bulk of a channel flow by DES, lending support for the method. Despite this, Hybrid RANS/LES has been shown by numerous authors to be sensitive to the streamwise spacing (e.g. Spalart et al., 1997; Baggett, 1998; Nikitin et al., 2000; Menter et al., 2003; Spalart et al., 2006). It should be noted that most of the analysis has been performed using DES; this does not reflect its shortcomings relative to other Hybrid Methodologies, rather the opposite. Early success of DES saw it become the industry standard in the 2000s and so the deficiencies of Hybrid RANS/LES were discovered with this technique first.

When an aggressive streamwise spacing is not used, the switch between RANS-LES is pushed deep into the inner layer. This is because the cell Reynolds number is reduced and resolved eddies are allowed to form. This lowers the modelled stress contribution which is not compensated for by resolved turbulence. This phenomena has become known as Model Stress Depletion (MSD) and in some cases has been shown to cause premature separation (Menter et al., 2003). Spalart et al. (2006) argues that this was slightly overstated but the sensitivity to grid spacing was acknowledged. Further, the near wall, being a RANS solution, contains its own log-layer several wall units shy of the correct value due to the model being artificially suppressed. Once LES takes over, the resolved stress dominates and a new log-layer is formed several wall units too big. This discrepancy, also called the log-layer mismatch, is amplified as the Reynolds number is increased (e.g. Piomelli et al., 2003). Baggett (1998) argues from channel flow results that both MSD and the log-layer mismatch are produced by the ‘artificial’ near wall turbulence cycle characterised by large streamwise streaks, which is entirely correct, although argues that this is resulting from resolved structures being entirely

parametrised by the grid. This conclusion was the result of a resolution much too low for relevant findings, and this author has numerous experiences of observing large scale streaks on much finer meshes.

Instead, an explanation of the artificial near wall turbulence is offered. Consider the decomposition,

$$u_i = \tilde{u}_i + u'_i, \quad (7.4)$$

where  $u'_i$  is the fluctuating motion with respect to an effective filtered velocity  $\tilde{u}_i$ . In the limit of solid boundaries, the damping function returns to unity  $F \rightarrow 1$ , the filter is considered a Reynolds operator  $\tilde{u}_i \rightarrow \bar{u}_i$  and the fluctuation transport equation reads,

$$\partial_t u'_i + \bar{u}_j \partial_{x_j} u'_i = -u'_j \partial_{x_j} \bar{u}_i - u'_j \partial_{x_j} u'_i - \partial_{x_i} p' + \nu \partial_{x_j} \partial_{x_j} u'_i + \partial_{x_j} \overline{u'_i u'_j} \quad (7.5)$$

where  $\bar{u}_i$  is the Reynolds averaged velocity and  $\overline{u'_i u'_j}$  is closed with a RANS model. At the RANS-LES interface of wall parallel flow, the following is true  $\bar{v} = \bar{w} = 0$  and  $u'_i \ll \bar{u}_i$ . This implies that the production terms of  $u'$ ,  $v'$  and  $w'$  respectively reduce to

$$\begin{aligned} P_1 &= -v' \partial_y \bar{u}_i \\ P_2 &= -v' \partial_y v' \\ P_3 &= -v' \partial_y w'. \end{aligned} \quad (7.6)$$

The magnitude of  $P_1$  is much greater than  $P_2$  and  $P_3$  as it depends on the mean velocity gradient, implying that the majority of produced motions enter into the streamwise component. This production of resolved motion has the effect of isotropically turning off the turbulence model and the turbulent diffusion for each component into a sum of the resolved motion and a RANS model evaluated using the grid filtered velocity,

$$\partial_{x_j} \overline{u'_i u'_j} \rightarrow \partial_{x_j} \tau_{ij}^{\text{rans}}|_{\tilde{u}_i} + \partial_{x_j} \widetilde{u'_i u'_j}. \quad (7.7)$$

This further compounds the issue; the resolved motions primarily contribute again into the streamwise direction. The result is an overall model contribution too low, as it is sensitised to the overly large fluctuations in the streamwise direction. The only way this large component can initially get redistributed is through the anisotropy of the RANS model, which is a strong argument to use a model that correctly captures the redistribution of  $\overline{u^2}$  into  $\overline{v^2}$  and  $\overline{w^2}$ . Further,  $u'$  is necessarily produced with the opposite sign to  $v'$  and the RANS-LES interface induces a blocking effect such that  $v' > 0$ , implying the primary structures in the near wall cycle will be ejections. Of course, this only happens once  $v'$  has been produced, and the final result is a lift up of streaks which pass too high intensity fluctuations into the free stream. Equation 7.7 is only a phenomenological argument and is not inserted into Eq. 7.5, as the fluctuation equation only holds in the limit of the effective filter being a Reynolds operator. Notice the term *effective* filter, which at the RANS-LES interface is dictated by the damping function

entering through the turbulence model and as such,  $u'_i$  can be interpreted as a resolved motion.

Several fixes for the sensitivity to the parallel grid spacing have arisen in varying degrees of success and complexity. Broadly speaking, efforts can be categorised as: wall function approaches (briefly discussed above), two-layer models and manual/implicit controlling of the RANS-LES interface by modifying the length scale blending function. Two layer models, first proposed by Balaras and Benocci (1994), use a coarse grid LES up to the wall, but embed a second finer grid for solving the near wall layer using the boundary layer equations closed with an algebraic eddy viscosity. The Poisson equation is not solved near the wall and the wall normal velocity is obtained by enforcing mass conservation across the interface. The wall stress components obtained from this inner layer are then applied as a boundary condition to the LES. This method only marginally increases the cost of computation and obtains accurate results in planar channel flow.

In recent advances of the Partially-Averaged Navier-Stokes (PANS) method (Girimaji, 2006), wall functions have been revisited in a VLES approach (Jakirlic et al., 2014). The method blends integration to the wall with equilibrium wall functions (Popovac and Hanjalic, 2007). The planar channel flow is very well predicted for  $Re_\tau = 395$  on a fine mesh, with no evidence of a log-layer mismatch. This is unsurprising however, as the model contribution was very low and as such the modelled log-layer is absorbed fully into the buffer layer.

In unified modelling, such as DES and FSM discussed above, methods have surfaced that more directly control the RANS-LES interface to reduce the grid sensitivity of the switch. Piomelli et al. (2003) introduced a backscatter method in the inner layer of DES, which helped breakdown the large streamwise streaks. Introduced as a proof of concept only, with no physical justification to the forcing term, the modelled log-layer was removed somewhat. Spalart et al. (2006) detailed the Delayed Detached Eddy Simulation (DDES) formulation which controls the length scale, whilst Weinmann et al. (2014) used a similar function that effectively acts on the model dissipation rate  $\varepsilon$ . These two approaches are the primary subject of this chapter, in an effort to marry the novel damping functions, Eq. 6.10 and Eq. 6.11, to the near wall region.

The DDES method uses the equation,

$$\ell^{\text{hyb}} = \ell_t - f_d \min \left( 0, \ell_t - F \ell_t \right), \quad (7.8)$$

where for the standard DDES approach,  $F = C_{\text{des}} \Delta / \ell_t$ . Equation 7.8 is a generalisation to other damping function options.  $f_d$  is given as,

$$f_d = 1 - \tanh(24r_d^3), \quad (7.9)$$

with

$$r_d = \frac{\nu_{sgs} + \nu}{\sqrt{\partial_{x_j} u_i \partial_{x_j} u_i \kappa^2 y^2}}. \quad (7.10)$$

$\kappa = 0.41$  is the von Kármán constant.  $r_d$  decides whether the point is inside the boundary layer, based on the effective viscosity and the length scale is adjusted using Eq. 7.8.

Weinmann et al. (2014) however, uses the switch on the damping function itself,

$$F = \min \left( \frac{F_{damp}}{1 - f_b}, 1.0 \right), \quad (7.11)$$

where the notation  $F_{damp}$  is used briefly to distinguish between near wall modification and length scale damping.  $f_b$  is the blending function,

$$f_b = \tanh \left( C_{f_b} \frac{500 \beta^* k \nu^4}{y^2 \varepsilon} \right). \quad (7.12)$$

$C_{f_b} = 16$  is a calibration coefficient. The original semantics for this asymptotic damping of  $F$  described the switch as a zonal phenomena and as such this author adopts the notation for the generic methodology as  $F_z$ , yet as the original formulation suggested two more functions over  $f_b$ ,  $F_{f_b}$  is used for complete distinction.

The function  $f_b$  is designed to be 1 at the wall and as such the limiter in Eq. 7.11 is activated. As  $f_b \rightarrow 0$  there is an interaction with  $F_{damp}$  such that the LES mode is not activated until the length scale is moderately damped. Once the limiter is no longer active, one can think of the philosophy in terms of the full dissipation term,

$$\varepsilon = (1 - f_b) \frac{k^{3/2}}{\ell^{hyb}}, \quad (7.13)$$

which implies a damping of the turbulence model linear in the boundary layer identification function. This is the inverse to the DDES approach which linearly damps  $\ell^{hyb}$  and asymptotically damps  $\varepsilon$ .

These two approaches to controlling the near wall switch are applied to the hybrid length scale damping functions presented in Chapter 6, namely Eq. 6.10 and Eq. 6.11. The test case is the planar channel flow. Each methodology is examined by observing their statistical predictions but also by looking at instantaneous structures within the flow field. The latter uses Gene Expression Programming to group structures of Reynolds stress from a DNS into distinct types. This grouping is then applied to the flow fields from Hybrid RANS/LES simulations to ascertain details about the artificial near wall turbulence. Further, two numerical schemes for convection are compared, one that blends between forward and central differencing for the RANS and LES zones respectively and one with a constant 95%-5% ratio between the two. This is to look at whether this is indeed a necessary requirement.

	damping	RANS model	convection scheme	near wall
FSM-SSG-95-5-DDES	FSM	SSG	blended 95-5	DDES
FSM-SSG-95-5-Fz	FSM	SSG	blended 95-5	$F_{f_b}$
FSM-SSG-HYB-Fz	FSM	SSG	HYB	$F_{f_b}$
HYB-SSG-95-5-DDES	HYB	SSG	blended 95-5	DDES
HYB-SSG-95-5-Fz	HYB	SSG	blended 95-5	$F_{f_b}$

TABLE 7.1: Hybrid RANS/LES cases considered for the planar channel flow.

## 7.2 Planar Channel Flow

### 7.2.1 Problem Definition

The turbulent channel flow simulation used is described as follows. The Reynolds number based on friction velocity  $u_\tau$  and channel half height  $h$  is  $Re_\tau = 590$ . The grid is deliberately prescribed so as to force the Hybrid RANS/LES to run with the so called ‘grey-area’ buffer layer. To achieve this  $\Delta_x \approx h/20$  and  $\Delta_z = \Delta_x/2$ . The streamwise spacing is set to match the original diagnosis by Spalart et al. (2006). Normally  $\Delta_x \geq \Delta_z$ , which assumes that the smallest structures are streaks. Note, the grid here is set such that near wall superstreaks of domain length are not governed by an overly coarse spanwise spacing (e.g. Baggett, 1998). Because the Hybrid RANS/LES formulation does not utilise wall functions,  $y_1^+$  is set to 0.7. These grid requirements are satisfied by a computational domain of  $2\pi \times h \times \pi$  spanned by  $108 \times 108 \times 108$  cells.

Table 7.1 details the cases considered. Damping is either FSM or HYB, corresponding to the functions Eq. 6.10 and Eq. 6.11. The blended convection corresponds to central differencing with 5% stabilising upwind globally and HYB convection is the hybrid blending scheme of Weinmann et al. (2014) that dynamically allocates central differencing in LES zones and upwinding in RANS. The near wall treatments DDES and  $F_{f_b}$  are Eq. 7.8 and Eq. 7.11 respectively. This series of cases tests several topics of interest. Firstly, under scrutiny are the novel damping functions produced by the GEP algorithm in Chapter 6. Secondly, the near wall RANS-LES switches can be directly compared with both damping functions. Finally, the necessity of using a blending scheme that recovers upwinding for RANS is considered. The SSG RANS model is that of Speziale et al. (1991), a non-linear explicit algebraic stress model.

In all cases, linear upwinding is used for turbulent quantities, velocity convection as outlined by Table 7.1 and backward marching in time is used. The grid scale is defined as the cube root volume  $\Delta = (\Delta_x \Delta_y \Delta_z)^{1/3}$ .

### 7.2.2 Statistical Results and Comments

Presented in this section are the time-, span- and stream- wise averaged quantities of typical interest in a planar channel flow. Table 7.2 is a list of global results for each case. The percentage skin friction error  $C_f^{\text{err}}$  is calculated as the difference from the estimate of Dean (1978),

$$C_f^{\text{err}} = 100 \cdot \frac{C_f - C_f^{\text{Dean}}}{C_f^{\text{Dean}}}, \quad (7.14)$$

where,

$$C_f^{\text{Dean}} = 0.073 \text{Re}_b^{-1/4} \quad (7.15)$$

and  $\text{Re}_b$  is the bulk Reynolds Number,

$$\text{Re}_b = 2U_b h / \nu. \quad (7.16)$$

$U_b$  is the average velocity in the channel. Typically Hybrid RANS/LES underestimates the skin friction in the order of 10-15%. It is unusual for a methodology to overestimate this quantity as observed by the cases -95-5-Fz. The contribution to skin friction can be observed as (Fukagata et al., 2002),

$$\frac{C_f}{4} = \frac{1 - \delta_d}{\text{Re}_h} - \frac{1}{h} \int (h - y) \bar{\tau}_{12}^{\text{sgs}} dy - \frac{1}{h} \int (h - y) \bar{\tau}_{12}^{\text{res}} dy. \quad (7.17)$$

This equation depends on the contributions from modelled and resolved shear stress and the shape of the boundary layer through the mean displacement thickness  $\delta_d$  and the Reynolds number  $\text{Re}_h = \bar{u}_\infty h / \nu$ . As such, the contribution from the first term is generally underpredicted because of the incorrect buffer layer. This is certainly the case for -95-5-Fz cases, which exhibit the latest switch to LES ( $F_{\text{switch}} = \min\{y|\bar{F} < 1\}$ ). Consequently the modelled log-layer has had plenty of time to set in, however errors have been cancelled by an overprediction of resolved stress in the bulk. See Fig. 7.1 for velocity profiles and Fig. 7.2 for the Reynolds shear stress break down. This cancellation of errors yields a minor overprediction in skin friction, but should not count in favour of the method and favourable predictions are unlikely to hold for other cases. Using the hybrid convection scheme does not generate this issue, as the resolved fluctuation generation at the interface is not as intense and therefore the skin friction is underpredicted due to the first term in Eq. 7.17. The DDES cases perform much more favourably, with only minor underpredictions resulting from an incorrect buffer layer but a correct log-layer intercept. The exception to this is the HYB-SSG-DDES-95-5, for which  $F_{\text{switch}}$  occurs on the edge of the viscous layer and consequently a log-layer intercept slightly too high.

Figure 7.1 is a plot of streamwise velocity for all cases. Encouragingly, the resolved log-layer is universally well predicted, implicating the success of the novel damping functions. Large discrepancies in the buffer layer, as alluded to above, can be observed between the near wall controlling methods.  $\delta_{\text{buff}}^+$  in Table 7.2 is defined as the distance

	$C_f^{\text{err}} (\pm\%)$	$y^+(\bar{\tau}_{12}^{\max})$	$y^+(\bar{\tau}_{12}^{\max})$	$y^+(\bar{\tau}_{12}^{\max})$	$F_{\text{switch}}^+$	$\delta_{\text{buff}}^+$
FSM-SSG-95-5-DDES	-4.47	15.69	84.27	53.89	17.67	68.58
FSM-SSG-95-5-Fz	+1.51	25.39	145.36	55.54	72.82	119.97
FSM-SSG-HYB-Fz	-5.18	27.25	152.81	53.67	76.89	125.56
HYB-SSG-95-5-DDES	-10.98	11.76	68.20	62.37	6.41	56.44
HYB-SSG-95-5-Fz	+2.08	25.69	145.79	55.70	79.80	120.32

TABLE 7.2: Error in skin friction, location of the peak modelled, resolved and total stresses, the RANS-LES interface and the size of the buffer layer for each case. The latter is defined by the distance between the modelled and resolved peaks.

between the peak of resolved and modelled stresses. For the -Fz cases, this number is approximately twice the -DDES cases which increases the time the flow field feels the RANS model. Whilst resolved structures are developing, the artificial log-layer is observed for approximately 80% of this buffer region. This motivates the development of a switch much faster than both DDES and Fz which correspondingly have artificial log-layers approximately 35 and 90 wall units in size. Faster is meant in the transition sense, not the location of  $F_{\text{switch}}$ .

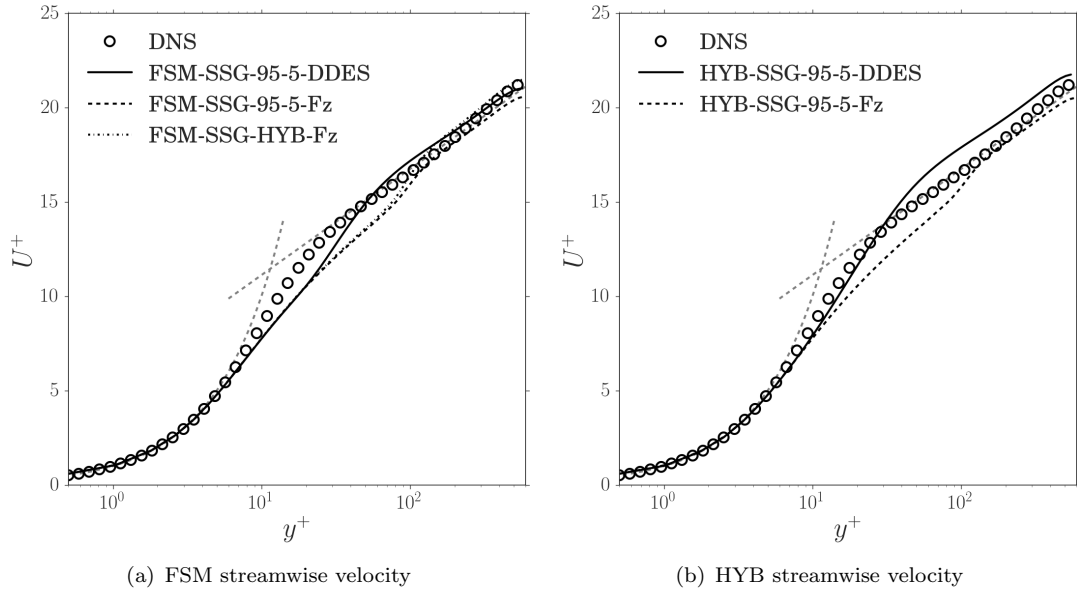


FIGURE 7.1: Average streamwise velocity for all cases.

Also alluded to in Table 7.2, is the amount of model and resolved contribution at the peak of shear stress. Compared with -DDES cases, -Fz cases produce a  $y^+(\bar{\tau}_{12}^{\max})$  much closer to  $y^+(\bar{\tau}_{12}^{\max})$ , again due to the late switch to LES. Consequently, predictions of peak values rely much more heavily on the quality of the turbulence model and less on resolved structures. A further comment on the underlying RANS model dependence can be deduced from plots of Reynolds stresses in Fig. 7.4. The growth of  $\bar{v}'v'$  at the wall is much too quick for all cases as it is governed by  $\bar{\tau}_{22}^{\text{sgs}}$ . The SSG turbulence model does not

contain any specific damping of this component, which should grow to the fourth power with wall distance, not the second as with the other normal components. As a result, some authors have combined Hybrid RANS/LES with an elliptic blending turbulence model (e.g. Weinmann, 2011; Jakirlic et al., 2014). One can see minor oscillations in the total stress profiles in Fig. 7.2. This is because the gradients of  $\overline{\tau_{12}^{\text{sgs}}}$  and  $\overline{\tau_{12}^{\text{res}}}$  are not equal and opposite. Small changes in the gradients will produce kinks in the their sum. This is a grid dependent phenomena, as the growth of the resolved structures depends on this. To remove this issue, the near wall switching mechanism must change. The resolved shear stress component grows much quicker than the normal counterparts and as such, the gradient is much greater. Individual damping of the components in the near wall region would help to solve this problem.

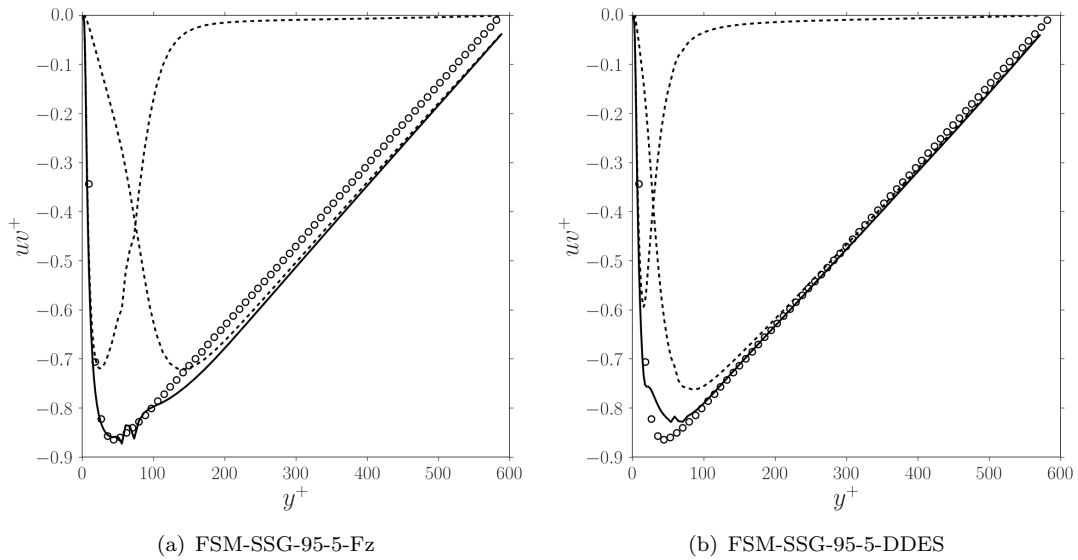


FIGURE 7.2: Shear stress for the differing wall methodologies. Dashed lines depict the modelled and resolved contributions.

Normal stress plots of Hybrid RANS/LES channel flows are somewhat of a rarity in the literature. Yet these stresses provide vital information with regards to the capability of the switching function. One could argue that the incorrect growth of  $\overline{v'v'}$  is not relevant because the main issue is the anisotropy of the normal stresses in the far field. An overprediction in the resolved  $\overline{u'u'}$  has not been redistributed correctly to the other components and can at worst be seen in the -95-5- cases. To illustrate, Fig. 7.6 is a plot of the anisotropy tensor  $b_{ij} = \overline{u'u'}/2k - 1/3\delta_{ij}$ . Note, this has not overly impacted on the turbulent kinetic energy (Fig. 7.3).

The -Fz cases also display twin peaks, most notably in the streamwise stress. This is an unfortunate consequence of a late  $F_{\text{switch}}$ . The switching function does not stop the development of artificial near wall turbulence, rather just delays. It is like the LES component of the flow field sees a wall at  $F_{\text{switch}}$ , using the mean velocity gradient at this location to generate the large streamwise structures. On this topic, the methodology is

on the border line of relaminarising and may be sensitive to such an issue, should  $F_{\text{switch}}$  be placed much further away (either by design or chance), the production term in the  $u'$  equation would not contain enough power through  $\partial_y \bar{u}$  to generate resolved motions. That said, the shear stress is universally well predicted and is unarguably the most vital. Of course, this is unsurprising considering the damping functions were calibrated to predict this quantity with the -HYB-Fz convection scheme and switch.

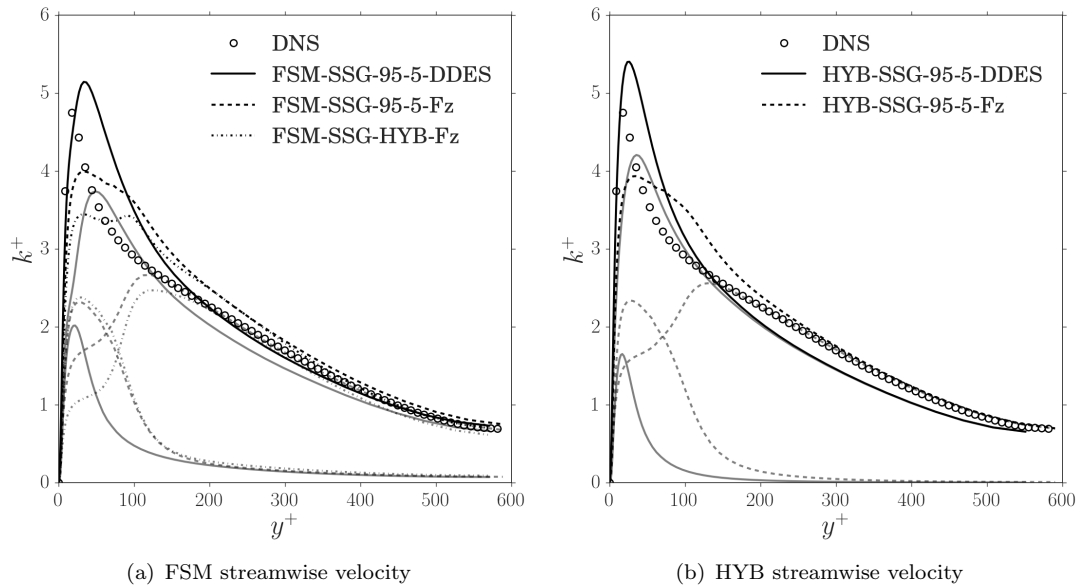


FIGURE 7.3: Turbulent kinetic energy for all cases. Grey lines depicted modelled and resolved contributions.

The SSG model was derived by enforcing a homogeneous turbulence assumption, which has impacted upon the near wall anisotropy. No case reproduces the correct two component nature of the Reynolds stress; this does reflect upon the Hybrid RANS/LES methodology *per se*, rather upon the choice of underlying turbulence model. The invariant map for each case is plotted in Fig. 7.7. The top boundary of the Lumley triangle represents the two component turbulence as the wall is approached. The extreme nature of the axisymmetric contraction moving from the bulk towards the buffer layer is further evidence of the overly strong streamwise component. The non-bijectivity of the Hybrid RANS/LES lines are an echo of the interface where the return to isotropy by the modelled stress is interrupted by the development of fluctuations. This is also the cause of the kinks in  $b_{ij}$ . Generally speaking, the -DDES cases have a marginally better bulk anisotropy than the -Fz, because of the delayed development in the latter. The exception to this is the HYB convection case, which has damped fluctuations somewhat.

Finally, a look at the average  $F$  for each methodology is plotted in Fig. 7.5. It should be noted that in this application,  $F$  is almost a passive quantity, reacting to the other mechanisms at play. Hence the reason for it last in this section and for large differences even within the FSM- and HYB- cases. Its job is to react spatially and temporarily to

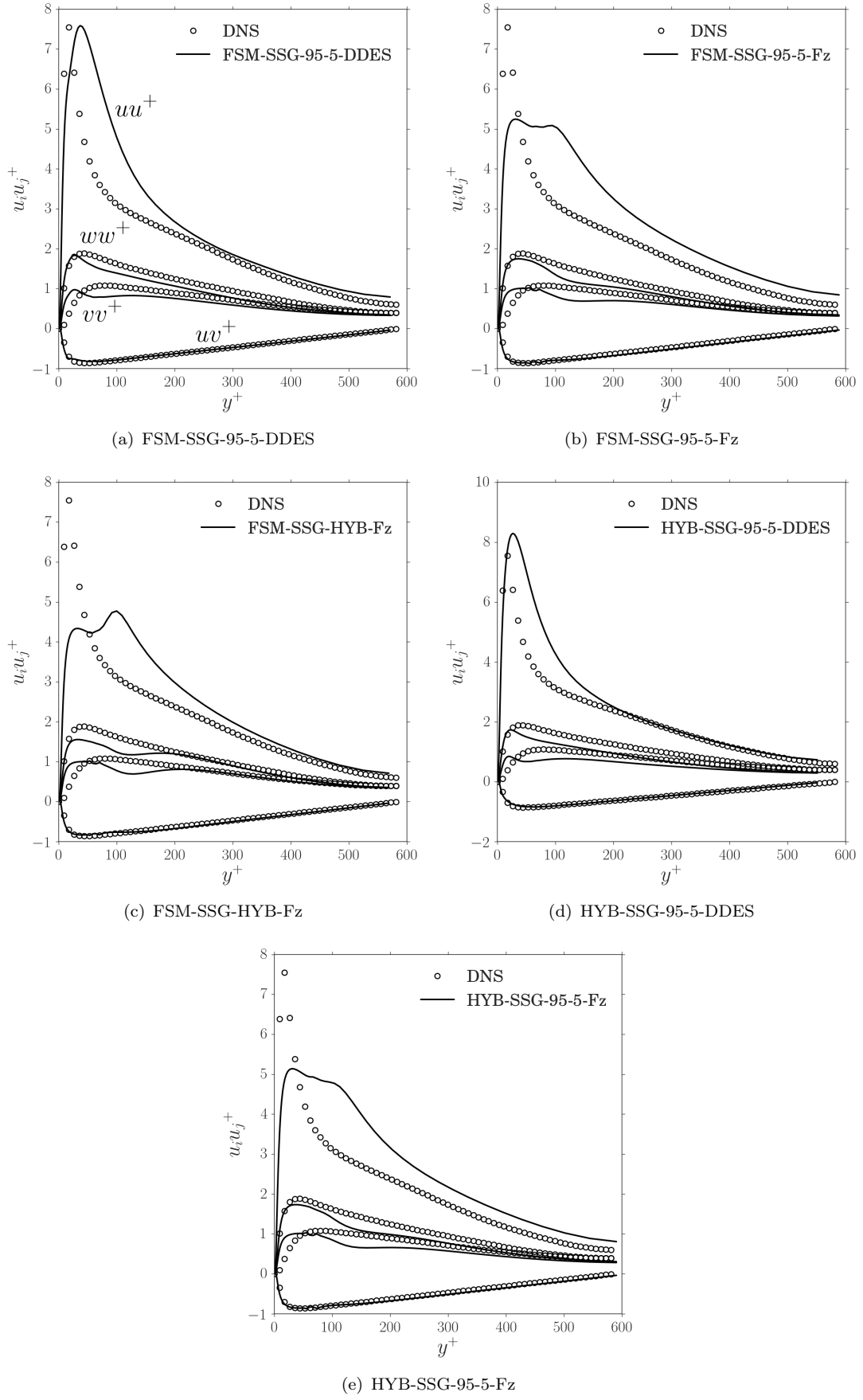


FIGURE 7.4: Total Reynolds stress profiles for each model.

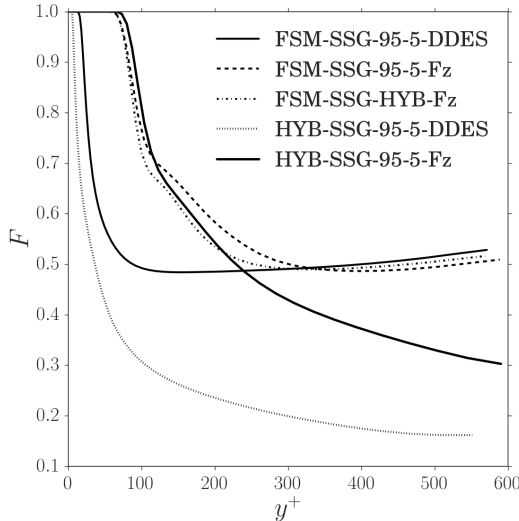


FIGURE 7.5: The length scale damping function  $F$  for each case.

the local turbulence and provide the correct length scale in its presence. It is not responsible for the production of resolved motion, only compensating the lack of. With this in mind and the above discussions, we can see the impact the resolved turbulence has had on  $F$ . Firstly, the -DDES RANS regions end visually closer to the wall. Secondly, the HYB- cases have dropped to a much lower value in the outer layer. This is because the dependence on the Taylor micro-scale, over the integral, effectively reports a lower value of the local turbulent state. The former is describing a scale closer to the grid cut-off, whilst the latter a scale closer to the largest present. One can see that the HYB convection scheme has slightly lowered the value of  $F$  initially, due to the convection being calculated with full central differencing as soon as  $F < 1$ . This increases the production of resolved structures at the interface, however the -95-5-Fz begins the production much deeper in the boundary layer as the numerics does not switch to linear upwinding (see Fig. 7.3). The -DDES cases force a faster damping of the turbulence model (the gradient of  $F$  is greater), through the faster damping of  $\varepsilon$ . This faster damping is then witnessed in  $F$  via a feedback loop with faster creation of resolved eddies.

In summary, statistics from the turbulent channel flow has provided insight into two available RANS/LES interfacing methods for controlling the contribution near the wall. The most successful method (in a statistical sense) is the DDES wall switch. The HYB convection scheme of Weinmann et al. (2014) also must be merited for damping the production of streamwise streaks (if only partially). In the next section, instantaneous structures are extracted to gain a better understanding of the make up of Hybrid RANS/LES flow fields.

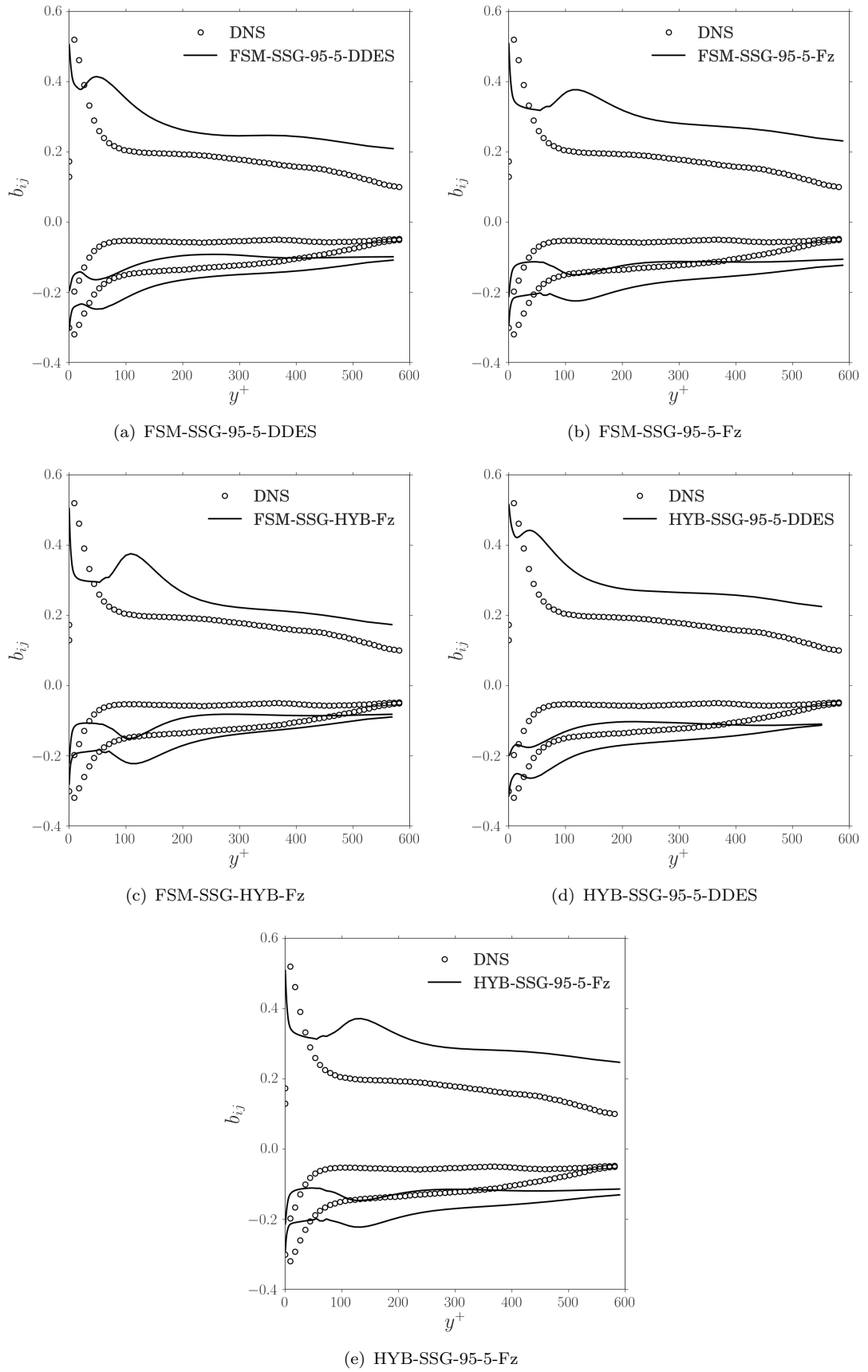


FIGURE 7.6: Anisotropy tensor normal components  $b_{ij} = \overline{u_i u_j}/2k - 1/3\delta_{ij}$ .

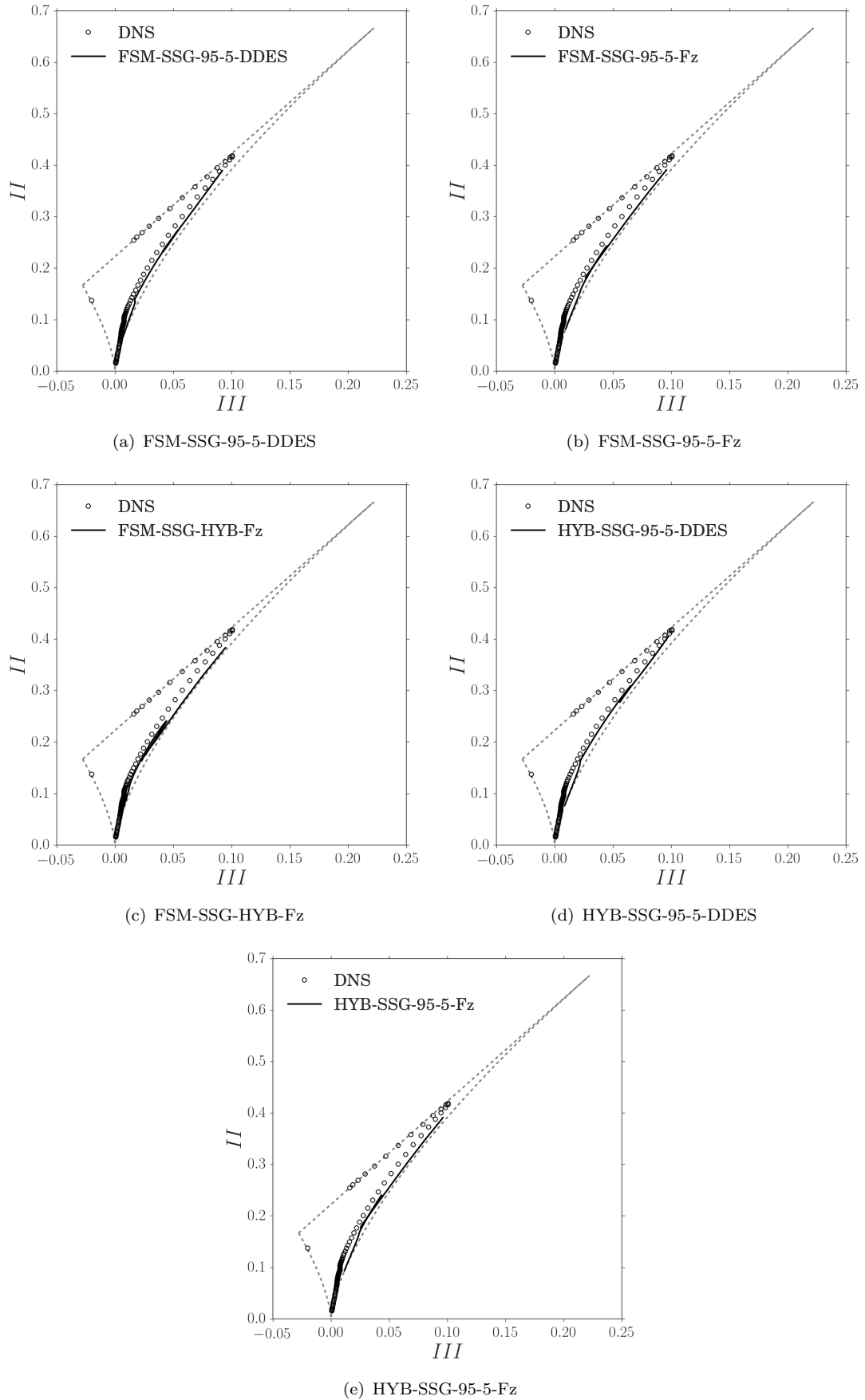


FIGURE 7.7: Invariant map for each case.

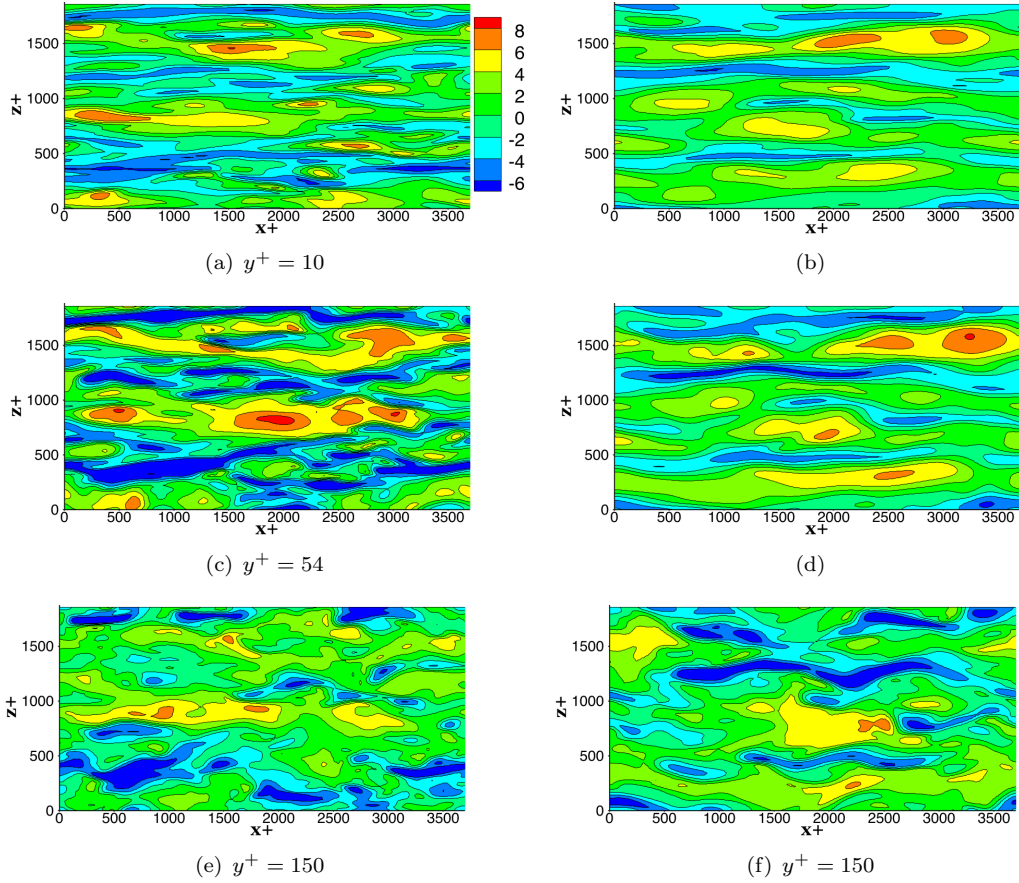


FIGURE 7.8: Streamwise velocity fluctuations at constant  $y^+$  profiles. Left: FSM-SSG-95-5-DDES. Right: FSM-SSG-95-5-Fz.

### 7.2.3 The Instantaneous Flow Field

#### 7.2.3.1 Overview

In order to better understand the statistical flow field and the mechanisms behind the near wall cycle of Hybrid RANS/LES, this section analyses the instantaneous field. In order to reduce the analysis, comments are restricted to the comparison of the two wall switching processes through the cases FSM-SSG-95-5-DDES and FSM-SSG-95-5-Fz.

Figure 7.8 are plots of fluctuating streamwise velocity at different  $y^+$  planes. The first,  $y^+ = 10$ , is deep in the RANS zone for both switching methods. The effective filter at this distance from the wall, primarily the turbulence model, is not enough to fully damp all resolved motions. This is true even for the FSM-SSG-95-5-Fz, where  $F_{\text{switch}}^+ = 72$ . The superstreaks are predominantly negative streamwise velocity, in line with the considerations in Section 7.1. The extended near wall RANS region for the Fz switch has not prevented the formation of near wall eddies, rather has slowed their breakdown, relative to the DDES and at  $y^+ = 150$  one can see the streaks are still present. It is such streaks that are providing the twin peak nature of the streamwise stress and further, the

skewed anisotropy of the normal components in favour of  $b_{11}$ , see Fig. 7.4 and Fig. 7.6. For a more accurate representation of the stress components, at least in a statistical sense, one should therefore focus on either breaking up these structures (e.g. the body force method of Piomelli et al. (2003)) or a tailored anisotropy tensor that takes energy from the  $\overline{u'u'}$  component. The latter could be achieved by considering that the subgrid anisotropy depends on the resolved structures via the strain and rotation tensors or via an anisotropic length scale damping function in place of  $F$ .

### 7.2.3.2 Extracting Turbulent Shear Stress Structures

In order to pursue a deeper understanding of the momentum transfer induced from the interface, structures of Reynolds shear stress are extracted from the flow field. To compare directly with DNS, the channel data of Del Álamo et al. (2004) is also given the same treatment, detailed by Lozano-Durán et al. (2012). Here a brief description of the methodology is given. A structure  $\mathcal{S}$  is defined as a connected region of space that satisfies,

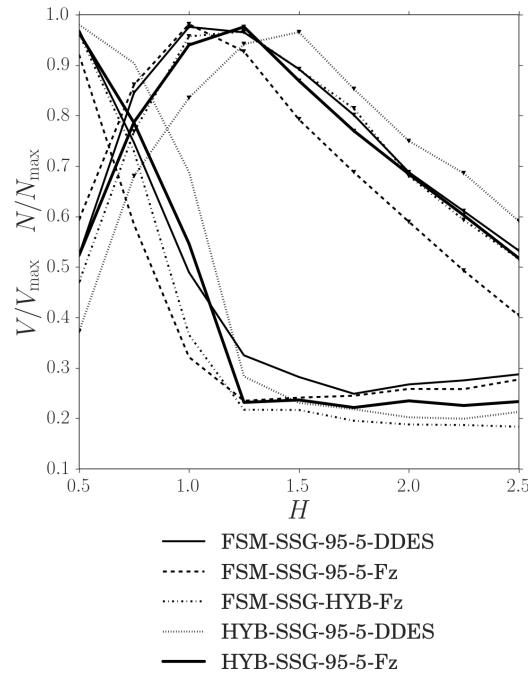
$$|u'v'(x, y, z)| \geq H \cdot u^{\text{rms}}(y)v^{\text{rms}}(y). \quad (7.18)$$

Connectivity is defined by considering the six adjacent points in the mesh including the periodic boundaries. Percolation analysis by Lozano-Durán et al. (2012) showed that a hyperbolic hole size  $H = 1.75$  yielded the highest number structures for the DNS. Because of the effective filter of the Hybrid RANS/LES, this value of  $H$  is not relevant and a new one must be found. Figure 7.9 is a percolation diagram of  $N/N_{\max}$  and  $V/V_{\max}$  for all cases in Table 7.1.  $N$  is the number of structures in a snapshot and  $V$  the volume of the largest in a given snapshot. The max subscript denotes the maximum found for all values of  $H$  in the percolation. Each line is an averaging over 20 snapshots from each case. The value  $H = 1.75$  is too high for the hybrids – the number of structures yielded by applying Eq. 7.18 is not maximal. Instead the value  $H = 1.25$  is taken to extract the highest number of structures across all hybrid cases. All cases are included to briefly note that the HYB- cases yield more structures than the FSM- showing that the nature of  $F$  (Eq. 6.11 compared to Eq. 6.10) has lowered the effective filter and fundamentally changed the resolved flow field, see Fig. 7.5. Lozano-Durán et al. (2012) points out that values of  $H \approx 1 - 3$  yield quantitatively similar results, so the value of  $H = 1.25$  is adopted for the Hybrid RANS/LES with confidence of making relevant comparisons. To give the reader an idea of the resolution difference between the Hybrid RANS/LES, this process yields approximately 5000 structures per DNS snapshot, but only 84 per hybrid. When one takes into account the differing size of the computational domains, the DNS produces approximately 6 times as many structures. Relating this factor to the different grid sizes, the grid is approximately 3 times coarser in both the stream- and span- wise directions and 4 times coarser in the wall normal. This reveals that halving the grid scale results in 3.3 times the number of structures. This last statement is confirmed with a simulation where the grid is coarsened by a factor of two in both the

quantity	definition	description
$y_{\min}/h$	$y_{\min} = \inf\{y_i   \underline{x}_i \in \mathcal{S}\}$	lowest point in the structure
$y_{\max}/h$	$y_{\max} = \sup\{y_i   \underline{x}_i \in \mathcal{S}\}$	highest point in the structure
$\ell_x/h$	$\ell_x = \sup\{x_i   \underline{x}_i \in \mathcal{S}\} - \inf\{x_i   \underline{x}_i \in \mathcal{S}\}$	streamwise extent of structure
$\ell_z/h$	$\ell_z = \sup\{z_i   \underline{x}_i \in \mathcal{S}\} - \inf\{z_i   \underline{x}_i \in \mathcal{S}\}$	spanwise extent of structure
$\bar{u}^+$	$\bar{u} = \int_{\mathcal{S}} u' dV / \int_{\mathcal{S}} dV$	average streamwise fluctuation
$\bar{v}^+$	$\bar{v} = \int_{\mathcal{S}} v' dV / \int_{\mathcal{S}} dV$	average wall normal velocity
$\bar{w}^+$	$\bar{w} = \int_{\mathcal{S}} w' dV / \int_{\mathcal{S}} dV$	average spanwise velocity
$\mathcal{V}/h^3$	$\mathcal{V} = \int_{\mathcal{S}} dV$	volume of structure

TABLE 7.3: Features of each structure considered.

stream- and span- wise directions. The total number of structures in one snapshot is approximately 24, the grid scale is 2/3 times smaller in the cases included in this chapter and the ratio of structures is 3.5. This comparison is with the FSM-SSG-95-5-DDES; Fz cases significantly reduce the number of structures because of the effective filter.

FIGURE 7.9: Percolation diagram of the number of structures  $N/N_{\max}$  and volume  $V/V_{\max}$  ratios and against  $H$ . Lines with symbols are  $N/N_{\max}$  and lines without symbols is  $V/V_{\max}$ 

Once a set of structures has been extracted from the flow, several features can be calculated for each  $\mathcal{S}$ . Table 7.3 is the list used in this study. This gives an eight dimensional parameter space defining each structure. Care is taken to ensure structures crossing periodic boundaries are given the correct length scales. Further, structures closer to the top wall are reflected in the plane  $y = h$  to ensure that  $y_{\min}$ ,  $y_{\max}$  and  $\bar{v}$  are of the same orientation as the bottom wall. Figure. 7.10 visualises the quantities of Table 7.3 for

an extracted structure from the case FSM-SSG-95-5-DDES. The size of the structure is approximately 650 wall units in length.

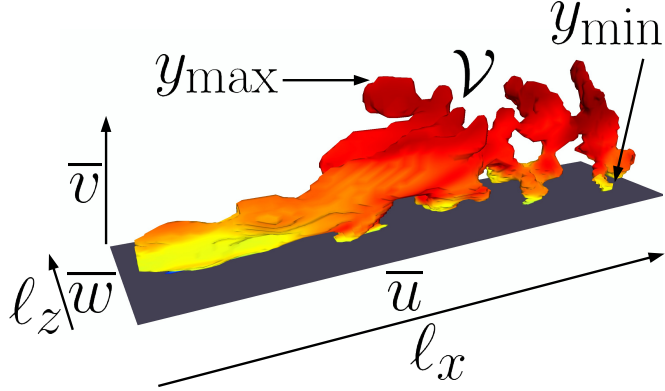


FIGURE 7.10: Extracted structure from FSM-SSG-95-5-DDES. Quantities from Table 7.3 are included for visual reference. Length of the structure is approximately 650 wall units. The structure is coloured by the flow field average velocity magnitude.

Quadrant analysis (Wallace et al., 1972; Willmarth and Lu, 1972) can be performed by considering the signs of  $\bar{u}$  and  $\bar{v}$ . The most common types of structures are ejections (Q2's,  $\bar{u} < 0, \bar{v} > 0$ ) and sweeps (Q4's,  $\bar{u} > 0, \bar{v} < 0$ ), smaller interactions of outward (Q1,  $\bar{u} > 0, \bar{v} > 0$ ) and inward (Q3,  $\bar{u} < 0, \bar{v} < 0$ ) natures complete the quadrant.

The DNS data, used as comparison, is at a higher Reynolds number  $Re_\tau = 950$ ; this is not an issue because the flow fields analysed by Lozano-Durán et al. (2012) at  $Re_\tau = 950$  and  $Re_\tau = 2000$  yielded similar results under the normalisation presented in Table 7.3. This statement is excepting the size of the largest structures, for which there was a Reynolds number dependence. Structures with  $\mathcal{V}^+ < 30^3$  were removed from the DNS flow field to avoid grid resolution issues.

Each structure represents a point in the feature space defined by Table 7.3. In order to identify distinct types of structures, a clustering algorithm is applied. This is a clustering in feature space of the extracted structures, not on the cartesian mesh, in other words a grouping of structures with similar length scales, velocities, etc. A clustering  $\mathcal{C}$  is defined as a list of centroids  $c_i$  that describe  $n$  groups of characteristic structures,

$$\mathcal{C} = \{c_i | c_i \in \mathbb{R}^8, i = (0, 1, \dots, n - 1)\}. \quad (7.19)$$

$c_i = ((y_{\min}/h)_i, (y_{\max}/h)_i, (\ell_x/h)_i, (\ell_z/h)_i, \bar{u}_i, \bar{v}_i, \bar{w}_i, (\mathcal{V}/h^3)_i)$  is therefore a list of characteristics of a ‘typical’ structure in group  $i$ . Each structure  $\mathcal{S}$  is assigned to a group by ascertaining the nearest  $c_i$  via the Mahalanobis distance (Eq. 4.29).

In order to determine the grouping, Gene Expression Programming (GEP) is applied to automatically define  $\mathcal{C}$ . Essentially an implementation of Zheng et al. (2012) is used,

Group	Description	DNS freq.	DDES freq.	Fz freq.
0	small wall attached/ detached structures	0.447	0.793	0.889
1	small wall attached ejections	0.279	0.142	0.0327
2	small wall attached sweeps	0.267	0.0431	0.00552
3	medium sized structures	0.00565	0.0224	0.0236
4	large structures	0.000418	0	0
5	super-size structures	0.000314	0	0

TABLE 7.4: The six different types of structure found by the GEP algorithm. The frequencies are for the DNS, FSM-SSG-95-5-DDES and FSM-SSG-95-5-Fz cases — the column headings are abbreviated for space.

although with a few modifications to account for ambiguities in the original methodology. This methodology is described in Section 4.4.

### 7.2.3.3 The Groups of Extracted Turbulent Shear Stress Structures and a Brief Defence of its Use

In Section 7.2.3.2, the methodology for extracting shear stress structures is described. This section introduces the grouping of extracted structures for the DNS, FSM-SSG-95-5-DDES and FSM-SSG-95-5-Fz and gives a brief defence of its use. The two hybrid cases chosen provide a direct comparison between the two wall switching methods. Some concerns were raised about using the full DNS as reference, instead of filtered DNS flow fields. No filtering is applied for several reasons. Firstly the benchmark must always be reality; in order to see the full effect of Hybrid RANS/LES in the vicinity of walls one must compare to DNS. It is believed this is the first study of this kind for Hybrid RANS/LES and it is required by model developers to know just how wrong Hybrid RANS/LES is. Secondly, the filter in Hybrid RANS/LES is a blurred combination of the turbulence model and the grid. This filtering inherently contains history effects embedded in the resolved structures such as: how the structures form, grow and merge, the contribution of the subgrid model contains a significant portion owed to convection of near wall values and the effect of the mechanisms in the artificial buffer layer propagate through the flow field. None of these phenomena are captured via filtered DNS. Finally, applying a convolution operator to a flow field that is never actually used in Hybrid RANS/LES does not provide a meaningful comparison. Common convolution operators, such as the box and Gaussian, cannot capture the instantaneous change in the strength of the Hybrid RANS/LES filter. As mentioned, the turbulence model plays a part in the implicit filtering of Hybrid RANS/LES which is a very dynamic process and is not by any means an operation at a constant wavenumber.

Table 7.4 is a list of the six groups identified by GEP. Each group is defined by a vector  $c_i$  and forms a complete clustering  $\mathcal{C}$  of the DNS data set, see Eq. 7.19. This clustering is

treated as a rule and applied to the Hybrid RANS/LES. Each extracted structure in the FSM-SSG-95-5-DDES and FSM-SSG-95-5-Fz cases is assigned a group by determining the nearest  $c_i$ . This is done in Mahalanobis space, defined by the metric in Eq. 4.29. Standard Euclidean space is not used for the group assigning, because the make-up of the flow fields are fundamentally different and groupings should be defined by their relative differences with other structures from the same flow field. It should be noted that the main argument for using filtered DNS is that the ratio of small to large structures is very different for the DNS and hybrid cases. However, by using Eq. 4.29 to define the distance, this is circumvented somewhat.

A brief description of each type of group is given in Table 7.4, serving as a reference and the distinct nature of each type of structure will be explored further throughout the next section. The colour for each group serves as a visual reference, every plot containing different groups of structures uses these colours for easy visual identification. This is one of the beauties of giving each structure a distinct type. One can instantly see how certain types of structures fit into a flow field, making conclusions instantly evident. That said, one must apply a level of caution — a clustering is not optimal for human consumption. The algorithm does not know sensible values for where to draw boundaries, say  $\bar{u} = 0$ . Whilst the algorithm has done a very good job of finding such distinctions unsupervised, there are a few structures that a human would place in a different group. This can be a problem considering the huge difference in the relative sizes of the groups - see Table 7.4. Just a few structures in the ‘wrong’ group can mislead the reader. So whilst visual identification of patterns is extremely useful, one must still check any meaningful conclusions manually.

Another criticism of the method is that Table 7.4 is just one grouping and that a further application of the algorithm would provide a different  $\mathcal{C}$ . This is completely true and the argument implicitly raises an attack on two fronts. For the defence of pure optimality of the algorithm, in terms of finding  $\mathcal{C}$  such that,

$$\sum_{x_i \in \mathcal{X}} d(x_i, c_j) \cdot s_{ij} \quad (7.20)$$

is minimal for all data points  $\mathcal{X}$  is practically impossible.<sup>1</sup>  $s_{ij}$  is 1 if  $x_i$  belongs to group  $j$  and 0 otherwise. With the used chromosome head length of 20 and the number of DNS structures totalling 10000 in the training data, the degrees of freedom in an individual is up to  $20^{10003} \cdot 21^{10000}$ . Whilst this upper bound is never hit, a more realistic estimate would lie between this and  $20^3 \cdot 21^{10000}$ , it is clear to the reader that we do not have any computer or method capable of an optimisation on this scale. Note that once a clustering has been found, the centres  $c_i$  of each group are recalculated by using all data points in each group. This helps to ensure each structure belongs to the correct  $\mathcal{C}$ .

---

<sup>1</sup>This is assuming that  $n$  is a practical value. Clearly  $\mathcal{X} = \mathcal{C}$  minimises Eq. 7.20.

For the defence of using a particular clustering, in this case Table 7.4, the algorithm often finds similar groupings and secondly it should be recalled each structure is given a distinct group, allowing for immediate visual representation of an entire set of flow fields. So whilst it is only one particular grouping of the extracted structures, it still provides insight into the make up of the respective flow fields.

#### 7.2.3.4 Comparisons of Extracted Turbulence Shear Stress Structures

Table 7.3 provides an eight dimensional space for analysis and in this section decompositions of this space are provided in order to draw conclusions about Hybrid RANS/LES. From Table 7.4, one can see that approximately 45% of all DNS structures are group 0. These are best understood by considering Fig. 7.11, a histogram of  $y_{\max}$  against  $y_{\min}$ . They form the thin region from  $y_{\max} = y_{\min}$  to  $y_{\max} = y_{\min} + 0.3h$ . This coefficient provides insight into the maximum vertical size of this group. Structures above this are formed by group 3, however they do not feature in the histogram due to their relative rarity. Group 0 is effectively the work-horse group; it does not contain anything particularly interesting. They exist in all four quadrants of velocity, see Fig. 7.13 and are more homogeneous in shape than the other groups (if slightly flatter in the wall normal direction), see Fig. 7.14. Figure 7.11 shows that groups 1 and 2 both exist very close to the wall, but sit in different velocity quadrants. Group 1 structures are small near wall ejections and group 2 structures are small near wall sweeps. From Fig. 7.11, we can see that the small sweeps start from higher than the near wall ejections. The major difference between group 0 and group 1 and 2 is their velocity magnitude; group 0 contains structures with a lower fluctuation value.

Figure 7.14 is a histogram of spanwise length against streamwise length. The regression line  $\ell_x = 2.75\ell_z$ , fit by considering group 0, 1 and 2 data is also included. This is very similar to the linear relation  $\ell_x = 3\ell_z$  (Lozano-Durán et al., 2012), however the regression line in Fig. 7.14 is only including structures with  $\ell_y < 0.3h$  (Fig. 7.11) and  $\mathcal{V} \lesssim 20^{-3}h^3$  (see Fig. 7.18). This relation gives an idea of how streaky the smallest structures are and upon further inspection of Fig. 7.14 we can see that the more intense ejections (group 1) sit below this line indicating that these small ejections are longer in the streamwise direction. Figure 7.17 is a histogram of the streamwise length against the volume of the structure. Groups 0, 1 and 2 form a distinct relationship of the form,

$$e^{\ell_x/h} = c(\mathcal{V}/h^3)^m, \quad (7.21)$$

where  $m$  and  $c$  are the gradient and intercept of the regression line respectively. Groups 3, 4 and 5 also satisfy Eq. 7.21, but with different values of  $m$  and  $c$ . One can see therefore, that the smaller structures (groups 0, 1 and 2) have a smaller streamwise length given their volume and the large structures (groups 3, 4 and 5) have a much larger streamwise length. The crossover between the distinct regions is at  $\mathcal{V}/h^3 = 30^{-3}$  and above this

value structures tend to be much longer in the streamwise direction. Generally the largest are wall attached (Fig. 7.11) and near the regression line of Fig. 7.14 indicating that they are very tall and long structures.

Now we come to the second three groups. Groups 3, 4 and 5 only make up 0.6% of all extracted structures, however are much larger in volume. Groups 4 and 5 can almost be considered outliers in the following analysis, with a streamwise length 3-6 channel heights with the largest of all structures having a volume  $\mathcal{V} = 2.33h^3$  — a value 5% of the computational domain for the hybrid cases but its bounding box is almost exactly this computational domain. As no group 4 and 5 structures are present in the hybrid cases, we shall not dwell on them here. Group 3 yields a very interesting pattern by considering its divide with group 0 in Fig. 7.14. This divide can be expressed as,

$$\frac{4}{5}\ell_x + \ell_z = h. \quad (7.22)$$

By use of the regression line, we arrive at  $\ell_x \gtrsim 10h/17$  for group 3 structures. Also considering Fig. 7.11, group 3 are predominantly wall attached with  $y_{\max} > 0.2h$ . These constraints provide information on how large a large structure, above the constraint Eq. 7.22, must be in order to detach. Once  $y_{\max} > 0.4h$  these structures begin to detach and follow the line,

$$y_{\max} = y_{\min} + 0.6h. \quad (7.23)$$

For structures below Eq. 7.22, these detach much earlier. This relationship is shown via the scatter in Fig. 7.12. Note the highlighted points are *all* structures above the constraint Eq. 7.22, not just group 3. In practice this is precisely groups 3, 4 and 5. We can see that these structures do not detach until approximately  $y_{\max} > 0.6h$ . Then by following the included line, Eq. 7.23, these structures keep a constant height.

The volume of the group 3 structures is best shown in Fig. 7.18. The near wall structures range from  $10^{-6} < \mathcal{V}/h^3 < 10^{-1}$ , with group 3 in the range  $40^{-3} < \mathcal{V}/h^3 < 10^{-1}$ . This is a much narrower band of existence than the smaller near wall structures, whom range 4 orders of magnitude. The volume of group 3 structures displays another division in feature space made by GEP in order to distinguish them. It shows that these medium wall attached structures can be categorised by a volume greater than  $40^{-3}h^3$  and above the division dictated by Eq. 7.22. A final remark on this group of structures is that with roughly equal probability they exist as Q2 or Q4 events and only a very small chance of being Q1 or Q3.

Before mentioning the hybrid cases, it is noted that for further understanding of the clustering in Table 7.4, time correlated data should be analysed. First by clustering a snapshot and then tracking the structures temporally. Particularly interesting studies would involve watching the change in group of a given structure. The interaction between group 1 and 2 — the small scale sweeps and ejections — would show how many times in a structure's lifecycle it comes into contact with the wall and by implication crosses  $F_{\text{switch}}$ .

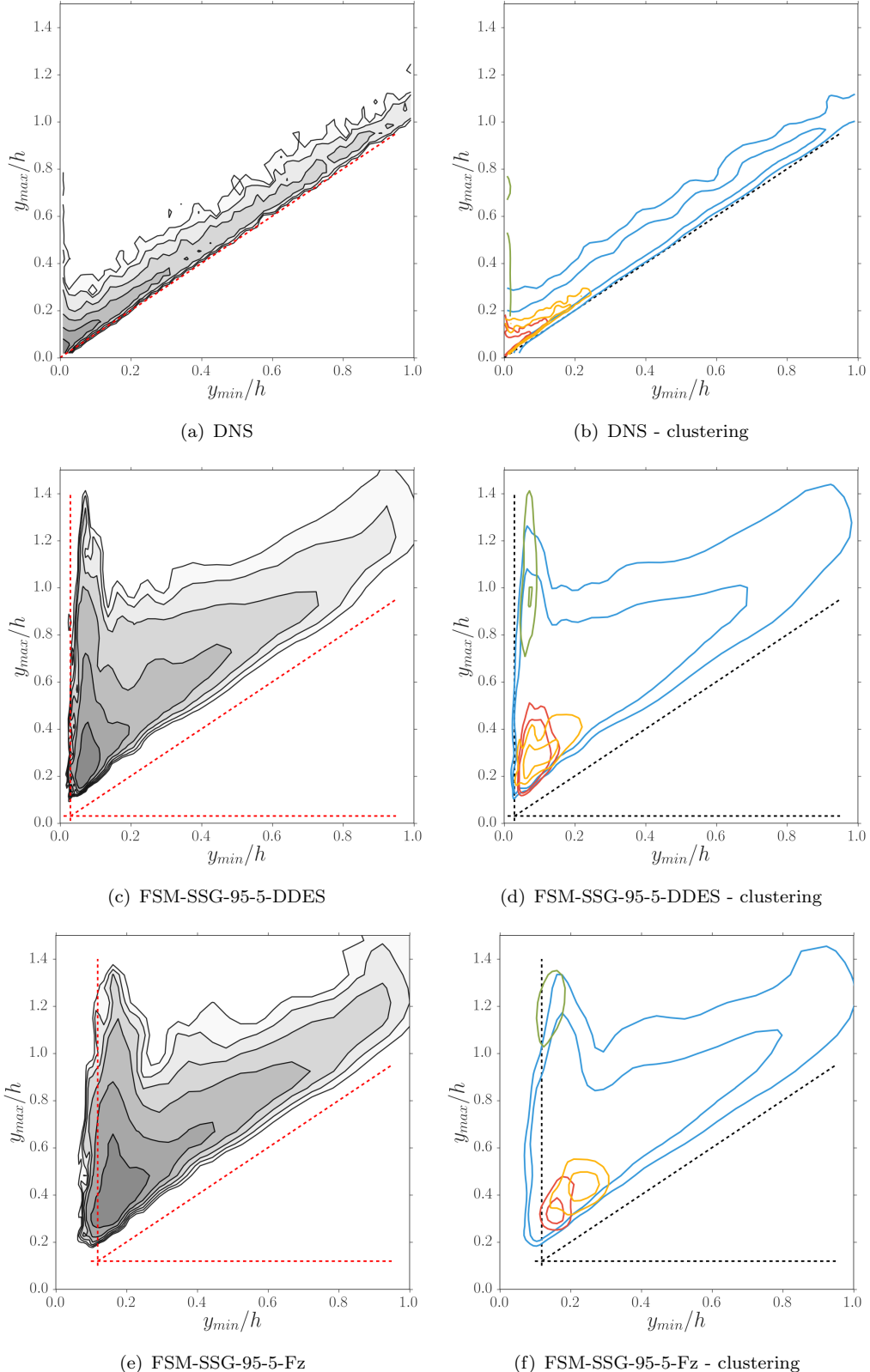


FIGURE 7.11: Probability density function of  $y_{\max}/h$  against  $y_{\min}/h$ . Comparison of DNS with FSM-SSG-95-5-DDES and FSM-SSG-95-5-Fz. Grey contours are the full set of structures, the levels are increments of 10% the maximum value on a logarithmic scale starting from 40%. Coloured lines are contours of each cluster type, colours follow that in Table 7.4. Groups 4 and 5 have been omitted due to too few samples. The levels shown for the cluster groups are 40% and 60% of the maximum on a logarithmic scale. The constraint  $y_{\max} = y_{\min}$  is included, along with  $F_{\text{switch}}$  for the hybrid cases.

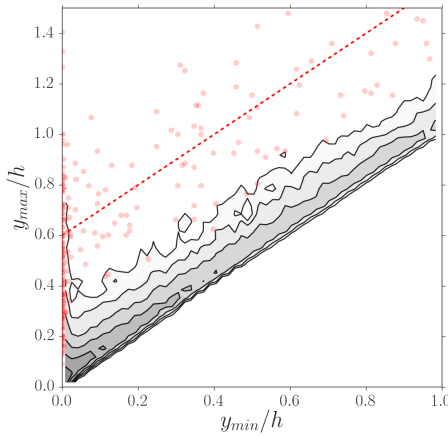


FIGURE 7.12: Probability density function of  $y_{\max}/h$  against  $y_{\min}/h$  for DNS. Grey contours are the full set of structures, levels are 10% increments of the maximum value on a logarithmic scale starting at 40%. Red scatter points are the structures that lie above the line Eq. 7.22. The included line is Eq. 7.23.

Secondly, studies should be conducted into the development of group 3 structures. By following their trajectory through the physical domain and analysing the time history of the detached structures scattered in Fig 7.12, the proportion of detached group 3 structures that originate as an attached group 3 or transition from a detached group 0 can be ascertained. This would provide a good test for the constraint Eq. 7.22 and whether it is a requirement for large structures to detach.

The hybrid cases have been plotted alongside the DNS for comparison in Fig. 7.11-7.18. As the reader has probably noticed, the FSM-SSG-95-5-DDES and FSM-SSG-95-5-Fz cases provide a very different picture of resolved turbulence. Firstly, the success of applying the rule learnt by GEP using the DNS should not be overlooked. Despite clear differences, each of the groupings are qualitative cousins of their DNS counterparts, allowing for direct comparisons. Secondly, the terms attached and detached are seen to mean different things for hybrid and DNS. Due to the near wall RANS zone, the hybrid cases do not contain wall attached structures, as seen in Fig. 7.11. Instead, the ‘attached’ structures can be thought of as ‘interface’ attached. In other words, attached refers to the structures around the RANS-LES switching location,  $y = F_{\text{switch}}$ .

For both FSM-SSG-95-5-DDES and FSM-SSG-95-5-Fz, the frequency of group 0 structures is approximately 1.8 times greater than for DNS. This consequently implies the other groups are much rarer. The lack of group 4 and group 5, large and super-sized structures, is because size is a relative concept. The increased size of the smallest structures means that no structures are deemed to lie in these categories. For DNS, the ratio  $\mathcal{V}_{\max}/\mathcal{V}_{\min} = 2.74 \times 10^6$ , which given the smallest structure in the hybrid cases implies that the domain used is not big enough for the presence of group 4 and 5 structures. However, due to their rarity in DNS, it is not seen as an issue. The high frequency of group 0 can be explained by the RANS-LES interface. The presence of increased

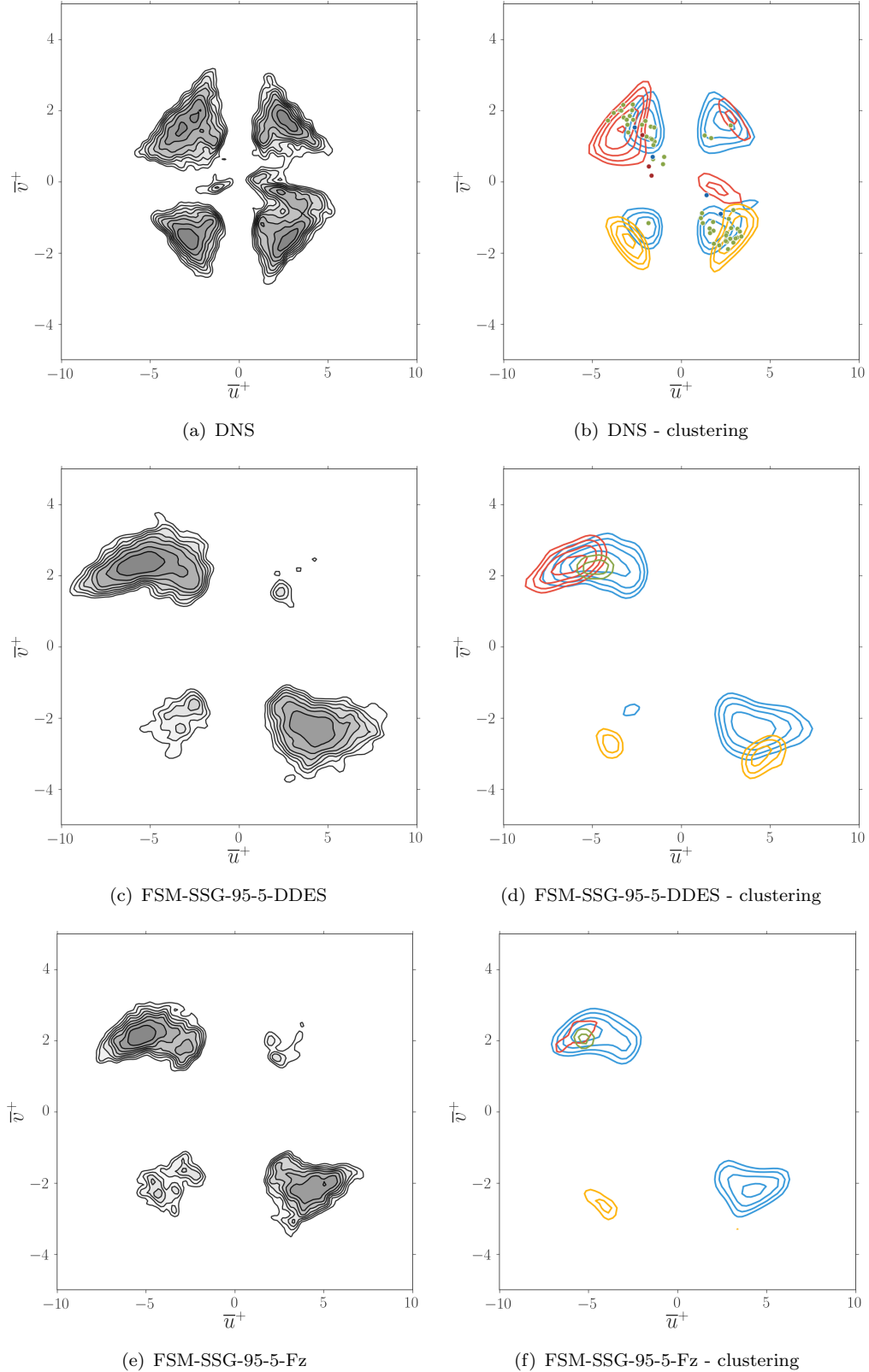


FIGURE 7.13: Probability density function of  $\bar{v}^+$  against  $\bar{u}^+$ . Comparison of DNS with FSM-SSG-95-5-DDES and FSM-SSG-95-5-Fz. Grey contours are the full set of structures, the levels are 10% increments of the maximum value on a logarithmic scale starting from 20%. Coloured lines are contours of each cluster type, colours follow that in Table 7.4. Groups 3, 4 and 5 (DNS only) have been scattered due to too few samples. The levels shown for the cluster groups are 10% increments of the maximum value on a logarithmic scale starting from 50%.

viscosity has reduced the frequency of the *relative* intense resolved sweeps and ejections, which exist in the region  $y < 0.3h$ , less than double the height of the RANS region created by the Fz switching mechanism.

The average number of structures per snapshot is 84 and 51 for the FSM-SSG-95-5-DDES and FSM-SSG-95-5-Fz respectively. The difference in  $F_{\text{switch}}$  is responsible for this large disparity. The velocity shear available to generate structures is progressively lower further from the wall; the Fz switch occurs around  $y^+ = 75$  which appears too far to be an effective generator of resolved turbulence. This has consequences for other applications — by reducing the level of resolved turbulence, one would expect a slower formation of resolved eddies and breakdown of RANS free-shear layers, especially when separation is mild and from curved surfaces.

As previously discussed regarding Fig. 7.8, the later switch does not prevent streamwise velocity fluctuations deep in the RANS layer and this is also true for shear stress structures. Instead, the model is running in URANS mode, with a highly unphysical resolved flow field. This can be seen clearly in Fig. 7.11. Whilst the resolved structures satisfying Eq. 7.18 have been shifted to a minimum of  $y^+ = 29.5$ , this cannot be considered a success. The problem is due to the slow damping of the model dissipation rate  $\varepsilon$  (see Eq. 7.13) and the philosophy behind the damping mechanism. The second point can be expressed via Eq. 7.11.  $F$  only becomes less than 1, when  $F_{\text{damp}} \ll 1$  — in order to combat the inequality  $1/(1 - f_b) > 1$ . Further,  $F_{\text{damp}}$  only becomes significantly less than 1 when there is plenty of resolved turbulence. In other words, the shielding function is contradictory to its main purpose — it only switches off once it has failed. The DDES approach in contrast performs better, due to the closer near wall switch and faster damping of  $\varepsilon$ , the URANS mode is acting in a smaller region of the flow and as a result the artificial buffer layer is shorter and predictions are greatly improved.

The histogram of  $y_{\max}/h$  against  $y_{\min}/h$  in Fig. 7.11 reveals a curious pattern regarding the smallest height of resolved structures. Included in the plots is the line  $y_{\max} = y_{\min}$ , a theoretical lower bound on the vertical height of a structure. For the hybrid cases, the resolved structures are shifted by a constant above this line, implying a consistent smallest height throughout the domain. This is despite the grid stretching in this direction, which one would expect  $\ell_y/h$  to be a function of. The smallest structures near the wall are of a vertical height,

$$\ell_y/h = \Delta_x = 2\Delta_z. \quad (7.24)$$

Therefore the smallest structures resolved in the normal direction are consequences of small streamwise structures; the generation of the smallest structures rely on a wall normal velocity (Eq. 7.6) and a difference from grid point to grid point in the streamwise direction. Secondly, it is hard to see how these small scale structures are physical. The third worthwhile point is that the cube root volume  $\Delta = (\Delta_x \Delta_y \Delta_z)^{1/3}$  is not a meaningful scale, rather a maximum function such as  $\Delta = \max(\Delta_x, \Delta_y, \Delta_z)$  is seen to

be more relevant in light of Eq. 7.24. A second alternative, more tricky for a complex geometry, would be to define  $\Delta$  as the spacing in the average streamwise direction. In order to probe this further, coarser spanwise spacings should be used to test the effect on the resolved turbulence.

Despite the  $\ell_y$  dependence on  $\Delta_x$  for the smallest structures, the volume is still a function of  $y$  — as can be seen in Fig. 7.18. The lefthand side of the histograms show that the smallest structures are near the wall. These are approximately three orders of magnitude larger than the DNS, whilst the volume of each cell is approximately an order of magnitude higher. The functional dependence is weaker for the FSM-SSG-95-5-Fz as it is not allowed to generate as many structures near the wall as the FSM-SSG-95-5-DDES. Equation 7.24 aside, the constant shift from  $y_{\max} = y_{\min}$  on the lower bound of the probability density functions in Fig. 7.11 is  $c \approx 0.1$ , which implies  $\ell_y > 2\Delta_x$  holds for all but 0.2% of the resolved structures. Therefore, the wall normal size of structures is not dependent on the grid size in this direction. Further in this regard, structures satisfying Eq. 7.24 can be seen as noise and do not contribute to statistical results.

Figure 7.11 shows that large attached structures are much more prevalent for both hybrid cases. They grow on average much larger than their DNS counterparts, consider especially group 3 structures that are large in the streamwise and spanwise directions. Examples are shown in Fig. 7.15 and Fig. 7.16. The peak in  $y_{\max}$  is over half a channel height greater than for DNS. The growth of these large attached structures is in place of the detachment that occurs in reality, along the line Eq. 7.23. Further, structures detach from the RANS-LES interface with a much wider range of wall normal heights than do from the wall in DNS. The detached flow field is a mixture of structures created from the large block of interface attached structures, as they leave the wall sporadically during growth. Note, the differences between DNS and hybrid cases in the overall shape of the PDF is not down to the ratio of small to large scales. Upon removing comparable scales from the DNS data set, the shape of the histogram is largely unchanged. As a consequence we can say that the detached flow field is dictated by the shedding of these growing interface structures — especially true in the buffer layer as we shall see below, which do not resemble those leaving the wall in DNS. Therefore, the break up or control of the size of these attached structures would seem necessary in order to improve the global flow field.

The velocity fluctuations can be compared in Fig. 7.13. FSM-SSG-95-5-DDES and FSM-SSG-95-5-Fz contain remarkably different quadrants. Both have a reduced number of inward and outward interactions because generally these are the smaller scales and get removed by the effective filter. The intensity of the sweeps and ejections are the major difference between the two cases. Compared with DNS, the FSM-SSG-95-5-DDES contains fluctuations in the streamwise direction much too great. On the other hand, the FSM-SSG-95-5-Fz predicts this intensity reasonably well. From the GEP grouping, it is evident the near wall ejections (group 1) are the culprits of  $\bar{u}^+$  values up to double

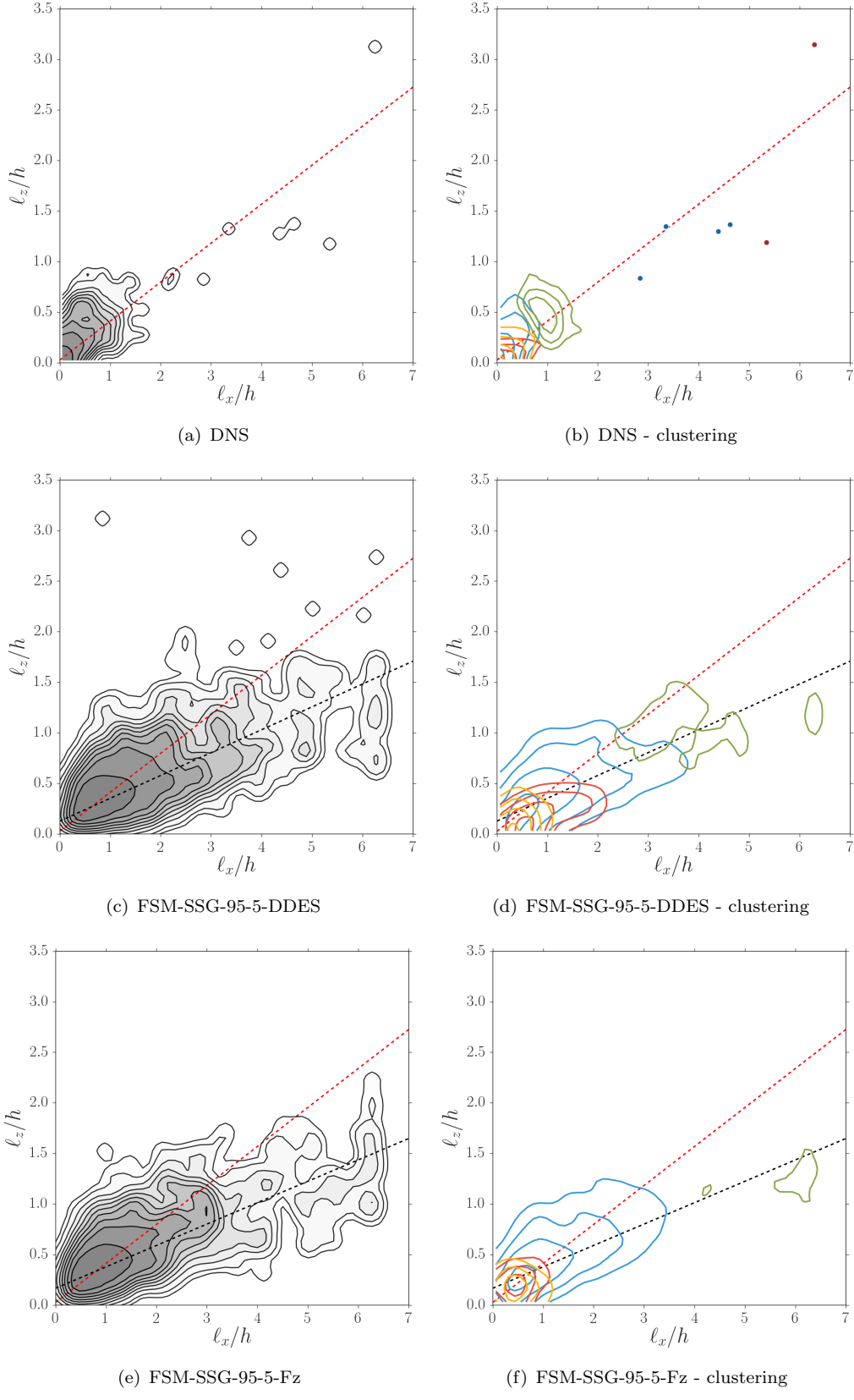


FIGURE 7.14: Probability density function of  $\ell_z/h$  against  $\ell_x/h$ . Comparison of DNS with FSM-SSG-95-5-DDES and FSM-SSG-95-5-Fz. Grey contours are the full set of structures, the levels are 10% increments of the maximum value on a logarithmic scale. Coloured lines are contours of each cluster type, colours follow that in Table 7.4. Groups 4 and 5 have been scattered due to too few samples. The levels shown for the cluster groups are 20% increments of the maximum value on a logarithmic scale. Linear regression lines are shown for the DNS (red) and hybrid (black).

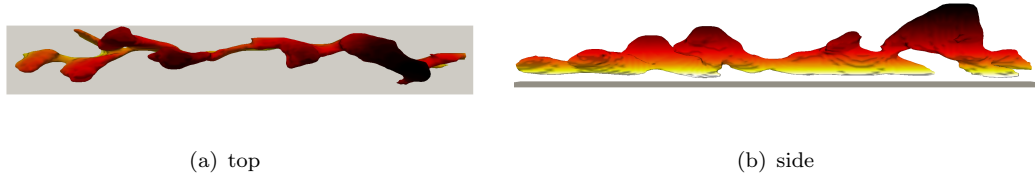


FIGURE 7.15: Example large group 3 structure. Structure is 6 channel heights long.

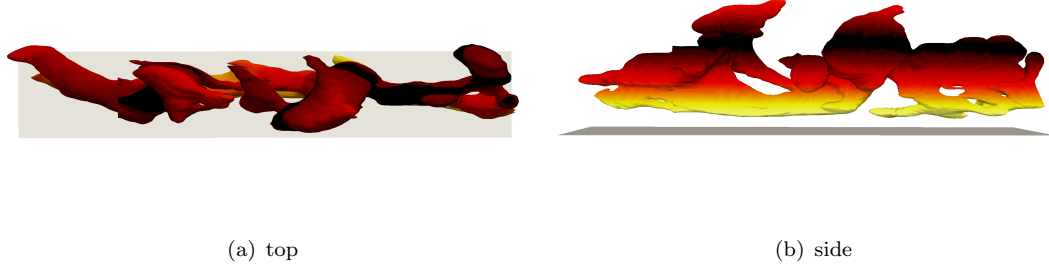


FIGURE 7.16: Example large group 3 structure. Structure is 4 channel heights long.

that seen in the DNS. Given that these structures are much taller than in DNS, existing throughout the buffer layer (Fig. 7.11), the large peak in  $\overline{u'u'}^+$  (Fig. 7.4) is explained. Therefore the reasonable prediction of  $\overline{u}^+$  by FSM-SSG-95-5-Fz is not down to correct physics, rather the calibration of the model generates these large streaky structures in the artificial buffer layer and as such an overprediction of streamwise stress is still observed in Fig. 7.4 . Despite the large streamwise intensity, the wall normal fluctuation level is inline with that observed in DNS.

The overall greater streamwise orientation of structures can be seen in Fig. 7.14. The black linear regression lines,

$$\ell_z = m\ell_x + c, \quad (7.25)$$

are fit using structures from the respective hybrid cases. The red lines are the DNS equivalents. Both hybrid cases predict the relationship with  $m \approx 0.22$ , such that  $\ell_x \approx 5\ell_z$ . This is significantly greater than the value of  $2.75 - 3$  discussed for DNS structures. Also evident, is the elongated nature of the near wall ejections in DDES, for which a significant portion lie below the regression line implying structures of length  $10\ell_z$ . This in turn results in detached group 0 structures of a similar topology. The corresponding sweeps however are much closer to the global regression line. For the FSM-SSG-95-5-Fz, these ejections are not as severe which improves the overall shape of the velocity quadrant histogram.

This elongated streamwise length is seen at all scales by considering the relationship with volume, Fig. 7.17. For both small and large scales, structures are too long given their volume. Whilst the comparison between the small scale regression lines, described in Eq. 7.21, is slightly unfair due to the differing grid resolutions, the gradient of DNS

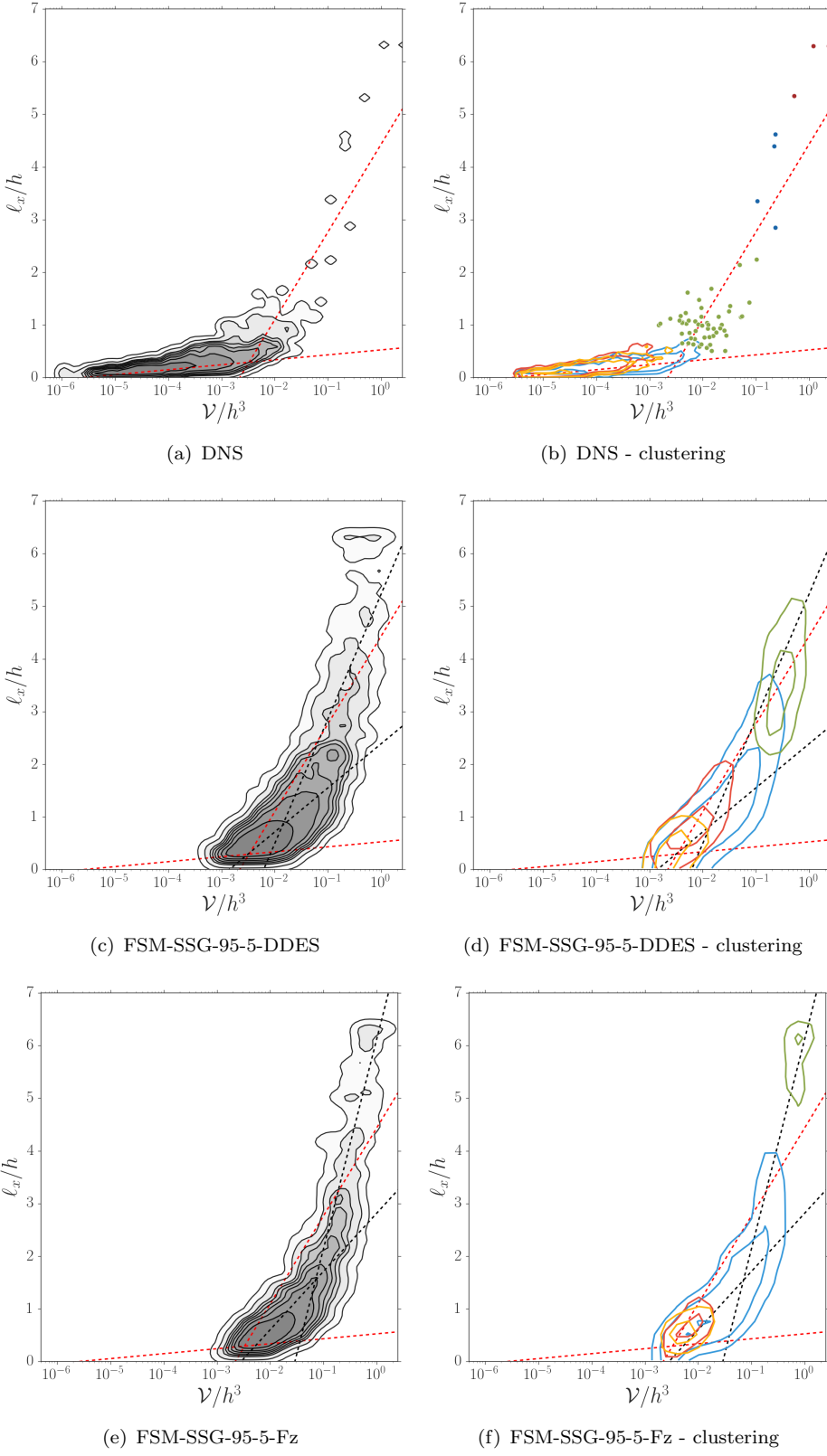


FIGURE 7.17: Probability density function of  $\ell_x/h$  against  $\mathcal{V}/h^3$ . Comparison of DNS with FSM-SSG-95-5-DDES and FSM-SSG-95-5-Fz. Grey contours are the full set of structures, levels are 10% increments of the maximum value on a logarithmic scale. Coloured lines are contours of each cluster type, colours follow that in Table 7.4. Groups 3, 4 and 5 (DNS only) have been scattered due to too few samples. The levels shown for the cluster groups are 20% increments of the maximum value on a logarithmic scale. Regression lines are shown for the DNS (red) and hybrid (black). For the regression,  $\log(\mathcal{V}/h^3)$  is used as the independent variable and the data is split into two groups, the clusterings  $c_0, c_1, c_2$  and  $c_3, c_4, c_5$ .

structures greater than the minimum hybrid structure is still only a third of the value predicted by FSM-SSG-95-5-DDES and FSM-SSG-95-5-Fz. The large scale regression line is also too steep, because of the presence of domain length group 3 structures. This is accentuated with the Fz switch, the large attached structures have grown to the length of the domain due to the lack of unsteadiness in the artificial buffer layer. Indeed they have a reasonable chance of existing below  $y = F_{\text{switch}}$  — see Fig. 7.11.

To further assess these streamwise streaks, structures less than 10% the width of the domain are extracted from the full set of hybrid structures. Violin plots of the number of streamwise grid points against the streamwise length are shown in Fig. 7.19. Each violin is a direct comparison between FSM-SSG-95-5-DDES and FSM-SSG-95-5-Fz at each number of grid points. The shape of the violin is an estimate of the distribution whilst the scatter shows the location of samples. Note that in this scatter only the  $x$  direction matters, the  $y$  direction is purely for visual aid. Note that the delta in the scatter reveals the streamwise grid spacing. Firstly, the early DDES switch has allowed structures of just 3 grid points wide to form, which already have a length of around a half channel height. The median of structures of more than 4 grid points are comparatively similar for both cases and there is a reasonable skew towards shorter structures. With regards to the longest structures, there is evidence of structures just 6 cells wide but two channel heights long. Further, there is a loose parametrisation of the longest structures,

$$n \cdot \Delta_z = m\ell_x, \quad (7.26)$$

where  $m \approx 3$  for the FSM-SSG-95-5-DDES and  $m = 2.5$  for the FSM-SSG-95-5-Fz. The height and location of these structures are assessed with similar violin plots in Fig. 7.20 and Fig. 7.21. From the distribution of  $y_{\min}$  and  $\ell_y$ , the growth of group 3 structures can be seen, which are as tall as, and exist primarily in, the buffer layer. These structures characterise the buffer layer, or rather are characterised by the buffer layer — dictated by the speed of the RANS-LES switch. The delayed break up of these structures due to slower damping of the turbulence model stretches this region for the Fz switch where as the DDES buffer layer is much smaller due to the existence of these structures lower in the flow field. It should be noted that the reduced buffer layer does not prevent the growth of these into fully fledged group 3's, but does reduce the chance of structures with  $y_{\max} \approx 1.4$  and significantly, it reduces their streamwise length by 2 channel heights.

Figure 7.22 is a plot of the absolute resolved shear stress within a structure  $|\overline{u'v'}^+|$  as a function of wall normal velocity  $\bar{v}^+$  for the hybrid flow fields. The asymmetry between sweeps (left finger) and ejections (right finger) is evident, with the sweeps being weaker for a given  $\bar{v}^+$ . This is also observed for the DNS (Lozano-Durán et al., 2012) and is well known (Nakagawa and Nezu, 1977). The asymmetry is caused by the relative starting positions of sweeps and ejections; sweeps originate from higher in the velocity profile (smaller  $\partial_y \bar{u}_i$ ) and consequently not as much shear stress is generated.

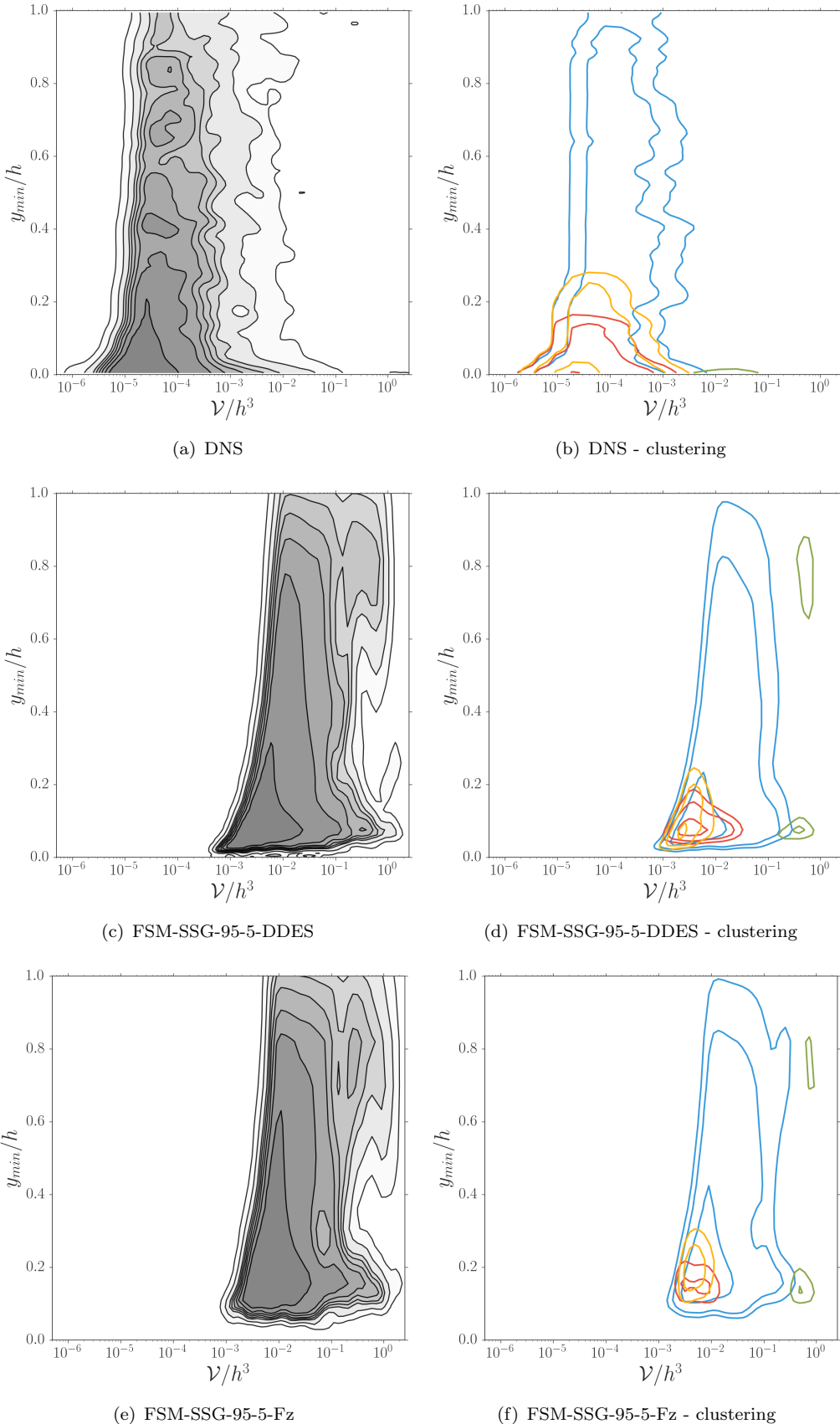


FIGURE 7.18: Probability density function of  $y_{\min}/h$  against  $\mathcal{V}/h^3$ . Comparison of DNS with FSM-SSG-95-5-DDES and FSM-SSG-95-5-Fz. Grey contours are the full set of structures, levels are 10% increments of the maximum value on a logarithmic scale. Coloured lines are contours of each cluster type, colours follow that in Table 7.4. Groups 4 and 5 have been omitted due to too few samples. The levels shown for the cluster groups are 20% increments of the maximum value on a logarithmic scale.

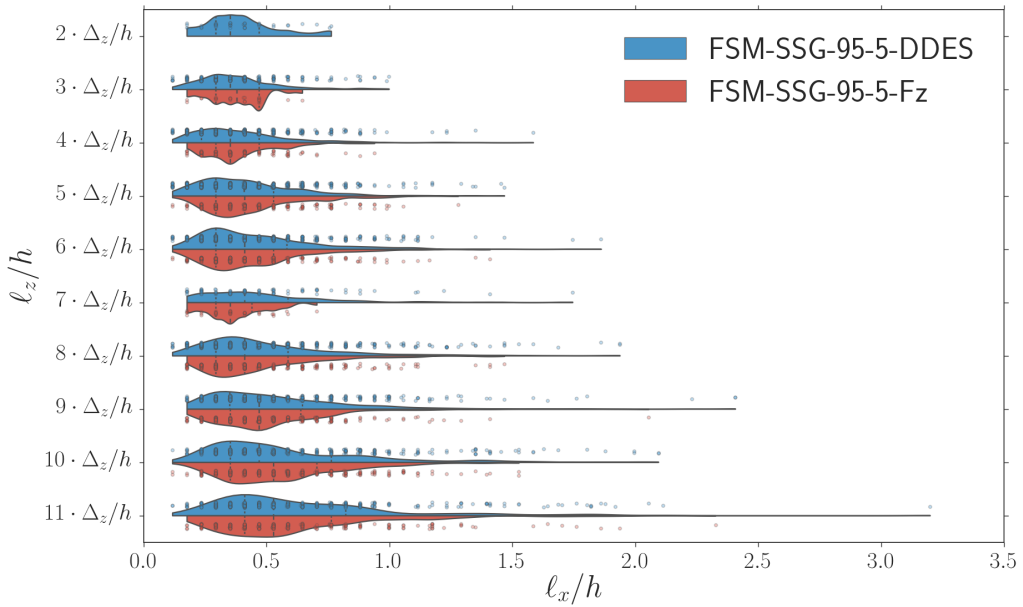


FIGURE 7.19: Violin plot of the variation in streamwise length  $\ell_x/h$  given number of grid points in the spanwise direction. Scatter shows individual structures. Shape of violin is an estimate of the distribution. Dashed lines are the median and lower and upper quartiles.

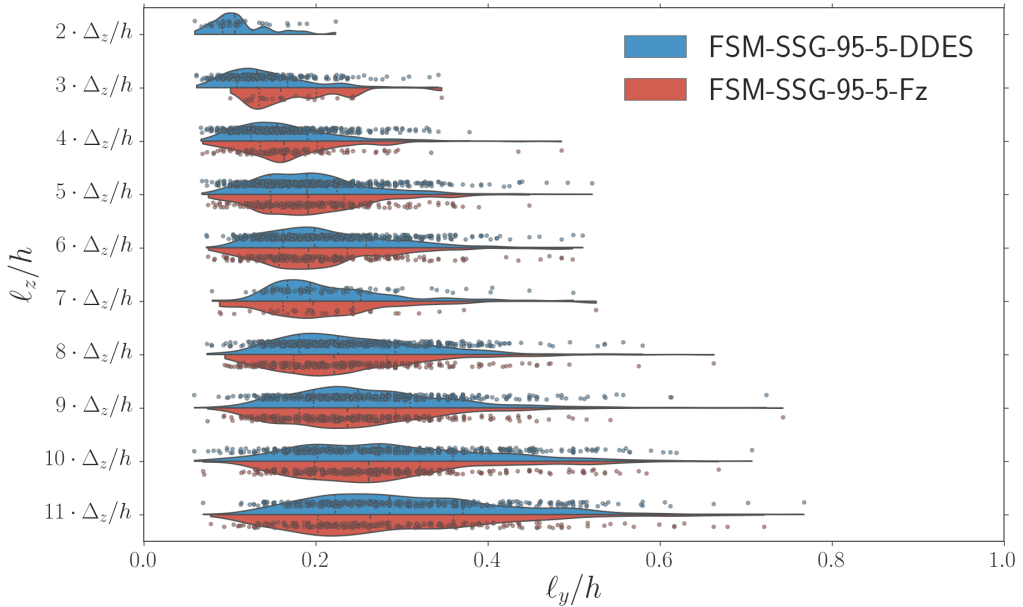


FIGURE 7.20: Violin plot of the variation in streamwise length  $\ell_x/h$  given number of grid points in the spanwise direction. Scatter shows individual structures. Shape of violin is an estimate of the distribution. Dashed lines are the median and lower and upper quartiles.

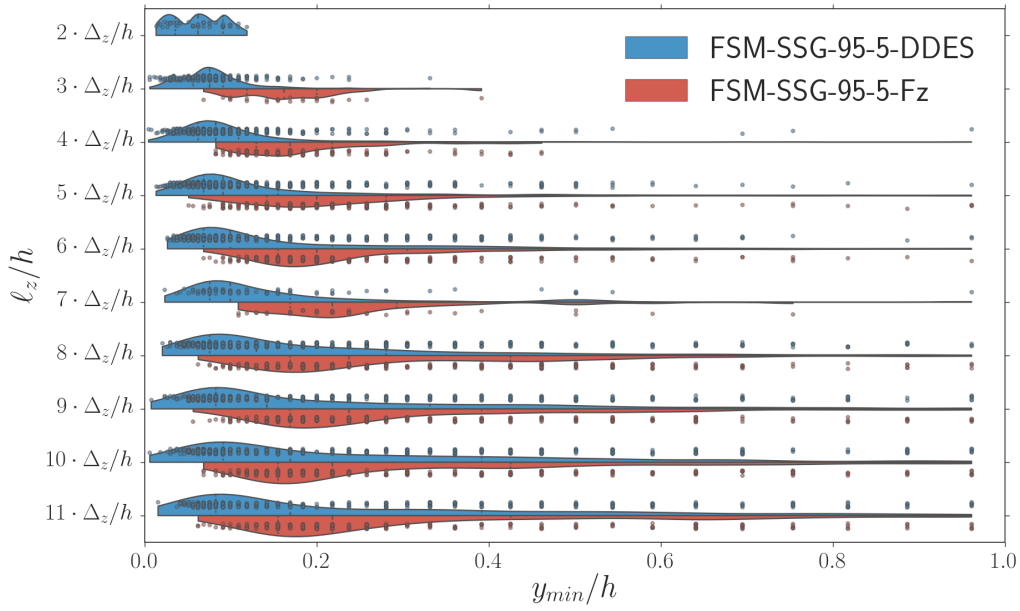


FIGURE 7.21: Violin plot of the variation in streamwise length  $\ell_x/h$  given number of grid points in the spanwise direction. Scatter shows individual structures. Shape of violin is an estimate of the distribution. Dashed lines are the median and lower and upper quartiles.

As with the velocity quadrant in Fig 7.13, the FSM-SSG-95-5-Fz produces structures with less shear stress contained within. Despite the reasonable magnitude prediction of fluctuations, the resolved shear stress is much lower when comparing to the DNS (see Lozano-Durán et al. (2012)). This is an effect of the Reynolds stress averaging out within a structure, as the averaging operator acts on the product of  $u$  and  $v$ . This is also evidently a feature of the FSM-SSG-95-5-DDES structures.

The right hand side plots of Fig. 7.22 are for structures in the log-layer only. This is defined as  $y < 0.2h$ . To extract data for these log-layer plots, structures satisfying  $y_{\max} > 0.2h$  are removed. Firstly, we see that there are no ejections that exist only in the FSM-SSG-95-5-Fz log-layer. This is because the artificial buffer layer extends to  $y = 0.23h$ . On the other hand, the FSM-SSG-95-5-DDES closely follows the included lines. These lines are (Lozano-Durán et al., 2012),

$$|\bar{uv}^+| = \pm 2.5\bar{v}^+. \quad (7.27)$$

This is based on the mixing length argument, that  $\ell \propto y$  and the fluctuation (displacement of velocity mean) is proportional to this eddy size  $\ell$ ,

$$\bar{uv}^+ \propto (\bar{v}\ell\partial_y\bar{u})^+ \propto \bar{v}^+. \quad (7.28)$$

The last simplification is based on the log-law equation,

$$\partial_y \bar{u} = \frac{u_\tau}{\kappa y}. \quad (7.29)$$

Therefore resolved structures in Hybrid RANS/LES, once developed, do reproduce the correct mixing. The model has been calibrated such that this is reproduced, however because of the well documented increase in streamwise fluctuations occurring from the RANS-LES interface, it becomes an impossibility to tune the model for both  $\bar{u}\bar{u}$  and  $\bar{u}\bar{v}$  in its current state and we see an over prediction in the normal stress (Fig. 7.4).

The final topic of this now lengthy section is the convection of modelled kinetic energy  $k_{sgs}$ . Because the philosophy of the seamless blending approach dictates the RANS region to act in unsteady mode, there is a convection of modelled turbulent kinetic energy. This is illustrated in Fig. 7.23, a histogram of  $k_{sgs}^+$  against  $\bar{v}^+$ . One can see that all levels of turbulent kinetic energy are convected and in Fig. 7.24 the position of  $k_{sgs}$  within structures in the channel is given. The line included in these plots is the flow field averaged  $k_{sgs}$ .

The sweeps are responsible for moving model contribution back down, which is countered by the ejections. The asymmetry in the tear drops of Fig. 7.23 is due to the inhomogeneity of the kinetic energy profile. This convection is undoubtedly having an effect on the overall  $k_{sgs}$  profile (Fig. 7.3), although the extent of its influence is still unknown. This in turn has an effect on the the rate of damping of the turbulence model and therefore the size of the artificial buffer layer. It is in the upper part of this layer that we see structures moving high levels of model contribution.

### 7.3 Summary

The planar channel is an extremely difficult case for Unified Hybrid RANS/LES. It highlights the main shortcomings of the methodology, namely the switch from RANS-LES in a fully turbulent flow. It should be noted that this kind of flow is not the intended application for this kind of closure. That said, such a case should remain a focus of model developers in order to better understand the mechanisms in play at the interface between the two modes. This chapter has presented a comprehensive study of both statistical and structural results to provide better understanding of two RANS-LES switching methods in the presence of attached boundary layers. Neither has performed satisfactorily.

Skin friction results were reasonably promising, despite a clear cancellation of errors for the -Fz cases. The prediction of the log-layer intercept was also excellent and consistent for the damping functions employed. Major differences occurred in the predictions as a result of the artificial buffer layer, which was elongated using the Fz switch. In terms

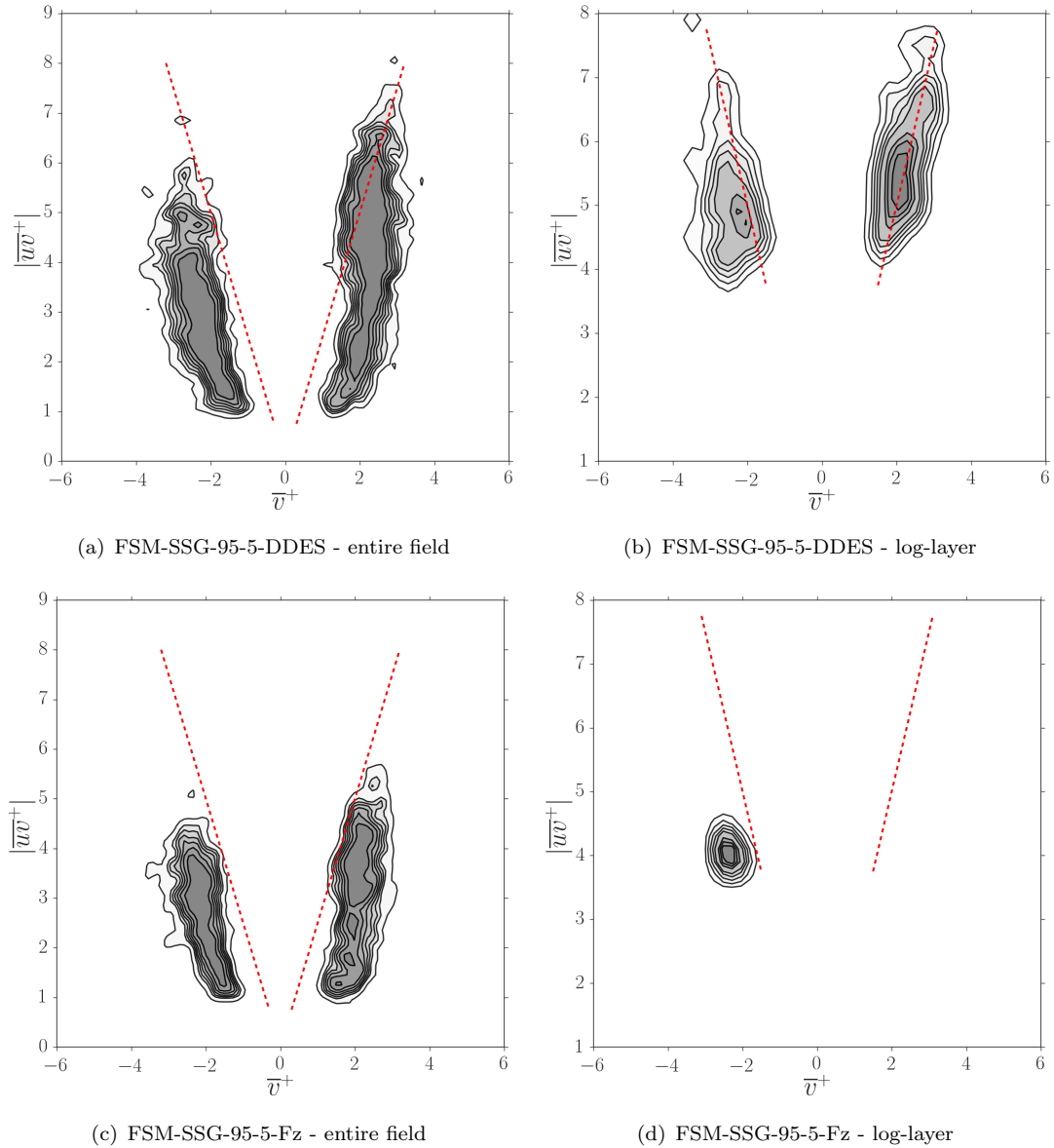


FIGURE 7.22: Probability density function of  $|\bar{u}'\bar{v}'|^+$  against  $\bar{v}^+$  for the FSM-SSG-95-5-DDES and FSM-SSG-95-5-Fz cases.  $\bar{(\cdot)}$  is the average over the structure. Only ejections and sweeps are included. Plots are for both the full flow field and the log-layer (defined by  $y/h < 0.2$ ). Contours are the full set of structures, levels are 10% increments of the maximum value on a logarithmic scale. Colours follow the ordering in Table 7.4. The red dashed lines are  $\bar{u}'\bar{v}'^+ = \pm 2.5\bar{v}^+$ .

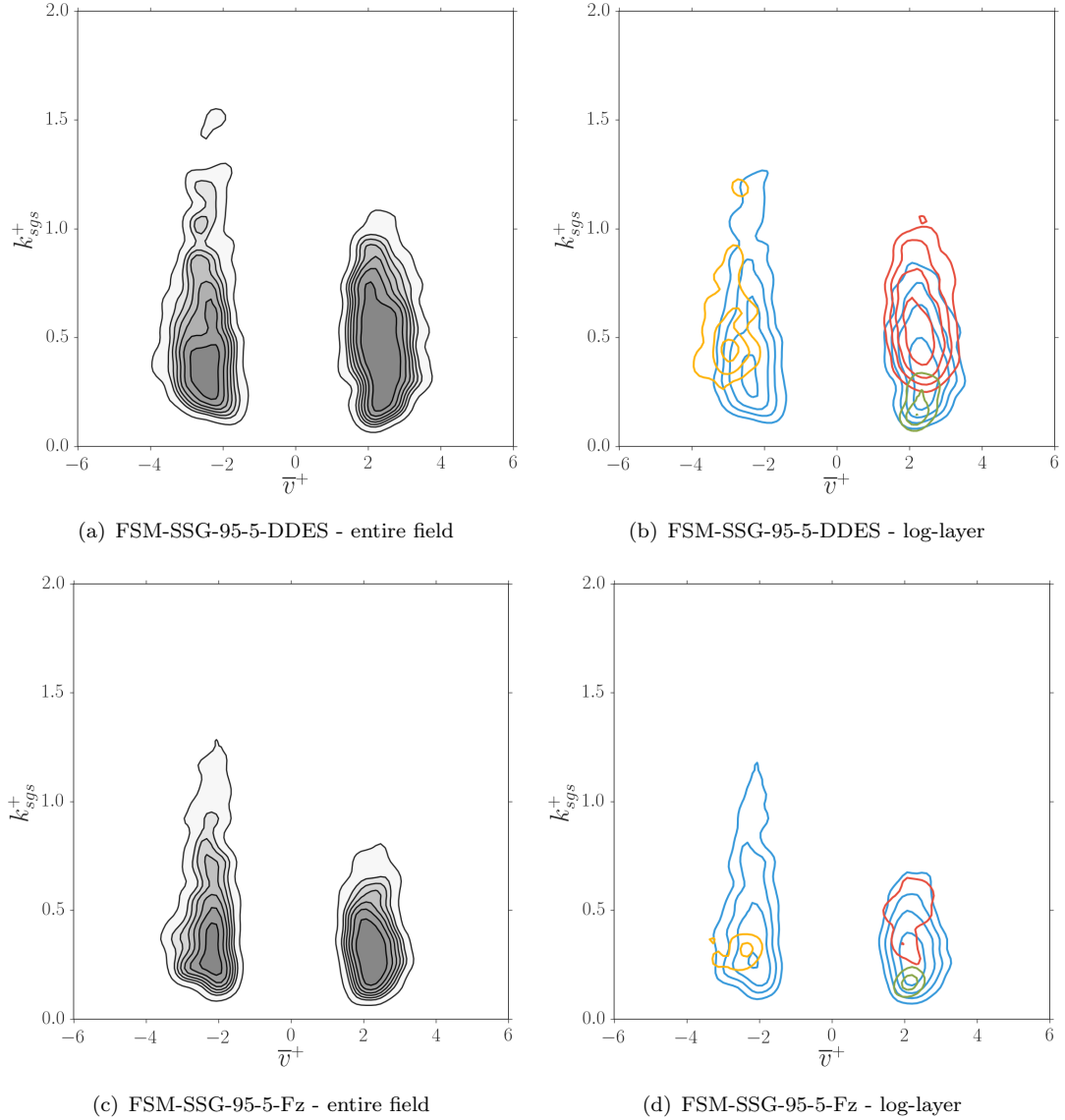


FIGURE 7.23: Probability density function of the modelled subgrid kinetic energy  $k_{sgs}^+$  inside a structure against the average fluctuation  $\bar{v}^+$  for the FSM-SSG-95-5-DDES and FSM-SSG-95-5-Fz cases. Grey contours are of structures within the buffer layer at 10% increments of the maximum value on a logarithmic scale. Coloured lines are contours for each cluster group, again only considering structures inside the buffer layer, at 20% increments of the maximum value on a logarithmic scale. Colours follow the ordering in Table 7.4.

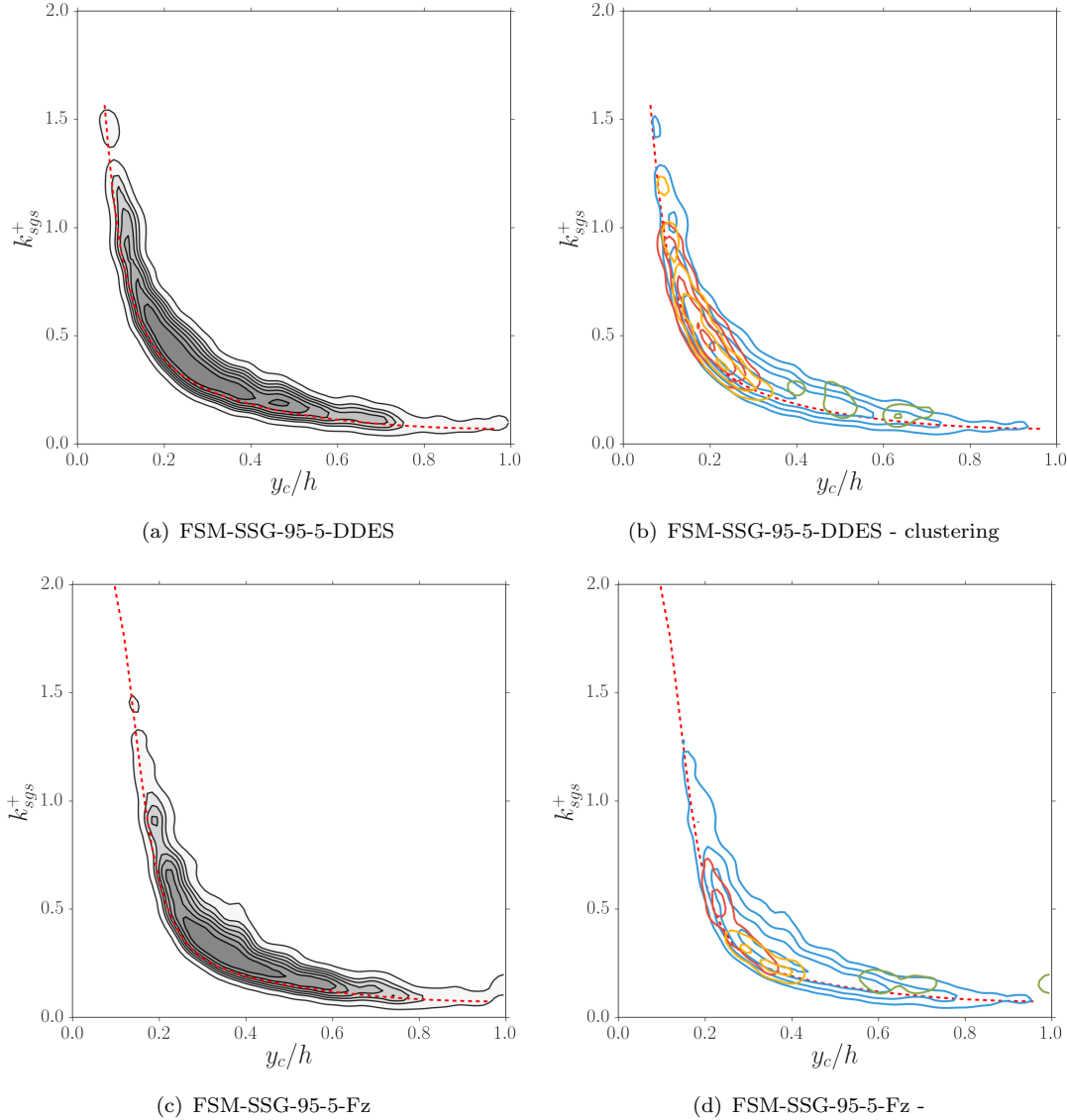


FIGURE 7.24: Probability density function of the modelled subgrid kinetic energy  $k_{sgs}^+$  inside a structure against the centre point of the structure  $y_c/h$  for the FSM-SSG-95-5-DDES and FSM-SSG-95-5-Fz cases. Grey contours are the full set of structures at 10% increments of the maximum value on a logarithmic scale. Coloured lines are contours for each cluster group at 20% increments of the maximum value on a logarithmic scale. Colours follow the ordering in Table 7.4. The red dashed line is the average  $k_{sgs}^+(y^+)$  for the entire flow field.

of choosing between the two methodologies, one would have to argue for the DDES switch based purely on statistical results, although it has been shown these statistics are comprised of well calibrated but unphysical structures.

It has been shown that the resolved flow field in the artificial buffer layer is dominated by overly long, tall and thin structures. Further, these structures define the detached flow field, consequently resulting in overly strong streamwise fluctuations. Overall, the streamwise/spanwise length ratio is approximately double that expected, with near wall streaks being significantly worse. These structures do not detach in the same way as DNS, rather continue to grow to approximately double the correct height. Their detachment occurs sporadically with a bigger range of heights observed in all regions away from the wall.

In the current state, Hybrid RANS/LES is able to correctly reproduce the shear stress statistically and the DDES switch contained a physical mixing length mechanism in the log-layer. However because of the increased anisotropy in the streamwise direction, dictated by the resolved flow field, the correct shear comes at the price of over predicting the streamwise stress. This implies that without careful control of the growth of these structures, both cannot be simultaneously correct with a seamless blending methodology. In order to improve the near wall behaviour, these structures must be broken up. Piomelli et al. (2003) added a stochastic forcing to the momentum equation. This kind of methodology should be pursued. However, this author believes that by damping each stress component anisotropically, a physical justification can be realised. Such a methodology would take the form,

$$\tau_{ij}^{\text{hyb}} = (F \circ \tau^{\text{rans}})_{ij}. \quad (7.30)$$

The second modification that would seem necessary is a significant change to the RANS equations used. Firstly, the SSG does not reproduce the correct anisotropy at the wall. This could potentially be accounted for in part by Eq. 7.30 as it implicitly imposes an anisotropic upper boundary condition on the modelled boundary layer. Secondly, in light of a methodology like Eq. 7.30, it may prove simpler to solve transport equations for the full Reynolds stress, with the damping function  $F_{ij}$  absorbed into the stress equations themselves. This would then provide length scale damping for each component of Reynolds stress.

The smallest structures in the flow field were found to be parametrised by the length of the largest grid side, this implies that the definition  $\Delta = \max(\Delta_x, \Delta_y, \Delta_z)$  is more appropriate. This would then have significant effects on the shape of the filter width, effectively raising it in the buffer layer which would result in more model damping.

This chapter also presents a novel application of the GEP clustering algorithm, which has greatly aided the analysis of the instantaneous flow field. The visual decomposition of the flow field shows the reader instantly where each type of structure fits for every feature

that defines them. Without the group 3 clustering, much of the analysis presented in this chapter would have been missed.

# Chapter 8

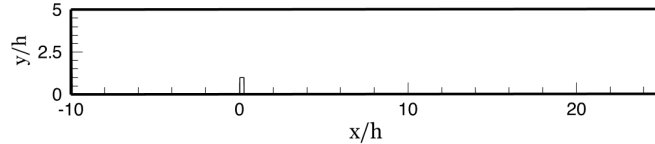
## Applications of Hybrid RANS/LES to Separated Flow

### 8.1 Introduction

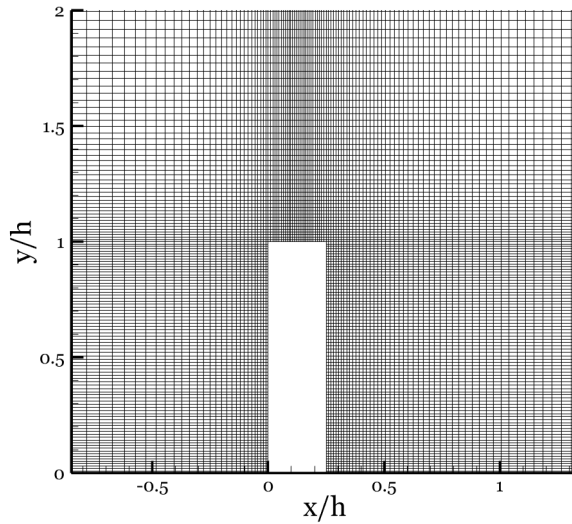
In this chapter, the efficacy of the modified Hybrid RANS/LES methodologies are scrutinised against existing techniques in the literature. All flows in this chapter contain regions of separated flow, the intended application of Hybrid RANS/LES. The thin boundary layers operate in RANS mode, whilst the separated flow operates in LES mode.

Three cases are presented in total, each with different elements to challenge the closures. The vertical fence presented in Section 8.2 is an attached boundary layer with an obstacle. Next in Section 8.3 the classical periodic hills case is discussed. This is an internal flow with a fully turbulent outer region and the point of separation fluctuates along a curved surface. Finally, the most demanding of the presented applications is the inline tandem cylinder geometry. This is an external flow of particular interest to aviation engineering as it is an extremely simplified landing gear. The wake behind a cylinder impinges on a second inline cylinder. Therefore the prediction of the wake strongly influences downstream results and small errors upstream tend to be amplified in statistics around the second cylinder.

The final aspect in this chapter is the decreasing mesh resolution from one case to the next. It is important to provide evidence of successful or unsuccessful model response to the instantaneous local turbulence levels and cell size. The mesh for the vertical fence is fine, for which the model contribution should be small, whilst a relatively coarser mesh is used for the periodic hills case and the flow around the inline tandem cylinders is solved on an extremely coarse mesh, where the model contribution should be significant. Of the closures tested, all perform well for the first two applications whilst many start



(a) Computational domain. The obstacle is mounted at  $x/h = 0$ .



(b) The grid around the obstacle.

FIGURE 8.1: Vertical fence case computational domain and grid around the surface mounted obstacle.

to struggle with the demands of the tandem cylinder case. In particular SAS and LNS fail to capture the essence of the flow field, whilst DDES is shown to be more sensitive to the numerics. In all cases the modified Hybrid RANS/LES performs reliably and robustly with any sensible numerical scheme.

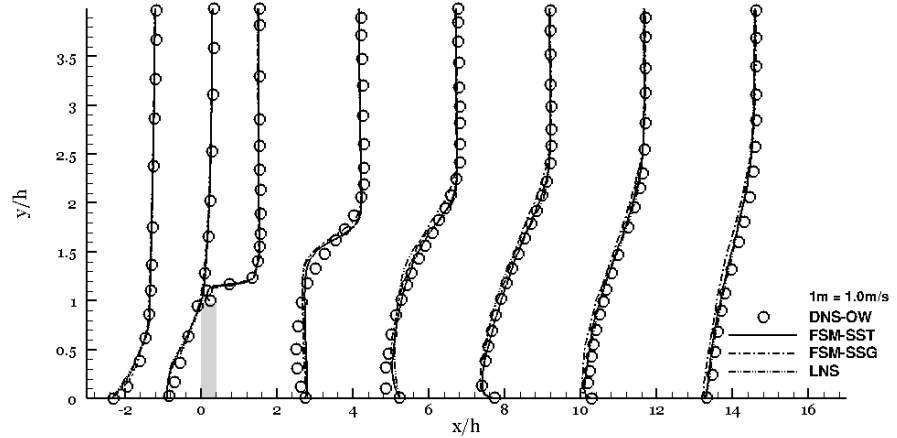
## 8.2 Vertical Fence

### 8.2.1 Geometry Definition

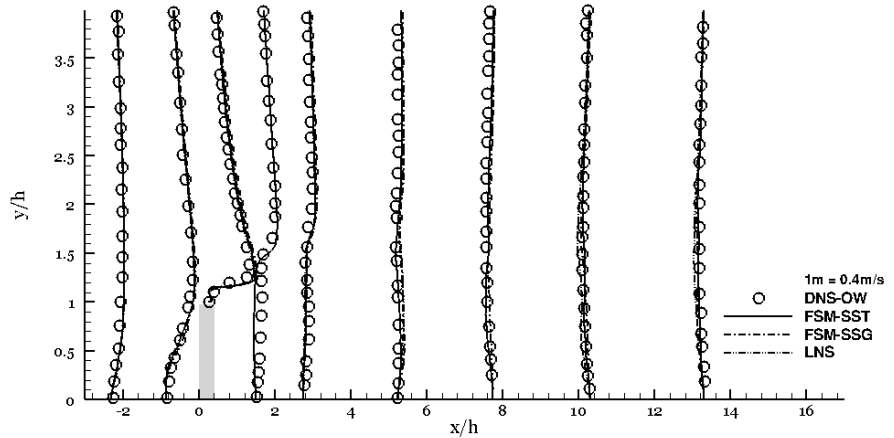
The flow field around a surface mounted obstacle is presented against the DNS of Orellano and Wengle (2000). The computational domain is shown in Fig. 8.1(a) where  $h$  denotes the height of the hill. The flow separates behind the obstacle where the free shear layer exhibits a Kelvin-Helmholtz instability as it breaks down. The entire separation bubble contains a shedding instability, analogous to the Kàrmàn vortex street behind a cylinder, caused by an interaction between vortices and the wall (Sigurdson, 1995). As a consequence this type of flow has received a lot of attention in the field of flow control. This section looks purely at the uncontrolled reference data provided by Orellano and Wengle (2000).

The step height Reynolds number is 3000. The obstacle is placed at  $x/h = 0$ , with the inflow and outflow at  $x/h = -10$  and  $x/h = 25$  respectively. The upper boundary is at  $y/h = 5$  where a Neumann boundary condition is applied. The spanwise extent is  $6h$ , allowing for periodic boundary conditions. The total number of cells is 3.5 million, a subset around the obstacle is shown in Fig 8.1(b). The mesh is fine enough to allow integration down to the wall and no slip boundary conditions are applied, with the maximum instantaneous value of  $y_1^+ \approx 1.5$ .

Orellano and Wengle (2000) provides the streamwise root mean square  $u^{\text{rms}}$  and mean  $\langle u \rangle$  velocity of the upstream boundary layer, which serve as inflow conditions to the Hybrid RANS/LES.  $k$  is estimated as  $1.5u^{\text{rms}}{}^2$  and  $\omega$  is prescribed using the wall boundary condition of Wilcox (1994) up until  $y^+ = 2.0$  and then is held constant up to  $y/h = 5$ . This results in the flow upstream of the fence running in RANS mode.



(a) Streamwise velocity in the  $x - y$  plane.



(b) Wall normal velocity in the  $x - y$  plane.

FIGURE 8.2: Mean velocity profiles at eight streamwise locations.

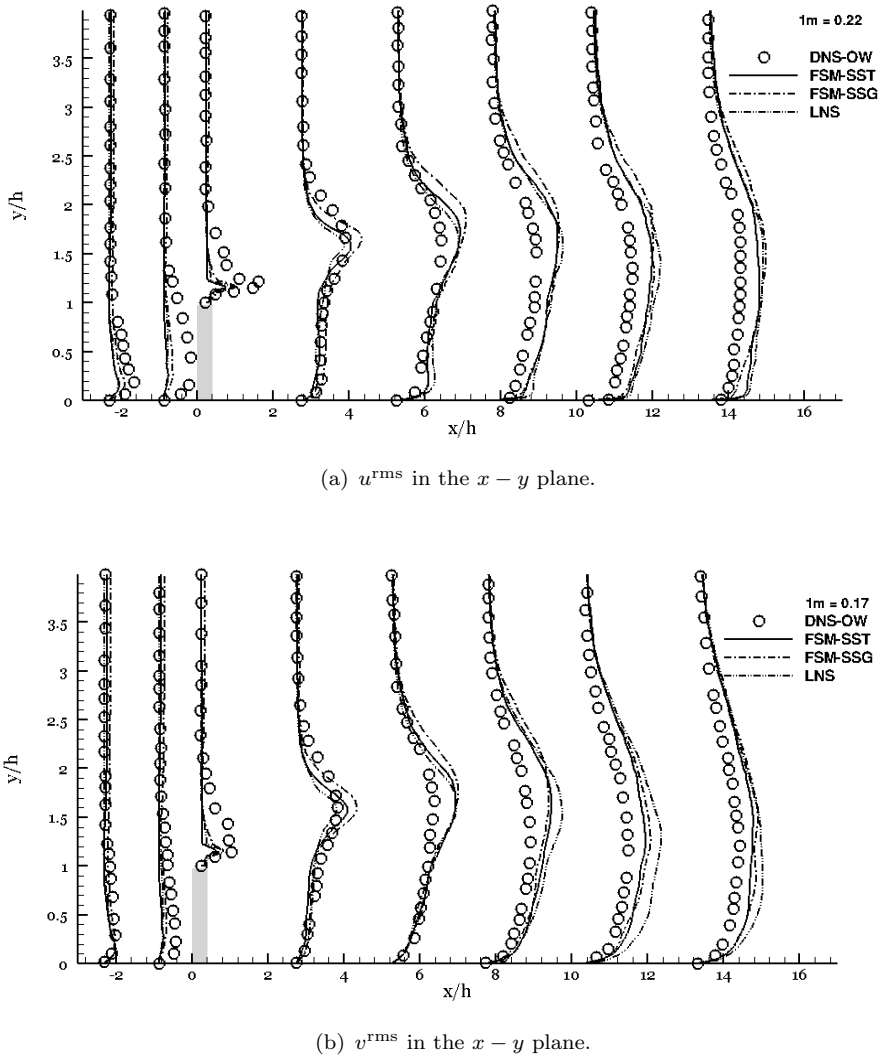


FIGURE 8.3: Root mean square velocity profiles at eight streamwise locations.

### 8.2.2 Results and Discussion

Results are presented for two FSM formulations, differing only by the underlying RANS model. The first is closed with the SST (see Section 2.2.3.1) and the second with the SSG (see Section 2.2.3.3). The modified damping function Eq. 6.10 with the near wall treatment Eq. 6.12 controls the level of model contribution. The FSM is compared with the LNS methodology (see Section 2.2.4.3) also with the same near wall treatment. In all cases the hybrid convection scheme of Weinmann et al. (2014) is used for  $\tilde{u}_j \partial_j \tilde{u}_i$  and second order implicit backward discretisation for time. The subgrid quantities are discretised using linear upwinding.

Velocity profiles at eight locations are compared to the DNS in Fig. 8.2. All three methodologies capture the essence of the velocity field downstream of the fence, including the reattachment location but with a slight under prediction of the reverse flow velocity.

Upstream of the fence, due to the steady nature of the RANS boundary layer, a small separation bubble is observed at  $x/h = -1$  which is only found instantaneously in the DNS. As a consequence, the shear layer is at marginally too steep an angle. These facts are best visualised in Fig. 8.3, plots of  $u^{\text{rms}}$  and  $v^{\text{rms}}$ . The FSM-SSG, with a non-linear stress-strain relationship, marginally holds onto the turbulent profile until  $x/h = -2.2$ , whilst the linear FSM-SST and LNS relaminarise earlier. All models exhibit an almost laminar separation from the fence and consequently the shear layer takes longer to develop. After  $x/h = 5$  all models have over predicted the Reynolds stress, but the FSM-SSG shows at least an interest in recovery after reattachment.

In an effort to improve Hybrid RANS/LES of this type Anupindi and Sandberg (2015) added turbulent structures using the digital filtering approach of Kim et al. (2013). The addition of the digital filter removed the upstream mean separation bubble and added resolved structures that allowed the free shear layer to develop more quickly. Further Anupindi and Sandberg (2015) tested with the damping functions Eq. 6.10 and Weinmann et al. (2014). The former was more sensitive to the fine resolution and as a result lowered the model contribution more effectively, consequently improving results.<sup>1</sup>

## 8.3 Two Dimensional Periodic Hills

### 8.3.1 Flow Description

The flow over a series of continuously differentiable constrictions, or ‘hills’, in a two dimensional channel is both very interesting and challenging to the turbulence modeller. Separation from a curved surface is inherently unsteady, induced via the action of the adverse pressure gradient, with the instantaneous point of zero wall shear stress fluctuating significantly along the domain (Fröhlich et al., 2005). This kind of variable separation is another challenge for Hybrid RANS/LES, for which the classical application is sharp corner separation.

The unsteadiness of the separation line has implications in the shear layer; generally, additional large structures of a turbulent nature, often periodic, are present which increases mixing and thus reduces the reattachment length (Jakirlić et al., 2001, 2002). The success of a closure depends on the ability to resolve these structures. For this reason, the two dimensional periodic hills has become a benchmark case for turbulence resolving closures. DES has been comprehensively studied by Šarić et al. (2007) with good agreement, however the turbulent statistics in the free shear layer deviated from the reference LES of Breuer et al. (2009) and the reattachment point was slightly too far downstream. On coarser grids, the quality of DES deteriorated significantly. Fröhlich and von Terzi (2008) also reported a sensitivity to initial conditions, when starting from

---

<sup>1</sup>This last comparison remained unpublished.

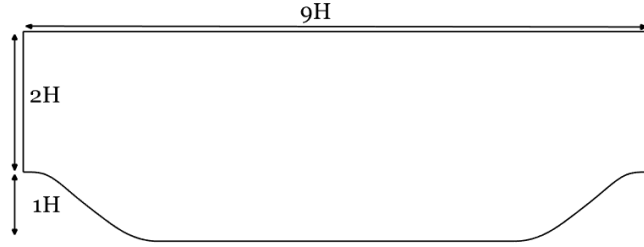
an existing RANS solution or from a nominal constant value. Chaouat and Schiestel (2013) performed the PITM method for a flow at a higher Reynolds number and compared to the experiments of Rapp and Manhart (2011). The results were reasonable, yielding an improvement over the RSM solution also reported, but suffered from major near wall overpredictions of Reynolds stress. The separation length was found to be sensitive to the grid. PITM significantly underpredicted the point of separation and so the location of reattachment was also incorrect. Segregated RANS-LES modelling has been applied to the periodic hills, with both a RANS-LES interface (Mathey et al., 2006) and LES-RANS interface (von Terzi et al., 2005) normal to the flow. It is shown that for both directions of coupling, the results depend strongly on the handling of the interface. Davidson and Peng (2003) coupled near-wall RANS with LES in the bulk. Once again, the treatment of the matching plane caused difficulties. Kinks in the profiles were visible across the interface and the inconsistency between RANS and LES length scales affected the quality of the solution in the bulk.

### 8.3.2 Computational Domain and Boundary Conditions

Studies on similar geometries have been conducted in the past (Armenio and Piomelli, 2000; Henn and Sykes, 1999; Salvetti et al., 2001); these simulations looked at the geometrical impact — with atmospheric applications in mind. As a result, the upper surface is generally open and recirculation lengths are small. Instead, the geometry here was modified (Mellen et al., 2000) from an original experiment (Almeida et al., 1993) to become a more challenging environment for turbulence closures. Whilst LES studies look at understanding the physical processes behind the structural features; turbulence models should be primarily concerned with evaluating performance. The reattachment length in this case is not governed by geometry, presenting a major challenge for the reasons outlined above.

The hill height is denoted  $H$ , with the peaks separated by  $9H$  in the streamwise direction. The domain height is set to  $3.035H$ . These are the two geometrical changes from the original experiment (Almeida et al., 1993). The first change allows the reattachment zone to occur on the flat section between the hills. This represents a doubling of hill pitch from  $4.5H$ . The reattachment was originally governed by the geometry of the next hill and did not fully exercise the involved model. The second change from the original experiment is a reduction in channel height from  $6.071H$ ; which removes considerably the number of grid points required and thus lowers the cost. The  $x - y$  plane of the geometry is plotted in Fig. 8.4.

The hill is a continuously differentiable function,  $H(x)$ . This function, in units where  $H(\text{s.t. } H(0) = 28H)$  and  $x_M(\text{s.t. } H(x_M) = 0) \in \mathbb{Z}$ , is left unchanged from the first

FIGURE 8.4:  $x - y$  plane of the two dimensional periodic hills geometry.

experiment and given to four significant figures as:

$$H(x) = \begin{cases} 28 & + 0.006775x^2 - 0.002125x^3, & 0 \leq x < 9 \\ 25.07 & + 0.9755x - 0.1016x^2 + 0.001890x^3, & 9 \leq x < 14 \\ 25.80 & + 0.8207x - 0.09055x^2 + 0.001627x^3, & 14 \leq x < 20 \\ 40.46 & - 1.380x + 0.01946x^2 - 0.0002070x^3, & 20 \leq x < 30 \\ 17.92 & + 0.8744x - 0.05567x^2 + 0.0006278x^3, & 30 \leq x < 40 \\ 56.39 & - 2.0105x + 0.01645x^2 + 0.00002675x^3, & 40 \leq x \leq 54 \end{cases}$$

The Reynolds number, based on bulk velocity  $U_b$  above the hills and hill height, is  $\text{Re}_H = U_b H / \nu = 10'595$ .  $H$  is set to 0.028 and  $\nu = 1.81 \times 10^{-5}$ , this leaves the desired  $U_b = 6.849$  — which is found by integrating at the inflow or outflow. A Reynolds number of 10'595 is a massive reduction (Mellen et al., 2000) from the original experiment, motivated to set up a good test case for LES. The lower Reynolds number allows to-the-wall integration, without removing the main physical flow features (Fröhlich et al., 2005). The test case is designed to be periodic in the streamwise direction, therefore a pressure gradient drives the flow ensuring the correct mass flow rate.

The spanwise direction has an extent of  $4.5H$ . With this value, the LES studies of Temmerman and Leschziner (2001) and Fröhlich et al. (2005) reported a non-negligible correlation coefficient. However it was deemed to not influence the results drastically and in the interest of creating a benchmark case, the domain was not widened. The geometry is homogeneous in the span, allowing for periodic boundary conditions in this direction.

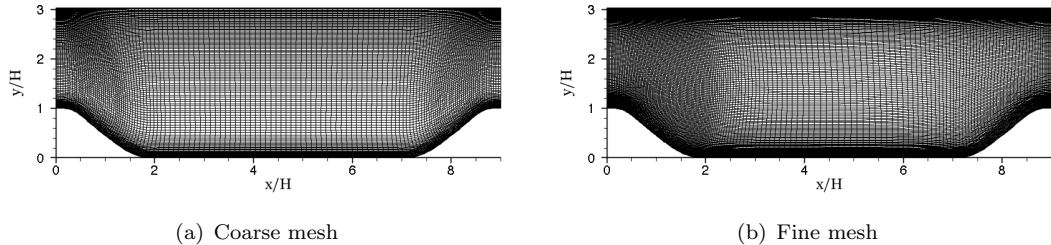


FIGURE 8.5: The two meshes used for the Periodic Hills test case. Left: coarse mesh. Right: fine mesh.

case	method	RANS model	mesh	convection scheme	near wall treatment
FSM-SSG-F	FSM	SSG	fine	HYB	$F_{f_b}$
FSM-SSG-C	FSM	SSG	coarse	HYB	$F_{f_b}$
HYB-SSG-C	HYB	SSG	coarse	HYB	$F_{f_b}$
LNS-SST-F	LNS	SST/Smag <sup>3</sup>	fine	HYB	$F_{f_b}$
SAS-SST-F	SAS	SST	fine	UP	none

TABLE 8.1: Hybrid RANS/LES periodic hills cases

Two meshes are used in this study, one fine (1.5 million cells) and one coarse (0.8 million cells). The  $x - y$  plane of both is shown in Fig. 8.5. The fine mesh, is a coarsening of the mesh used by Breuer et al. (2009) and is available from the ATAAC database<sup>2</sup>. The  $x - y$  plane is comprised of  $160 \times 160$  cells and ensures that for the first grid point,  $y_1^+ < 1$  everywhere, except for the acceleration region on the upstream facing side of the hill. In this region  $y_1^+ \approx 1.6$ . Sixty cells are used in the spanwise direction. The coarse mesh comprises of  $137 \times 120 \times 50$  cells. In order to make significant savings over the fine mesh,  $y_1^+ \approx 2$  on the upper boundary, however as will be seen below, this does not significantly alter the results in the free shear layer. However, as the normalisation is by  $U_b$ , this is estimated by the edge of the boundary layer velocity instead. Because savings are made along the upper wall, the mesh is almost as fine in the region  $2H \leq x \leq 7H$ . This coarse mesh has also been deliberately designed to keep the mesh perpendicular to the lower surface and with minimum curvature in the gap between the hills.

Table 8.1 is a list of all the cases considered in this section. FSM denotes the damping function Eq. 6.10, whilst HYB the damping function Eq. 6.11. The SSG RANS model is the Explicit Algebraic Stress Model of Speziale et al. (1991) and SST is the Shear-Stress Transport of Menter (1994). The HYB convection scheme is the blending formulation of Weinmann et al. (2014) and UP is linear upwinding. The near wall treatment  $F_{f_b}$  is the RANS-LES switching mechanism of Weinmann et al. (2014). Note that SAS does not contain a natural damping function so a sophisticated convection scheme or near wall treatment is not applied. For all cases, backward marching in time is used from an initial condition of  $u_i = 0$ .  $\Delta$  is defined as the cube root volume,

$$\Delta = (\Delta_x \Delta_y \Delta_z)^{\frac{1}{3}}. \quad (8.1)$$

To compare the hybrid case profiles to a reference, the LES of Mellen Fröhlich and Rodi is used (Fröhlich et al., 2005) and is denoted MFR. Two further LES studies are also used for further comparisons, namely those of Temmerman and Leschziner (2001) and Breuer et al. (2009). To compare the relative cost of the simulations, the most expensive (Breuer et al., 2009) used a grid of 13 million cells whilst the cheapest (Temmerman and

<sup>2</sup><http://cfm.mace.man.ac.uk/twiki/bin/view/ATAAC/ATAACTestCases>

<sup>3</sup>Limited Numerical Scales is a RANS limited LES so requires both a RANS and LES closure. Smag denotes the Smagorinsky (1963) subgrid model.

	$x_{s_1}/H$	$x_{r_1}/H$	$x_{s_2}/H$	$x_{r_2}/H$
MFR	0.20	4.56		
TL	0.22	4.72		
B	0.19	4.69		
FSM-SSG-F	0.210	4.654	6.960	7.348
FSM-SSG-C	0.218	4.415		
HYB-SSG-C	0.238	4.512		
SAS-SST-F	0.224	4.797	6.883	7.407
LNS-SST-F	0.200	4.610	7.025	7.255

TABLE 8.2: Separation and reattachment points for reference LES and hybrid simulations. The LES simulations are MFR (Fröhlich et al., 2005), TL (Temmerman and Leschziner, 2001) and B (Breuer et al., 2009).

Leschziner, 2001) used 4.5 million cells. Therefore the finest mesh used in the hybrid study is a third of the grid points of the total LES, whilst the coarse mesh uses a sixth.

### 8.3.3 Results and Discussion

Table 8.2 lists the points of separation and reattachment for all hybrid cases listed in Table 8.1 and for three reference LES cases: MFR (Fröhlich et al., 2005), TL (Temmerman and Leschziner, 2001) and B (Breuer et al., 2009). Note that the values in Table 8.2 have been calculated using linear interpolation between two cells where  $C_f$  is of the opposite sign. Firstly, one can see that the main separation bubble, a statistical feature parametrised by  $x_{s_1}$  and  $x_{r_1}$ , is predicted uniformly well. The coarse mesh cases have a slightly reduced reattachment length; however this underprediction is the equivalent of only two grid cells. The secondary separation bubble is a grid dependent phenomena — only the fine mesh predicts its presence. This is reasonably large for the SAS-SST-F, the least unsteady closure, which has a reduced level of resolved scale mixing. This is further reflected in the higher value of  $x_{r_1}$ .

Figure 8.6(a) is a plot of the time and spanwise averaged skin friction  $C_f$  for all cases. All methodologies agree with the reference LES and is a major improvement over steady closures (e.g Jakirlić et al., 2001). RANS has difficulties due to the absence of unsteady structures in the free shear layer and the favourable pressure gradient boundary layer on the upstream side of the hills. These problems have been overcome; whilst the first is obvious, the second is because Hybrid RANS/LES has responded well to the strong pressure gradient in the second half of the domain as it runs in URANS mode near the wall. The unsteady nature of the near wall region has also resulted in the correct prediction of the fluctuating separation point. The magnitude of  $C_f$ , a quantity that depends on contributions from resolved and modelled stress, the shape of the velocity

profiles and numerics, has been overpredicted in the reverse flow region. Whilst cancellation of errors is likely, Fig. 8.6(d) shows an overprediction in Reynolds shear stress magnitude at its peak location. Further, linear upwinding is performed near the wall to accommodate the RANS model which contributes numerical error.

Figures 8.6(b)-8.6(f) are plots of time and spanwise averaged total<sup>4</sup> turbulent kinetic energy  $k$ , streamwise velocity  $U$  and three of the total Reynolds stress components  $\overline{u'u'}$ ,  $\overline{u'v'}$  and  $\overline{v'v'}$  at the location  $x/H = 2.0$ . This profile exhibits the challenges involved in this case; traversing from  $y = 0$ , the profile crosses the reverse flow region, the separated shear layer and the bulk flow region. The main features of this profile can be seen in the velocity profile: the reverse flow region ends at  $y/H = 0.5$ , the free shear layer at  $y/H = 1.3$  and the bulk flow is affected by the top wall at  $y/H = 2.7$  where the boundary layer starts. In general, all closures have captured these features but with minor disagreements in the peak negative value. FSM-SSG-C and SAS-SST-F have the largest value, resulting in a minor increase in average velocity gradient  $\partial_y U$ .

Turbulent kinetic energy, is a better prediction on the coarse mesh — compare FSM-SSG-C and FSM-SSG-F. This is because the mesh topologies are different and there are more grid cells in the wall normal direction near the region of separation. This has allowed a faster break up of the RANS shear layer and in turn more resolved structures which are vital to a correct shear layer. This sentiment is best seen with the LNS-SST-F, which has the most unsteady structures of all models tested and the best prediction of  $k$ , especially considering closures on the same grid have a moderate overprediction of the peak value.

The shear stress contains, as discussed above, an overprediction in the peak value which contributes to skin friction magnitude error, however it also provides insight into the nature of the structures in the free shear layer. The FSM-SSG-F, HYB-SSG-C and SAS-SST-F provide a mildly accentuated kink slightly above the free shear layer. This can be understood by considering the normal stress profiles. Whilst  $\overline{u'u'}$  is of the correct magnitude,  $\overline{v'v'}$  is overpredicted by these cases. As Reynolds stress structures are formed by the shear, then lifted up and ejected to the bulk, they are overly displaced by large wall normal fluctuations. An overprediction of normal stress but correct prediction of streamwise stress in the free shear layer is the opposite to the wall bounded flow in Chapter 7. The production of Reynolds stress at this point depends strongly on wall normal fluctuating and mean velocity, unlike in the channel where  $P_{22} \approx 0$  at the RANS-LES interface. This implies a generation mechanism as the RANS shear layer breaks down similar to that described in Section 7.1, but this time in the wall normal direction. Note this is also a slight problem in the streamwise component for the FSM-SSG-F and SAS-SST-F.

---

<sup>4</sup>modelled and resolved contributions.

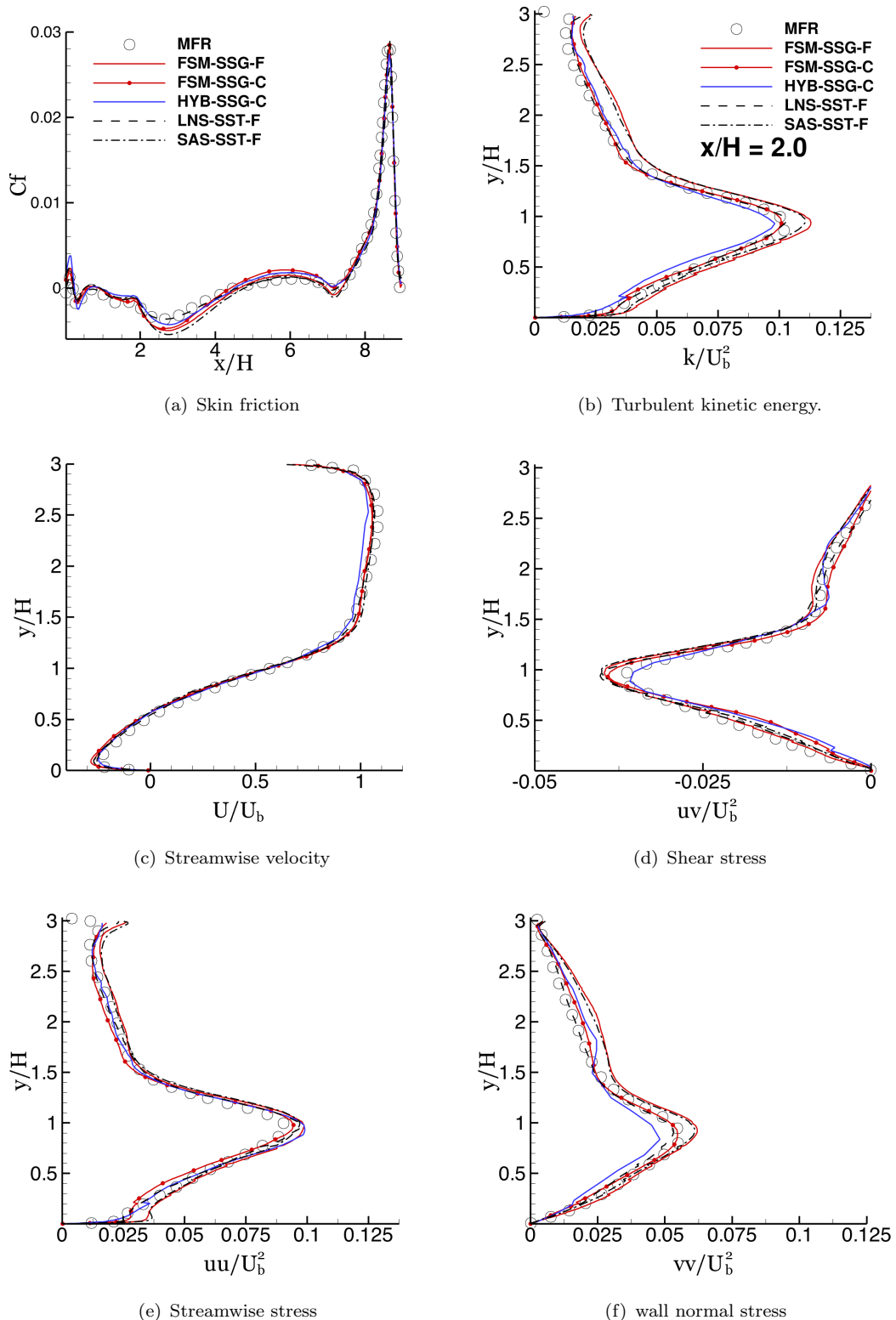


FIGURE 8.6: Skin friction along lower surface and profiles of turbulent kinetic energy, streamwise velocity and component of Reynolds stress along the plane  $x/H = 2.0$ .

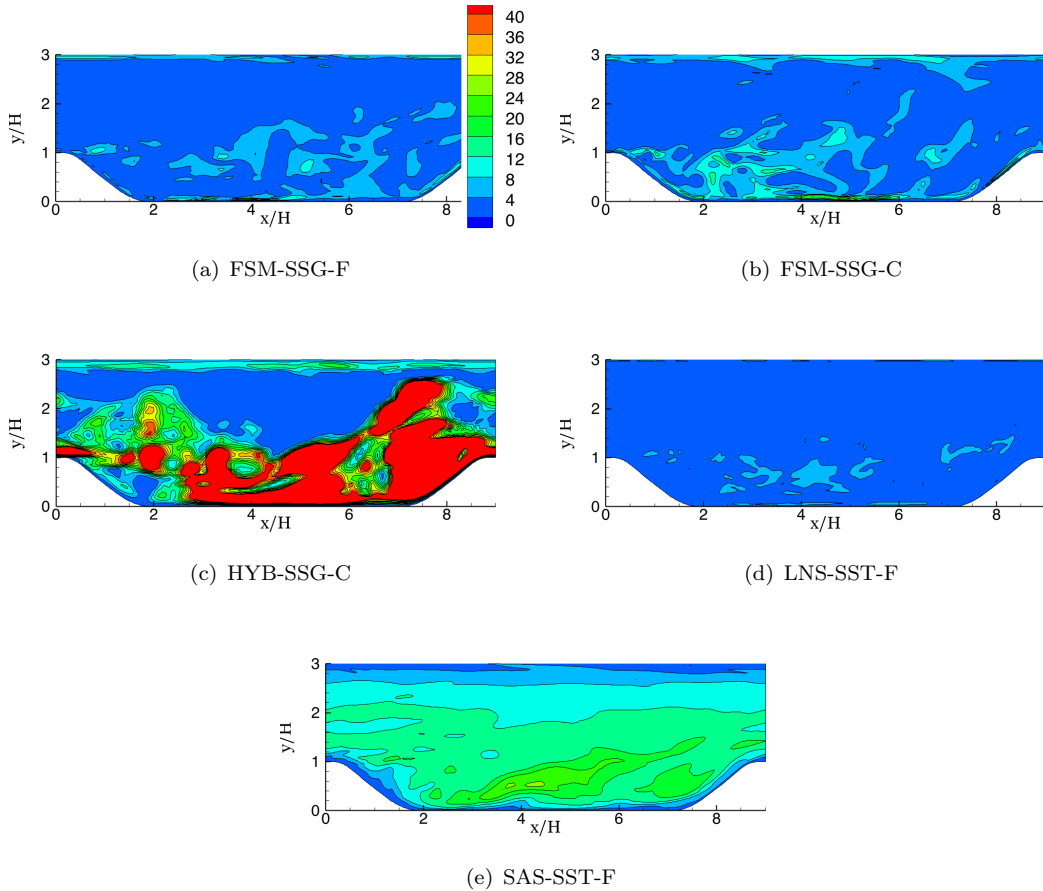
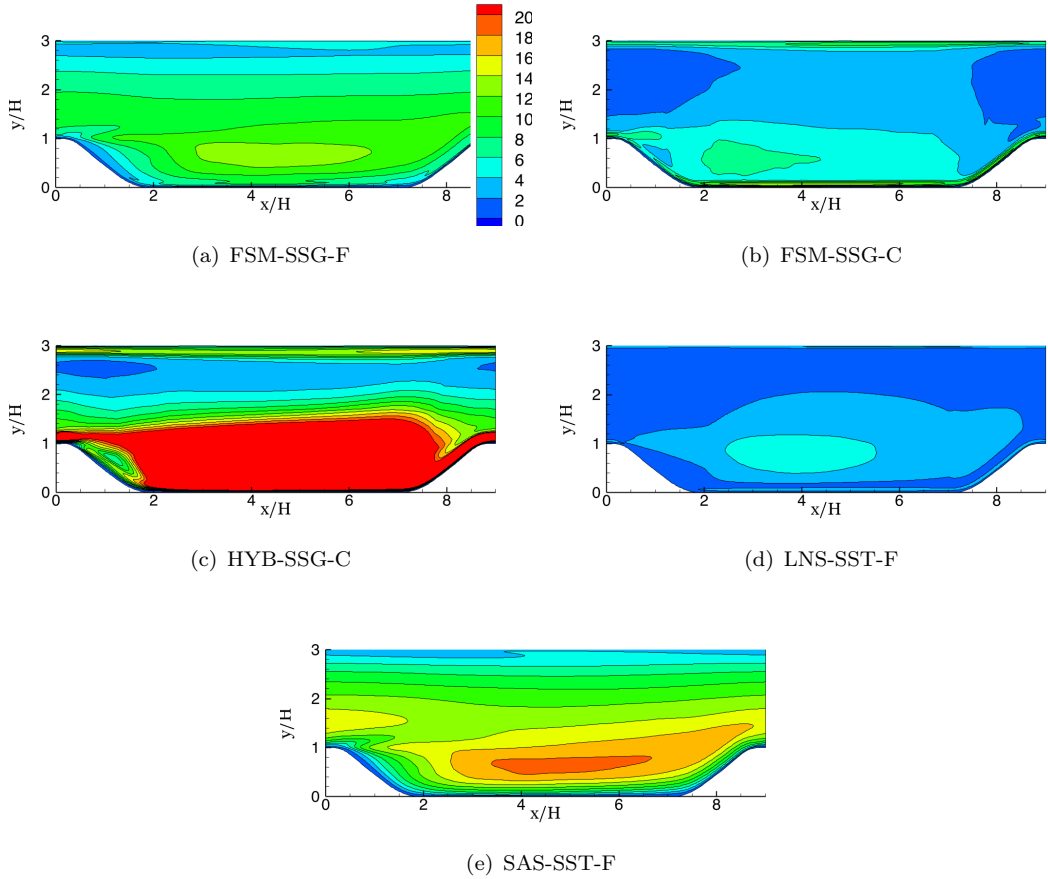


FIGURE 8.7: Instantaneous values of  $\nu^{\text{sgs}}/\nu$ .

Near the lower surface, FSM-SSG-F and SAS-SST-F strongly overpredict the streamwise stress. This inner peak is precisely the RANS region in size and is created by the presence of super-streaks penetrating this zone. This phenomena is also seen in the LNS-SST-F and FSM-SSG-C to a lesser extent. The HYB-SSG-C does not predict their presence, mainly because the  $F_{fb}$  switch is very active with this damping function and mesh. Note, this is in stark contrast to the planar channel case, see Chapter 7, where the model effectively ran as an LES. For the other cases, the finer mesh has allowed the model to go more unsteady in the RANS region due to smaller streamwise grid spacing. The coarse mesh however appears to be coarse enough in the streamwise direction in this region to not support these structures.

Instantaneous contours of  $\nu^{\text{sgs}}/\nu$  are shown in Fig. 8.7. The FSM-SSG-C exhibits large levels of  $\nu^{\text{sgs}}/\nu$  in the RANS region as the model runs in URANS mode which is seen to a greater extent in the HYB-SSG-C case.

The URANS methodology SAS-SST-F, contains the highest bulk values of  $\nu^{\text{sgs}}/\nu$ , indicating the lack of sensitivity to the grid scale, as the closure is only weakly dependent on  $\Delta$ . On the other hand, HYB-SSG-C shows the largest range of  $\nu^{\text{sgs}}/\nu$ . The maximum value is 98, but because of the huge variation in test cases this value is truncated to

FIGURE 8.8: Mean values of  $\nu^{\text{sgs}}/\nu$ .

allow for a uniform colour scale. This huge variation is observed for two reasons. Firstly, Eq. 6.11 is sensitive to the smallest scales of motion present so will naturally vary more than the FSM- cases. Secondly, the shielding function has failed with the HYB damping function. Because the smallest scale dependence lowers the value of  $F$ , the cell Reynolds number becomes instantaneously very low as such the damping function,

$$F = \min \left( \frac{F_{\text{damp}}}{1 - f_b}, 1.0 \right), \quad (8.2)$$

becomes unity. The notation  $F_{\text{damp}}$  is used briefly to distinguish between near wall modification and length scale damping.  $f_b$  is the blending function,

$$f_b = \tanh \left( C_{f_b} \frac{500 \beta^* k \nu^4}{y^2 \varepsilon} \right) \quad (8.3)$$

and is the culprit for  $F \rightarrow 1$ . As the cell Reynolds number is very low  $k/\epsilon \rightarrow \infty$  and  $f_b \rightarrow 1$ . These large regions of  $F = 1$  can be seen in Fig. 8.9(c). It is unclear how these RANS packets influence the overall result, but could potentially relaminarise the flow in other configurations.

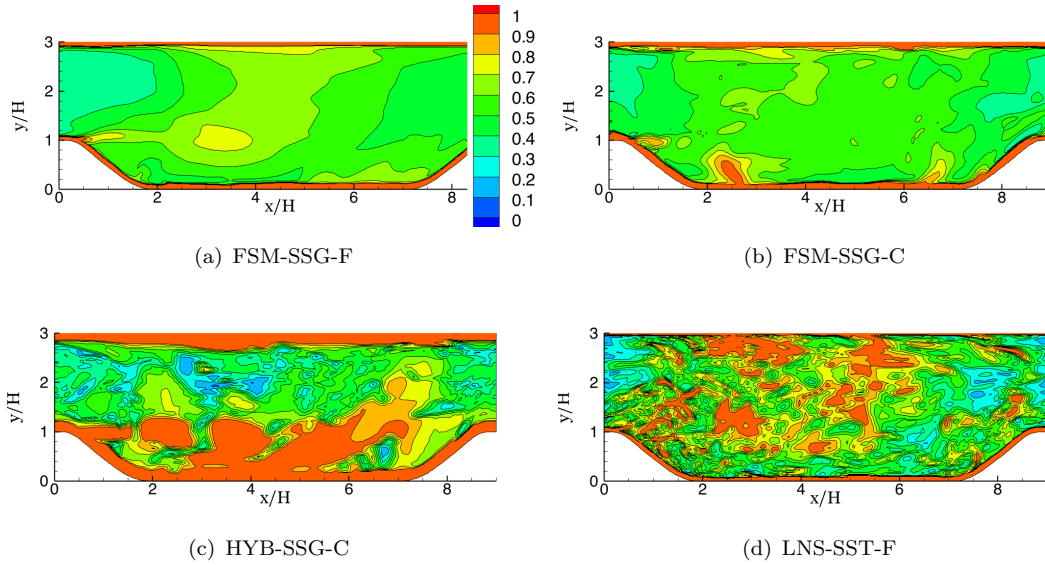


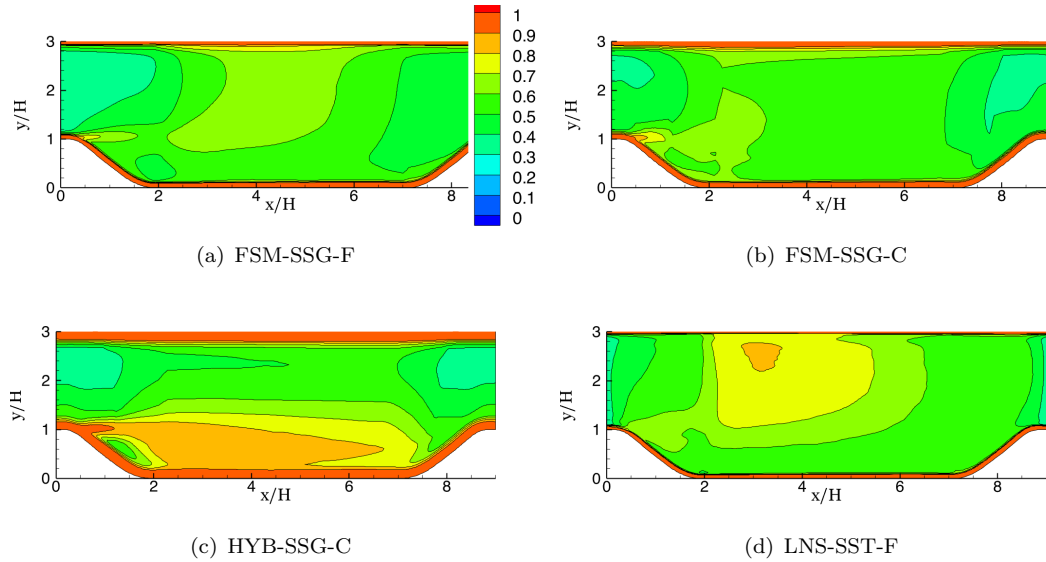
FIGURE 8.9: Instantaneous values of the damping functions  $F$ .

To compare FSM-SSG-F and LNS-SST-F, we must look at the mean values of  $\nu^{\text{sgs}}/\nu$  in Fig. 8.8. The LNS-SST-F is effectively running in LES mode for this geometry and has therefore reduced average subgrid contribution. Each resolved large scale structure is carrying less model contribution than the FSM-SSG-F. In turn the FSM-SSG-C (see Fig. 8.7) is carrying more subgrid contribution, however the value is much lower on average than the FSM-SSG-F. This is surprising considering the differing cell counts between the two meshes, but is attributed to differing topology.

Final comments are reserved for the damping functions themselves. Instantaneous contours (for the same timestep as Fig. 8.7) are plotted in Fig. 8.9 and mean values in Fig. 8.10. Note, SAS-SST-F does not contain a natural damping function so is omitted. Much of the nature of these contours has been discussed, but a few key points are highlighted. The topology of the fine mesh can be ascertained by considering the mean values of  $F$ . Despite contrasting differences between instantaneous values, the LNS-SST-F and FSM-SSG-F contain very similar averaged profiles that show a coarsening on the bulk region. Interestingly the LNS-SST-F has a higher average value despite being more responsive to the mesh.

As mentioned, the HYB-SSG-C is responsive to the smallest scale, not the largest, and as such  $\partial_{x_j} F$  is significantly higher than the FSM-SSG-C. The large RANS packets have produced a large mean region behind the hill. Note that in light of the mean  $F$  for the HYB-SSG-C and LNS-SST-F cases, it is not a useful quantity to consider when assessing the ability of a closure to go unsteady.

In the contours of  $F$ , at the point of separation, the separating shear layer can be observed in the FSM and HYB methodologies. This is an undesirable feature of requiring a RANS layer at the wall — once it separates, this region of high viscosity delays the

FIGURE 8.10: Mean values of the damping functions  $F$ .

formation of resolved eddies. The LNS-SST-F does a better job of breaking up the shear layer, allowing the model to go unsteady. This is because the LNS is running as a Smagorinsky LES, but with the coefficient set to the low value of 0.05. For this case this works as expected, however this author has severe reservations about low coefficients in the damping function, which can cause poor recovery of the RANS limit or as is the case with LNS, reduces the ability to adapt to very coarse meshes. Consequently the methodology performs very poorly for the tandem cylinder geometry in the next section. Despite this comment, there is still the lesson to be learnt that the current formulation of Eq. 6.10 requires more sophisticated damping in the presence of separation.

## 8.4 Inline Tandem Cylinders

### 8.4.1 Flow Description

The geometry consists of two inline tandem cylinders. The upstream cylinder creates an unsteady wake which interacts with the downstream cylinder. The problem is therefore an issue of wake interference. The gap between the cylinders dictates the type of flow structures. At large distances, regular vortex shedding from the upstream cylinder occurs. As the distance is reduced, vortex shedding is suppressed and the flow reattaches on the downstream cylinder (Meneghini et al., 2001). The flow setup is similar to that of a simplified landing gear and has therefore received much attention with regards to understanding noise generation. Experiments in the Basic Aerodynamic Research Tunnel (BART) and in the Quiet Flow Facility (QFF) at the NASA Langley Research Center have provided a huge data base for hybrid model validation studies (Jenkins et al., 2006; Lockard et al., 2007; Khorrami et al., 2007; Neuhart et al., 2009). Recently

the inline tandem cylinders has been subjected to Benchmark problems for Airframe Noise Computations (BANC) workshops (Lockard, 2011).

In order to bridge the gap between computations and experiments, the front cylinder was tripped in the experiments. Further these experiments show that the wake behind the rear cylinder strongly depends on the state of the boundary layer. Two data sets are available, one with the rear cylinder tripped and another with no tripping. When comparing to the tripped data, the boundary layer can be treated as fully developed and transition does not need to be accounted for, justifying the use of a RANS region near the wall.

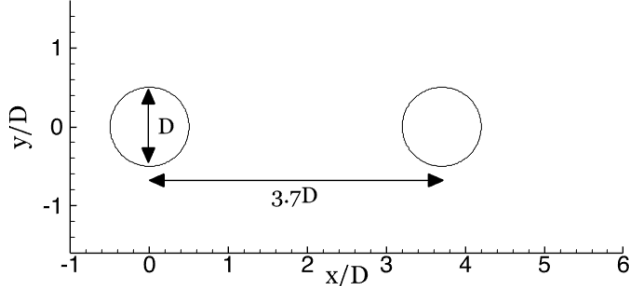
The particular cylinder spacing chosen is designed to keep computational costs down, but still provide a flow setup with vortex shedding and wake/body interaction. Because the spacing is close to the point where vortex shedding is suppressed, this behaviour is occasionally seen in computational studies. The main challenge for hybrid techniques is to appropriately capture the wake/body interaction and by association the development of the downstream boundary layer. If this interaction is incorrectly predicted, it has consequences in the flow field further downstream.

#### 8.4.2 Computational Domain and Setup Conditions

The Reynolds number for the flow based on cylinder diameter  $D$  and freestream velocity  $U_0$  is  $\text{Re}_D = 1.66 \times 10^5$ , although it is argued by Lockard (2011) that the tripping of the boundary layer results in the pressure distribution resembling that for a flow with a Reynolds number over  $8 \times 10^6$ . The cylinder spacing, defined from centre to centre, is set to  $3.7D$ . The two dimensional profile of the geometry can be seen in Fig. 8.11. The domain in the spanwise direction has a width of  $3D$ . Despite being a predominantly two dimensional flow, three dimensional effects cannot be ignored. Spanwise correlations approach zero for a width of  $7D$  Lockard (2011) and the experiments were performed at spanwise widths of  $12.4D$  (BART) and  $16D$  (QFF). Ideally simulations would match these aspect ratios, but in order to reduce computational costs, the standard in numerical studies is to set the spanwise domain at  $3D$  (Lockard, 2011). Studies by Lockard et al. (2007) showed that some of the three dimensional structures can be captured with this domain width.

Inflow turbulence levels in the experimental studies were less than 0.10% and for the CFD calculations the inflow condition is prescribed as  $k_0 = 10^{-6}U_0^2$  and  $\omega_0 = 5U_0/D$  considering the discussions of Spalart and Rumsey (2007). Neumann boundary conditions are applied at the outlet and spanwise periodic boundary conditions are used.

The mesh is a C-type grid, shown in Fig. 8.12. The overall number of points is  $1 \times 10^6$ , which is an approximate saving by a factor of 7 compared to the other hybrid simulations submitted to the BANC workshop (Lockard, 2011). An FSM contribution was also made

FIGURE 8.11:  $x - y$  plane of the Tandem Cylinders geometry.

to this workshop, however this used a total of 2 million cells and so the mesh used in this study requires FSM to apply a significantly greater model contribution. Despite the coarse nature of the grid, special care was taken to ensure sensible  $y_1^+$  values and enable to-the-wall integration. The average  $y_1^+$  value is therefore 0.7 and the maximum is 1.7.

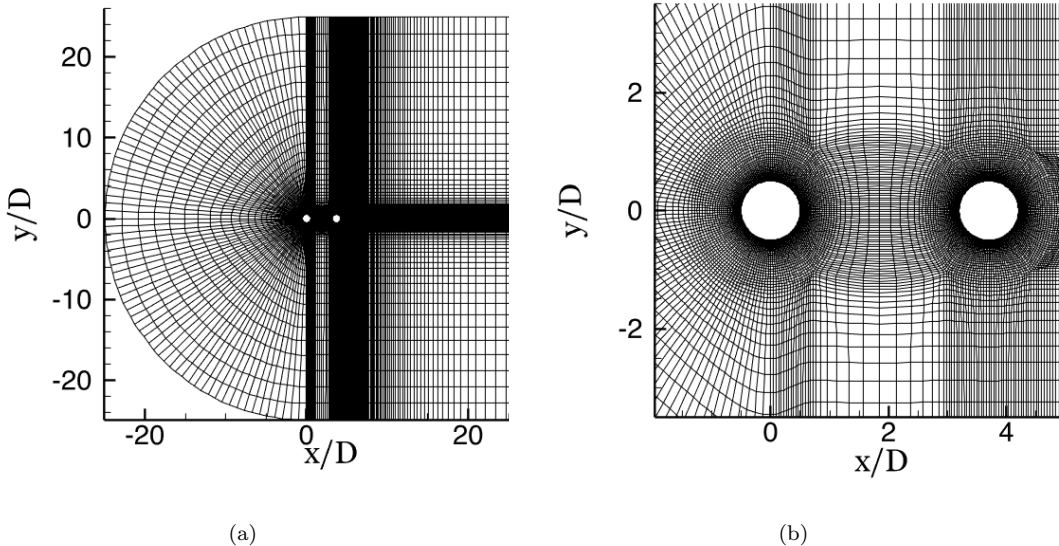


FIGURE 8.12: Mesh for the inline tandem cylinders case.

### 8.4.3 Results and Discussion

A total of eight cases are presented in this section and so in the interest of sanity not all information can be conveyed. The results are compared to the experiments of Jenkins et al. (2006); Lockard et al. (2007); Khorrami et al. (2007); Neuhart et al. (2009). Primarily this section is a comparison of DDES and the modified FSM in the coarse mesh limit with differing numerical schemes. To complement this LNS (Section 2.2.4.3) and SAS (Section 2.2.4.2) are included primarily to highlight the challenge and a second subgrid model for FSM is also tested. Each case is encoded METHOD-RANS MODEL-CONVECTION SCHEME and are summarised in Table 8.3. Note, the hybrid convection scheme is the blending method of Weinmann et al. (2014), UP is linear upwinding,

case	method	RANS model	convection scheme	near wall treatment
FSM-SSG-HYB	FSM	SSG	hybrid	$F_{fb}$
FSM-SSG-LUST	FSM	SSG	LUST	$F_{fb}$
FSM-SSG-95-5	FSM	SSG	blended 80-20	$F_{fb}$
FSM-SST-HYB	FSM	SST	hybrid	$F_{fb}$
DDES-SA-95-5	DDES	SA	blended 95-5	DDES
DDES-SA-80-20	DDES	SA	blended 80-20	DDES
LNS-SST-HYB	LNS	SST/Smag <sup>5</sup>	hybrid	$F_{fb}$
SAS-SST-UP	SAS	SST	hybrid	none

TABLE 8.3: Hybrid RANS/LES tandem cylinder cases

blended X-Y is a fixed percentage of X central and Y linear upwinding and LUST is a blended 80-20 scheme that maintains second order accuracy (Jasak et al., 2007).  $F_{fb}$  is shorthand for the near wall treatment Eq. 6.12. All methods use second order implicit backward discretisation in time and subgrid quantities are discretised by linear upwinding. Note that because SAS does not contain a natural damping function  $F$ , no near wall treatment could be applied.

Clearly the matrix of cases considered is far from complete. Much of this is down to time constraints but some are due to convergence issues. The notable exceptions because of the latter are DDES-SA-LUST and DDES-SA-HYB. Both of these strategies converged to the unphysical flow state, discussed in Section 8.4.3.2, rendering direct comparisons between the FSM counterparts impossible. As a consequence, FSM-SSG-LUST must be directly compared with DDES-SA-80-20.

#### 8.4.3.1 The Comparison of DDES with the Modified FSM

The instantaneous resolved flow fields are visualised with snapshots of  $Q = 0.5(\Omega^2 - S^2)$  criterion in Fig. 8.13 for the FSM cases and the DDES cases in Fig. 8.14. The differences in the FSM and DDES cases are primarily through the chosen numerical scheme. The hybrid blending has produced the least noisy flow field whilst maintaining a breakdown of the free shear layer. Higher levels of FSM model contribution have made it far less sensitive to the numerical scheme. The FSM-SSG cases visually maintain the physical processes of the flow field, but the least numerically dissipative schemes introduce small unphysical structures — the appearance becoming increasingly hectic as the level of upwinding is reduced.

---

<sup>5</sup>Limited Numerical Scales is a RANS limited LES so requires both a RANS and LES closure.

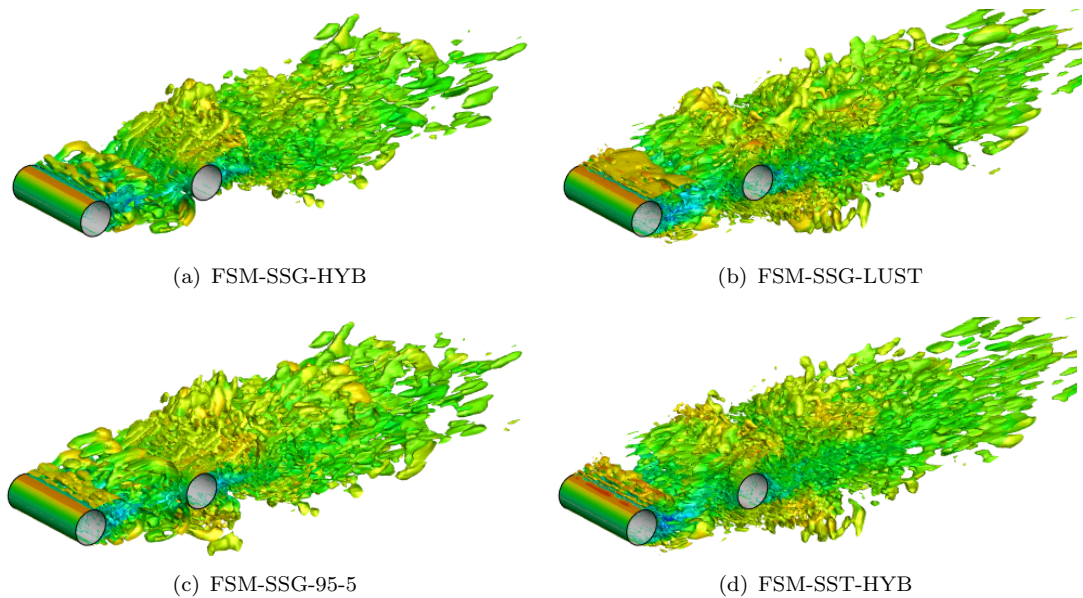


FIGURE 8.13: Isosurfaces of  $Q$  criterion at  $170000ms^{-2}$ , coloured by instantaneous streamwise velocity  $u_x$ , for the FSM cases.

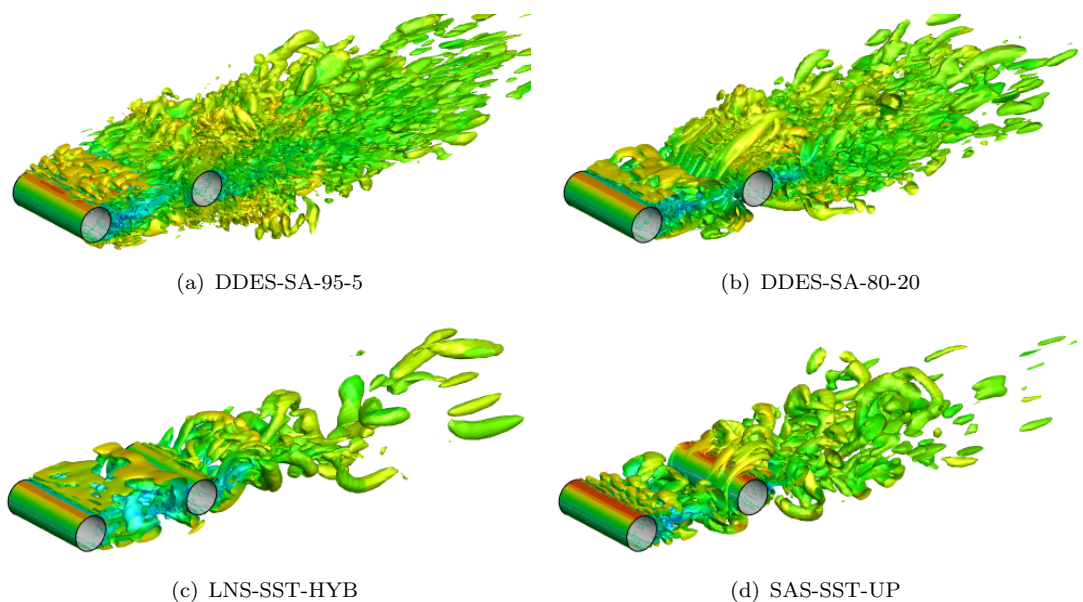


FIGURE 8.14: Isosurfaces of  $Q$  criterion at  $170000\text{ms}^{-2}$ , coloured by instantaneous streamwise velocity  $u_x$ , for non-FSM cases.

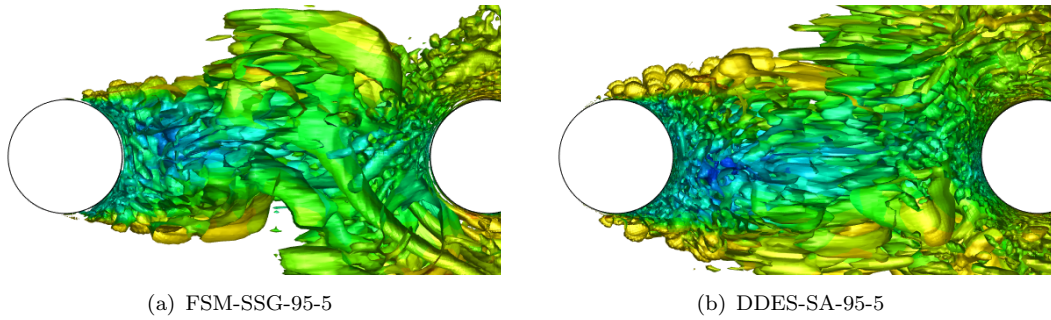


FIGURE 8.15: Isosurfaces of  $Q$  criterion at  $170000 \text{ m s}^{-2}$ , coloured by instantaneous streamwise velocity  $u_x$ , a side view comparison of FSM-SSG-95-5 and DDES-SA-95-5.

This is more pronounced in the DDES-SA-95-5 case however, Fig. 8.15 shows a side view of  $Q$  criterion along with the direct comparison FSM-SSG-95-5. The combined model and numerical dissipation is no longer adequate, not only is the flow field visually polluted, the separation point is far too early and large structures are created from the first cylinder. There are two possible reasons for these large structures deep in the boundary layer: firstly the coefficient  $C_{\text{ddes}} = 0.65$  is too low at the RANS-LES interface or secondly the early switch to LES mode that DDES specifies. In either case, the numerical scheme does not dissipate the structures in the boundary layer and so the model must perform this operation. This has not happened, resulting in  $\nu^{\text{sgs}}$  being too low and the boundary layer appears subject to grid induced separation. The low value of global  $\nu^{\text{sgs}}$  can be seen in Fig. 8.16, comparing to the FSM-SSG-95-5.

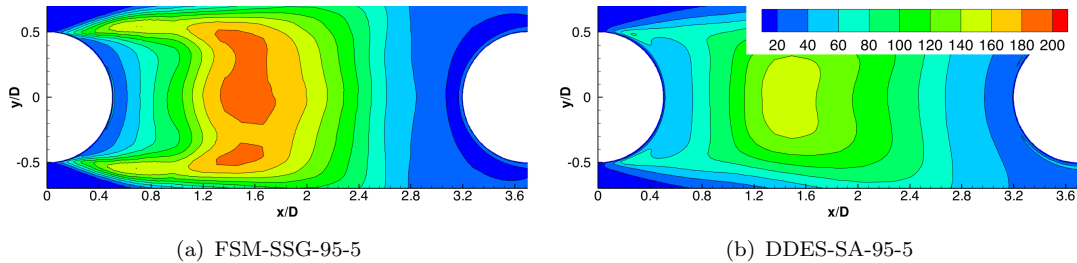


FIGURE 8.16: Mean values of  $\nu^{\text{sgs}}/\nu$ .

Contours of streamwise velocity and two dimensional turbulent kinetic energy are plotted in Fig. 8.17 and Fig. 8.19. The comparison in velocity is reasonable for all cases. The FSM-SSG-LUST is in good agreement up until  $x/D = 0.8$ , but elongates the reverse flow region. DDES closures predict a bubble too intense and too close to the upstream cylinder, especially the DDES-SA-95-5 case where the separation point is seen statistically too early, but prediction improves beyond  $x/D \approx 1.0$ . The implication is the deviation in the separation point is producing wakes at the wrong angle. Figure 8.18 is an extraction of the profile  $y = 0$  to further emphasise this point.

Turbulent kinetic energy is a large differentiator in closure performance. The contours of two-dimensional turbulent kinetic energy  $k^{2D}$  in the gap, Fig. 8.19, and the profile  $y = 0$ ,

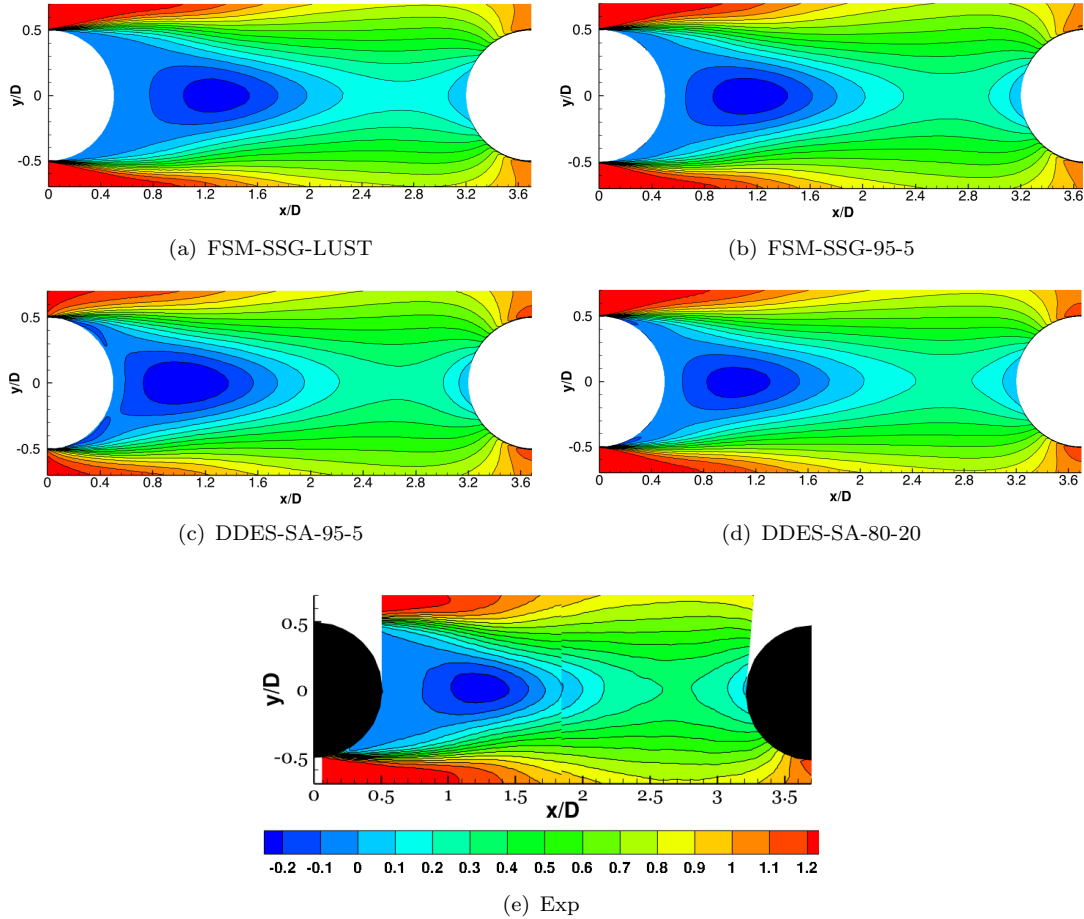
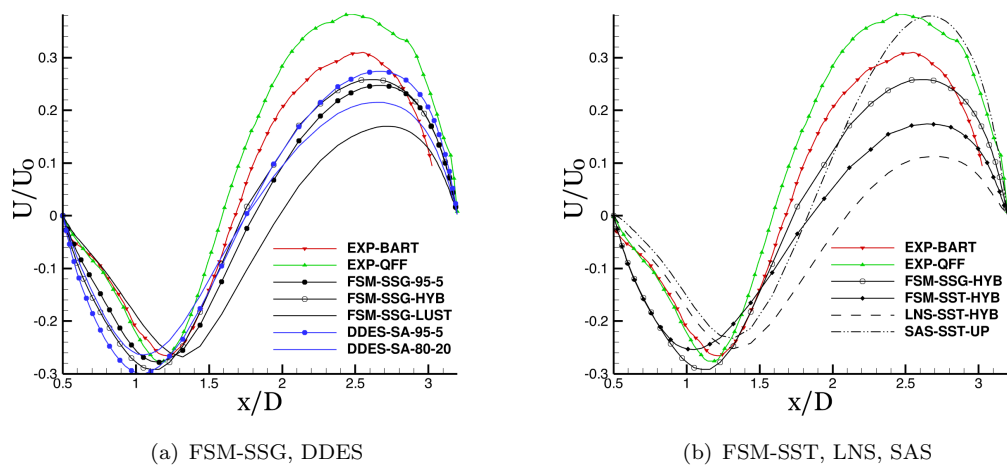
FIGURE 8.17: Averaged streamwise velocity  $U_x/U_0$  in the gap region.FIGURE 8.18: Averaged streamwise velocity  $U_x/U_0$  in the gap region.

Fig. 8.20, show the DDES to under predict in the detached shear layer and overpredict at the separation point. Further the base of the downstream cylinder shows too much turbulent activity. It should be noted that the FSM-SSG-LUST has not converged, but is still included for completeness. The line plots show a general overprediction in turbulent kinetic energy immediately downstream of the upstream cylinder due to the RANS layer. Beyond the initial high value, the trend is then similar to the experimental results.

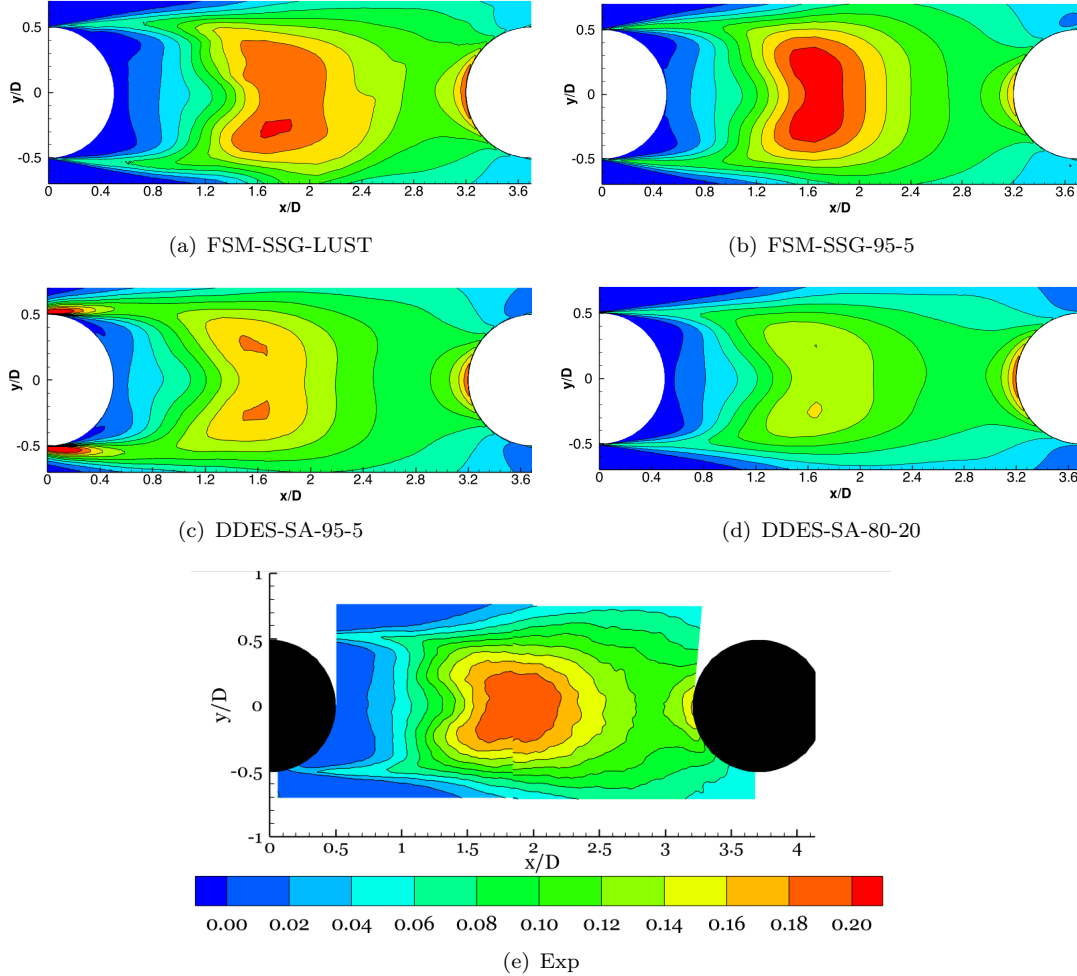


FIGURE 8.19: Averaged two dimensional turbulent kinetic energy  $k^{2D} = 0.5(\bar{u}'\bar{u}'^{\text{res}} + \bar{v}'\bar{v}'^{\text{res}} + \tau_{11}^{\text{rans}} + \tau_{22}^{\text{rans}})$  in the gap region. DDES is resolved  $k^{2D}$  only.

The pressure coefficients  $C_p$  and  $C_p^{\text{rms}}$  are plotted in Fig. 8.21 and Fig. 8.22. The point of peak suction is generally good on the upstream cylinder. However the wake impinging on the second cylinder is too slow, raising the pressure. The downstream cylinder peak suction is marginally better for the DDES cases, possibly due to the underprediction in  $k^{2D}$  in the gap. The improved velocity prediction around the second cylinder can be seen in Fig. 8.17.

$C_p^{\text{rms}}$  is another large model differentiator. Around upstream cylinder, the  $C_p^{\text{rms}}$  predicted by the DDES-SA-95-5 is highly overpredicted and the width of the peak indicates the

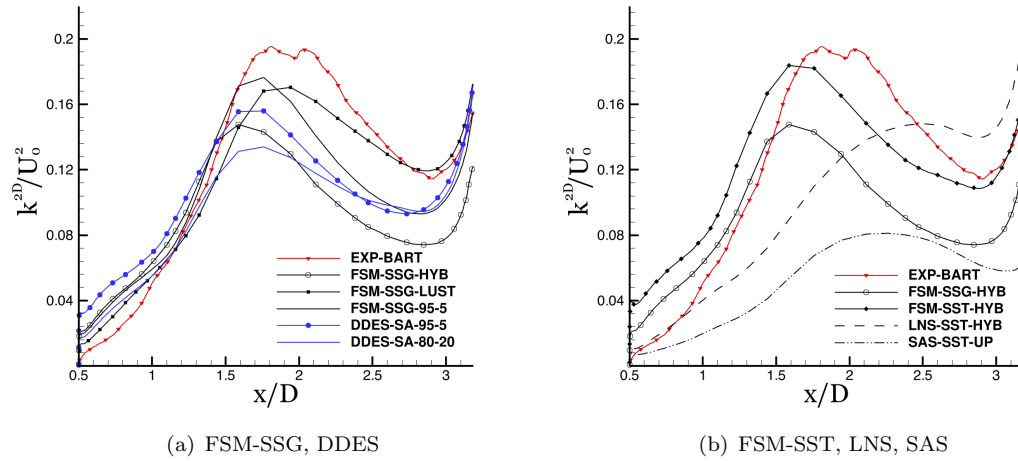


FIGURE 8.20: Averaged two dimensional turbulent kinetic energy  $k^{2D} = 0.5(\overline{u'u'}^{\text{res}} + \overline{v'v'}^{\text{res}} + \tau_{11}^{\text{rans}} + \tau_{22}^{\text{rans}})$  in the gap region. DDES is resolved  $k^{2D}$  only.

degree the separation point moves. These large values are expected to have consequences in the acoustic predictions. This is also a problem somewhat for the DDES-SA-80-20 and to some extent the FSM-SSG cases, but reduced in gravity. The point of separation for the FSM-SSG cases and DDES-SA-80-20 is reasonable, although the shift in peaks indicate a moderate sensitivity to the numerical scheme.

The large peak in the downstream cylinder  $C_p^{\text{rms}}$  provides information on the wake impingement and the secondary peak the point of separation. It is the opinion of this author that the closures should represent the tripped experimental data because of the enforced RANS mode near the wall, but the untripped data is included should the reader disagree. Again the pressure fluctuates highly at the point of separation for all closures, with the exception of the FSM-SSG-HYB. This is probably unsurprising considering the hybrid blending scheme enforces near wall upwinding that is highly dissipative. The remaining schemes used with the FSM-SSG closure predict the point of separation well, whilst the DDES-SA are too late.

#### 8.4.3.2 On the Difficulty of the Tandem Cylinder Geometry

The complex physics and coarse mesh produce a challenging case for any modelling strategy. To highlight this, the LNS-SST-HYB and SAS-SST-UP have been included in Fig. 8.14, Fig. 8.18, Fig. 8.20 and Fig. 8.22. Both closures have an incorrect global flow field because the wake behind the first cylinder is poorly predicted. The LNS-SST-HYB takes too long to break down the free shear layer and switch to full LES mode. Therefore the vortices are shed directly onto the downstream cylinder. The SAS-SST-UP separates far too late and the fluctuation in pressure is hugely overpredicted.

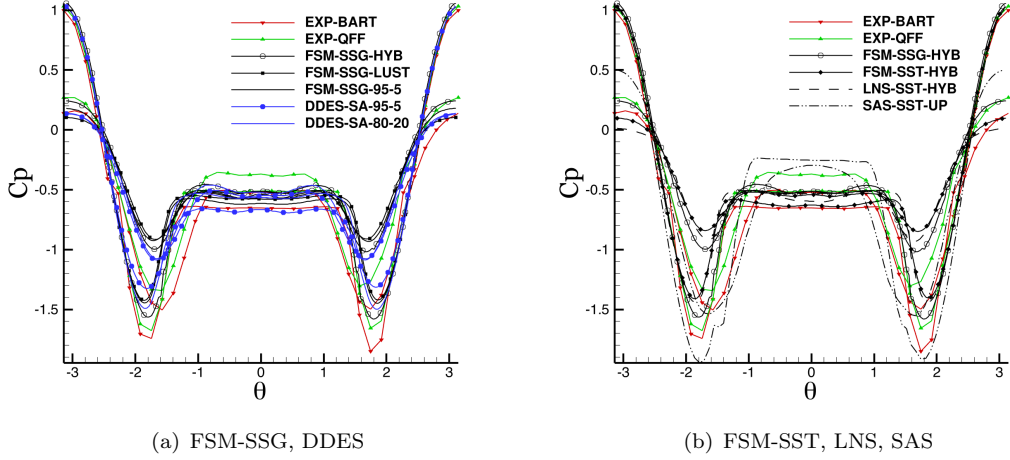


FIGURE 8.21: Steady pressure coefficient  $C_p$  on the upstream and downstream cylinders.

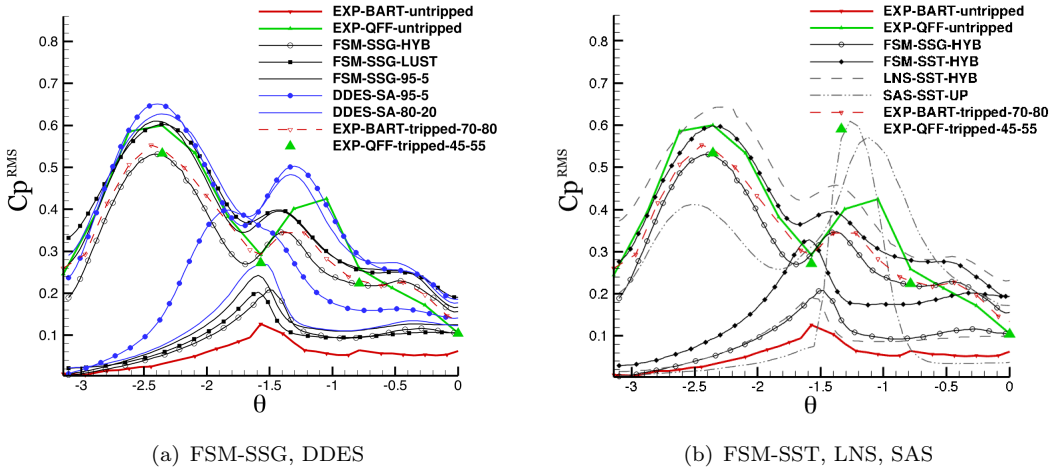


FIGURE 8.22: Fluctuating pressure coefficient  $C_p^{rms}$  on the upstream and downstream cylinders.

As mentioned in Section 8.4.1, the spacing between the cylinders is at the critical point where the flow field bifurcates from vortex shedding to vortex suppression. As a result there are two possible flow field states during CFD simulations. The majority of closures correctly predicted the vortex shedding state, however a few reverted to suppressing the vortex shedding after some time, hence the lack of direct comparisons between FSM and DDES.  $U/U_0$  with mean streamlines and  $\omega_z D/U_0$  have been plotted in Fig. 8.23. The large recirculation zone spanning the entire gap in Fig. 8.23(b) has its focal point towards the second cylinder, whilst the vortex shedding in Fig. 8.23(d) is entirely suppressed. The FSM-SSG-HYB model has been plotted for a direct comparison. It is worth noting with this snapshot, there is a presence of vortical structures near the downstream base of the first cylinder, which is inline with experiments and is not predicted by all methodologies.

Further, there is the presence of small structures in the second half of the gap. The implication is that the contribution function is only resolving some of the structures when possible.

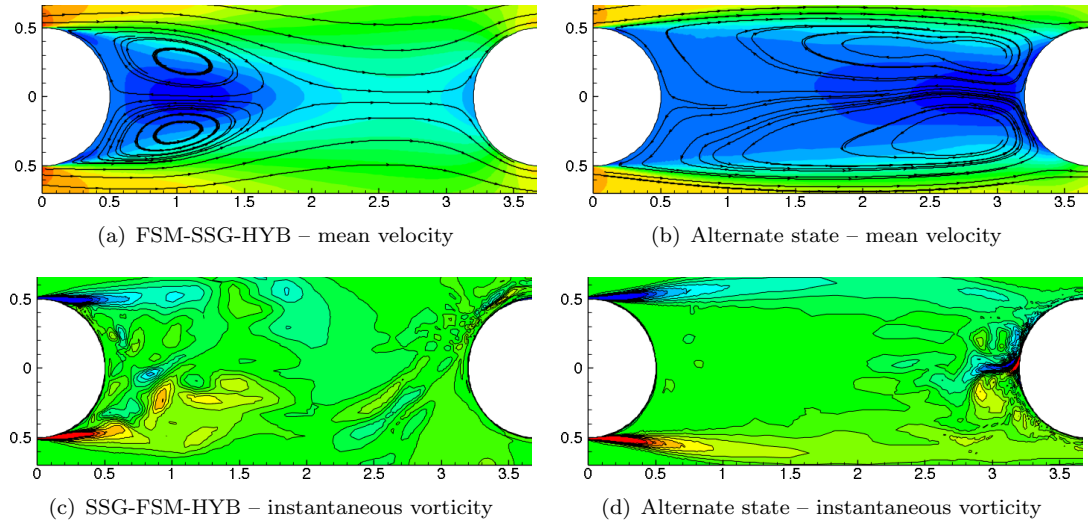


FIGURE 8.23: The two different flow field states.

#### 8.4.3.3 Further Comments Specific to the Modified FSM

Two subgrid models were tested for the hybrid blending scheme: FSM-SSG-HYB and FSM-SST-HYB. In Fig. 8.13, Fig. 8.18, Fig. 8.20 and Fig. 8.22 these have been plotted for a direct comparison. One can see large differences in the flow fields. Whilst this is possibly not the best test case to understand the effect of the underlying RANS model, it is important to observe the differences. Evidently as the grid is coarsened the model plays a large part in dictating the global flow field. The SSG closure provides markedly different dissipation to the SST, the latter having less — seen in the Q criterion and also in Fig. 8.24. It is unclear as to whether this is primarily caused by the separation or is an inherent property of the transport equations. The echo of higher separation point fluctuation is seen in the mean velocity profile — the flow does not spend enough time parallel to the x-axis in the gap region, implicating incorrect wake angles. Further, early separation is consistent with too little dissipation — similar to the grid induced separation seen with the DDES-SA-95-5. This can be clearly seen in the contours of  $F$ , the RANS region near the wall is entirely destroyed — see Fig. 8.24. We can conclude that the subgrid model matters. However the evidence is not yet compelling enough to suggest a more complex model is better, rather a deeper understanding is still required.

A snapshot of the damping function  $F$  is plotted for the FSM-SSG-95-5 and FSM-SST-HYB in Fig. 8.24. Two effects are at play, first the numerical scheme and second the underlying RANS model. It is unclear why near wall central differencing would cause the large RANS contribution in the centre of the free shear layer, so it is assumed that

the RANS model makes a very large difference. Secondly, there are higher gradients in the FSM-SSG-95-5 case, likely due to the numerical scheme.

On balance, the FSM-SSG has performed particularly well for this case. The modified damping function, Eq. 6.10, is found to respond well to the instantaneous wakes and provide temporally and spatially changing levels of model contribution. Further it is more robust to the numerical scheme used, which is important considering that many CFD codes provide their favourite. There are almost more questions than answers however; the marrying of  $F$  to numerical scheme and RANS model is not yet understood for complex cases and prompts further research.

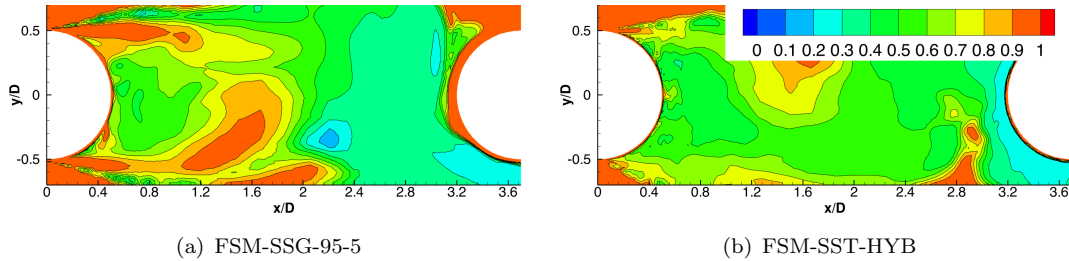


FIGURE 8.24: Instantaneous modified FSM damping function  $F$ .

## 8.5 Summary

This chapter represents the main validation of the new Hybrid RANS/LES formulations created in Chapter 6. Their ability to predict statistics in a range of complex flows is testament to the Gene Expression Programming framework utilised throughout this thesis.

Of particular note, is the success of the closure denoted FSM at predicting the tandem cylinder geometry. Whilst the flow over the vertical fence and periodic hills (Sections 8.2 and 8.3 respectively) were calculated well by a range of existing closures, this was not the case for the tandem cylinder geometry. This contained a number of potential stumbling blocks. Firstly, the complexity of the wake-body interaction made the fluctuating pressure difficult to obtain around the second cylinder. The modelling strategy strongly influenced the separation point on the first cylinder. Without this, the quality of results quickly deteriorated. Finally, the mesh was extremely coarse which meant the novel damping function had to provide the appropriate length scale to get the contribution of the model correct. All of these were achieved by the novel FSM, such that predictions were good and reasonably insensitive to the numerical method used. This last point is an important one to stress, predictions by the DDES started to deteriorate once the level of upwinding was reduced. This implies that the contribution function is not providing the correct dissipation length scale close to the RANS limit.

Future tests should begin with more complex geometries. Currently, neither of the novel damping functions have been tested on a three dimensional geometry. The DNS of Vinuesa et al. (2015) provides a reference for a mounted square cylinder and would make an ideal test case for the new closures.



# Chapter 9

## Conclusions and Outlook

### 9.1 Advances in Gene Expression Programming

This thesis has, at its core, developed and used Gene Expression Programming (GEP) for the primary purpose of furthering models of turbulence. GEP is an evolutionary algorithm specifically well suited to regression problems because of its variable length phenotype, naturally allowing for the expression of any mathematical equation. The non-deterministic flavour and the ability to traverse the search space has provided an excellent tool for developing turbulence models that otherwise rely on assumptions or *ad hoc* formulations.

To this end, a scalar field framework has been implemented that differs from the original algorithm of Ferreira (2001) to incorporate an insertion operator that promotes sharing of good portions of the genotype. The fitness function has been slightly modified for extensive use in a ‘batch’ environment where one may wish to change the range of selection and/or the number of data points. In other words, when one is testing parameters, the image of the fitness function still spans  $[0,1]$  which is helpful for immediate comparisons.

A novel tensor field regression algorithm has been presented in Section 4.3. This shares an analogy with plasmids, symbiotic structures that improve their hosts’ fitness by altering their phenotype. This symbiotic GEP algorithm in its current form can perform tensor regression, however can be readily expanded for other duties, say simply vector regression or highly involved decision trees. Plasmids, at the lowest level, could be used as another means of information transport in a population of chromosomes. The most useful fitness function was found to be the higher dimensional analogy to an angle, Eq. 4.14. This allowed for the creation of tensors well aligned with the training data and through careful scaling of independent variables, distance metrics were not required.

The last GEP framework, detailed in Section 4.4, to be utilised within this thesis is a variant on the clustering algorithm of Zheng et al. (2012). The algorithm was devised for

use with large data sets, hence its steady state nature. Further, elitism was sacrificed at the cost of evaluating the fitness of an individual and only those chosen for selection had their fitness evaluated. Because of the variable length phenotype in GEP, the number of groups does not need to be specified which fits perfectly with the GEP ethos. This allowed for the probing of high dimensional data sets and the discovery of features that otherwise would have been missed.

## **9.2 Advances in Turbulence Modelling**

These three implementations of GEP have been applied to problems faced when developing turbulence models. The regression tools have been used to develop new functions and terms within equations, whereas the clustering algorithm was used more as an exploratory tool.

In Chapter 5, extra anisotropy terms were added to the Boussinesq approximation to create Explicit Algebraic Stress Models (EASMs). These RANS models were created using Direct Numerical Simulation (DNS) data from the adverse pressure gradient region in a backward facing step geometry and applied on the classic periodic hills test case. This class of RANS model, although performing very well for the periodic hills, was not created and described with the intention of promoting their use. Rather, they were created to advocate the underlying framework that produced them. Focus on the link between the chromosome fitness and performance in actual CFD use was analysed and evidence shows a positive correlation for the case considered. This important link should be further tested, but adds weight to the process as a viable tool for the creation of specialist models. The process also shows that entire stress-strain relationships can be constructed by sensitising GEP to DNS data.

It should be reiterated that the creation of 50 models was for the purposes of analysis only, this thesis does not suggest that 50 models should be used for prediction purposes. This is one of the advantages of the speed of RANS calculations. One can create a subclass of models and then evaluate them in a CFD setting, in a way that can be seen as an extension of their phenotype. Despite the clear syntax and structural differences between the produced models, their CFD performance is relatively similar on a different geometry to that which they were trained with. This goes some way to showing that a small number of models is required to produce acceptable levels of uncertainty in the quality of results. As a consequence, this kind of process could be envisaged in a parametric design study where one has infrequent access to high fidelity methods such as a wind tunnel or computing cluster. Models could be trained on the results from this and then used to drive design with much cheaper, but topologically similar flow configurations.

Chapter 6 detailed the use of the scalar field implementation of GEP to devise new length scale damping functions for Unified Hybrid RANS/LES. This was achieved by filtering DNS data of a pipe and backward facing step. Each data set was used to create a new damping function. The filtered data was used to mimic Hybrid RANS/LES flow fields, for which an idealised value of the damping function could be calculated via Eq. 2.76 for a given filter width. Length scales could then also be calculated which acted as independent variables for the regression. As such, damping functions were produced that could be inserted into almost any unified framework.

Because the runtime of Hybrid RANS/LES is much slower than steady RANS, one is left with concentrating on first regressing a new damping function, say Eq. 6.10 or Eq. 6.11, then accepting it if: it is amongst the fittest seen and also it seems sensible. The more rigorous statistical work of Chapter 5 was simply not possible due to the number of hybrid simulations required for a meaningful sample. Instead, Eq. 6.11 was found by reducing the number of independent variables, then observing that with this reduced set, a common functional form was obtained. These new damping functions, when inserted into a RANS model, provide a Flow Simulation Methodology (FSM) style of closure. These FSM approaches were then put through their paces for three separated flow applications. Three relative mesh resolutions were used: the vertical fence (Section 8.2) was solved using a coarse mesh, the periodic hills (Section 8.3) using both a coarse and medium resolution mesh and the inline tandem cylinders (Section 8.4) using a coarse mesh. At all three levels of resolution, the new FSM approaches gave good predictions. Further, alongside existing closures, the new methodologies performed very well. Particularly the performance of Eq. 6.10 for the tandem cylinder geometry, shows that this function is a viable alternative to Detached Eddy Simulation variants — a current popular choice in industry. Especially considering the modified FSM displayed less sensitivity to the numerics on coarser meshes, due to the higher coefficient. Note this higher coefficient is damped via the logarithmic term on finer meshes.

In Chapter 7, these new FSM-hybrids were used as a tool for exploring the deficiencies of blending RANS into LES in fully turbulent boundary layers. Reynolds stress structures were extracted for DNS and also for the hybrids. These were then compared with one another to ascertain problem areas with Hybrid RANS/LES. This was achieved via the clustering implementation of GEP; the DNS structures were classified into six groups and then this grouping was applied to the hybrids. Whilst producing visually similar groups,<sup>1</sup> findings quantified the Reynolds stress structures that characterise the artificial buffer layer and showed that a slower transition between the two modelling philosophies produces worse structures, which were linked to poor statistical results. These comments are not just specific to the new FSM approaches detailed throughout this thesis, but rather are more universal to Hybrid RANS/LES in general. The exception to this is

---

<sup>1</sup>The DNS near wall ejections group did not suddenly exist in a different spatial location, for example.

Zonal Hybrid RANS/LES, which is designed such that the entire boundary layer runs in LES or RANS mode.

### 9.3 Outlook and Recommendations

With regards to the future of the work contained within this thesis, there are many avenues one could pursue. Some are more fundamental to the evolutionary side of development whilst some combine the GEP framework to further the methodologies described within this thesis.

At a fundamental level, one could develop the GEP framework to be more efficient such that very large data sets could be used. The larger the data set, the better coverage of all possible values the desired function should take. This would be especially useful for the RANS application highlighted in Section 5.6. One could therefore train a model not only on an adverse pressure gradient, but on a favourable pressure gradient etc. This ‘Big-Data’ framework would have to be considered carefully. Preliminary studies in this direction have shown that performing regression using contrasting data points yields a cancellation of features. In other words, the function tries to do too much and simultaneously does nothing. In the worst case scenario the returned function is just constant. One possible solution would be to consider island population models (Collins and Jefferson, 1991), where an island looks after a data set and has limited communication with other islands. A second approach would be to set out the data in a ring, where each chromosome can see a window on this ring. As the ring rotates the window is fixed, such that the chromosome sees a new subset of the overall data set. This would keep execution costs down, reducing the number of comparisons for each chromosome. The genetic operators would have some kind of localisation to their functionality, selection could be done by placing a Gaussian distribution over the individual meaning a low probability of sharing information with chromosomes with a different training window. As the data moves, this should encourage the propagation of components that are useful for a variety of environments. One would need to test the speed of genetic transfer against the speed of data point transfer from window to window. With this kind of ring structure, the algorithm is forced to not converge, promoting the continual evolution of useful code and various points of the ring would produce specialised individuals — creating something similar to a Pareto front but with respect to the data, not the independent variables.

A larger data set is not the only way to improve the RANS development framework. One could, as alluded to in Section 5.6, individually train extra anisotropy terms. The challenge then becomes one of developing identification functions that should activate each specific component at runtime. This is especially important because, as seen in Chapter 5, if a model is active in a flow regime different from its associated training data then the probability of non-realism is very high. Currently with the applications

in this thesis these are not required, however more complex geometries would almost certainly cause instabilities.

With respect to the Hybrid RANS/LES models presented in this thesis, these should be continually tested. Currently, the obvious lack of validation is a fully three dimensional geometry. A mounted square cylinder (Vinuesa et al., 2015) would provide the perfect test case. This kind of test case should hopefully shed light on whether the damping function should be uniform, as it is currently, or whether each stress component should be damped individually, as discussed in Section 7.3.

The other major issue, predominantly highlighted in Chapter 7, is that of the near wall switching process. It is clear that the overly tall structures must be broken up to control the shape of the artificial buffer layer or stopped from forming entirely. Currently this is unlikely to be performed via filtering DNS data because of the lack of appropriate training data. Instead, this author believes that an online training could provide the best options. At uncorrelated time steps, Reynolds stress structures could be extracted and compared with DNS. Another option would be to perform some kind of forcing similar to the work by Piomelli et al. (2003). The functional form could be obtained either by regressing a stochastic forcing function such that the break up produces correct Reynolds stress structures or by relating a function to the statistical profiles and thresholding the length scale damping function if some value of velocity fluctuation is exceeded.

Generally speaking, to further the work in this thesis, one requires more high fidelity data from a range of different flows. Lacking from this thesis are fully three dimensional flow fields and high Reynolds number flows. Both of these could be obtained by using experimental data and would provide an interesting study, both for the development of turbulence models and testing the applicability of the current framework in more demanding situations.



## Appendix A

### Equations for Each Model $a_{ij}^x$

Listed in Eq. A.1-A.50 are the fifty models produced by GEP in Chapter 5. These are listed for completeness and transparency only! Each model is an expression for  $a_{ij}^x/k$  where the  $\tau$  superscript denotes a scaling by  $2\beta^*k/\varepsilon$ . Each expression is a simplified form of the phenotype of each individual  $P_n^j$  produced from raw output of GEP. This simplification only groups similar terms and does not change the mathematical structure of the equations.

$$- (S_{ik}^\tau \Omega_{kj}^\tau - \Omega_{ik}^\tau S_{kj}^\tau) - (S_{ik}^\tau S_{kj}^\tau - \frac{1}{3} \delta_{ij} S_{mn}^\tau S_{nm}^\tau) - 1.866 S_{ij}^\tau S_{mn}^\tau S_{mn}^\tau (S_{mn}^\tau S_{mn}^\tau + 0.99) \\ \quad (A.1)$$


---

$$- (S_{ik}^\tau \Omega_{kj}^\tau - \Omega_{ik}^\tau S_{kj}^\tau) - (S_{ik}^\tau S_{kj}^\tau - \frac{1}{3} \delta_{ij} S_{mn}^\tau S_{nm}^\tau) (-0.99 S_{mn}^\tau S_{mn}^\tau + 0.195) - (S_{ik}^\tau S_{kj}^\tau - \frac{1}{3} \delta_{ij} S_{mn}^\tau S_{nm}^\tau) + \\ 2 S_{ij}^\tau (-0.99 S_{mn}^\tau S_{mn}^\tau + 0.195 \Omega_{mn}^\tau \Omega_{mn}^\tau + 0.00195) \\ \quad (A.2)$$


---

$$- (S_{ik}^\tau \Omega_{kj}^\tau - \Omega_{ik}^\tau S_{kj}^\tau) - (S_{ik}^\tau S_{kj}^\tau - \frac{1}{3} \delta_{ij} S_{mn}^\tau S_{nm}^\tau) (-3 S_{mn}^\tau S_{mn}^\tau - \Omega_{mn}^\tau \Omega_{mn}^\tau + 1.109) - \\ (S_{ik}^\tau S_{kj}^\tau - \frac{1}{3} \delta_{ij} S_{mn}^\tau S_{nm}^\tau) + S_{ij}^\tau (-2 S_{mn}^\tau S_{mn}^\tau - \Omega_{mn}^\tau \Omega_{mn}^\tau + 0.01) + S_{ij}^\tau (-2 S_{mn}^\tau S_{mn}^\tau + \\ \Omega_{mn}^\tau \Omega_{mn}^\tau (S_{mn}^\tau S_{mn}^\tau - 0.109) - \Omega_{mn}^\tau \Omega_{mn}^\tau) \\ \quad (A.3)$$


---

$$- (S_{ik}^\tau S_{kj}^\tau - \frac{1}{3} \delta_{ij} S_{mn}^\tau S_{nm}^\tau) (-2 S_{mn}^\tau S_{mn}^\tau - \Omega_{mn}^\tau \Omega_{mn}^\tau + 1) + S_{ij}^\tau (-2 S_{mn}^\tau S_{mn}^\tau + 1.01) - S_{ij}^\tau + \\ (\Omega_{ik}^\tau \Omega_{kj}^\tau - \frac{1}{3} \delta_{ij} \Omega_{nm}^\tau \Omega_{mn}^\tau) \\ \quad (A.4)$$


---

---


$$S_{ij}^\tau(-S_{mn}^\tau S_{mn}^\tau + \Omega_{mn}^\tau \Omega_{mn}^\tau + 1.03) - S_{ij}^\tau + (\Omega_{ik}^\tau \Omega_{kj}^\tau - \frac{1}{3} \delta_{ij} \Omega_{nm}^\tau \Omega_{mn}^\tau) \quad (\text{A.5})$$


---

---


$$\begin{aligned} & - (S_{ik}^\tau \Omega_{kj}^\tau - \Omega_{ik}^\tau S_{kj}^\tau) - (S_{ik}^\tau S_{kj}^\tau - \frac{1}{3} \delta_{ij} S_{mn}^\tau S_{nm}^\tau) + \\ & ((S_{ik}^\tau S_{kj}^\tau - \frac{1}{3} \delta_{ij} S_{mn}^\tau S_{nm}^\tau) - 2S_{ij}^\tau)(2S_{mn}^\tau S_{mn}^\tau + \Omega_{mn}^\tau \Omega_{mn}^\tau - 0.01) \end{aligned} \quad (\text{A.6})$$


---

---


$$\begin{aligned} & - (S_{ik}^\tau S_{kj}^\tau - \frac{1}{3} \delta_{ij} S_{mn}^\tau S_{nm}^\tau) + \\ & (S_{ij}^\tau(2S_{mn}^\tau S_{mn}^\tau + \Omega_{mn}^\tau \Omega_{mn}^\tau - 0.071) + S_{ij}^\tau)(-S_{mn}^\tau S_{mn}^\tau + \Omega_{mn}^\tau \Omega_{mn}^\tau + 0.01) + \\ & (\Omega_{ik}^\tau \Omega_{kj}^\tau - \frac{1}{3} \delta_{ij} \Omega_{nm}^\tau \Omega_{mn}^\tau) \end{aligned} \quad (\text{A.7})$$


---

---


$$\begin{aligned} & - 2(S_{ik}^\tau \Omega_{kj}^\tau - \Omega_{ik}^\tau S_{kj}^\tau) - (S_{ik}^\tau S_{kj}^\tau - \frac{1}{3} \delta_{ij} S_{mn}^\tau S_{nm}^\tau) + \\ & S_{ij}^\tau(-S_{mn}^\tau S_{mn}^\tau 3 - S_{mn}^\tau S_{mn}^\tau - \Omega_{mn}^\tau \Omega_{mn}^\tau + 0.01) + \\ & S_{ij}^\tau(-S_{mn}^\tau S_{mn}^\tau (S_{mn}^\tau S_{mn}^\tau + 1) - S_{mn}^\tau S_{mn}^\tau - \Omega_{mn}^\tau \Omega_{mn}^\tau + 0.01) - \\ & 2(\Omega_{ik}^\tau \Omega_{kj}^\tau - \frac{1}{3} \delta_{ij} \Omega_{nm}^\tau \Omega_{mn}^\tau) \end{aligned} \quad (\text{A.8})$$


---

---


$$- 1.01(S_{ik}^\tau \Omega_{kj}^\tau - \Omega_{ik}^\tau S_{kj}^\tau) - (S_{ik}^\tau S_{kj}^\tau - \frac{1}{3} \delta_{ij} S_{mn}^\tau S_{nm}^\tau) + 2S_{ij}^\tau(-S_{mn}^\tau S_{mn}^\tau + \Omega_{mn}^\tau \Omega_{mn}^\tau) \quad (\text{A.9})$$


---

---


$$\begin{aligned} & - 2(S_{ik}^\tau \Omega_{kj}^\tau - \Omega_{ik}^\tau S_{kj}^\tau) - (S_{ik}^\tau S_{kj}^\tau - \frac{1}{3} \delta_{ij} S_{mn}^\tau S_{nm}^\tau) + \\ & S_{ij}^\tau(-S_{mn}^\tau S_{mn}^\tau 2 - S_{mn}^\tau S_{mn}^\tau + \Omega_{mn}^\tau \Omega_{mn}^\tau + 1.01) - S_{ij}^\tau - 2(\Omega_{ik}^\tau \Omega_{kj}^\tau - \frac{1}{3} \delta_{ij} \Omega_{nm}^\tau \Omega_{mn}^\tau) \end{aligned} \quad (\text{A.10})$$


---

---


$$\begin{aligned} & - 0.222(S_{ik}^\tau \Omega_{kj}^\tau - \Omega_{ik}^\tau S_{kj}^\tau) - 0.444(S_{ik}^\tau S_{kj}^\tau - \frac{1}{3} \delta_{ij} S_{mn}^\tau S_{nm}^\tau) - \\ & 2S_{ij}^\tau S_{mn}^\tau S_{mn}^\tau + (\Omega_{ik}^\tau \Omega_{kj}^\tau - \frac{1}{3} \delta_{ij} \Omega_{nm}^\tau \Omega_{mn}^\tau) \end{aligned} \quad (\text{A.11})$$


---

---


$$\begin{aligned} & - (S_{ik}^\tau \Omega_{kj}^\tau - \Omega_{ik}^\tau S_{kj}^\tau) + S_{ij}^\tau(-2S_{mn}^\tau S_{mn}^\tau - \Omega_{mn}^\tau \Omega_{mn}^\tau + 1.01) - \\ & 2S_{ij}^\tau + (-(S_{ik}^\tau S_{kj}^\tau - \frac{1}{3} \delta_{ij} S_{mn}^\tau S_{nm}^\tau) + S_{ij}^\tau)(-2S_{mn}^\tau S_{mn}^\tau - \Omega_{mn}^\tau \Omega_{mn}^\tau + 1.01) \end{aligned} \quad (\text{A.12})$$


---

---


$$\begin{aligned}
& - (S_{ik}^\tau \Omega_{kj}^\tau - \Omega_{ik}^\tau S_{kj}^\tau) - (S_{ik}^\tau S_{kj}^\tau - \frac{1}{3} \delta_{ij} S_{mn}^\tau S_{nm}^\tau) + \\
& ((S_{ik}^\tau S_{kj}^\tau - \frac{1}{3} \delta_{ij} S_{mn}^\tau S_{nm}^\tau) - S_{ij}^\tau) (S_{mn}^\tau S_{mn}^\tau 2 + S_{mn}^\tau S_{mn}^\tau (S_{mn}^\tau S_{mn}^\tau - 0.01)) + \\
& (-S_{ij}^\tau + (\Omega_{ik}^\tau \Omega_{kj}^\tau - \frac{1}{3} \delta_{ij} \Omega_{nm}^\tau \Omega_{mn}^\tau)) (2S_{mn}^\tau S_{mn}^\tau - 0.01)
\end{aligned} \tag{A.13}$$


---

$$S_{ij}^\tau (-2.01 S_{mn}^\tau S_{mn}^\tau - \Omega_{mn}^\tau \Omega_{mn}^\tau + 0.01) + (\Omega_{ik}^\tau \Omega_{kj}^\tau - \frac{1}{3} \delta_{ij} \Omega_{nm}^\tau \Omega_{mn}^\tau) \tag{A.14}$$


---

$$\begin{aligned}
& - (S_{ik}^\tau \Omega_{kj}^\tau - \Omega_{ik}^\tau S_{kj}^\tau) - (S_{ik}^\tau S_{kj}^\tau - \frac{1}{3} \delta_{ij} S_{mn}^\tau S_{nm}^\tau) - S_{ij}^\tau (2S_{mn}^\tau S_{mn}^\tau 2 + 2S_{mn}^\tau S_{mn}^\tau - 0.004)
\end{aligned} \tag{A.15}$$


---

$$\begin{aligned}
& - (S_{ik}^\tau \Omega_{kj}^\tau - \Omega_{ik}^\tau S_{kj}^\tau) - (S_{ik}^\tau S_{kj}^\tau - \frac{1}{3} \delta_{ij} S_{mn}^\tau S_{nm}^\tau) - S_{ij}^\tau + \\
& (2S_{mn}^\tau S_{mn}^\tau - 1.07) (-0.1859923 (S_{ik}^\tau S_{kj}^\tau - \frac{1}{3} \delta_{ij} S_{mn}^\tau S_{nm}^\tau) \Omega_{mn}^\tau \Omega_{mn}^\tau - S_{ij}^\tau)
\end{aligned} \tag{A.16}$$


---

$$\begin{aligned}
& - (S_{ik}^\tau \Omega_{kj}^\tau - \Omega_{ik}^\tau S_{kj}^\tau) - (S_{ik}^\tau S_{kj}^\tau - \frac{1}{3} \delta_{ij} S_{mn}^\tau S_{nm}^\tau) + \\
& S_{ij}^\tau (-S_{mn}^\tau S_{mn}^\tau 2 - 2S_{mn}^\tau S_{mn}^\tau - \Omega_{mn}^\tau \Omega_{mn}^\tau + 0.01) - \\
& (\Omega_{ik}^\tau \Omega_{kj}^\tau - \frac{1}{3} \delta_{ij} \Omega_{nm}^\tau \Omega_{mn}^\tau)
\end{aligned} \tag{A.17}$$


---

$$- S_{ij}^\tau (S_{mn}^\tau S_{mn}^\tau - 0.193 \Omega_{mn}^\tau \Omega_{mn}^\tau + 1) + S_{ij}^\tau + (\Omega_{ik}^\tau \Omega_{kj}^\tau - \frac{1}{3} \delta_{ij} \Omega_{nm}^\tau \Omega_{mn}^\tau) \tag{A.18}$$


---

$$\begin{aligned}
& - (S_{ik}^\tau \Omega_{kj}^\tau - \Omega_{ik}^\tau S_{kj}^\tau) - (S_{ik}^\tau S_{kj}^\tau - \frac{1}{3} \delta_{ij} S_{mn}^\tau S_{nm}^\tau) - S_{ij}^\tau + \\
& (- (S_{ik}^\tau S_{kj}^\tau - \frac{1}{3} \delta_{ij} S_{mn}^\tau S_{nm}^\tau) + S_{ij}^\tau) (-2.177 S_{mn}^\tau S_{mn}^\tau + 1.01)
\end{aligned} \tag{A.19}$$


---

$$\begin{aligned}
& - (S_{ik}^\tau S_{kj}^\tau - \frac{1}{3} \delta_{ij} S_{mn}^\tau S_{nm}^\tau) + \\
& (- (S_{ik}^\tau S_{kj}^\tau - \frac{1}{3} \delta_{ij} S_{mn}^\tau S_{nm}^\tau) + 2S_{ij}^\tau) (-S_{mn}^\tau S_{mn}^\tau - 0.17635 \Omega_{mn}^\tau \Omega_{mn}^\tau) + \\
& (\Omega_{ik}^\tau \Omega_{kj}^\tau - \frac{1}{3} \delta_{ij} \Omega_{nm}^\tau \Omega_{mn}^\tau)
\end{aligned} \tag{A.20}$$


---

$$\begin{aligned}
& - (S_{ik}^\tau S_{kj}^\tau - \frac{1}{3} \delta_{ij} S_{mn}^\tau S_{nm}^\tau) + S_{ij}^\tau (-S_{mn}^\tau S_{mn}^\tau + 1.618 \Omega_{mn}^\tau \Omega_{mn}^\tau + 0.01) + \\
& (\Omega_{ik}^\tau \Omega_{kj}^\tau - \frac{1}{3} \delta_{ij} \Omega_{nm}^\tau \Omega_{mn}^\tau)
\end{aligned} \tag{A.21}$$

$$\begin{aligned}
& - (S_{ik}^\tau S_{kj}^\tau - \frac{1}{3} \delta_{ij} S_{mn}^\tau S_{nm}^\tau) + 2S_{ij}^\tau (S_{mn}^\tau S_{mn}^\tau 2\Omega_{mn}^\tau \Omega_{mn}^\tau - S_{mn}^\tau S_{mn}^\tau + \Omega_{mn}^\tau \Omega_{mn}^\tau 2) + \\
& (\Omega_{ik}^\tau \Omega_{kj}^\tau - \frac{1}{3} \delta_{ij} \Omega_{nm}^\tau \Omega_{mn}^\tau)
\end{aligned} \tag{A.22}$$

$$0.198(S_{ik}^\tau \Omega_{kj}^\tau - \Omega_{ik}^\tau S_{kj}^\tau) + S_{ij}^\tau (-S_{mn}^\tau S_{mn}^\tau + 0.01) + (\Omega_{ik}^\tau \Omega_{kj}^\tau - \frac{1}{3} \delta_{ij} \Omega_{nm}^\tau \Omega_{mn}^\tau) \tag{A.23}$$

$$- (S_{ik}^\tau \Omega_{kj}^\tau - \Omega_{ik}^\tau S_{kj}^\tau) - (S_{ik}^\tau S_{kj}^\tau - \frac{1}{3} \delta_{ij} S_{mn}^\tau S_{nm}^\tau) + S_{ij}^\tau (-3S_{mn}^\tau S_{mn}^\tau + 1.02) - S_{ij}^\tau \tag{A.24}$$

$$\begin{aligned}
& - 2(S_{ik}^\tau \Omega_{kj}^\tau - \Omega_{ik}^\tau S_{kj}^\tau) - S_{ij}^\tau + \\
& (-(S_{ik}^\tau S_{kj}^\tau - \frac{1}{3} \delta_{ij} S_{mn}^\tau S_{nm}^\tau) + S_{ij}^\tau)(-S_{mn}^\tau S_{mn}^\tau + \Omega_{mn}^\tau \Omega_{mn}^\tau + 1.027) - \\
& (\Omega_{ik}^\tau \Omega_{kj}^\tau - \frac{1}{3} \delta_{ij} \Omega_{nm}^\tau \Omega_{mn}^\tau)
\end{aligned} \tag{A.25}$$

$$\begin{aligned}
& 0.091 \Omega_{mn}^\tau \Omega_{mn}^\tau ((S_{ik}^\tau S_{kj}^\tau - \frac{1}{3} \delta_{ij} S_{mn}^\tau S_{nm}^\tau) - S_{ij}^\tau) + \\
& 2\Omega_{mn}^\tau \Omega_{mn}^\tau (0.091(S_{ik}^\tau S_{kj}^\tau - \frac{1}{3} \delta_{ij} S_{mn}^\tau S_{nm}^\tau) \Omega_{mn}^\tau \Omega_{mn}^\tau + S_{ij}^\tau) + \\
& (\Omega_{ik}^\tau \Omega_{kj}^\tau - \frac{1}{3} \delta_{ij} \Omega_{nm}^\tau \Omega_{mn}^\tau)
\end{aligned} \tag{A.26}$$

$$\begin{aligned}
& - (S_{ik}^\tau \Omega_{kj}^\tau - \Omega_{ik}^\tau S_{kj}^\tau) - (S_{ik}^\tau S_{kj}^\tau - \frac{1}{3} \delta_{ij} S_{mn}^\tau S_{nm}^\tau) - \\
& S_{ij}^\tau (4S_{mn}^\tau S_{mn}^\tau + \Omega_{mn}^\tau \Omega_{mn}^\tau 2 - 0.01) + (\Omega_{ik}^\tau \Omega_{kj}^\tau - \frac{1}{3} \delta_{ij} \Omega_{nm}^\tau \Omega_{mn}^\tau)
\end{aligned} \tag{A.27}$$

$$\begin{aligned}
& - (S_{ik}^\tau \Omega_{kj}^\tau - \Omega_{ik}^\tau S_{kj}^\tau) - (S_{ik}^\tau S_{kj}^\tau - \frac{1}{3} \delta_{ij} S_{mn}^\tau S_{nm}^\tau) - S_{ij}^\tau - \\
& (-(S_{ik}^\tau S_{kj}^\tau - \frac{1}{3} \delta_{ij} S_{mn}^\tau S_{nm}^\tau) + S_{ij}^\tau)(3S_{mn}^\tau S_{mn}^\tau - 1.01) + (\Omega_{ik}^\tau \Omega_{kj}^\tau - \frac{1}{3} \delta_{ij} \Omega_{nm}^\tau \Omega_{mn}^\tau)
\end{aligned} \tag{A.28}$$

$$S_{ij}^\tau (-1.304 S_{mn}^\tau S_{mn}^\tau + 0.01) + (\Omega_{ik}^\tau \Omega_{kj}^\tau - \frac{1}{3} \delta_{ij} \Omega_{nm}^\tau \Omega_{mn}^\tau) \tag{A.29}$$

$$\begin{aligned}
& - (S_{ik}^\tau \Omega_{kj}^\tau - \Omega_{ik}^\tau S_{kj}^\tau) - (S_{ik}^\tau S_{kj}^\tau - \frac{1}{3} \delta_{ij} S_{mn}^\tau S_{nm}^\tau) (-S_{mn}^\tau S_{mn}^\tau + 1.104) + \\
& S_{ij}^\tau (-0.114 S_{mn}^\tau S_{mn}^\tau + \Omega_{mn}^\tau \Omega_{mn}^\tau - 0.00114) - (\Omega_{ik}^\tau \Omega_{kj}^\tau - \frac{1}{3} \delta_{ij} \Omega_{nm}^\tau \Omega_{mn}^\tau) \quad (\text{A.30})
\end{aligned}$$


---

$$\begin{aligned}
& - (S_{ik}^\tau \Omega_{kj}^\tau - \Omega_{ik}^\tau S_{kj}^\tau) - (S_{ik}^\tau S_{kj}^\tau - \frac{1}{3} \delta_{ij} S_{mn}^\tau S_{nm}^\tau) + \\
& S_{ij}^\tau (2 S_{mn}^\tau S_{mn}^\tau 2 \Omega_{mn}^\tau \Omega_{mn}^\tau - S_{mn}^\tau S_{mn}^\tau + 0.01) - \\
& (\Omega_{ik}^\tau \Omega_{kj}^\tau - \frac{1}{3} \delta_{ij} \Omega_{nm}^\tau \Omega_{mn}^\tau) \quad (\text{A.31})
\end{aligned}$$


---

$$\begin{aligned}
& - (S_{ik}^\tau \Omega_{kj}^\tau - \Omega_{ik}^\tau S_{kj}^\tau) - (S_{ik}^\tau S_{kj}^\tau - \frac{1}{3} \delta_{ij} S_{mn}^\tau S_{nm}^\tau) - \\
& S_{ij}^\tau (S_{mn}^\tau S_{mn}^\tau (S_{mn}^\tau S_{mn}^\tau - \Omega_{mn}^\tau \Omega_{mn}^\tau) + S_{mn}^\tau S_{mn}^\tau - 0.023) - (\Omega_{ik}^\tau \Omega_{kj}^\tau - \frac{1}{3} \delta_{ij} \Omega_{nm}^\tau \Omega_{mn}^\tau) \quad (\text{A.32})
\end{aligned}$$


---

$$\begin{aligned}
& - (S_{ik}^\tau \Omega_{kj}^\tau - \Omega_{ik}^\tau S_{kj}^\tau) - (S_{ik}^\tau S_{kj}^\tau - \frac{1}{3} \delta_{ij} S_{mn}^\tau S_{nm}^\tau) - \\
& S_{ij}^\tau (-S_{mn}^\tau S_{mn}^\tau 2 \Omega_{mn}^\tau \Omega_{mn}^\tau + S_{mn}^\tau S_{mn}^\tau) - S_{ij}^\tau (2 S_{mn}^\tau S_{mn}^\tau + \Omega_{mn}^\tau \Omega_{mn}^\tau - 0.01) \quad (\text{A.33})
\end{aligned}$$


---

$$- (S_{ik}^\tau \Omega_{kj}^\tau - \Omega_{ik}^\tau S_{kj}^\tau) - (S_{ik}^\tau S_{kj}^\tau - \frac{1}{3} \delta_{ij} S_{mn}^\tau S_{nm}^\tau) - S_{ij}^\tau (2.054 S_{mn}^\tau S_{mn}^\tau - 0.059) \quad (\text{A.34})$$


---

$$\begin{aligned}
& - (S_{ik}^\tau \Omega_{kj}^\tau - \Omega_{ik}^\tau S_{kj}^\tau) - (S_{ik}^\tau S_{kj}^\tau - \frac{1}{3} \delta_{ij} S_{mn}^\tau S_{nm}^\tau) + S_{ij}^\tau (S_{mn}^\tau S_{mn}^\tau \Omega_{mn}^\tau \Omega_{mn}^\tau - S_{mn}^\tau S_{mn}^\tau + 1) + \\
& S_{ij}^\tau (S_{mn}^\tau S_{mn}^\tau 2 \Omega_{mn}^\tau \Omega_{mn}^\tau - S_{mn}^\tau S_{mn}^\tau + 0.02) - S_{ij}^\tau \quad (\text{A.35})
\end{aligned}$$


---

$$- (S_{ik}^\tau \Omega_{kj}^\tau - \Omega_{ik}^\tau S_{kj}^\tau) - (S_{ik}^\tau S_{kj}^\tau - \frac{1}{3} \delta_{ij} S_{mn}^\tau S_{nm}^\tau) - S_{ij}^\tau (S_{mn}^\tau S_{mn}^\tau + 0.936) (2 S_{mn}^\tau S_{mn}^\tau - 0.013) \quad (\text{A.36})$$


---

$$\begin{aligned}
& - (S_{ik}^\tau \Omega_{kj}^\tau - \Omega_{ik}^\tau S_{kj}^\tau) - (S_{ik}^\tau S_{kj}^\tau - \frac{1}{3} \delta_{ij} S_{mn}^\tau S_{nm}^\tau) (-2 S_{mn}^\tau S_{mn}^\tau + 2) + \\
& S_{ij}^\tau (-2 S_{mn}^\tau S_{mn}^\tau + \Omega_{mn}^\tau \Omega_{mn}^\tau + 1) - S_{ij}^\tau \quad (\text{A.37})
\end{aligned}$$


---

$$\begin{aligned}
& - (S_{ik}^\tau \Omega_{kj}^\tau - \Omega_{ik}^\tau S_{kj}^\tau) - (S_{ik}^\tau S_{kj}^\tau - \frac{1}{3} \delta_{ij} S_{mn}^\tau S_{nm}^\tau) + \\
& S_{ij}^\tau (S_{mn}^\tau S_{mn}^\tau + 1) (-S_{mn}^\tau S_{mn}^\tau + \Omega_{mn}^\tau \Omega_{mn}^\tau + 0.01) \quad (\text{A.38})
\end{aligned}$$


---

---


$$- (S_{ik}^\tau \Omega_{kj}^\tau - \Omega_{ik}^\tau S_{kj}^\tau) + S_{ij}^\tau (-S_{mn}^\tau S_{mn}^\tau + 1.02)(-S_{mn}^\tau S_{mn}^\tau - 2\Omega_{mn}^\tau \Omega_{mn}^\tau + 1.02) - S_{ij}^\tau - \\ (\Omega_{ik}^\tau \Omega_{kj}^\tau - \frac{1}{3}\delta_{ij}\Omega_{nm}^\tau \Omega_{mn}^\tau) \quad (\text{A.39})$$


---

---


$$- (S_{ik}^\tau S_{kj}^\tau - \frac{1}{3}\delta_{ij}S_{mn}^\tau S_{nm}^\tau) - S_{ij}^\tau (S_{mn}^\tau S_{mn}^\tau 2 + 2S_{mn}^\tau S_{mn}^\tau - \Omega_{mn}^\tau \Omega_{mn}^\tau - 0.01) + \\ 2(\Omega_{ik}^\tau \Omega_{kj}^\tau - \frac{1}{3}\delta_{ij}\Omega_{nm}^\tau \Omega_{mn}^\tau) \quad (\text{A.40})$$


---

---


$$- (S_{ik}^\tau \Omega_{kj}^\tau - \Omega_{ik}^\tau S_{kj}^\tau) - S_{ij}^\tau - \\ (\Omega_{ik}^\tau \Omega_{kj}^\tau - \frac{1}{3}\delta_{ij}\Omega_{nm}^\tau \Omega_{mn}^\tau)(-0.01S_{mn}^\tau S_{mn}^\tau + 1)(S_{mn}^\tau S_{mn}^\tau - 1.01) + \\ ((S_{ik}^\tau S_{kj}^\tau - \frac{1}{3}\delta_{ij}S_{mn}^\tau S_{nm}^\tau) - S_{ij}^\tau + \\ (\Omega_{ik}^\tau \Omega_{kj}^\tau - \frac{1}{3}\delta_{ij}\Omega_{nm}^\tau \Omega_{mn}^\tau))(S_{mn}^\tau S_{mn}^\tau - 0.144\Omega_{mn}^\tau \Omega_{mn}^\tau 2 - 1.01) - \\ (\Omega_{ik}^\tau \Omega_{kj}^\tau - \frac{1}{3}\delta_{ij}\Omega_{nm}^\tau \Omega_{mn}^\tau) \quad (\text{A.41})$$


---

---


$$- (S_{ik}^\tau \Omega_{kj}^\tau - \Omega_{ik}^\tau S_{kj}^\tau) - (S_{ik}^\tau S_{kj}^\tau - \frac{1}{3}\delta_{ij}S_{mn}^\tau S_{nm}^\tau) - \\ S_{ij}^\tau (S_{mn}^\tau S_{mn}^\tau 2 + 2S_{mn}^\tau S_{mn}^\tau + \Omega_{mn}^\tau \Omega_{mn}^\tau - 0.015) + \\ ((S_{ik}^\tau S_{kj}^\tau - \frac{1}{3}\delta_{ij}S_{mn}^\tau S_{nm}^\tau) - S_{ij}^\tau)(S_{mn}^\tau S_{mn}^\tau 2 + S_{mn}^\tau S_{mn}^\tau + \Omega_{mn}^\tau \Omega_{mn}^\tau) \quad (\text{A.42})$$


---

---


$$0.318(S_{ik}^\tau \Omega_{kj}^\tau - \Omega_{ik}^\tau S_{kj}^\tau) + S_{ij}^\tau (-S_{mn}^\tau S_{mn}^\tau + \Omega_{mn}^\tau \Omega_{mn}^\tau + 0.01) + 2(\Omega_{ik}^\tau \Omega_{kj}^\tau - \frac{1}{3}\delta_{ij}\Omega_{nm}^\tau \Omega_{mn}^\tau) \quad (\text{A.43})$$


---

---


$$- (S_{ik}^\tau \Omega_{kj}^\tau - \Omega_{ik}^\tau S_{kj}^\tau) - (S_{ik}^\tau S_{kj}^\tau - \frac{1}{3}\delta_{ij}S_{mn}^\tau S_{nm}^\tau) + \\ S_{ij}^\tau (S_{mn}^\tau S_{mn}^\tau (-S_{mn}^\tau S_{mn}^\tau + \Omega_{mn}^\tau \Omega_{mn}^\tau) - 2S_{mn}^\tau S_{mn}^\tau + 0.01) \quad (\text{A.44})$$


---

---


$$- (S_{ik}^\tau \Omega_{kj}^\tau - \Omega_{ik}^\tau S_{kj}^\tau) - (S_{ik}^\tau S_{kj}^\tau - \frac{1}{3}\delta_{ij}S_{mn}^\tau S_{nm}^\tau) + S_{ij}^\tau (-2S_{mn}^\tau S_{mn}^\tau + 0.01)(S_{mn}^\tau S_{mn}^\tau + 0.99) \quad (\text{A.45})$$


---

---


$$- (S_{ik}^\tau \Omega_{kj}^\tau - \Omega_{ik}^\tau S_{kj}^\tau) - (S_{ik}^\tau S_{kj}^\tau - \frac{1}{3}\delta_{ij}S_{mn}^\tau S_{nm}^\tau)(-S_{mn}^\tau S_{mn}^\tau + 0.01) - \\ (S_{ik}^\tau S_{kj}^\tau - \frac{1}{3}\delta_{ij}S_{mn}^\tau S_{nm}^\tau) - 2S_{ij}^\tau S_{mn}^\tau S_{mn}^\tau \quad (\text{A.46})$$


---

$$\begin{aligned}
& - (S_{ik}^\tau \Omega_{kj}^\tau - \Omega_{ik}^\tau S_{kj}^\tau) - (S_{ik}^\tau S_{kj}^\tau - \frac{1}{3} \delta_{ij} S_{mn}^\tau S_{nm}^\tau) + S_{ij}^\tau (-S_{mn}^\tau S_{mn}^\tau 2 - S_{mn}^\tau S_{mn}^\tau + 0.01) - \\
& S_{ij}^\tau (S_{mn}^\tau S_{mn}^\tau 2 + S_{mn}^\tau S_{mn}^\tau + 0.01)
\end{aligned} \tag{A.47}$$


---

$$\begin{aligned}
& - 0.333 (S_{ik}^\tau S_{kj}^\tau - \frac{1}{3} \delta_{ij} S_{mn}^\tau S_{nm}^\tau) - S_{ij}^\tau (S_{mn}^\tau S_{mn}^\tau + 0.01) + (\Omega_{ik}^\tau \Omega_{kj}^\tau - \frac{1}{3} \delta_{ij} \Omega_{nm}^\tau \Omega_{mn}^\tau)
\end{aligned} \tag{A.48}$$


---

$$\begin{aligned}
& - (S_{ik}^\tau \Omega_{kj}^\tau - \Omega_{ik}^\tau S_{kj}^\tau) - (S_{ik}^\tau S_{kj}^\tau - \frac{1}{3} \delta_{ij} S_{mn}^\tau S_{nm}^\tau) - 2S_{ij}^\tau S_{mn}^\tau S_{mn}^\tau (2S_{mn}^\tau S_{mn}^\tau - 0.01) - \\
& (\Omega_{ik}^\tau \Omega_{kj}^\tau - \frac{1}{3} \delta_{ij} \Omega_{nm}^\tau \Omega_{mn}^\tau)
\end{aligned} \tag{A.49}$$


---

$$\begin{aligned}
& - (S_{ik}^\tau \Omega_{kj}^\tau - \Omega_{ik}^\tau S_{kj}^\tau) - (S_{ik}^\tau S_{kj}^\tau - \frac{1}{3} \delta_{ij} S_{mn}^\tau S_{nm}^\tau) + \\
& S_{ij}^\tau (2S_{mn}^\tau S_{mn}^\tau - 1)(\Omega_{mn}^\tau \Omega_{mn}^\tau - 1.01) - S_{ij}^\tau
\end{aligned} \tag{A.50}$$



# Bibliography

- Abe , K., Jang , Y. J., and Leschziner , M. A. An investigation of the wall-anisotropy expressions and length-scale equations for non-linear eddy-viscosity models. *International Journal of Heat and Fluid Flow*, 24:181–198, 2003.
- Abe , K., Kondoh , T., and Nagano , Y. On Reynolds-stress expressions and near-wall scaling parameters for predicting wall and homogeneous turbulent shear flows. *International journal of heat and fluid flow*, 18(3):266–282, 1997.
- Al-Sharif , S. F. Reynolds Stress Transport Modelling. In Zhu , J., editor, *Computation Simulations and Applications*. InTech, 2011. ISBN 978-953-307-430-6.
- Almeida , C. P., Gonçalves , R. A., Delgado , M. R., Goldbarg , E. F., and Goldbarg , M. C. A Transgenetic Algorithm for the bi-objective traveling purchaser problem. In *Evolutionary Computation (CEC), 2010 IEEE Congress on*, pages 1–8, July 2010.
- Almeida , G. P., Durao , D. F. G., and Heitor , M. V. Wake flows behind two-dimensional model hills. *Experimental Thermal and Fluid Science*, 7(1):87–101, 1993.
- Anderson , J. *Computational Fluid Dynamics*. McGraw-Hill Science/Engineering/Math, 1995.
- Anupindi , K. and Sandberg , R. D. An embedded les-rans solver for aerodynamic simulations. In *22nd AIAA Computational Fluid Dynamics Conference*, page 2920, 2015.
- Applegate , D. L. *The traveling salesman problem: a computational study*. Princeton University Press, 2006.
- Armenio , V. and Piomelli , U. A Lagrangian mixed subgrid-scale model in generalised coordinates. *Flow, Turbulence and Combustion*, 65:51–81, 2000.
- Baggett , J. S. On the feasibility of merging les with rans for the near-wall region of attached turbulent flows. *Annual Research Briefs*, pages 267–277, 1998.
- Baker , J. E. Reducing Bias and Inefficiency in the Selection Algorithm. In *Proceedings of the Second International Conference on Genetic Algorithms on Genetic Algorithms and Their Application*, pages 14–21, Hillsdale, NJ, USA, 1987. L. Erlbaum Associates Inc. ISBN 0-8058-0158-8.

- Balaras , E. and Benocci , C. Subgrid-scale models in finite-difference simulations of complex wall bounded flows. *AGARD, Neuilly-Sur-Seine, France*, 1994.
- Bandyopadhyay , S. and Saha , S. Gaps: A clustering method using a new point symmetry-based distance measure. *Pattern Recognition*, 40(12):3430–3451, 2007.
- Batten , P., Goldberg , U., and Chakravarthy , S. Sub-grid turbulence modeling for unsteady flow with acoustic resonance. In *AIAA Paper 00-0473, 38th AIAA Aerospace Sciences Meeting, Reno, NV*, 2000.
- Batten , P., Goldberg , U., and Chakravarthy , S. LNSan approach towards embedded LES. *AIAA paper*, 427:2002, 2002.
- Bech , K. H., Tillmark , N., Alfredsson , P. H., and Andersson , H. I. An investigation of turbulent plane Couette flow at low Reynolds numbers. *Journal of Fluid Mechanics*, 304:285–319, 1995.
- Boussinesq , J. Essai sur la theorie des eaux courantes. *Memoires presentes par divers savants a l'Academie des Sciences XXIII*, 1:1–680, 1877.
- Braza , M. The direct numerical simulation at the service of turbulence modelling methodologies for unsteady aerodynamic flows. In *Proceedings, ECCOMAS 2000 Conference, Barcelona*, pages 11–14, 2000.
- Breuer , M., Peller , N., Rapp , C., and Manhart , M. Flow over periodic hills - Numerical and experimental study in a wide range of Reynolds numbers. *Computers and Fluids*, 38:433–457, 2009.
- Brindle , A. *Genetic Algorithms for Function Optimization*. Phd thesis, University of Alberta, 1981.
- Brownlee , J. *Clever Algorithms: Nature-Inspired Programming Recipes*. Lulu.com, 1st edition, 2011. ISBN 1446785068, 9781446785065.
- Cantwell , B. and Coles , D. An experimental study of entrainment and transport in the turbulent near wake of a circular cylinder. *Journal of fluid mechanics*, 136:321–374, 1983.
- Chaouat , B. and Schiestel , R. A new partially integrated transport model for subgrid-scale stresses and dissipation rate for turbulent developing flows. *Physics of Fluids (1994-present)*, 17(6):65106, 2005.
- Chaouat , B. and Schiestel , R. Hybrid RANS/LES simulations of the turbulent flow over periodic hills at high Reynolds number using the PITM method. *Computers & Fluids*, 84:279–300, 2013.
- Chapman , D. R. Computational aerodynamics development and outlook. *AIAA*, 17, 1979.

- Chen , Y., Tang , C., Zhu , J., Li , C., Qiao , S., Li , R., and Wu , J. Clustering without prior knowledge based on gene expression programming. In *Natural Computation, 2007. ICNC 2007. Third International Conference on*, volume 3, pages 451–455. IEEE, 2007.
- Choi , H. and Moin , P. Grid-point requirements for large eddy simulation: Chapman’s estimates. *Physics of Fluids*, 24, 2012.
- Chou , C.-H., Su , M.-C., and Lai , E. Symmetry as a new measure for cluster validity. In *2nd WSEAS Int. Conf. on Scientific Computation and Soft Computing*, pages 209–213, 2002.
- Chou , P. Y. On velocity correlations and the solutions of the equations of turbulent fluctuation. *Quart. Appl. Math*, 3(1):38–54, 1945.
- Collins , R. J. and Jefferson , D. R. *Selection in massively parallel genetic algorithms*. Citeseer, 1991.
- Craft , T., Launder , B., and Suga , K. Development and application of a cubic eddy-viscosity model of turbulence. *International Journal of Heat and Fluid Flow*, 17(2):108–115, 1996.
- Cramer , N. L. A Representation for the Adaptive Generation of Simple Sequential Programs. In *Proceedings of the 1st International Conference on Genetic Algorithms*, pages 183–187, Hillsdale, NJ, USA, 1985. L. Erlbaum Associates Inc. ISBN 0-8058-0426-9.
- Daly , B. J. and Harlow , F. H. Transport Equations in Turbulence. *Physics of Fluids*, 13(11):2634–2649, 1970.
- Darwin , C. On the origin of species by means of natural selection. (1968). *Murray, London*, 1859.
- Davidson , L. and Peng , S.-H. Hybrid LES-RANS modelling: a one-equation SGS model combined with  $\alpha k - \omega$  model for predicting recirculating flows. *International Journal for Numerical Methods in Fluids*, 43(9):1003–1018, 2003.
- Davidson , P. A. *Turbulence: An Introduction to Fluid Dynamics*. Oxford University Press, 2004. ISBN 019852949.
- Davydov , B. I. A Contribution to the statistical dynamics of an incompressible turbulent fluid. *Doklady Akademii Nauk SSSR*, 136(1):47, 1961.
- Dawkins , R. *River Out of Eden: A Darwinian View of Life*. Science masters series. Weidenfeld & Nicolson, 1995. ISBN 9780297815402.
- De Jong , K. A. *An Analysis of the Behavior of a Class of Genetic Adaptive Systems*. PhD thesis, University of Michigan, Ann Arbor, MI, USA, 1975.

- Dean , R. Reynolds number dependence of skin friction and other bulk flow variables in two-dimensional rectangular duct flow. *Journal of Fluids Engineering*, 100(2):215–223, 1978.
- Deardorff , J. W. A numerical study of three-dimensional turbulent channel flow at large reynolds numbers. *Journal of Fluid Mechanics*, 41(02):453–480, 1970.
- Deb , K. *Optimization for engineering design: Algorithms and examples*. PHI Learning Pvt. Ltd., 2012.
- Del Álamo , J. C., Jiménez , J., Zandonade , P., and Moser , R. D. Scaling of the energy spectra of turbulent channels. *Journal of Fluid Mechanics*, 500:135–144, 2004.
- Dembski , W. A. and Ruse , M. *Debating Design: From Darwin to DNA*. Cambridge University Press, 2004. ISBN 9781139459617.
- Deprés , D. *Analyse physique et modélisation des instationnarités dans les écoulements d'arrière-corps transsoniques*. PhD thesis, Université Aix-Marseille 2, 2003.
- Dow , E. and Wang , Q. Quantification of structural uncertainties in the k-  $\omega$  turbulence model. *AIAA Paper*, 1762, 2011.
- Duraisamy , K. and Durbin , P. A. Transition modeling using data driven approaches. In *Proceedings of the Summer Program*, page 427, 2014.
- Durbin , P. A. Near-Wall Turbulence Closure Modeling Without Damping Functions. *Theoretical and Computational Fluid Dynamics*, 3:1–13, 1991.
- Eiben , A. E., Raué , P.-E., and Ruttkay , Z. Genetic Algorithms with Multi-parent Recombination. In *Proceedings of the International Conference on Evolutionary Computation. The Third Conference on Parallel Problem Solving from Nature: Parallel Problem Solving from Nature*, PPSN III, pages 78–87, London, UK, UK, 1994. Springer-Verlag. ISBN 3-540-58484-6.
- El-Behery , S. M. and Hamed , M. H. A comparative study of turbulence models performance for separating flow in a planar asymmetric diffuser. *Computers & Fluids*, 44(1):248–257, 2011.
- Eldrandaly , K. and Negm , A. A. Performance Evaluation of Gene Expression Programming for Hydraulic Data Mining. *The International Arab Journal of Information Technology*, 5(2):126–132, 2008.
- Fabritius , B. *Application of Genetic Algorithms to Problems in Computational Fluid Dynamics*. PhD thesis, University of Exeter, 2014.
- Fasel , H. F., Seidel , J., and Wernz , S. A methodology for simulations of complex turbulent flows. *Journal of fluids engineering*, 124(4):933–942, 2002.

- Fasel , H. F., von Terzi , D., and Sandberg , R. D. A methodology for simulating compressible turbulent flows. *Journal of Applied Mechanics*, 73:405–412, 2006.
- Ferreira , C. Gene Expression Programming: A New Adaptive Algorithm for Solving Problems. *Complex Systems*, 13(2):87–129, 2001.
- Ferreira , C. Analyzing the Founder Effect in Simulated Evolutionary Processes Using Gene Expression Programming. In Abraham , I. A., Ruiz-del Solar , J., and Köppen , M., editors, *Soft Computing Systems: Design, Management and Applications*, pages 153–162. IOS Press, Netherlands, 2002a.
- Ferreira , C. Combinatorial optimization by gene expression programming: inversion revisited. In *Proceedings of the Argentine symposium on Artificial Intelligence*, pages 160–174, 2002b.
- Ferreira , C. Discovery of the Boolean Functions to the Best Density-Classification Rules Using Gene Expression Programming. In *4th European Conference on Genetic Programming, Euro GP*, volume 2278 of *Lecture Notes in Computer Science*, pages 51–60. Springer-Verlag, Berlin, Germany, 2002c.
- Ferreira , C. Function Finding and the Creation of Numerical Constants in Gene Expression Programming. In Benítez , J., Cordón , O., Hoffmann , F., and Roy , R., editors, *Advances in Soft Computing*, pages 257–265. Springer London, 2003. ISBN 978-1-84996-905-5.
- Ferreira , C. Automatically Defined Functions in Gene Expression Programming. In Nedjah , N., Mourelle , L. d. M., and Abraham , A., editors, *Genetic Systems Programming: Theory and Experiences, Studies in Computational Intelligence*, pages 21–56. Springer-Verlag, 2006.
- Ferreira , C. *Gene Expression Programming: Mathematical Modeling by an Artificial Intelligence*. Studies in Computational Intelligence. Springer, 2014. ISBN 9783642069321.
- Ferreira , C., Abraham , I. A., Baets , B. D., and Nickolay , B. Designing Neural Networks Using Gene Expression Programming. In *9th Online World Conference on Soft Computing in Industrial Applications, September 20*, 2004.
- Fogel , D. B. *Evolutionary Computation: Toward a New Philosophy of Machine Intelligence*. IEEE Press, Piscataway, NJ, USA, 1995. ISBN 0-7803-1038-1.
- Fogel , L. J. *Intelligence Through Simulated Evolution: Forty Years of Evolutionary Programming*. John Wiley & Sons, Inc., New York, NY, USA, 1999. ISBN 0-471-33250-X.
- Friedberg , R. M. A Learning Machine: Part I. *IBM Journal of Research and Development*, 2(1):2–13, January 1958. ISSN 0018-8646.

- Friedberg , R. M., Dunham , B., and North , J. H. A Learning Machine: Part II. *IBM Journal of Research and Development*, 3(3):282–287, July 1959. ISSN 0018-8646.
- Fröhlich , J., Mellen , C., Rodi , W., Temmerman , L., and Leschziner , M. Highly resolved large-eddy simulation of separated flow in a channel with streamwise periodic constrictions. *Journal of Fluid Mechanics*, 526:16–66, 2005.
- Fröhlich , J. and Rodi , W. Introduction to large eddy simulation of turbulent flows. *Closure strategies for turbulent and transitional flows*, 1(8):197–224, 2002.
- Fröhlich , J. and von Terzi , D. Hybrid LES/RANS Methods for the Simulation of Turbulent Flows. *Progress in Aerospace Sciences*, 44:349–377, 2008.
- Fukagata , K., Iwamoto , K., and Kasagi , N. Contribution of reynolds stress distribution to the skin friction in wall-bounded flows. *Physics of Fluids (1994-present)*, 14(11): L73–L76, 2002.
- Garnier , E., Mossi , M., Sagaut , P., Comte , P., and Deville , M. On the use of shock-capturing schemes for large-eddy simulation. *Journal of Computational Physics*, 153 (2):273–311, 1999.
- Gautier , N., Aider , J.-L., Duriez , T., Noack , B., Segond , M., and Abel , M. Closed-loop separation control using machine learning. *Journal of Fluid Mechanics*, 770: 442–457, 2015.
- Germano , M. Comment on “Turbulence Modeling for Time-dependent RANS and VLES: A Review”. *AIAA Journal*, 36(9), 1998.
- Gibson , M. M. and Launder , B. E. Ground Effects on Pressure Fluctuations in the Atmospheric Boundary Layer. *Journal of Fluid Mechanics*, 86:491–511, 1978.
- Girimaji , S. S. Fully-Explicit and Self-Consistent Algebraic Reynolds Stress Model. *Theoretical and Computational Fluid Dynamics*, 8(6):387–402, 1996.
- Girimaji , S. S. A Galilean invariant explicit algebraic Reynolds stress model for turbulent curved flows. *Physics of Fluids*, 9(4):1067–1077, 1997.
- Girimaji , S. S. Partially-averaged Navier-Stokes model for turbulence: A Reynolds-averaged Navier-Stokes to direct numerical simulation bridging method. *Journal of Applied Mechanics*, 73(3):413–421, 2006.
- Goldberg , D. E. *Genetic Algorithms in Search, Optimization and Machine Learning*. Addison-Wesley Longman Publishing Co., Inc., Boston, MA, USA, 1st edition, 1989. ISBN 0201157675.
- Goldberg , D. E. *The Design of Innovation: Lessons from and for Competent Genetic Algorithms*. Kluwer Academic Publishers, Norwell, MA, USA, 2002. ISBN 1402070985.

- Grundestam , O., Wallin , S., and Johansen , A. V. An explicit algebraic Reynolds stress model based on a nonlinear pressure strain rate model. *International Journal of Heat and Fluid Flow*, 26:732–745, 2005.
- Ha Minh , H. and Kourta , A. Semi-deterministic turbulence modelling for flows dominated by strong organized structures. In *Proceedings 9th International Symposium on Turbulent Shear Flows, Kyoto, Japan*. Springer-Verlag, Berlin, volume 1, pages 10–15, 1993.
- Han , J., Kamber , M., and Pei , J. *Data mining: concepts and techniques: concepts and techniques*. Elsevier, 2011.
- Hanjalic , K. Will RANS survive LES? A view of perspectives. *Journal of fluids engineering*, 127(5):831–839, 2005.
- Hanjalic , K. and Launder , B. E. A Reynolds stress model of turbulence and its application to thin shear flows. *Journal of fluid Mechanics*, 52(04):609–638, 1972.
- Hanjalić , K. and Kenjeres , S. Reorganization of turbulence structure in magnetic Rayleigh-Bnard convection: a T-RANS study. *Journal of Turbulence*, 1(1):8, 2000.
- Harvey , I. Artificial evolution: a continuing SAGA. In *Evolutionary robotics. From intelligent robotics to artificial life*, pages 94–109. Springer, 2001.
- Haykin , S. S., Haykin , S. S., Haykin , S. S., and Haykin , S. S. *Neural networks and learning machines*, volume 3. Pearson Education Upper Saddle River, 2009.
- Hellsten , A. Curvature Corrections for Algebraic Reynolds Stress Modeling: A Discussion. *AIAA Journal*, 40(9):1909–1911, 2002.
- Hellsten , A. K. New advanced kw turbulence model for high-lift aerodynamics. *AIAA journal*, 43(9):1857–1869, 2005.
- Henn , D. S. and Sykes , R. I. Large-eddy simulation of flow over wavy surfaces. *Journal of Fluid Mechanics*, 383:75–112, 1999.
- Holland , J. H. Outline for a Logical Theory of Adaptive Systems. *J. ACM*, 9(3): 297–314, July 1962. ISSN 0004-5411.
- Holland , J. H. *Adaptation in Natural and Artificial Systems*. MIT Press, Cambridge, MA, USA, 1975. ISBN 0-262-58111-6.
- Hunt , J. and Savill , A. Guidelines and criteria for the use of turbulence models in complex flows. *Prediction of Turbulent Flows*, pages 291–343, 2005.
- Ishihara , T., Gotoh , T., and Kaneda , Y. Study of high-Reynolds number isotropic turbulence by direct numerical simulation. *Annual Review of Fluid Mechanics*, 41: 165–180, 2009.

- Jain , A. K., Murty , M. N., and Flynn , P. J. Data clustering: a review. *ACM computing surveys (CSUR)*, 31(3):264–323, 1999.
- Jakirlić , S., Jester-Zucker , R., and Tropea , C. 9th ERCOFTAC/IAHR/COST Workshop on Refined Flow Modeling. Darmstadt University of Technology, Germany, 2001.
- Jakirlić , S., Jester-Zucker , R., and Tropea , C. ERCOFTAC Bulletin No.55. pages 36–43, 2002.
- Jakirlic , S., Chang , C.-Y., Kutej , L., and Tropea , C. A novel vles model accounting for near-wall turbulence: physical rationale and applications. *Bulletin of the American Physical Society*, 59, 2014.
- Jang , Y. J., Leschziner , M. A., Abe , M. A., and Temmerman , L. Investigation of anisotropy-resolving turbulence models by reference to highly-resolved LES data for separated flow. *Flow, Turbulence and Combustion*, 69:161, 2002.
- Jasak , H., Jemcov , A., and Tukovic , Z. Openfoam: A c++ library for complex physics simulations. In *International workshop on coupled methods in numerical dynamics*, volume 1000, pages 1–20, 2007.
- Jeans , S. J. H. *An Introduction to the Kinetic Theory of Gases*. The University Press, Cambridge, reprint edition, 1962.
- Jenkins , L., Neuhart , D., McGinley , C., and Choudhari , M. Measurements of Unsteady Wake Interference Between Tandem Cylinders. In *Paper No. AIAA-2006-3202*. In *36th AIAA Fluid Dynamics Conference and Exhibit*, 2006.
- Jones , W. P. and Launder , B. E. The Prediction of Laminarization with a Two-Equation Model of Turbulence. *International Journal of Heat and Mass Transfer*, 15: 301–314, 1972.
- Kaneda , Y. and Ishihara , T. High-resolution direct numerical simulation of turbulence. *Journal of Turbulence*, 7, 2006.
- Kaneda , Y., Ishihara , T., Yokokawa , M., Itakura , K., and Uno , A. Energy dissipation rate and energy spectrum in high resolution direct numerical simulations of turbulence in a periodic box. *Physics of Fluids*, 15(2):L21, 2003.
- Karakasis , V. K. and Stafylopatis , A. Data Mining based on Gene Expression Programming and Clonal Selection. In *Evolutionary Computation, 2006. CEC 2006. IEEE Congress on*, pages 514–521, 2006.
- Kaufman , L. and Rousseeuw , P. J. *Finding groups in data: an introduction to cluster analysis*, volume 344. John Wiley & Sons, 2009.
- Keane , A. and Nair , P. *Computational approaches for aerospace design: the pursuit of excellence*. John Wiley & Sons, 2005.

- Khorrami , M. R., Choudhari , M. M., Lockard , D. P., Jenkins , L. N., and McGinley , C. Unsteady Flow Field Around Tandem Cylinders as Prototype Component Interaction in Airframe Noise. *AIAA Journal*, 45(8):1930–1941, 2007.
- Khuri , S., Bäck , T., and Heitkötter , J. The Zero/One Multiple Knapsack Problem and Genetic Algorithms. In *Proceedings of the 1994 ACM Symposium on Applied Computing*, SAC '94, pages 188–193, New York, NY, USA, 1994. ACM. ISBN 0-89791-647-6.
- Kim , J., Moin , P., and Moser , R. Turbulence statistics in fully developed channel flow at low Reynolds number. *Journal of Fluid Mechanics*, 177:133–166, 1987.
- Kim , Y., Castro , I. P., and Xie , Z.-T. Divergence-free turbulence inflow conditions for large-eddy simulations with incompressible flow solvers. *Computers & Fluids*, 84: 56–68, 2013.
- Kiontke , K., Barrière , A., Kolotuev , I., Podbilewicz , B., Sommer , R., Fitch , D. H. A., and Félix , M.-A. Trends, stasis, and drift in the evolution of nematode vulva development. *Current Biology*, 17(22):1925–1937, 2007.
- Kipouros , T., Jaeggi , D., Dawes , B., Parks , G., Savill , M., and Clarkson , P. Insight into high-quality aerodynamic design spaces through multi-objective optimization. *CMES: Computer Modeling in Engineering and Sciences*, 37(1):1–23, 2008.
- Kolmogorov , A. N. The Local Structure of Turbulence in Incompressible Viscous Fluid for Very Large Reynolds Numbers. *Proceedings of the USSR Academy of Sciences*, 30: 299–303, 1941a.
- Kolmogorov , A. N. Equations of turbulent motion in an incompressible fluid. In *Dokl. Akad. Nauk SSSR*, volume 30, pages 299–303, 1941b.
- Kourta , A. Computation of vortex shedding in solid rocket motors using time-dependent turbulence model. *Journal of propulsion and power*, 15(3):390–400, 1999.
- Koza , J. R. *Genetic programming: on the programming of computers by means of natural selection*. MIT Press, Cambridge, MA, USA, 1992. ISBN 0-262-11170-5.
- Koza , J. R., Bennett , F. H., Andre , D., and Keane , M. A. Genetic Programming III: Darwinian Invention and Problem Solving [Book Review]. *Trans. Evol. Comp*, 3(3): 251–253, September 1999. ISSN 1089-778X.
- Koza , J. R. *Genetic Programming II: Automatic Discovery of Reusable Programs*. MIT Press, Cambridge, MA, USA, 1994. ISBN 0-262-11189-6.
- Langdon , W. B. Quadratic Bloat in Genetic Programming. In *Proceedings of the Genetic and Evolutionary Computation Conference (GECCO-2000)*, pages 451458, Las Vegas, pages 451–458. Morgan Kaufmann, 2000.

- Launder , B. E., Reece , G. J., and Rodi , W. Progress in the development of a Reynolds-stress turbulence closure. *Journal of fluid mechanics*, 68(03):537–566, 1975.
- Launder , B. E. and Sharma , B. I. Application of the Energy Dissipation Model of Turbulence to the Calculation of Flow Near a Spinning Disc. *Letters in Heat and Mass Transfer*, 1(2):131–138, 1974.
- Launder , B. E. and Spalding , D. B. Mathematical models of turbulence, 1972, 1972.
- Laurence , D. R., Uribe , J. C., and Utyuzhnikov , S. V. A robust Formulation of the  $v^2 - f$  Model. *Flow, Turbulence and Combustion*, 73:169–185, 2004.
- Lederberg , J. Cell Genetics and Hereditary Symbiosis. *Physiological Reviews*, 32(4): 403–430, 1952.
- Leschziner , M. A. and Lien , F. S. Numerical Aspects of Applying Second-Moment Closure to Complex Flows. In Launder , B. E. and Sandham , N., editors, *Closure Strategies for Turbulent and Transitional Flows*, chapter 5, pages 153–187. Cambridge Univ Press, 2002.
- Lien , F. S. and Leschziner , M. A. Upstream monotonic interpolation for scalar transport with application to complex turbulent flows. *International Journal for Numerical Methods in Fluids*, 19:527–548, 1994.
- Ling , J. and Templeton , J. Evaluation of machine learning algorithms for prediction of regions of high reynolds averaged navier stokes uncertainty. *Physics of Fluids (1994-present)*, 27(8):085103, 2015.
- Lipps , G. *Plasmids: Current Research and Future Trends*. Caister Academic Press, 2008. ISBN 9781904455356.
- Lloyd , S. P. Least squares quantization in pcm. *Information Theory, IEEE Transactions on*, 28(2):129–137, 1982.
- Lockard , D. P. Summary of the Tandem Cylinder Solutions from the Benchmark problems for Airframe Noise Computations-I Workshop. In *AIAA, Aerospace Sciences Meeting Including the New Horizons Forum and Aerospace Exposition*, Orlando, Florida, USA, 2011.
- Lockard , D. P., Khorrami , M. R., Choudhari , M. M., Hutcheson , F. V., Brooks , T. F., and Stead , D. J. Tandem Cylinder Noise Predictions. In *13th AIAA/CEAS Aeroacoustics Conference*, 2007.
- Lozano-Durán , A., Flores , O., and Jiménez , J. The three-dimensional structure of momentum transfer in turbulent channels. *Journal of Fluid Mechanics*, 694:100–130, 2012.

- Lumley , J. L. Computational modeling of turbulent flows. *Advances in applied mechanics*, 18:123–176, 1979.
- Lumley , J. L. and Khajeh-Nouri , B. Computational modeling of turbulent transport. *Advances in Geophysics A*, 18:169–192, 1974.
- Magnient , J.-C. *Simulation des grandes échelles(SGE) d'écoulements de fluides quasi incompressibles*. PhD thesis, Université de Paris, 2001.
- Magnient , J.-C., Sagaut , P., and Deville , M. A study of built-in filter for some eddy viscosity models in large-eddy simulation. *Physics of Fluids (1994-present)*, 13(5): 1440–1449, 2001.
- Manceau , R. and Bonnet , J. 10th ERCOFTAC/IAHR/QNET-CFD Workshop on Refined Turbulence Modelling. Laboratoire d'études Aerodynamics, UMR CNRS 6609, Universite de Poitiers, France, 2003.
- Mao , J. and Jain , A. K. A self-organizing network for hyperellipsoidal clustering (hec). *Neural Networks, IEEE Transactions on*, 7(1):16–29, 1996.
- Margulis , L. and Fester , R. *Symbiosis as a Source of Evolutionary Innovation: Specification and Morphogenesis*. MIT Press, 1991. ISBN 0262132699.
- Mathey , F., Cokljat , D., Bertoglio , J.-P., Sergent , E., and Others . Specification of LES inlet boundary condition using vortex method. *Progress in Computational Fluid Dynamics*, 6:58–67, 2006.
- Mellen , C., Fröhlich , J., and Rodi , W. Large-eddy simulation of the flow over periodic hills. In Deville , M. and Owens , R., editors, *16th IMACS world congress*, Lausanne, Switzerland, 2000.
- Meneghini , J. R., Saltara , F., Siqueira , C. L. R., and Ferrari Jr , J. A. Numerical simulation of flow interference between two circular cylinders in tandem and side-by-side arrangements. *Journal of fluids and structures*, 15(2):327–350, 2001.
- Menter , F. R. Zonal Two Equation  $k-\omega$  Turbulence Models for Aerodynamic Flows. *AIAA Paper 93-2906*, 1993.
- Menter , F. R. Two-Equation Eddy-Viscosity Turbulence Models for Engineering Applications. *AIAA Journal*, 32(8):1598–1605, 1994.
- Menter , F. R., Kuntz , M., and Bender , R. A scale-adaptive simulation model for turbulent flow predictions. *AIAA Paper 2003-0767*, 2003.
- Menter , F. R. Eddy viscosity transport equations and their relation to the  $k-\varepsilon$  model. *Journal of Fluids Engineering*, 119(4):876–884, 1997.
- Michalewicz , Z. *Genetic algorithms+ data structures= evolution programs*. New York: Springer-Verlag, 1996.

- Mitchell , M. Genetic algorithms: An overview. *Complexity*, 1(1):31–39, 1995. ISSN 1099-0526.
- Mitchell , M. An introduction to genetic algorithms. *Cambridge, Massachusetts London, England, Fifth printing*, 3, 1999.
- Monin , A. S. and Yaglom , A. M. *Statistical fluid mechanics Volume 1. Mechanics of turbulence*. MIT Press, Cambridge, 1971.
- Monteiro , S. M. D., Goldbarg , E. F. G., and Goldbarg , M. C. A plasmid based transgenic algorithm for the biobjective minimum spanning tree problem. In *Evolutionary Computation in Combinatorial Optimization*, pages 49–60. Springer, 2009.
- Moser , R., Kim , J., and Mansour , N. N. Direct numerical simulation of turbulent channel flow up to  $Re_\tau = 590$ . *Physics of Fluids*, 11:943–945, 1999.
- Mossi , M. and Sagaut , P. Numerical investigation of fully developed channel flow using shock-capturing schemes. *Computers & fluids*, 32(2):249–274, 2003.
- Murakami , S. Overview of turbulence models applied in CWE–1997. *Journal of Wind Engineering and Industrial Aerodynamics*, 74:1–24, 1998.
- Nakagawa , H. and Nezu , I. Prediction of the contributions to the reynolds stress from bursting events in open-channel flows. *Journal of fluid mechanics*, 80(01):99–128, 1977.
- Naot , D., Shavit , A., and Wolfshtein , M. Prediction of flow in square section ducts. *Mech. Engr. Rept., Technion, Haifa, Intern. Report*, 154, 1972.
- Neuhart , D. H., Jenkins , L. N., Choudhari , M. M., and Khorrami , M. R. Measurements of the flowfield interaction between tandem cylinders. *AIAA paper*, 3275:2009, 2009.
- Nikitin , N., Nicoud , F., Wasistho , B., Squires , K., and Spalart , P. An approach to wall modeling in large-eddy simulations. *Physics of Fluids (1994-present)*, 12(7):1629–1632, 2000.
- Nisizima , S. and Yoshizawa , A. Turbulent channel and Couette flows using a anisotropic k- $\epsilon$  model. *AIAA Journal*, 25:414–420, 1986.
- Orellano , A. and Wengle , H. Numerical simulation (DNS and LES) of manipulated turbulent boundary layer flow over a surface-mounted fence. *European Journal of Mechanics - B/Fluids*, 19(5):765–788, September 2000. ISSN 09977546.
- Parneix , S., Laurence , D., and Durbin , P. Second moment closure analysis of the back-step flow database. In *Proc. 1996 Summer Program, Center for Turbulence Research, NASA Ames/Stanford Univ*, pages 47–62. Citeseer, 1996.

- Piomelli , U., Balaras , E., Pasinato , H., Squires , K. D., and Spalart , P. R. The inner–outer layer interface in large-eddy simulations with wall-layer models. *International Journal of heat and fluid flow*, 24(4):538–550, 2003.
- Pope , S. B. A more general effective-viscosity hypothesis. *Journal of Fluid Mechanics*, 72(2):331–340, 1975.
- Pope , S. B. *Turbulent Flows*. Cambridge University Press, Cambridge, 2000.
- Pope , S. B. A perspective on turbulence modeling. In *Modeling Complex Turbulent Flows*, pages 53–67. Springer, 1999.
- Popovac , M. and Hanjalic , K. Compound wall treatment for rans computation of complex turbulent flows and heat transfer. *Flow, turbulence and combustion*, 78(2):177–202, 2007.
- Prandtl , L. Uber die ausgebildete Turbulenz. *ZAMM*, 5:136–139, 1925.
- Quadrio , M. and Luchini , P. Direct numerical simulation of the turbulent flow in a pipe with annular cross-section. *European Journal of Mechanics B/Fluids*, 21:413–427, 2002.
- Ramesh , T. Traveling purchaser problem. *Opsearch*, 18:78–91, 1981.
- Rapp , C. and Manhart , M. Flow over periodic hills: an experimental study. *Experiments in Fluids*, 51(1):247–269, 2011. ISSN 0723-4864.
- Rechenberg , I. Evolutionsstrategie. *Frommann-Holzboog, Stuttgart, Germany*, 1973.
- Renaud , T., Costes , M., and Péron , S. Computation of GOAHEAD configuration with Chimera assembly. *Aerospace Science and Technology*, 19(1):50–57, 2012.
- Reynolds , O. On the Dynamical Theory of Incompressible Viscous Fluids and the Determination of the Criterion. *Philosophical Transactions of the Royal Society of London. A*, 186:123–164, 1895.
- Reynolds , W. C. Computation of turbulent flows-state-of-the-art. *Technical Report MD-27*, 1970.
- Rodi , W. A new algebraic relation for calculating the Reynolds stresses. *Zeitschrift fuer angewandte Mathematik und Mechanik*, 56, 1976.
- Rodi , W., Bonnin , J., and Buchal , T. ERCOFTAC workshop on data bases and testing of calculation methods for turbulent flows. Karlsruhe, 1995.
- Rodi , W. *The prediction of free turbulent boundary layers by use of a two-equation model of turbulence*. Phd, University of London, 1972.

- Rodi , W. and G. , S. Calculation of Curved Shear Layers with Two-Equation Turbulence Models. *Physics of Fluids*, 26:1422–1436, 1983.
- Rotta , J. Statistische Theorie nichthomogener Turbulenz. *Zeitschrift für Physik*, 131 (1):51–77, 1951.
- Rumsey , C. L., Gatski , T. B., and Morrison , J. H. Turbulence Model Predictions of Extra-Strain Rate Effects in Strong-curved Flows. In *37th Aerospace Sciences Meeting & Exhibit, AIAA 99-0157*, Reno, NV, USA, 1999.
- Rumsey , C. L., Gatski , T. B., and Morrison , J. H. Turbulence Model Predictions of Strongly Curved Flow in a U-Duct. *AIAA Journal*, 38(8):1394–1402, 2000.
- Sagaut , P. *Large Eddy Simulation for Incompressible Flows: An Introduction*. Scientific Computation. Springer, 2006. ISBN 9783540263449.
- Sagaut , P. and Deck , S. Large eddy simulation for aerodynamics: status and perspectives. *Philosophical Transactions of the Royal Society A: Mathematical, Physical and Engineering Sciences*, 367(1899):2849–2860, 2009.
- Sagaut , P., Deck , S., and Terracol , M. *Multiscale and multiresolution approaches in turbulence*. World Scientific, 2013.
- Salvetti , M. V., Damiani , R., and Beux , F. Three-dimensional coarse large-eddy simulations of the flow above two-dimensional sinusoidal waves. *International Journal for Numerical Methods in Fluids*, 35:617–642, 2001.
- Sandberg , R. D. and Fasel , H. F. Application of a new flow simulation methodology for supersonic axisymmetric wakes. In *AIAA 42nd Aerospace Sciences Meeting and Exhibit, Reno, US*, 2004.
- Schmitt , F. G. About Boussinesq's turbulent viscosity hypothesis: historical remarks and a direct evaluation of its validity. *Comptes Rendus Mecanique*, 335(9-10):617–627, 2007.
- Schmitt , F. G. and Hirsch , C. Experimental study of the constitutive equation for an axisymmetric complex turbulent flow. *Zeit. ang. Math. Mech.*, 80:815–825, 2000.
- Schumann , U. Subgrid scale model for finite difference simulations of turbulent flows in plane channels and annuli. *Journal of computational physics*, 18(4):376–404, 1975.
- Schwefel , H.-P. *Numerische Optimierung von Computer-Modellen mittels der Evolutionsstrategie : mit einer vergleichenden Einführung in die Hill-Climbing- und Zu-fallsstrategie*. Birkhäuser, Basel; Stuttgart, 1 edition, 1977.
- Sigurdson , L. W. The structure and control of a turbulent reattaching flow. *Journal of Fluid Mechanics*, 298:139–165, 1995.

- Simonsen , A. J. and Krogstad , P.-A. Turbulent stress invariant analysis: clarification of existing terminology. *Physics of Fluids (1994-present)*, 17(8):88103, 2005.
- Sinkovics , J., Horvath , J., and Horak , A. The origin and evolution of viruses (a review). *Acta microbiologica et immunologica Hungarica*, 45(3-4):349–390, 1997.
- Smagorinsky , J. General circulation experiments with the primitive equations: I. The basic experiment\*. *Monthly weather review*, 91(3):99–164, 1963.
- Smith , J. M. and Szathmáry , E. *The Major Transitions in Evolution*. W.H. Freeman Spektrum, 1995. ISBN 9780716745259.
- Spalart , P. R. Direct simulation of a turbulent boundary layer up to  $Rt = 1410$ . *Journal of Fluid Mechanics*, 187:61–98, 1988.
- Spalart , P. R. Strategies for turbulence modelling and simulations. *International Journal of Heat and Fluid Flow*, 21(3):252–263, 2000.
- Spalart , P. R. and Allmaras , S. R. A one-equation turbulence model for aerodynamics flows. In *AIAA, Aerospace Sciences Meeting and Exhibit, 30th,,* page 23, Reno, NV, USA, 1992.
- Spalart , P. R. and Bogue , D. R. The role of CFD in aerodynamics, off-design. *Aeronautical Journal*, 107(1072):323–329, 2003.
- Spalart , P. R., Deck , S., Shur , M. L., Squires , K. D., Strelets , M., and Travin , A. A New Version of Detached-eddy Simulation, Resistant to Ambiguous Grid Densities. *Theoretical and Computational Fluid Dynamics*, 20(3):181–195, 2006. ISSN 0935-4964.
- Spalart , P. R., Jou , W.-H., Strelets , M., and Allmaras , S. R. Comments on the feasibility of LES for wings, and on a Hybrid RANS/LES approach. In Liu , C. and Liu , Z., editors, *Advances in DNS/LES*, pages 137–147. Gayden Press, 1997.
- Spalart , P. R. and Rumsey , C. L. Effective inflow conditions for turbulence models in aerodynamic calculations. *AIAA journal*, 45(10):2544–2553, 2007.
- Speziale , C. G. On nonlinear  $k-\ell$  and  $k-\epsilon$  models of turbulence. *Journal of Fluid Mechanics*, 178:458, 1987.
- Speziale , C. G. Analytical Methods for the Development of Reynolds-Stress Closures in Turbulence. *Annual Review of Fluid Mechanics*, 23(1):107–157, 1991.
- Speziale , C. G. Comparison of Explicit and Traditional Algebraic Stress Models of Turbulence. *AIAA Journal*, 35(9):1506–1509, 1997.
- Speziale , C. G. Turbulence modeling for time-dependent RANS and VLES: A review. *AIAA Journal*, 36(2):173–184, 1998.

- Speziale , C. G., Sarkar , S., and Gatski , T. B. Modelling the pressure-strain correlation of turbulence: an invariant dynamical systems approach. *Journal of Fluid Mechanics*, 227:245–272, 1991.
- Steeb , W.-H. *The nonlinear workbook: chaos, fractals, cellular automata, neural networks, genetic algorithms, gene expression programming, support vector machine, wavelets, hidden Markov models, fuzzy logic with C++, Java and SymbolicC++ programs*. World Scientific, 2011.
- Strelets , M. *Detached eddy simulation of massively separated flows*. American Institute of Aeronautics & Astronautics, 2001.
- Su , M.-C. and Chou , C.-H. A modified version of the k-means algorithm with a distance based on cluster symmetry. *IEEE Transactions on Pattern Analysis & Machine Intelligence*, 6:674–680, 2001.
- Syswerda , G. Uniform crossover in genetic algorithms. In *Third International Conference on Genetic Algorithms*. Morgan Kaufmann Publishers, Inc., 1989.
- Syswerda , G. A study of reproduction in generational and steady state genetic algorithms. *Foundations of genetic algorithms*, 2:94–101, 1991.
- Taulbee , S. B. An improved algebraic Reynolds stress model and corresponding non-linear stress model. *Physics of Fluids*, 4(11):2555–2561, 1992.
- Temmerman , L. and Leschziner , M. A. Large Eddy Simulation of separated flow in a streamwise periodic channel construction. In *International Symposium on Turbulence and Shear Flow Phenomena*, Stockholm, Sweden, 2001.
- Tennekes , H. and Lumley , J. L. *A first course in turbulence*. MIT Press, Cambridge, 1972.
- Ting , C.-K. On the Mean Convergence Time of Multi-parent Genetic Algorithms Without Selection. In *Proceedings of the 8th European Conference on Advances in Artificial Life*, ECAL’05, pages 403–412, Berlin, Heidelberg, 2005. Springer-Verlag. ISBN 3-540-28848-1, 978-3-540-28848-0.
- Townsend , A. Equilibrium layers and wall turbulence. *Journal of Fluid Mechanics*, 11 (01):97–120, 1961.
- Townsend , A. The structure of turbulent shear flow. *Cambridge UP, Cambridge*, 1976.
- Tracey , B. D., Duraisamy , K., and Alonso , J. J. A Machine Learning Strategy to Assist Turbulence Model Development. In *53rd AIAA Aerospace Sciences Meeting*, AIAA SciTech. American Institute of Aeronautics and Astronautics, January 2015.
- Travin , A., Shur , M., Spalart , P. R., and Strelets , M. On URANS solutions with LES-like behaviour. In *Proc. ECCOMAS*, 2004.

- Tritton , D. J. *Physical Fluid Dynamics (Oxford Science Publications)*. Oxford University Press, USA, 1988.
- Vinuesa , R., Noorani , A., Lozano-Durán , A., Khoury , G. K. E., Schlatter , P., Fischer , P. F., and Nagib , H. M. Aspect ratio effects in turbulent duct flows studied through direct numerical simulation. *Journal of Turbulence*, 15(10):677–706, 2014.
- Vinuesa , R., Schlatter , P., Malm , J., Mavriplis , C., and Henningson , D. S. Direct numerical simulation of the flow around a wall-mounted square cylinder under various inflow conditions. *Journal of Turbulence*, 16(6):555–587, 2015.
- von Terzi , D., Hinterberger , C., García-Villalba , M., Fröhlich , J., Rodi , W., and Mary , I. LES with downstream RANS for flow over periodic hills and a model combustor flow. In *EUROMECH colloquium*, volume 469, pages 6–8, 2005.
- Šarić , S., Jakirlić , S., Breuer , M., Jaffrézic , B., Deng , G., Chikhaoui , O., Fröhlich , J., von Terzi , D., Manhart , M., and Peller , N. Evaluation of Detached Eddy Simulations for Predicting the Flow over Periodic Hills. In Cancès , E. and Gerbeau , J., editors, *ESAIM proceedings*, pages 133–145, 2007.
- Wallace , J. M., Eckelmann , H., and Brodkey , R. S. The wall region in turbulent shear flow. *Journal of Fluid Mechanics*, 54(01):39–48, 1972.
- Wallin , S. and Johansen , A. V. An explicit algebraic Reynolds stress model for incompressible and compressible turbulent flows. *Journal of Fluid Mechanics*, 403:89–132, 2000.
- Wang , C., Yang , Y. A., and Leschziner , M. A. Modelling two- and three-dimensional separation from curved surfaces with anisotropy-resolving turbulence closures. *International Journal of Heat and Fluid Flow*, 25:499–512, 2004.
- Weatheritt , J. and Sandberg , R. D. A new Reynolds stress damping function for Hybrid RANS/LES with an evolved functional form. In *IUTAM Symposium on Advances in Computation, Modeling and Control of Transitional and Turbulent Flows*, Goa, India, 2014.
- Weatheritt , J. and Sandberg , R. D. Use of Symbolic Regression for construction of Reynolds-stress damping functions for Hybrid RANS/LES. In *53rd AIAA Aerospace Sciences Meeting*, AIAA SciTech. American Institute of Aeronautics and Astronautics, January 2015.
- Weinmann , M. *Simulation Strategies for Complex Turbulent Flows*. PhD thesis, University of Southampton, 2011.
- Weinmann , M., Sandberg , R. D., and Doolan , C. Tandem cylinder flow and noise predictions using a Hybrid RANS/LES approach. *International Journal of Heat and Fluid Flow*, 50:263—278, 2014.

- Weinmann , M. and Sandberg , R. D. Suitability of Explicit Algebraic Stress Models for predicting complex three-dimensional flows. In *19th AIAA Computational Fluid Dynamics*. 2009.
- Wilcox , D. C. Re-assessment of the scale-determining equation for advanced turbulence models. *AIAA Journal*, 26(11):1299–1310, 1988.
- Wilcox , D. C. *Turbulence Modeling for CFD*. DCW Industries, Michigan, 2 edition, 1994.
- Wilcox , D. C. *Turbulence modeling for CFD*, volume 2. DCW industries La Canada, CA, 1998.
- Willmarth , W. and Lu , S. Structure of the reynolds stress near the wall. *Journal of Fluid Mechanics*, 55(01):65–92, 1972.
- Xu , K., Liu , Y., Tang , R., Zuo , J., Zhu , J., and Tang , C. A novel method for real parameter optimization based on Gene Expression Programming. *Applied Soft Computing*, 9(2):725–737, 2009. ISSN 1568-4946.
- Xu , R., Wunsch , D., and others . Survey of clustering algorithms. *Neural Networks, IEEE Transactions on*, 16(3):645–678, 2005.
- Yamamoto , L. PlasmidPL: A plasmid-inspired language for genetic programming. In *Genetic Programming*, pages 337–349. Springer, 2008.
- Yarlanki , S., Rajendran , B., and Hamann , H. Estimation of turbulence closure coefficients for data centers using machine learning algorithms. In *Thermal and Thermo-mechanical Phenomena in Electronic Systems (ITherm), 2012 13th IEEE Intersociety Conference on*, pages 38–42. IEEE, 2012.
- Zelinka , I., Celikovsky , S., Richter , H., and Chen , G. *Evolutionary Algorithms and Chaotic Systems*. Studies in Computational Intelligence. Springer, 2010. ISBN 9783642107061.
- Zhang , H. L., Bachman , C. R., and Fasel , H. F. Application of a New Methodology for Simulations of Complex Turbulent Flows. *AIAA Paper*, pages 2000–2535, 2000.
- Zhang , Z. J. and Duraisamy , K. Machine Learning Methods for Data-Driven Turbulence Modeling. In *22nd AIAA Computational Fluid Dynamics Conference*, AIAA Aviation. American Institute of Aeronautics and Astronautics, June 2015.
- Zheng , Y., Jia , L., and Cao , H. Multi-Objective Gene Expression Programming for Clustering. *Information Technology And Control*, 41(3):283–294, 2012.
- Zhou , A., Qu , B.-Y., Li , H., Zhao , S.-Z., Suganthan , P. N., and Zhang , Q. Multiobjective evolutionary algorithms: A survey of the state of the art. *Swarm and Evolutionary Computation*, 1(1):32–49, 2011.